Experimental and analytical studies based on a high swirl combustion chamber representing the DI diesel engine combustion system

White, Colin Laurence

Award date:
1986

Awarding institution:
University of Bath

EXPERIMENTAL AND ANALYTICAL STUDIES BASED ON A HIGH SWIRL COMBUSTION CHAMBER REPRESENTING THE DI DIESEL ENGINE COMBUSTION SYSTEM

submitted by Colin Laurence White
for the degree of Ph.D
of the University of Bath
1986

ProQuest LLC
789 East Eisenhower Parkway
P.O. Box 1346
Ann Arbor, MI 48106-1346

Acknowledgements

I wish to thank the following:-

Professor Frank Wallace & Dr Julian Packer for their guidance and support throughout.

Mr John Pearson for his excellent machining.

Mr Ian Marsh for his invaluable instrumentation work and advice.

Summary

A unique constant volume combustion bomb has been constructed, which can simulate conditions in the small direct injection diesel engine. Initial pre-combustion pressures upto 55 bar, temperatures upto 600 C & air swirl rates upto 10,000 rev/sec have been achieved. Swirl is generated by a drum, located in the chamber, which may be rotated at speeds upto 20,000 rev/sec.

An extensive series of heat release and photographic tests were completed and from these results the effects of pressure, temperature & swirl on the combustion were examined. Also spray penetrations were compared with a number of experimental correlations.

The most interesting qualified conclusions from these results were that:-

1) Ignition delay decreases with swirl.
2) At low initial pressures and temperatures (35 bar, 500 C), the peak burning rate increased with swirl.
3) At higher initial pressures & temperatures (55 bar, 600 C), there was a transition to the peak burning rate decresing slightly with swirl.

In addition to this, a multizone combustion model was developed, which was based on the work of Shahed, Chiu and Lyn. This model was able to reproduce the heat release results obtained from the combustion bomb. However, the model was only really applicable to low swirl, high temperature (short ignition delay) conditions.

CONTENTS Page No.

CONTENTS cont'd Page No.

CONTENTS cont'd Page No.

Notation

For chapters 1 to 5

A_b	-	surface area of bead (m^2)
A_1	-	cross-sectional area of wire (m^2)
B'	-	Temperature coefficient (equ. 5.1)
C_1 to C_5	-	empirical constants in generalised Arrhenius equation
d	-	nozzle orifice diameter (m)
d_m	-	diameter of molecule (m)
E	-	Youngs modulus (N/m^2)
E_a	-	activation energy (J/kgmol)
f_i	-	mass fraction; ratio of mass injected to mass in chamber
h	-	heat transfer coefficient (W/m^2K)
h_c	-	height of combustion chamber (m)
id	-	ignition delay (ms)
I	-	second moment of area (m^4)
k	-	thermal conductivity of wire (m)
k_g	-	radius of gyration (m)
K	-	constant (equ. 5.1)
l	-	shaft length (m)
L	-	nozzle hole length (m)
L_p	-	circumference of wire (m)
L_w	-	length of thermocouple wire (m)
m	-	mass (kg)
m_A	-	mass fraction of A
m_B	-	mass fraction of B
m_{fu}	-	mass fraction of fuel
m_{ox}	-	mass fraction of oxygen
M_A	-	molecular weight of species A
M^*	-	reduced mass of molecule
$\bar{M}$	-	mean molecular weight of mixture
n'	-	index (equ. 5.1)

N_A	-	Avogadro's constant 6.023e26/kgmol
N_S	-	swirl rate (rev/min)
NH	-	number of injector holes
p	-	pressure (N/m^2)
P_A	-	pressure (atmospheres)
r	-	whirl radius (m)
R	-	universal gas constant (kJ/kgmol K)
R_A	-	Arrhenius reaction rate (kg/m^3s)
RPMS	-	swirl rate (rev/min)
s	-	spray penetration (m)
s_w	-	spray penetration in swirl (m)
S	-	Steric factor
t	-	time
t_i	-	injection period (s)
T	-	temperature (K)
T_A	-	air temperature (K)
T_g	-	gas temperature (K)
T_1	-	wire temperature [f(x)] (K)
T_2	-	hot wall temperature (K)
T_3	-	cold wall temperature (K)
$\bar{V}_o$	-	mean discharge velocity (m/s)
w	-	rotational velocity (rad/s)
w_n	-	whirling velocity (rad/s)
x	-	distance from base of thermocouple wire (m)
y_o	-	end deflection of a cantilever with an end load (m)
α_2	-	angle factor for hot wall
α_3	-	angle factor for cold wall
ΔP	-	effective injection pressure (N/m^2)
E_o	-	emissivity of all surfaces (0.7)
ρ_a	-	specific weight of gas (kg/m^3)
ρ_a	-	air density (kg/m^3)
ρ_{atm}	-	atmospheric density (kg/m^3)
ρ_d	-	diesel fuel density (kg/m^3)
ρ_r	-	reference density of diesel fuel (kg/m^3)

		(kg/m^3)
σ	–	Stefan-Boltzmann constant (W/m^2K^4)
ϕP	–	dimensionless parameter for penetration
ϕR	–	ratio of S/ P
ϕS	–	dimensionless parameter for swirl

Subscripts

b	–	bead
d	–	drum
int	–	initial
max	–	maximum
s	–	shaft
w	–	wire

CHAPTER 1

Introduction.

Chapter 1: Introduction

1.1.a General Background

The diesel engine has established itself as the most dominant power unit for commercial vehicles. It has achieved this supremacy by its intrinsic reliability & good fuel economy, with the larger DI units approaching 40% thermal efficiency. In addition it has a good power to weight ratio (particularly in turbocharged form), low pollution levels & reasonable capital cost.

Inroads into the passenger car market are also being made by the diesel engine, but invariably in IDI form. The reasons for this will be discussed in the next section, but may be summarised by saying that the IDI requires less development & a cheaper fuel injection system.

Clearly it would be desirable for the more efficient DI diesel to be adopted for the passenger car in preference to the IDI diesel, particularly if its capital cost could be reduced. Unfortunately the information & resources available for the engine manufacturers to produce a small bore diesel are limited & this has stimulated research in this direction.

1.1.b DI Diesel engine systems

The DI diesel system, also known as the open chamber system, has traditionally been divided into two types; quiescent & swirling. Typically, the quiescent combustion chamber is of the shallow bowl type, as shown by the example in figure 1.1, although the air flow in this system is better described as semi-quiescent. It is necessary to ensure proper fuel distribution for efficient combustion, which is achieved by a multiple hole nozzle with upto 10 holes. However the number of holes is limited in small engines, due to practical problems such as hole blockages & nozzle tip strength.

The swirled DI combustion chamber has a deep bowl, an example of which is shown in figure 1.2. This system is generally used in the smaller bore engines (eg bus & truck engines) where the number of holes is limited & a certain amount of swirl is required for efficient combustion.

Various inlet port designs are used to generate the swirl. Figure 1.3 shows some of the more common designs used. The advantages & disadvantages of each system will not be discussed here, but any design needs to be a compromise with the best performance achieved over a narrow range of engine speed. This range may be extended by the better matching of the injection system to the swirl.

A third type of DI system, which may be considered as a subset of the swirled DI engine, is the MAN M-system. The fuel is sprayed onto the piston wall

through a single hole nozzle, as shown in figure 1.4. where it spreads into a thin film. Combustion is controlled by the rate of fuel evaporation from the piston wall.

1.1.c Combustion in the DI Diesel Engine

In a typical engine with swirl, diesel fuel is injected through a multi-hole nozzle under high pressure (200 to 600 bar). The spray breaks up into droplets a short distance from the nozzle, with a mean diameter around 15 micrometers (3). As the combustion chamber air temperatures & pressures normally exceed the critical point for the fuel, these droplets quickly evaporate (4) & the outer portion of the spray will primarily be in gaseous form.

A short delay from the start of the injection to the ignition of the fuel occurs. The length of this delay can be difficult to determine under abnormal conditions, although under normal conditions it is fairly clear. From the engine performance point of view, the point of ignition is defined as the start of rapid pressure rise. The time difference between the appearance of visible flame & rapid pressure rise is normally negligible (5).

Combustion takes place in the vapour phase & it is generally accepted that the ignition delay is a combination of both physical & chemical delays which overlap (5,6,7). Lyn & Valdmanis (5) split the physical factors into two groups; those pertaining to fuel spray characteristics & those pertaining to the

engine conditions. The factors considered under spray characteristics are:-

a) Injection timing
b) Quantity of fuel injected
c) Velocity of fuel injected
d) Rate of injection
e) Drop size
f) Spray form

The factors grouped under the heading of engine characteristics are:-

g) Compression temperature
h) Compression pressure
i) Air velocity
j) Engine speed

In an engine under normal operating conditions, compression temperature & pressure are the major factors affecting ignition delay. All the other factors have only secondary effects. For example, the injection timing determines the mean pressure & temperature seen by the fuel before ignition & a change in engine speed alters the temperature/time & pressure/time relationships. Other factors such as fuel quantity injected, only become significant under abnormal engine operating conditions such as starting.

The chemical delay is controlled by chemical kinetics; ie the fuel/air reaction rate increases with temperature, so that the relationship between the reaction rate & time is as shown in figure 1.5.

Ignition is normally considered to be at the point where the reaction rate increases dramatically. The temperature at this point is called the autoignition temperature for the fuel.

The essential conditions for ignition are that a region of vapour/air mixture within the inflammability limits, must be formed & suspended within these limits, for a sufficient length of time for the chemical delay to lapse. Wakil et al (6) studied the relationship between the vapour fuel/air ratio and equilibrium temperature when different quantities of liquid fuel and hot air are combined. This relationship is shown in figure 1.6. Clearly, as the quantity of cold fuel is reduced relative to the air, the resulting equilibrium temperature must increase. For zero fuel the equilibrium temperature equals the initial air temperature and vice versa for zero air. However, the peak fuel vapour/air ratio will occur when there is only enough energy in the air to just convert all the liquid fuel into vapour; ie, the saturation point 'A' in figure 1.6. There are also two bands in which the ratio of liquid fuel to air will produce a vapour/air mixture between the inflammability limits for the fuel; ie, bands 'B' and 'C' in figure 1.6. Ignition, if possible, will always occur in the upper band 'C' first. Wakil et al also demonstrated that for small quantities of fuel, the time to equilibrium was very short, relative to ignition delay times.

When this theory is applied to a fuel spray, the only place where ignition may occur is towards the outer boundary of the spray, where the fuel vapour/air

ratio is within the inflammability limits and above the autoignition temperature. At any point in a fuel spray, the ratio of liquid fuel to air is always changing. Therefore for ignition to occur, the correct fuel vapour/air ratio must be suspended for a long enough time within the inflammability limits for the chemical (ignition) delay to pass. Several workers (5, 7, 8) have observed that the initiation of combustion is not at the fringe of the fuel jet, but between the fringe and the core in the above mentioned zone.

Pre-mixed combustion

In a DI diesel engine, the spatial position where ignition occurs is not fixed, but varies slightly from cycle to cycle. Quite often there may be several ignition points. Combustion spreads from these points and consumes the fuel/air mixture that is within the limits of inflammability. This pre-mixed phase, which is mainly controlled by the chemical reaction rate, continues until the prepared fuel is consumed and mixing controlled combustion takes over.

Combustion generated noise mainly occurs during this pre-mixed phase of combustion, where the rates of pressure rise are highest. In a typical DI engine rates of pressure rise of 8 to 10 bar/crank angle can be expected. This may be reduced by decreasing the ignition delay or the initial rate of mixing. The ignition delay may be reduced, for example, by turbocharging or adjusting the ignition timing for minimum noise. These measures effectively increase the mean temperature & pressure seen by the fuel

before ignition. Turbocharging is only effective in decreasing the ignition delay while there is some boost pressure, which cannot be ensured due to turbo-lag during acceleration. A method of controlling the mixing rate is by the MAN M-system, in which the fuel is deposited on the piston wall by a single spray. The combustion rate is then controlled by the rate of mixing off the wall.

Diffusion Combustion

By the end of the pre-mixed stage, when the piston is around TDC, the pressures & temperatures reached in the chamber are high enough for the fuel to burn almost as it enters the chamber. Combustion is then mainly controlled by the mixing rate, piston movement & availability of oxygen. If the ignition delay is short enough for the mixing rate to be increasing after the pre-mixed spike, the heat-release rate reaches a 2nd peak as demonstrated in figure 1.7.

For optimum thermal efficiency, it would be desirable if the heat release rate could be such that a constant peak pressure could be maintained until the fuel is consumed, the constraint on the peak pressure being the mechanical strength of the engine. Unfortunately the process of combustion in a confined space is inherently incompatible with this desired situation. As the piston progresses down the engine cylinder the driving forces for combustion reduce. The pressure & temperature drop due to the increasing volume & the mixing rate decreases due to: a) the end of injection, b) reduced gas velocities, c) depletion of the available reactants. This causes the

combustion to tail off & continue inefficiently at low temperature well down the piston stroke.

Pollutants: Particulates & Unburned Hydrocarbons

Various forms of particulates are produced by the diesel engine, depending on the operating conditions & combustion system. These particulates may be sub-divided into the following three groups:-

1) Liquid particulates, which appear as white or blue smoke. These are emitted under cold starting conditions, idling & low loads. They are formed from unburnt or partially burnt hydrocarbons & the colour is a function of droplet size. Blue smoke results from particulates less than 0.5 micrometers in diameter which are formed from recondensed HC's (hydrocarbons) their derivatives. White smoke particulates are formed from the original fuel droplets.

2) Soot or black smoke is formed as a product of incomplete combustion, particularly at high loads.

3) Other particulates include lubricating oil & fuel additives. Smoke from lubricating oil is not normally a problem in a well designed engine that is in good condition.

The sources of liquid particulates are numerous. They may be caused by shortcomings in the injection system, some of which may be easily solved & some of

which are inherent in operating over a wide speed range. For example, low injector closing pressure, leads to injector dribble as does a large sac volume. Secondary injections are also a source of liquid particulates, or unburned HC's.

Unburned HC's may also be caused by wall impingement of the fuel spray, where, due to the proximity of the wall, combustion is not possible. The amount of unburned HC's is inversely related to the wall temperature & evaporation rate. A large top band clearance can also produce HC emissions from the combustion free zone between the piston & cylinder wall. The minimum size of the top band clearance is limited by the maximum permissible piston ring temperature.

During the ignition delay a certain amount of fuel will be over diluted & too lean to burn once combustion is initiated. This region may be referred to as the Lean Flame Out Region or LFOR for short (9). It is believed that this area is one of the main sources of unburnt HC's. The size of this region depends on many factors, such as the pressure & temperature in the chamber, air motion & the type of fuel (ie lean flammability limit of the fuel). Higher temperatures & pressures decrease the lean inflammability limit & the ignition delay & therefore the LFOR. Also, under idling conditions, a large proportion of the fuel injected will be in this LFOR & the ratio of unburned HC's formed in this region to the total fuel injected will be at its highest.

At higher loads, the unburned HC's from the LFOR, the core & the fuel deposited on the walls, will be partially oxidised later in the combustion process, because of the higher temperatures & pressures. The relationship between fuel air ratio & HC emission is shown in figure 1.8. At high loads, most of the HC's come from the walls (9). The higher pressures & temperatures associated with turbocharging also reduce HC emissions (10).

An advance in injection timing has also been shown to increase the HC emissions (11). Advanced injection timing causes a longer ignition delay, which allows a larger LFOR to be formed & more fuel to be deposited on the walls.

Black smoke or soot consists of irregularly shaped, agglomerated, fine carbon particles. The major source of black smoke is in the spray core, where there is a shortage of oxygen. The process of soot formation within the core is considered to be as follows (12):-

1) Pyrolysis & incomplete combustion of the fuel molecules produces a supersaturated agglomeration of condensible precurser molecules, which are the building blocks of soot nuclei. This process takes a few microseconds.

2) Within a further few microseconds, these soot nuclei combine, coagulate & grow to spherules of 20 nanometers diameter (time duration 0.05ms).

3) These spherules form chains to make up soot particules until either the precurser molecules are depleted or their formation is terminated by expansion & cooling.

Oxidation of the spherules also occurs, as they are diluted with air, but the time required for the oxidation of 40 nanometer particles is of the same order as the cycle time. So if particulates grow above a certain size, they will not be completely consumed later on in the cycle. 60% of soot formed may be consumed later by oxidation. The extent of oxidation depends on the concentration of oxygen, temperature & residence time in the chamber (8, 12, 13). Smoke particulates may also be formed from fuel deposited on the chamber wall by the same process as occurs in the spray core.

Khan I.M. (14) found that an increase in the proportion of diffusion burning increases the net exhaust smoke. This was demonstrated by:-

a) Increasing the initial air temperature to shorten the ignition delay & therefore increase the amount of diffusion burning.

b) Adjusting the injection timing for minimum ignition delay.

c) Lower injection rates.

d) Pilot injections.

He also found that a decrease in the burning rate increased smoke emissions. Larger diameter nozzle holes increased smoke due to poorer atomization & slower burning. Short nozzle holes decreased smoke by producing bushier, faster burning sprays, although this effect may have also been due to the effectively smaller sac volume.

Nitric Oxides (NOx)

It is now generally accepted that nitric oxide from the exhaust gases of diesel engines, is one of the pollutants which react in the atmosphere to form photochemical smog (15). It is also a well established fact that the formation of NOx in a diesel engine is a non-equilibrium process (16); ie, its production & decomposition is a rate controlled process. Unfortunately, the decompostion of NOx is a relatively slow process compared to cycle events & when combustion gas temperatures have cooled by expansion, the NOx concentrations are effectively frozen at their high temperature levels.

The rate of production of NOx is highly temperature dependent. Chemical equilibrium requirements dictate that most NOx will be concentrated in the lean area of combustion (excess O_2), where the flame temperature is below the peak flame temperature. Peak flame temperatures normally occur at just above the stoichiometric fuel/air ratio.

NOx emissions are difficult to control, as their reduction by present methods is normally at the expense of increased fuel consumption or an increase

in other pollutants. Generally, any reduction in combustion temperature, caused by a change in engine conditions, will decrease NO_x emissions. Retarding the injection timing will decrease the NO_x emissions as a result of reduced combustion temperatures, but this invariably leads to increased smoke & fuel consumption (8,9,17). However, the fuel consumption & smoke may be improved by increasing the injection rate, although this will produce an increase of NO_x. This may be useful when a trade off between fuel consumption, smoke & NO_x emissions is required (17).

Normally, any effect which increases the amount of pre-mixed burning & therefore flame temperature, will increase NO_x emissions. For example, increasing the swirl ratio will increase the mixing rates & therefore the pre-mixed burning, which results in an increase in NO_x emissions (17).

Increasing the compression ratio or using turbocharging both increase the cycle temperatures & it has been observed that this causes an increase in NO_x emissions. Fortunately, it is the peak temperature reached, which affects NO_x emissions most & the reduction in ignition delay, produced by turbocharging for example, may allow the ignition timing to be retarded. This can offset the increase in NOx emissions by decreasing the peak temperature reached, although the mean temperatures will be higher (1,8,9,18).

Exhaust gas recirculation (EGR) may be used to decrease NOx emissions by decreasing the peak

temperature reached. There is a penalty to pay, as usual, with increased particulate emissions, although the increase in fuel consumption is not significant unless more than 15% EGR is used (9). EGR is not used much with automotive engines yet, but its use may increase if the regulations become more servere.

Carbon Monoxide

Carbon monoxide is formed throughout the flame, but only as an intermediate compound (8,19). In the lean flame region at the peak of combustion it is oxidised to CO_2 almost immediately, due to the excess oxygen.

The present low smoke limits require diesel engines to be run with excess air, so most CO formed within a rich zone will eventually be oxidised to CO_2 as it is diluted with excess air. Thus diesel engines usually have little difficulty in meeting legislated levels.

1.2 The Particular Problems of the High Speed Passenger Car Diesel Engine

Market Sector for the Passenger Car Diesel Engine

The diesel engine has for many years provided a high fuel economy alternative to the petrol engine. However, the fuel economy of a vehicle engine is not the only economic consideration. The diesel powered vehicle has always suffered from a first cost premium, which has to be offset against its fuel economy benefits. The economic factors which are of prime importance in the choice of power plant are:-

1) The first cost.
2) The fuel economy of the petrol engine compared with the diesel engine.
3) The cost of diesel & petrol.
4) The distance travelled per annum.
5) The depreciation rates of the petrol powered vehicle & the equivalent diesel powered vehicle.

Generally, the diesel powered vehicle becomes a 'real' economic alternative when the annual mileage is above a certain figure. For the small passenger car, 12000 miles is an often quoted figure, although it can be much higher.

For the private market, economy is not of prime importance; eg the demand for luxury cars.

The performance of the diesel engine in terms of power to weight ratio, even in turbocharged form, has

always been inferior to the petrol engine. Most passenger car diesel engines have a specific output of 24kw/l, with turbocharged diesels reaching specific outputs of upto 33kW/l. Against this, the normally aspirated petrol engine has a specific output of around 37 kW/l (1). In addition, on a litre for litre basis, the diesel engine is heavier.

To obtain the equivalent performance of a petrol powered vehicle by a diesel, one could always use a larger engine, although this would increase the first cost premium. Above a certain performance requirement it may be argued that there is no overall economic advantage in using a diesel.

Noise has, in the past, been a problem with diesel engines. This appears to have been solved and generally the diesel is no noisier than the petrol driven equivalent in the drive by test (1, 20). Also with the CDI wall wetting system (based on the MAN M-system), the typical diesel idle noise is hardly noticeable.

The noise reduction in the drive by test for a typical passenger car diesel, has been achieved by retarding the injection timing from that for optimum performance. As noise regulations become more severe, a retard in injection timing alone will not be satisfactory in meeting these requirements.

To date, the passenger car diesel has had little problem in coping with emission regulations in general for CO, NO_x & HC's. It is only in the area of particulate emissions & smoke that there have been

any real problems & this is reflected in the smoke limited power outputs.

It is not the emissions, which are the real problem, as far as the potential owner of a diesel powered car is concerned, but the effect on the performance of meeting these regulations. The same could be said of noise, although the character or pleasantness of the noise does have an influence on the choice of power plant.

DI Combustion Systems

In the previous section, the type of combustion system was not specified, but a common feature of most passenger car diesel engines is the use of the IDI combustion system, of which there are fundamentally two types; the pre-chamber & the swirl chamber shown in figure 1.9.

The DI system is extensively used in bus & truck engines, because it offers the best economy, reliability & service life (1). The fuel economy is gained from lower heat transfer & friction losses, along with the absence of pumping losses associated with a separate combustion chamber. Investigations by several workers (eg 20, 21) have shown that there would also be a fuel economy benefit if the DI engine were used as the power plant for a passenger car. For example, Monaghan (21) converted an IDI engine (figure 1.10a) into a DI engine (figure 1.10b), which produced a decrease in fuel consumption at equivalent loads.

Although the DI may be able to achieve a 10 to 20% improvement in fuel consumption, manufacturers probably consider that compliance with emission regulations will reduce this advantage to a slight improvement only, if any. For example, Monaghan (21) found that a straight change from an IDI to an equivalent low cost DI would produce a 10% reduction in fuel consumption, but this could be lost if equivalent performance or emissions were desired. The cheaper IDI can also compensate for its poorer fuel economy by inexpensive gearbox modifications or a 5th gear. In addition, because of the IDI's better air utilization, it tends to be 10 to 15% better off in terms of smoke limited power.

Combustion Problems & Advantages of the DI

The requirements for good combustion in a high swirl DI diesel, by comparison to the IDI are much more precise. In the DI, the effect of fuel injection characteristics on engine performance is significant. Timing, duration, shape of the injection rate diagram & spray distribution are all important. It also appears that as the cylinder bore size is decreased, the performance of the DI becomes very sensitive to small changes in combustion chamber shape & form (21).

In the high swirl IDI, spray configuration is not very critical, as mixing is dependent almost entirely on air momentum. The level of swirl is not critical either, as long as it produces thorough mixing of the fuel spray.

To achieve minimum emissions in a DI engine, along with efficient combustion, it is necessary to match the fuel injection to the level of swirl. The problem arises in trying to achieve this match over the full speed range of the engine. The required level of swirl is affected by many factors, the most important of which is the number of nozzle holes. There is an approximate inverse relationship between the number of holes & the level of swirl (22). With a large number of holes, the smoke level is more sensitive to swirl, as shown by figure 1.11, & also the combustion duration is longer due to the lower mixing rates associated with low swirl levels. A long combustion duration is undesirable for high speed operation, because of its adverse effect on emissions & fuel consumption. With a small number of nozzle holes, the generation of the associated high swirl levels by the inlet system tends to reduce the volumetric effeciency. Therefore the swirl generating system has to be carefully designed to minimise its losses, while still being able to generate the required amount of swirl.

There is a rapid decrease in air utilization at high engine speeds, whether the DI engine has a large or small number of nozzle holes. With a large number of nozzle holes, the longer combustion restricts the fuel/air ratio. With a small number of nozzle holes & the associated high swirl levels, the poorer volumetric efficiency reduces the amount of air available. At high engine speeds, the poor volumetric efficiency of the DI has less effect on the thermal efficiency than the high heat transfer losses of the IDI have (22).

For most swirl generating systems, the swirl level is directly related to engine speed (23). It is therefore desirable for the injection angle to be constant, so that the injection rate is directly related to the swirl level. With normal inline &, in particular, rotary fuel pumps, the injection angle increases with engine speed, because of the long injection pipes & general elasticity of the injection system. There are several methods of maintaining a constant injection angle over the full speed range & part loads, but these all involve more expensive fuel injection equipment. The ideal & most expensive solution would be a load & speed governed unit injector.

The mismatch of the swirl to the fuel injection either results in overswirl or underswirl. Overswirl prevents the fuel sprays reaching the air close to the wall & mixing is restricted to the centre of the chamber. Poor mixing also occurs after ignition, because the hot combustion gases & unburnt fuel are held in the centre by the density gradient resulting from the high swirl (24). This leads to smoke limited power, increased HC's & particulates.

Underswirling allows excessive wall impingement to take place, which causes increased smoke & HC's (23). This is due to the relatively cool walls of the DI engine inhibiting combustion & mixing. After the ignition, buoyancy forces assist in the mixing of the hot unburnt fuel & cooler central air (24). In an IDI

engine, wall impingement by the spray in the pre-chamber is not a problem, because of the much hotter walls.

The economic restriction to cheap, low pressure injection equipment, introduces other problems as well as those associated with matching swirl to injection rate over the full speed range. The low pressure gives higher smoke & HC levels as shown in figure 1.12, because of the poor atomization and longer combustion tail (21, 23). The low pressure also leads to a longer injection duration &, from a smoke point of view, it is desirable for the duration to be as short as possible (22).

The DI engine also suffers from higher noise & NO_x levels than the IDI, because of the higher heat release rates (23). However, these may be reduced by using higher injection pressures & retarding the injection timing. Using a higher injection pressure by itself would increase the pre-mixed heat release spike & therefore NO_x & noise, but the shorter combustion duration allows the injection to be retarded. This gives a shorter ignition delay, which reduces the pre-mixed spike & peak temperatures reached with only a slight increase in fuel consumption (23).

Turbocharging can improve the fuel consumption & power of both the IDI and DI diesel engine without increasing emissions. It is particularly beneficial with the DI, as the extra cost of the turbocharger may be offset by less critical fuel injection requirements (21). With a slight retard of the

injection timing away from minimum fuel consumption, the heat release diagram may be changed so that both noise & NOx at full load are reduced without penalising efficiency at part load. Turbocharging decreases the ignition delay, with a resulting decrease in the pre-mixed spike & peak temperatures reached. Also, the low volumetric efficiency, associated with high swirl ports in the DI, becomes less significant with turbocharging.

Although the DI engine may require more expensive fuel injection equipment & turbocharging to achieve emissions & performance equivalent to the IDI engine, there are other areas in which this expense may be offset. In the IDI engine, the compression ratio needs to be comparatively high to assist cold starting, even with a starting aid. This means that production line tolerances would be much more critical than with the lower compression ratio DI engine.

The heat flux to critical parts is lower in the DI engine (eg the heat flux to the valve bridge is 30% less for the DI (21)), which means that it may be boosted to higher pressures without needing special cylinder head or piston designs. Also the heat loss to coolant is lower, so the power to the cooling fan may be reduced along with the size of the radiator.

From the above analysis, it would appear that a small passenger car DI diesel would require high pressure fuel injection equipment or turbocharging to be competitive with the IDI. However, with careful development, a competitive DI engine with a cheaper

specification may be produced, although to do this would require improvements in the design & development tools available to overcome the lack of experience in this area. The most important of these is in the area of combustion & gas flow models.

1.3 Fuel Injection & Air Motion Interaction: Swirl

In the previous section, the overall effects of fuel injection & air interaction on emissions & fuel consumption were considered. To be able to predict these effects, requires a good understanding of the complex physical & chemical processes involved & the way they interact.

The first factor to consider is the interaction of the fuel spray with the air. After the fuel spray leaves the nozzle, it becomes turbulent & breaks up into droplets a short distance from the nozzle. The mean size of the droplets is dependent on several factors. Figure 1.13 from Lee (18) shows the change in droplet size distribution for different nozzle diameters. Increases in chamber or injection pressure produces a decrease in mean droplet size as shown by figure 1.14. The distribution of mean droplet diameters varies from the largest at the jet centre line, to the smallest at the periphery, an example of which is shown in figure 1.15. For a normal diesel spray, the droplets range in size from 10 to 100 microns (27).

As the temperatures & pressures in the diesel combustion chamber approach the critical pressure & temperature of the fuel, droplets of this size, if immersed in an infinite volume of air, would quickly evaporate a very short distance from the nozzle (28, 29, 300). However, the close proximity of the other droplets within the spray will inhibit the evaporation so that the central core will have a fog of fuel droplets that will penetrate some way into

the chamber, with an outer periphery of fuel vapour. The distance that the droplets will survive will be primarily dependent on their size & the gas pressure & temperature.

For practical purposes, the fuel spray is often considered as a variable density turbulent gas jet submerged in air (28,31,32), although the high density of the jet close to the nozzle (upto 30 orifice diameters) complicates the comparison. Even under poor injection conditions, the fuel spray has been observed to behave as a gas jet with similar velocity & concentration profiles (33,34,35).Thus, the transfer of momentum from the droplets to the air quickly reduces the relative velocity between the two, so that the fuel spray may be considered as an air jet bearing a fog of fuel droplets.

The growth in cross-section of the spray as it penetrates into the air is caused by the shearing action between the jet & air, which entrains air into the spray. The growth rate of the spray width in unswirled air may be derived from the Prandtl mixing length theory (36). There is a central core close to the nozzle, consisting of relatively shear free flow in which the nozzle leaving velocity is preserved. This core decreases in size as the jet progresses & is known as the potential core. With a crossflow of air or swirl, this core has been observed to reduce in length because of the enhanced air entrainment (24,37). As well as increasing entrainment, the effect of swirl on the jet is to deflect & distort

it. Adler & Lyn (38) have also shown that the trajectory of a transient spray coincides with that for a steady state spray at the same swirl level.

To help with flow visualization, a hydraulic analogue may be made of the gas jet into gas model. An equivalent air jet into air may be represented by a water jet into water on a larger scale & at a slower speed. Way (39) constructed a water rig, as shown in figure 1.16, in which flow visualization was achieved by injecting a weak alkali into a weak acid with an indicator (phenolphthein), which showed the neutral boundary. By adjusting the relative strengths of the acid & alkali, the boundary at a particular mixture ratio could be shown. Figures 1.17a & 1.17b are two examples taken from Way (39), which show the effects at different swirl levels. The numbers indicate spray development with respect to time. Figure 1.17b shows the good mixing pattern of a spray which is well matched to the swirl level, while 1.17a shows the effect of overswirl in which the spray fails to reach the wall.

1.4 A Survey of Combustion Bombs as an Experimental Tool

There appear to have been three basic approaches used in simulating diesel combustion. These may be classified under the following headings:-

1) Rapid compression machines.

2) Constant volume combustion bomb with internal heating of the pressurised gas.

3) Constant volume combustion bomb with external heating of the pressurised gas.

The rapid compression machine simulates a single isolated compression stroke followed by a constant volume combustion. Its main advantage is its ability to simulate closely end of compression conditions, but with much better visual access than would be possible in an engine.

There have been several designs of which three will be described. The first is the rapid compression machine built at the Massachussetts Institute of Technology (MIT) (32). This consists of a combustion chamber in which air is compressed by a piston located in a long bore. Visual access is restricted to a window through the top of the cylinder head. The piston is forced up the bore by compressed air & the speed & stroke are controlled by an oil filled snubbing chamber. After compression, the piston is held at TDC by non-return pawls, so that combustion

may occur at constant volume. The fuel is supplied to the injection nozzle from a pressurised accumulator via an electronically controlled valve.

Before any test, the chamber may be heated by passing a continuous flow of heated dry air through the chamber. The inlet air may also be introduced tangentially to induce swirl. By these means, typical TDC conditions for a diesel engine may be reproduced, although the tests presented in reference (32) were at relatively low pressures & swirls (ie 15 bar & 180 rad/s maximum).

The next rapid compression machine, as descibed in reference (4), is similar in concept to the MIT machine, but has better visual access as shown in figure 1.19. The piston and cylinder head both incorporate windows so that 'through visual access' is possible.

The piston is driven up the bore by a pressurised gas supply, as in the MIT design. The speed & braking of the piston are controlled by an oil filled snubbing chamber & the piston is held at TDC by the high pressure driving gas. The maximum pressures & temperatures which were quoted are 36 bar & 535 C respectively.

A single fuel injection was achieved by opening the needle valve in the injection nozzle by an electromagnet while maintaining a fuel line pressure of 260 bar.

The third rapid compression machine (taken from reference (42)) is based on a free piston design, which is again driven by a compressed gas supply as shown in figure 1.19. The use of a light, free piston allows very rapid compression rates, with minimum losses. The piston is stopped & held by a tapered stopper ring, which also produces an effective seal with the piston.

The fuel injection system uses a pintle type nozzle fed from a pressurised reservoir at 175 bar via a servo valve. The servo valve also depressures the line to produce a clean injection cutoff.

In performance terms, this rapid compression machine was the best of the three designs presented here, with quoted compression temperatures upto 725 C & compression pressures upto 83 bar.

A particular disadvantage of any rapid compression machine is the difficulty in controlling the final compression pressure & temperature directly. The constant volume bomb with internal heating, does not have this problem, as both pressure & temperature may be controlled directly & independently. An example of this type of design is shown in figure 1.20 (43). It has heating elements situated in one wall, which produce a stratified temperature profile in the chamber. The most extreme pre-combustion conditions achieved with this bomb were an air pressure of 80 bar at 350 C & an air temperature of 530 C at 45 bar. Limitations with this type of design are the restriction to quiescent conditions & hot combustion chamber walls.

A further example of this type of bomb is shown in figure 1.21 with the additional facility of through visual access. Lakshiminarayan & Dent (44) used this bomb to investigate, by holographic interferometry, the radial & axial concentrations in the vapourising non-burning spray. They also investigated species concentrations & temperature profiles within the burning spray. However, conditions were limited to a maximum pressure of 7 bar & an air temperature of 450 C, which are well below the conditions found in a diesel engine at TDC.

Fuel injections were achieved through an electronically controlled jerk pump, which is similar in concept to the design used in this work (see chapter 2).

A constant volume bomb with external heating of the pressurised air allows colder wall temperatures in the bomb to be maintained & also the possibility of introducing some swirl within the bomb. An example of this type of bomb, taken from reference (31), is shown in figure 1.22. The pressurised air is pre-heated in a separate reservoir upto the desired temperature, and is released into the bomb via a solenoid valve through a tangential slot, which induces some swirl. Quartz windows fitted to both sides of the bomb, allow through visual access.

The main disadvantages of this type of bomb are the difficulties in controlling the final pre-injection conditions of air pressure, temperature & swirl. All these conditions, in particular swirl, will decay

with time, so the injection timing is critical. Also the range of swirl levels will be a function of the initial air pressures.

1.5 The Bath High Swirl Bomb

At Bath a phenomenological jet mixing model with swirl has been developed (40,45). It is hoped that combustion may be imposed on this model, so that combustion in a high swirl DI diesel engine may be simulated. To develop a model such as this requires a detailed quantitative understanding of the combustion process in a diesel engine. This cannot be obtained readily from an engine because of difficulties in gaining access to the combustion chamber and of controlling temperature, pressure & swirl independently. Thus a combustion bomb has been developed, which gives a fine control over these three conditions.

The design for the bomb may be categorised as a constant volume combustion bomb with internal heating, but with an unusual method of swirl generation. Swirl is generated by a drum inside the combustion chamber, which may be rotated at speeds of upto 20,000 rpm. A more detailed description of this design may be found in the next chapter, but the method of swirl generation is based on a water rig design shown in figure 1.16..

This water rig, which is described by Way in reference (39), was built & developed to simulate a diesel injection into a swirling flow by a water analogy. Swirl is generated by a semi open ended closely fitting drum.

The main advantages of this design of combustion bomb over the rapid compression machine & the constant volume bomb with external heating of the air are more precise & independent control over pressure, temperature & swirl. However, this design is restricted to unrealistic hot walls & reduced visual access.

This bomb has been used to study the effects of pressure, temperature & in particular swirl on the various aspects of combustion. This has been done by optical means (films) & heat release analysis of the pressure/time records. The films provided details on spray trajectory & also combustion in qualitative terms. The heat release analysis provided a more detailed quantitative description of combustion. These results are presented in chapters 4 & 5.

In addition to this practical work, a multizone combustion model has been written to help provide a better insight into the practical combustion work. The combustion model was based on work by Shahed, Chiu & Lyn (31,46), but adapted to constant volume conditions. This model was additional to the single zone heat release program, written by Packer (40), used to provide heat release details from the pressure/time records.

Although some interesting results have been produced by both the practical & theoretical work, the quantity was limited by lack of time. This was mainly due to the problems & obstacles, which had to be

overcome in developing a combustion bomb of unique design. These will be highlighted in the next chapter.

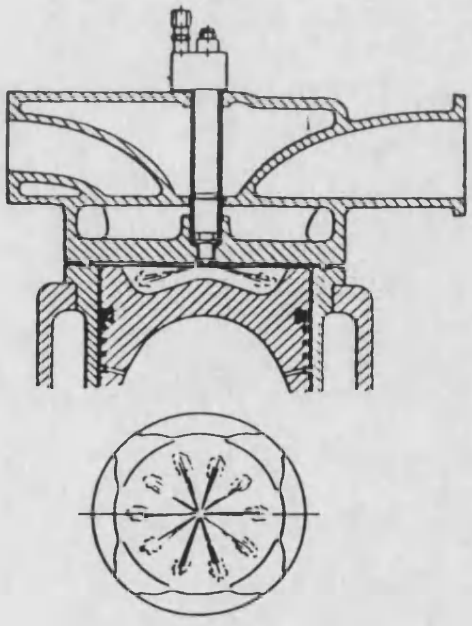

Figure 1.1 Shallow bowl combustion chamber. Taken from reference (1).

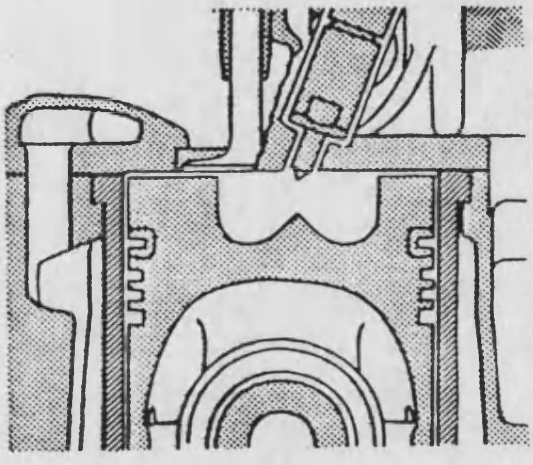

Figure 1.2 Deep bowl combustion chamber. Taken from reference (1).

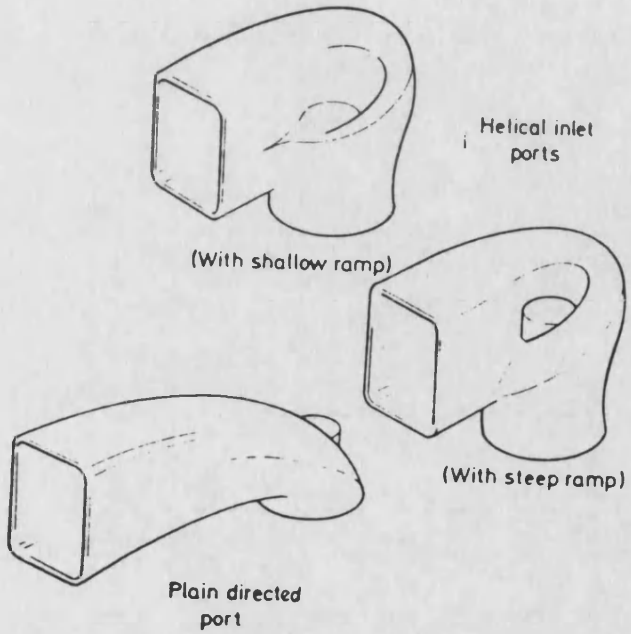

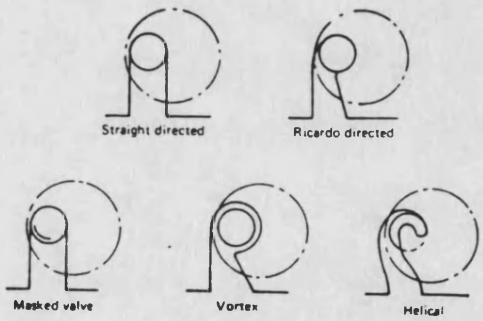

Figure 1.3 Inlet port designs. Taken from references (1) & (2).

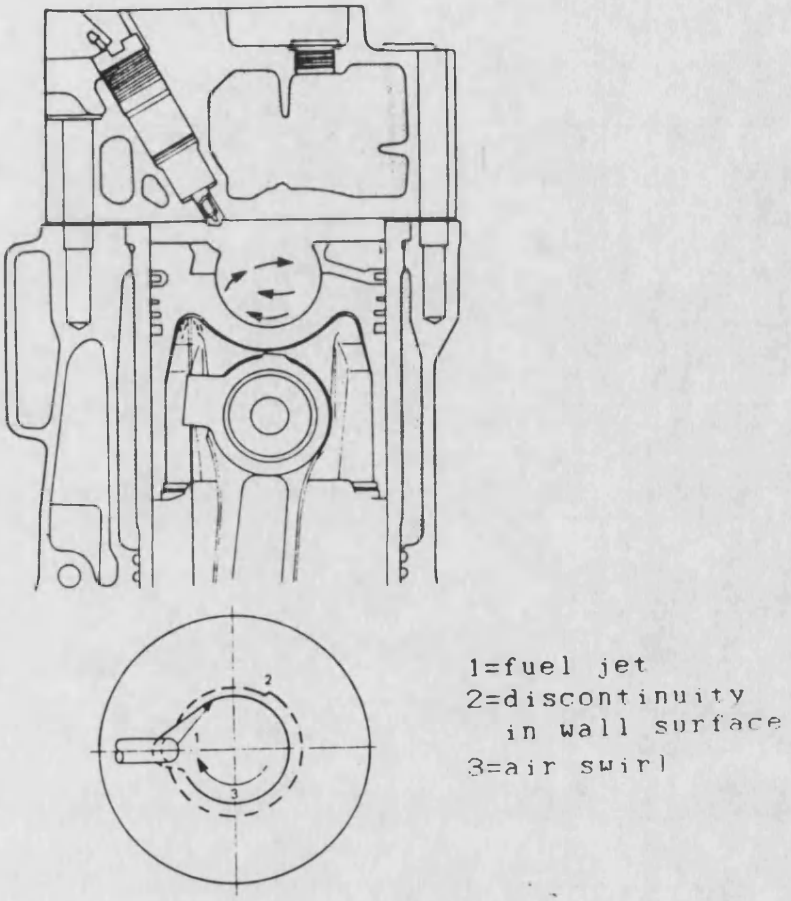

Figure 1.4 MAN M-system combustion chamber.
Taken from refenence (1).

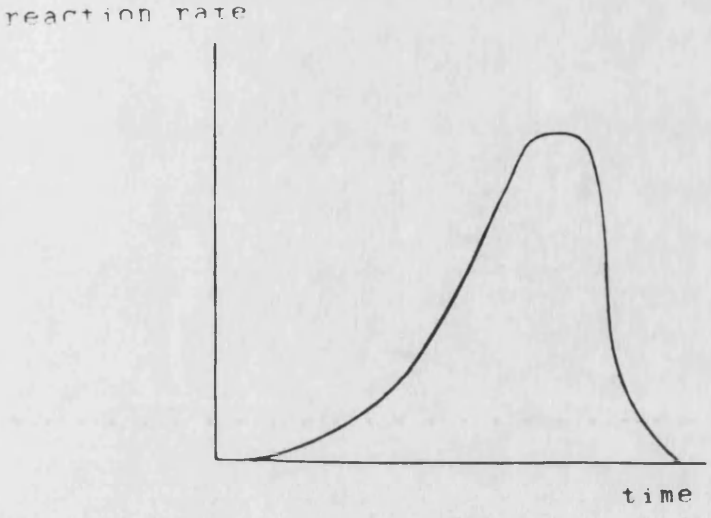

Figure 1.5 The fuel/air reaction rate related to time.

Air Pressure	-	34.5 bar
Initial Fuel temp.	-	93.3 C
Initial Air temp.	-	538 C

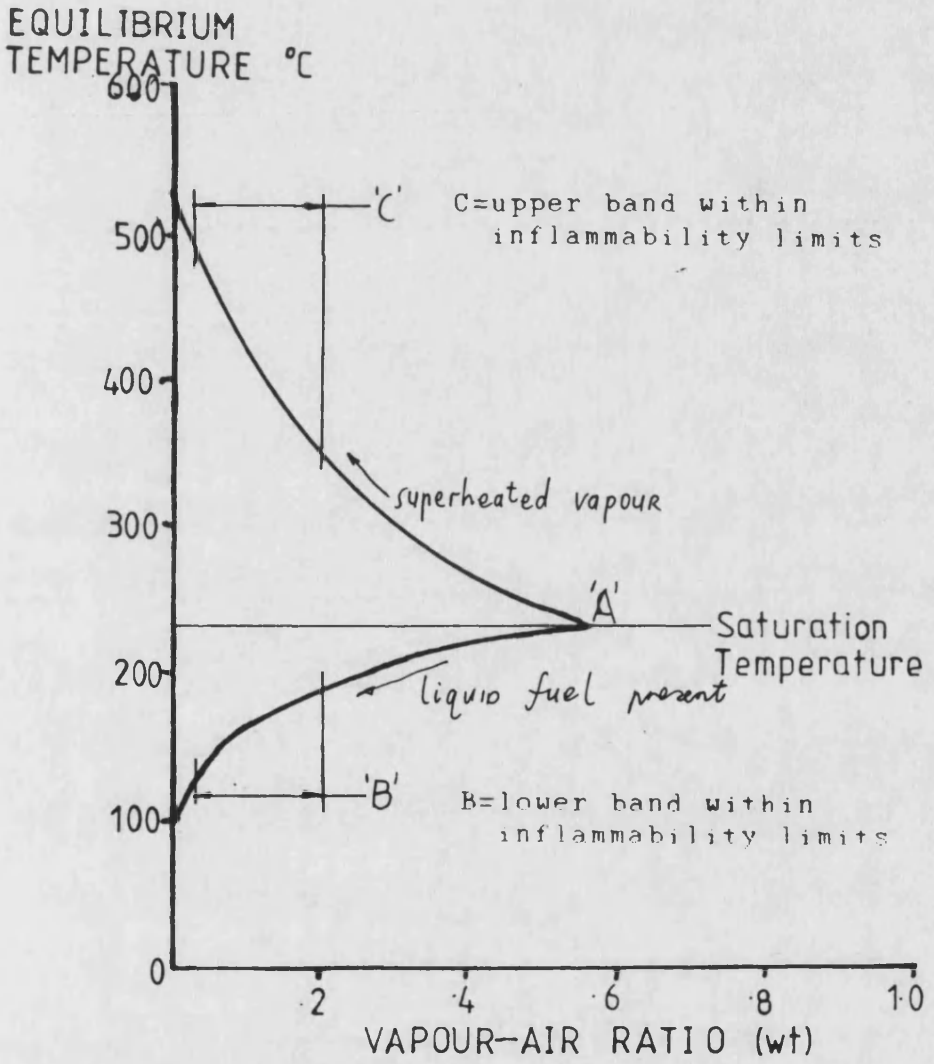

Figure 1.6 Adiabatic saturation temperature versus fuel/air ratio (6)

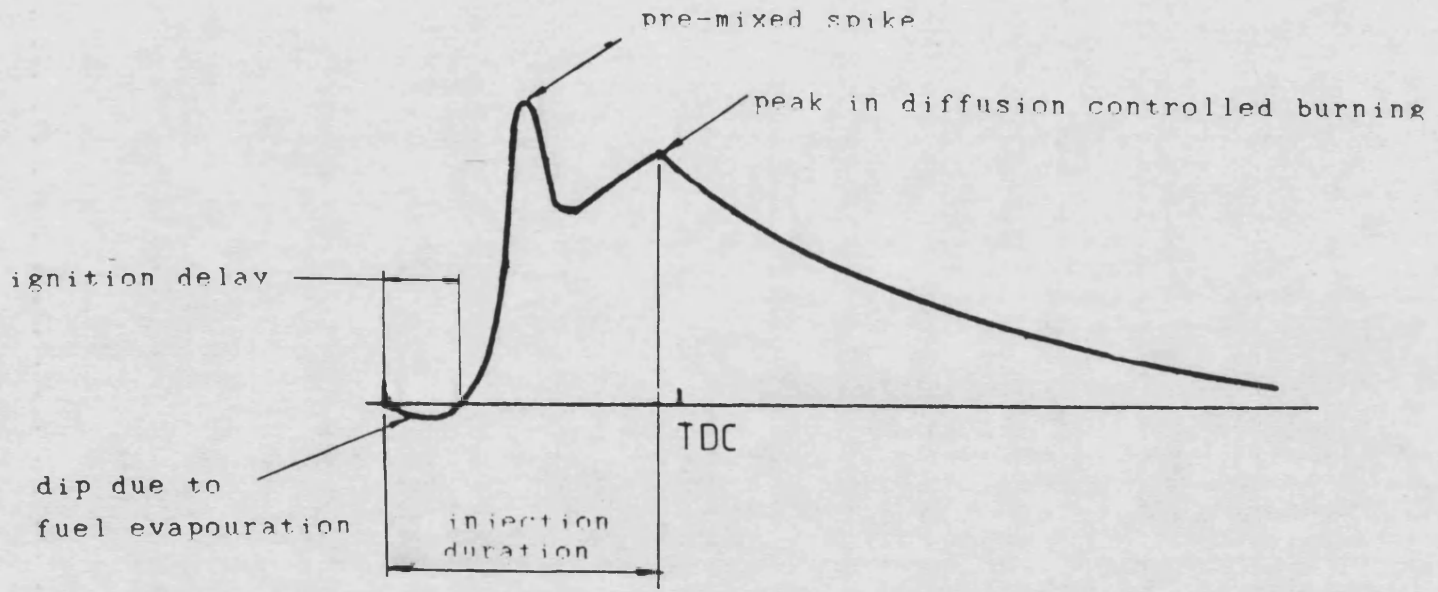

Figure 1.7 Heat release diagram produced by a short ignition delay & long injection. The mixing rate is still increasing after the pre-mixed spike.

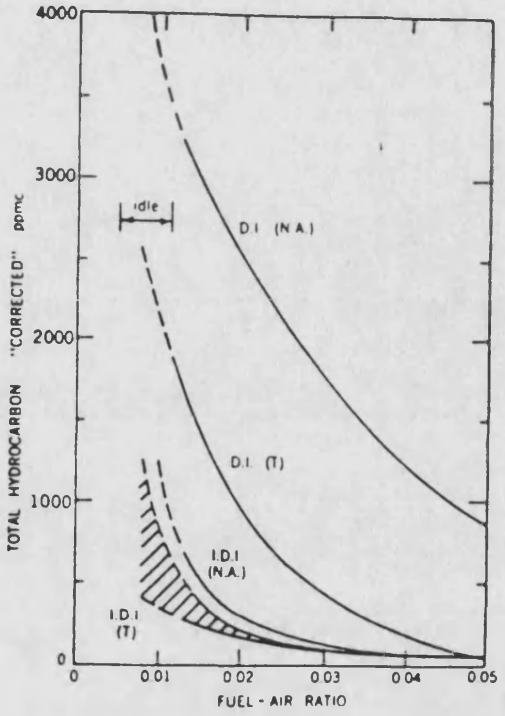

Figure 1.8 Effect of fuel/air ratio on the unburned hydrocarbon emissions in DI & IDI engines. (NA): naturally aspirated; (T): Turbocharged (9).

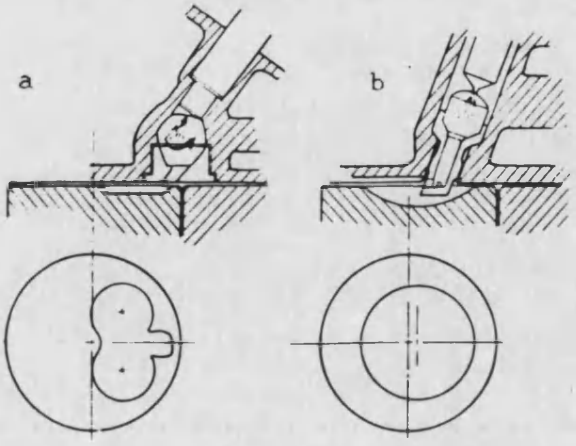

Figure 1.9 Examples of the swirl chamber (a) & pre-chamber (b) combustion systems. taken from reference (1).

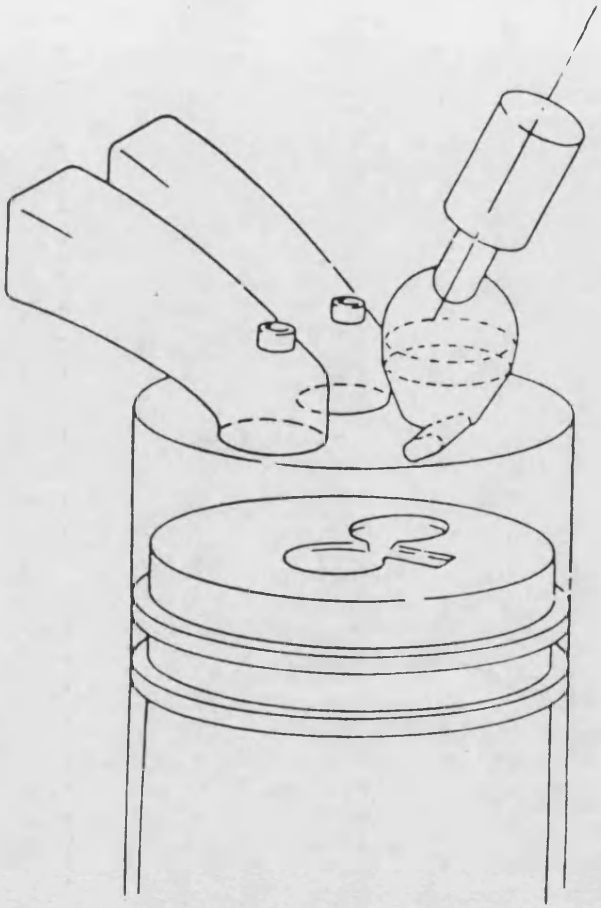

Figure 1.10a IDI diesel engine. Taken from reference (21).

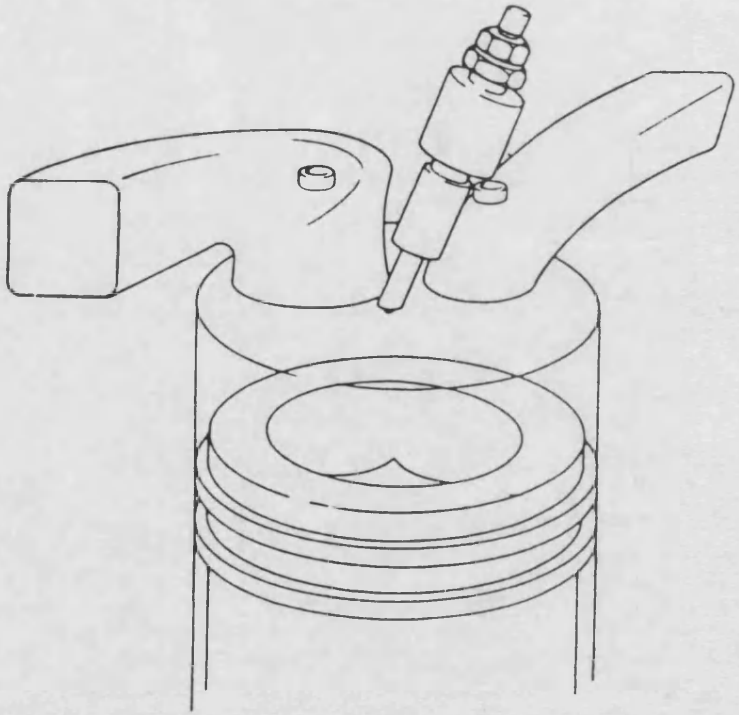

Figure 1.10b DI diesel engine converted from IDI engine (figure 1.10a).

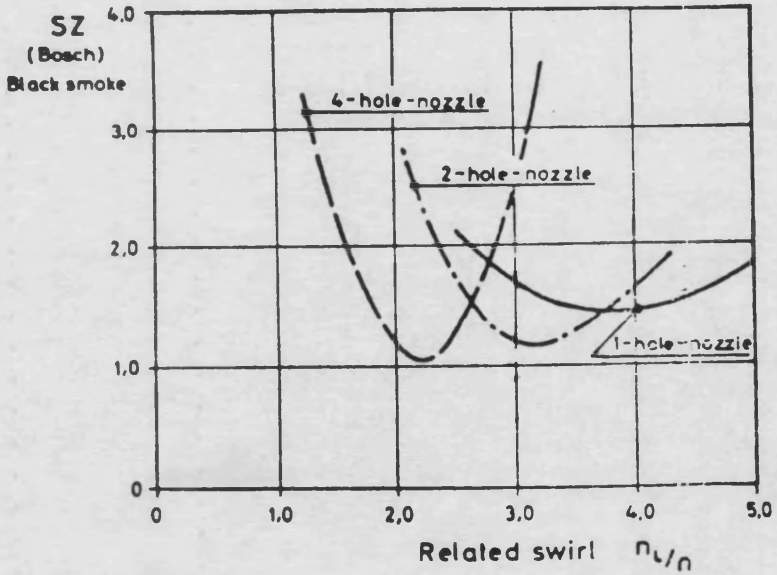

Figure 1.11 Number of nozzle holes & related swirl level versus smoke emissions (23)

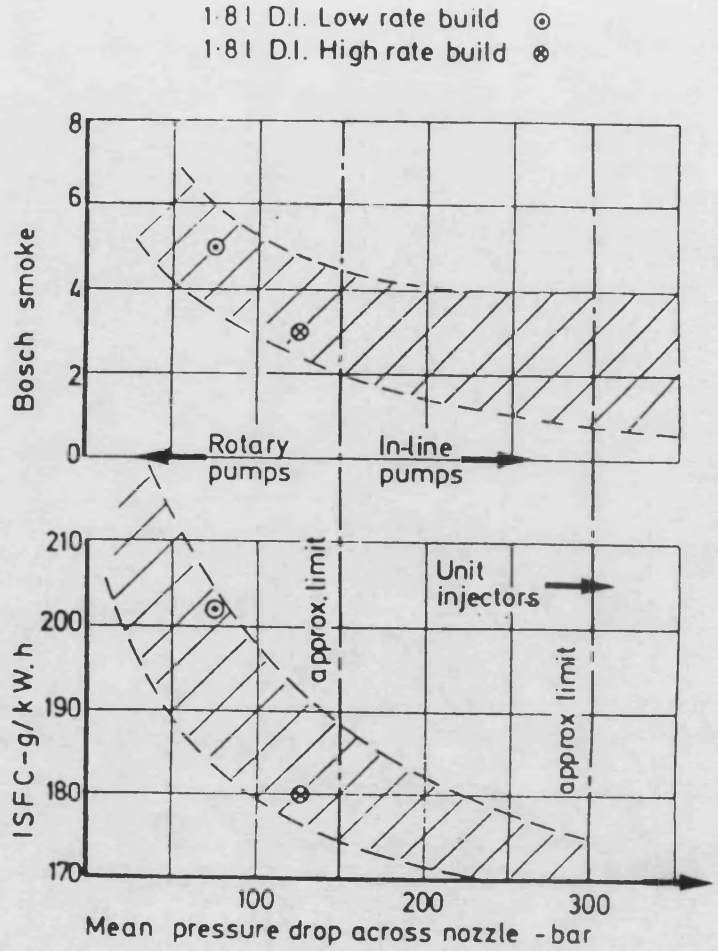

Figure 1.12 Effect of mean nozzle pressure drop on smoke and i.s.f.c at 22:1 A/F ratio (21).

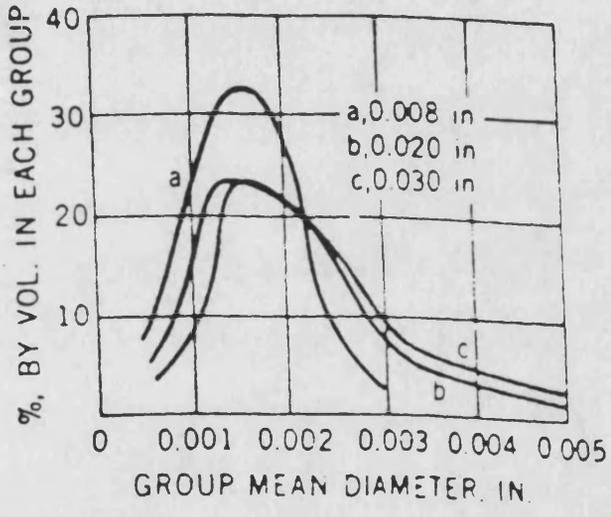

Figure 1.13 Effect of nozzle hole diameter (a,b,c) on droplet size distribution. Taken from reference (18).

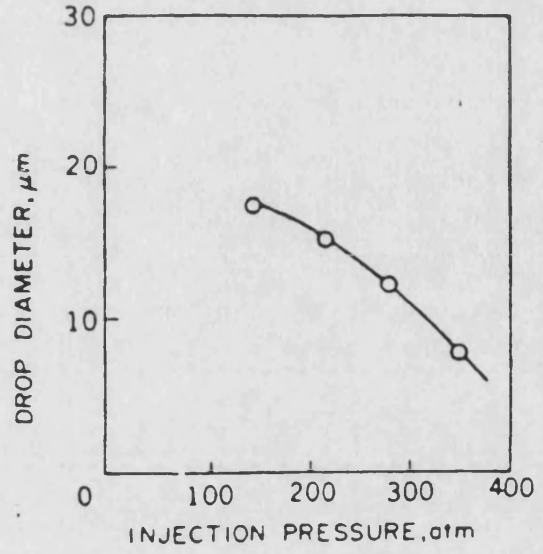

a

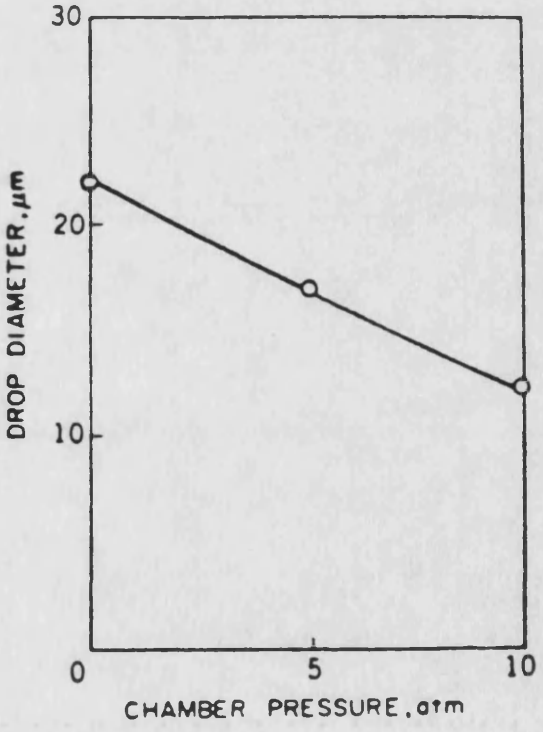

b

Figure 1.14 Effect of injection pressure (a) & chamber pressure (b) on mean droplet size. Taken from reference (25).

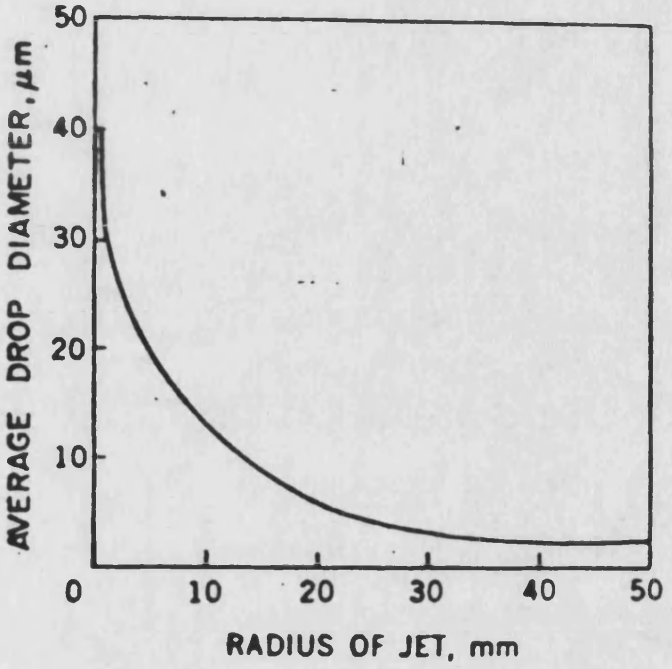

Figure 1.15 Mean droplet diameter relative to the spray centre line. Taken from reference (26).

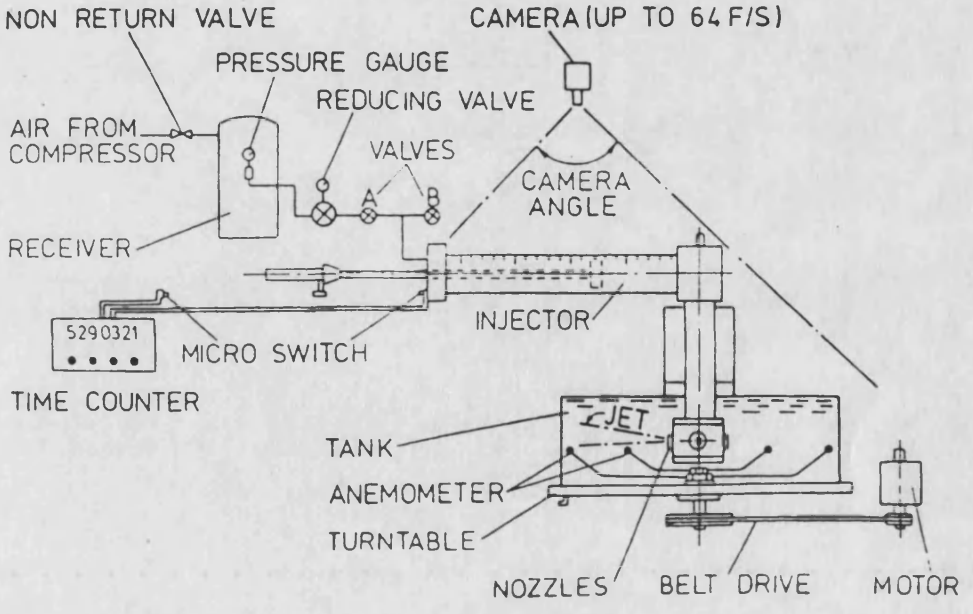

Figure 1.16 Water rig used to simulate diesel injections in a swirling flow by a water analogy. Taken from reference (40).

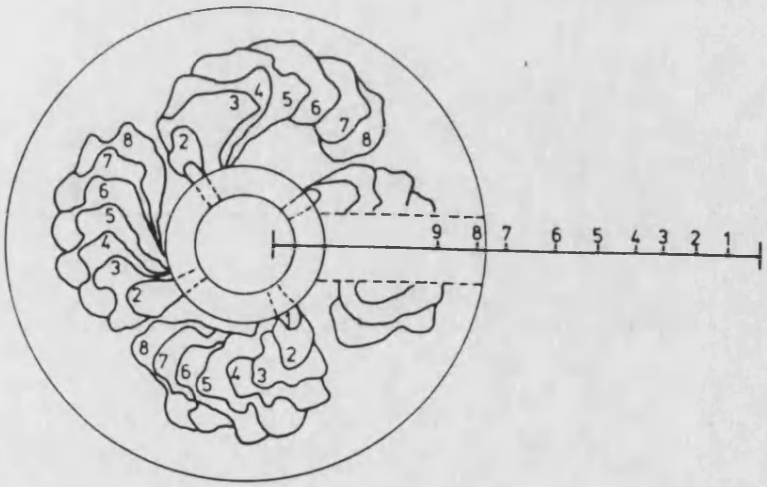

Figure 1.17a Overswirled jet produced by water rig of reference (39).

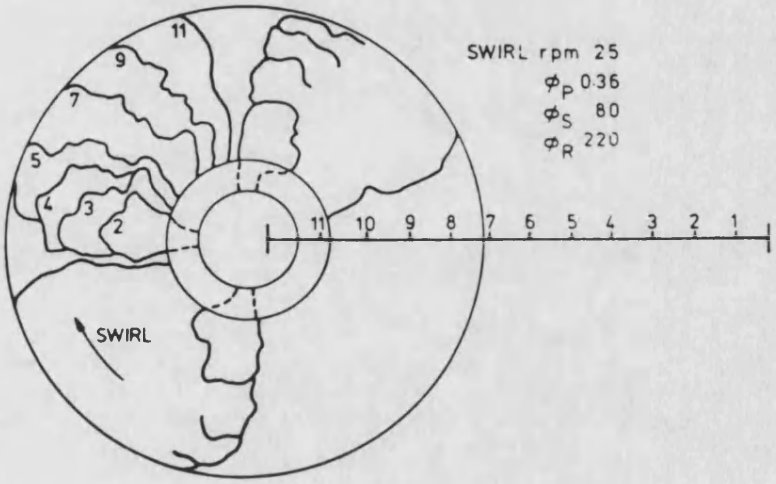

Figure 1.17b Optimum level of swirl.

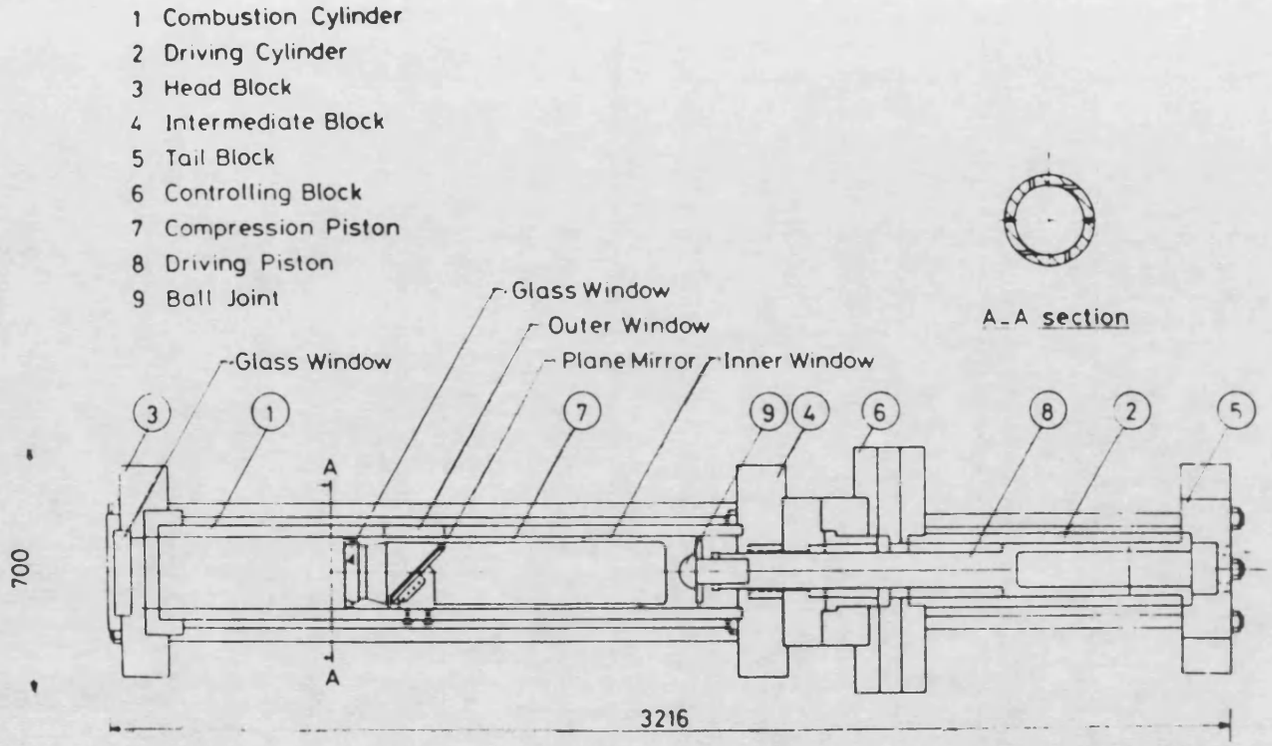

Figure 1.18 Rapid compression machine. Taken from reference (41).

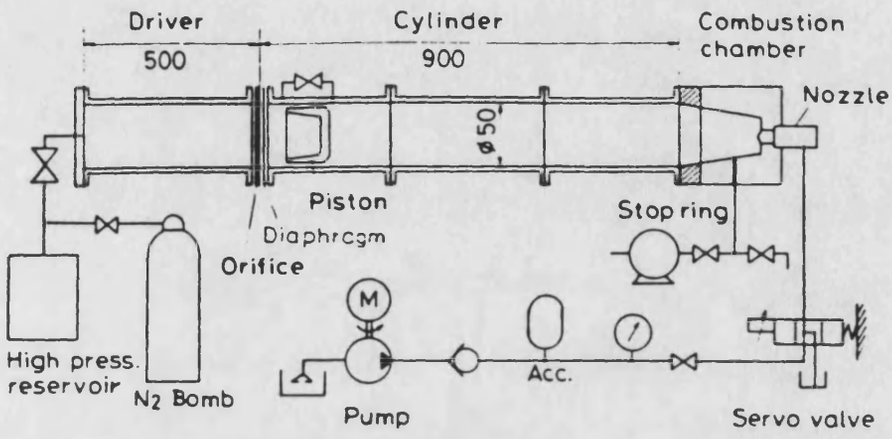

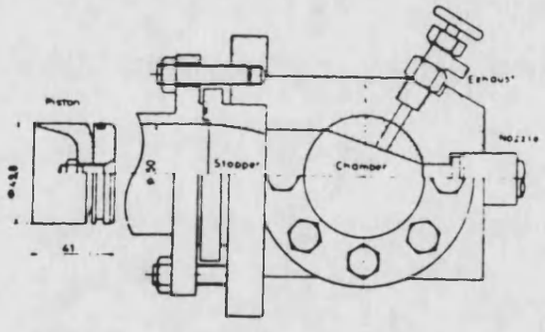

Figure 1.19 Rapid compression machine. Taken from reference (42).

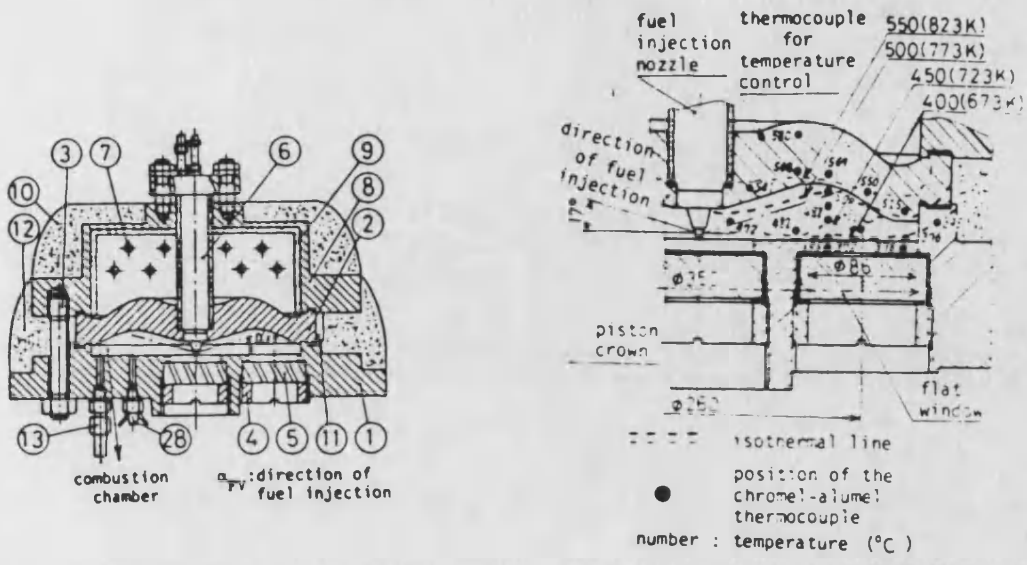

Figure 1.20 Constant volume combustion bomb with internal heating. Taken from reference (43).

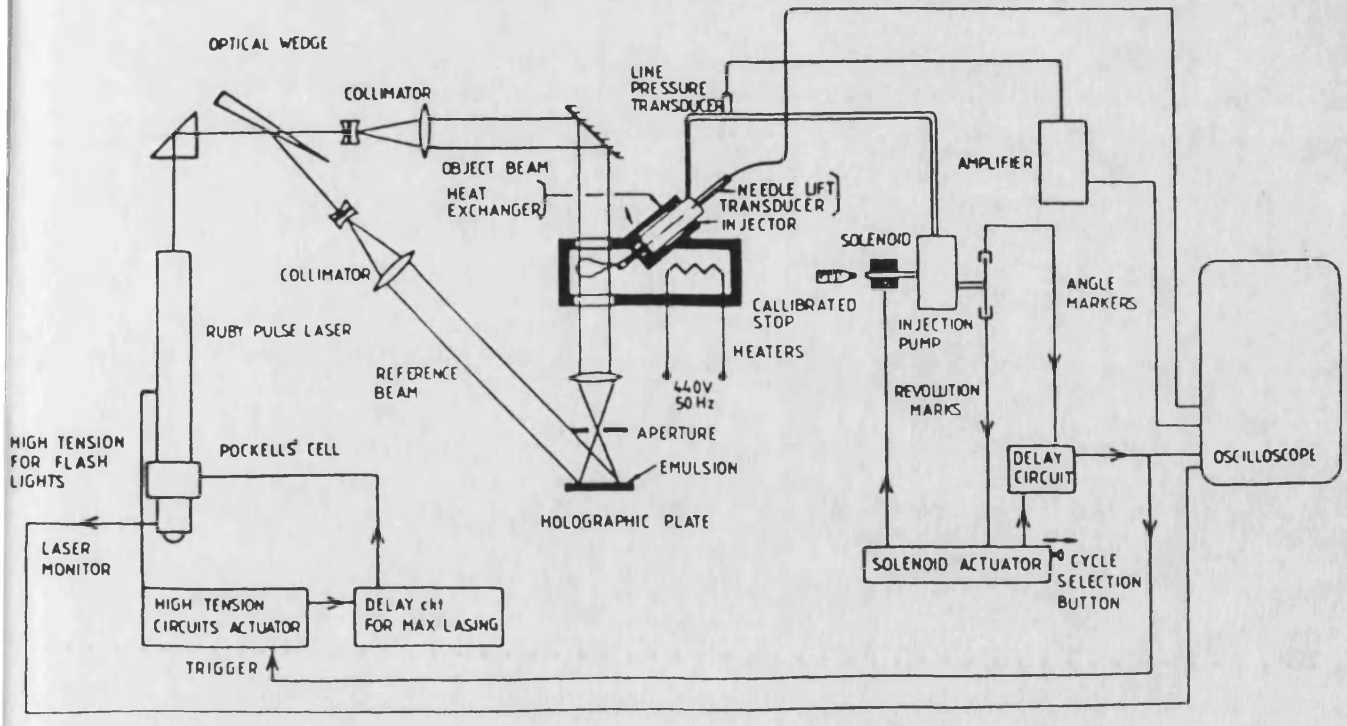

Figure 1.21 Constant volume combustion bomb with internal heating. Taken from reference (44).

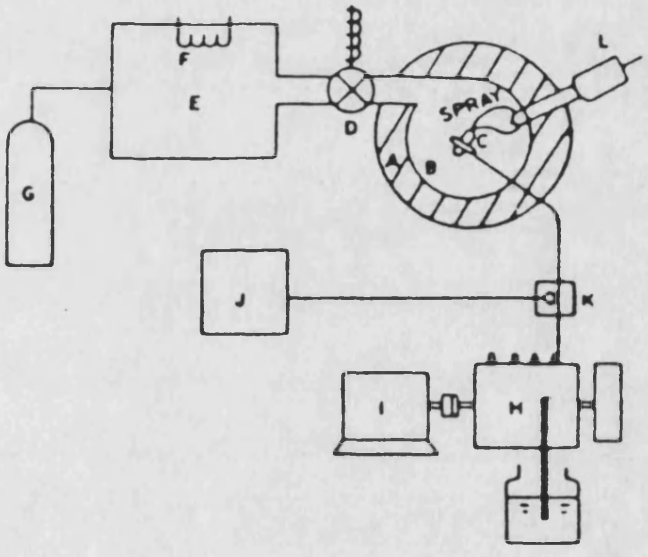

A - CONSTANT VOLUME CHAMBER
B - QUARTZ WINDOWS
C - FUEL INJECTION NOZZLE
D - PNEUMATIC VALVE
E - GAS RESERVOIR
F - HEATER
G - GAS BOTTLE (N_2)
H - FUEL PUMP
I - DC MOTOR
J - HYDRAULIC PUMP
K - CHECK VALVE
L - SAMPLING PROBE

Figure 1.22 Constant volume combustion bomb with external heating of gas. Taken from reference (31).

CHAPTER 2

Description of High Swirl Combustion Bomb.

Chapter 2. Description of high swirl combustion bomb

2.1 Basic Specification

The main requirement for the combustion bomb was to have close and repeatable control over the swirl level. Also investigations into engine swirl levels have revealed that the mean swirl level around TDC approaches 20,000 rev/min (47). Thus the swirl level that should be generated by the bomb should be of the same order of magnitude.

The basic design concept of the bomb dictated a single shot injection system. In addition as the aim of the project was to simulate diesel combustion, injection characteristics similar to those found in a normal DI diesel engine were specified.

It was also necessary to reproduce the same pre-ignition pressures and temperatures that would be reached in a typical diesel engine. These would be at pressures and temperatures up to 50 bar and 900 K respectively.

As the combustion bomb is of constant volume form, the maximum pressures produced by combustion will be higher than are found in an engine. The maximum combustion temperature likely to be seen in the combustion bomb will be limited to around 2500 K, because of dissociation and heat transfer. Therefore for an initial pressure and temperature of 50 bar and

700 K respectively, the maximum pressure using the following equation:-

$$p_{max}=p_{int}* T_{max}/T_{int}$$

should be 180 bar! The final pressure specification for the bomb was based on a pressure of this order, with stresses restricted to those specified by the ASME boiler code.

The degree of accuracy and repeatability specified for the initial (pre-combustion) pressures and temperatures dictates that the gas leakage from the chamber should be kept to a minimum. Heat release analysis also requires that the leakage rate during and after combustion should be kept to a minimum.

Ideally, it would be desirable to have optical access through the chamber, but unfortunately the method of swirl generation, restricts the optical access to one direction or view and forward lighting.

The degree of optical access required is dependent on the type of information that is required from the chamber. In this case, a knowledge of spray trajectories and velocities (with and without combustion) was required. To achieve this, a representative section of the combustion chamber needs to be in view and illuminated. The size of this representative section will depend on four conditions: a) the symmetry of the gas flow within the chamber, b) the location of the injection nozzle, c) the number of nozzle holes and d) the spray distribution.

For a centrally mounted four holed nozzle with a symmetrical spray distribution, one quarter of the chamber needs to be visible. However, in a swirling flow, when the fuel spray is likely to be distorted, a larger area needs to be covered.

The high initial steady state temperatures and pressures dictated fused quartz as the material for the windows.

A full description of the initial and transient conditions is necessary for control of these conditions and heat release analysis. The physical measurements required to produce a full description were as follows:-

1. Air swirl (velocity distribution)
2. Wall temperature
3. Gas temperature (initial)
4. Gas pressure (initial and during combustion)

High speed measurement of the fuel line pressure and nozzle needle lift were also required for the prediction of fuel mass injected and injection rate.

The high speed data acquisition system was required to measure chamber pressure, fuel line pressure and injector nozzle needle lift. This data was recorded in digital form so that it could be simply transfered to and analysed on the main frame computer. The system was also used to control and monitor the injection process

2.2 Major Rig Components

Introduction

The combustion rig consists of five major sub assemblies, namely:-

2.2.1 The combustion chamber and drive assembly
2.2.2 Seal chamber pressurisation system
2.2.3 The single shot fuel injection system
2.2.4 Data acquisition and control system
2.2.5 Air temperature control system

Parts of these systems were extant at the beginning of this project and further details of these components may be found in reference (40).

What follows is a detailed description of these sub-assemblies and how they were developed.

2.2.1 Combustion Chamber and Drive Assembly

A cross-section of the combustion chamber and drive assembly is shown in figure 2.1, with the optical head attached. Combustion chamber design was fairly simple, being based on the ASME boiler code, for maximum safety. Inside wall temperatures were expected to be very high so EN58 stainless steel, which has good high temperature properties, was used. The basic chamber is shown in figure 2.2.

The location of the heating coil within the combustion chamber is shown in figure 2.1. It consists of 14m of sheathed heating element

sandwiched between two Nimonic 80A drums, which are shown in figure 2.3.

There is a choice of three types of head, which may be used: an instrumented head, an anemometry head and an optical head. The instrumented head (figure 2.4) is used for detailed heat release analysis, being fitted with a pressure transducer, head temperature thermocouple and several thermocouples for measuring gas temperatures at different locations. Velocity surveys may be effected with the anemometry head (figure 2.5), which has the facility to traverse axially a hot wire probe across the chamber at 6 different locations. High speed filming may be done with the optical head (figure 2.6).

The optical head consists of three quartz windows held in position by 10 Allen screws, which facilitate their cleaning. Originally the quartz windows sealed on the inner flange shown in figure 2.1, but at high pressure the windows were forced off these, unless high clamping forces were used. To reduce the high stresses generated, the clamping rings were modified so that sealing was effected between the windows and clamping rings themselves. However, this design, which is shown in figure 2.7, required water cooling as Viton o-rings had to be used. This restricted the pre-combustion temperatures that could be generated, because of the heat lost to the cooling water.

All the heads are held down onto the bomb by 8 half inch Nimonic 80A bolts, which pass through the chamber walls into 8 captive nuts welded to a split mounting plate. Sealing between the two is

satisfactorily achieved by a Corruplus self pressurising seal.

Although any symmetrical shape could have been chosen, to keep the geometry simple a shallow drum configuration (figure 2.3) was used, based on the design lessons learnt from the water rig (39).

The swirl generating drum had to withstand high temperatures and thermal and pressure shocks from combustion, as well as the stresses induced by rotation at 20,000 rpm. With these conditions in mind, Nimonic 80A was chosen as a suitable material for the drum. The drum is located on a shouldered spigot on the end of the drive shaft and is clamped in place by a simple nut.

Drive Shaft Bearings and Lubrication

Originally, gas bearings were used to support the shaft, rather than oil lubricated plain or ball bearings, because of worries about possible oil ingress into the combustion chamber and the high temperatures they would be exposed to. Unfortunately these suffered from insurmountable development problems and they were eventually abandoned in favour of a ball bearing system.

Two systems were developed. The first, designed by J.Packer, used two extra light radial ball bearings and is described, along with the radial gas bearing system, in reference (40). The second system consisted of two opposed angular ball bearings of sturdier dimensions as shown in figure 2.1. These are mounted in a

stainless steel housing, with the inner bearing (nearest the combustion chamber) rigidly clamped in place. Shims in the end plate, press against the outer bearing to take up any free play and pre-load the bearings.

The bearing choice was based on the guidelines set out in the RHP standard bearings technical handbook (48). Loads and speeds for the bearings were based on the worst running conditions. These were calculated to be an axial load of 1874 N, (from an expected combustion chamber pressure of 60 bar), a radial load at 10% of this and a continuous running speed of 20,000 rpm. The small radial load was assumed to come from slight differences in the tensioning of the twin opposed drive belts. Under these conditions the handbook gave a bearing life of 250 hrs with a 10% failure rate.

Lubrication of the bearings is by an SAE 20/50 motor oil, which is circulated from a separate oil reservoir. The oil is pumped to the bearings by an electronic car fuel pump and returns to the reservoir through four drainage holes. An oil flinger provides effective sealing at the outer end of the shaft.

Two electric motors situated on either side of the bearing housing drive the shaft. Power is transmitted from the motors to the shaft by two high speed flat belts mounted on crowned pulleys. The motors are 1.1 kW router motors with a free speed of 27,000 rpm. Their use stems from the gas bearing design, which used direct drive and therfore required a motor which could run at the required shaft speed. Speed control

of the motors is effected by control of the voltage supply with a Variac. The speed range of the shaft depends on the ratio of the shaft pulley to motor pulley diameters.

2.2.2 Sealing between Drive Shaft and Chamber

Successful sealing between the shaft and combustion chamber was hampered by the combination of four arduous conditions. These were as follows:-

1. Continuous chamber pressures upto 55 bar with higher intermittent combustion pressures.

2. High shaft speeds with the associated surface velocities.

3. High temperatures.

4. A limited space, between the bearings and drum, to fit a sealing system. This is due to the whirl speed restriction on the length of shaft overhang.

A labyrinth seal was developed as a first solution, details of which may be found in reference (40), but the leakage rate could not be reduced to an acceptable level. This gave way to the present design (figure 2.1), which incorporates two carbon faced, pressure balanced, rotary type seals mounted in tandem. These were supplied by EG and G Sealol Ltd. Cooling and lubrication is provided by a recirculating pressurised oil buffer, which also provides a pressure drop between the two seals. Each

seal may withstand a pressure differential of 70 bar, thus giving a combined differential of 140 bar for the pair.

Sealing between the rotating shaft and fixed seals is effected by an intermediate stainless steel mating ring (figure 2.1). The mating rings are clamped to the shaft by an end sleeve, which also provides a shoulder for the swirl generating drum to sit on.

Although the shaft speed of 20,000 rpm may appear excessive, the surface velocity at this speed is only 20 m/s, which is well within the limits for a seal of this type. At a negligible pressure differential the seals are designed to withstand a surface velocity of 80 m/s, although this specification reduces slightly with pressure. The biggest problem associated with this shaft speed was maintaining the runout of the mating rings to less than 0.0005". This required precision machining of all the components, plus stress relieving heat treatment of the stainless steel shaft, before its final machining.

The seals were protected from the combustion chamber temperature of upto 650 C by isolating the seals from the combustion chamber and cooling them with the buffer oil. Also the spacer between the mating rings was machined from copper to aid conduction of heat away from the inner mating ring to the buffer oil. Fins were also machined in the copper spacer to aid this process (figure 2.8). These precautions reduced the effective temperature at the seal to less than 200 C.

The distance between the drum and inner bearing support was such that there was a possibility of the critical whirling speed being within the operating range of the system. Whirling is the condition where the shaft axis leaves the axis of rotation (see figure 2.9), which would not be tolerated by the seals or drum. Thus a theoretical analysis was made, with a few pessimistic simplifications, to find the critical whirling speed.

For a cantilevered shaft with an end mass, the critical whirling speed is equal to the natural frequency of transverse vibration. This may be found from the following equation (49):-

$$W_n = \sqrt{\left[\frac{3 E_s I_s}{l_s^3 (m_d + 0{\cdot}23\, m_s)} \right]} \qquad - 2.1$$

where I - second moment of area
m_d - drum mass
m_s - shaft mass
l_s - shaft length

Using the minimum shaft diameter of 11 millimeters:-

W_n = 16247 rpm

This is within the operating speed of the shaft, but fortunately the drum applies a virtual stiffness to

the shaft by gyroscopic action. The actual whirling speed may then be derived from the following three simultaneous equations (50):-

$$W_n^2 = \frac{1}{y_o}\left[\frac{1+r}{1+\frac{1}{4}r}\right] \qquad - 2.2$$

$$r = 3W_n^2 y_o \left(\frac{k_g}{l_s}\right)^2 \qquad - 2.3$$

$$y_o = \frac{m_d l_s^3}{3E_s I_s} \qquad - 2.4$$

This gives a whirling speed of 21441 rpm, which is just outside the shaft operating range, but as the assumptions made were on the pessimistic side, it is quite likely that the whirling speed will be above this. No whirling was experienced at 20,000 rpm or below during the tests.

Seal Chamber Pressurisation System

Of the three main requirements for the seal chamber pressurisation system, the most important was to minimize the pressure difference between the combustion chamber gas and the buffer oil. The principle behind this was: "the lower the pressure difference, then the lower the gas leakage rate". At the same time, the buffer oil pressure could not exceed the combustion chamber pressure by more than 0.7 bar or exceed 70 bar in total. It would have also been unrealistic to expect the pressurisation system to follow the changes in pressure during combustion.

The final hydraulic circuit which was developed is shown in figure 2.10. The hydraulic power pack (figure 2.11) consists of a three phase 2.24 kW electric motor, which drives a 200 bar gear pump. The pump is housed inside the oil reservoir, which acts as a heat sink for the oil returning from the hot seal chamber. An oil cooler was considered unneccessary, because of the large capacity and surface area of the reservoir. Filtration is by paper element and the maximum system pressure is restricted to 70 bar by a pressure relief circuit.

Three valves are used to control system pressure. On the outlet of the hydraulic pack, a manually operated needle valve, limits the seal chamber pressure to less than 0.7 bar, when both solenoid operated valves are open and the circuit is unrestricted. A Mannesmann Rexroth pressure relief valve (type DBEM 20-30/200Y) shown in figure 2.12, controls the system pressure from 6 bar to 70 bar. The system pressure is controlled by the level of current fed to a proportional solenoid in this valve.

Parallel to the pressure relief valve is a solenoid operated Keelavite valve, which has been converted to on/off operation. When the system pressure needs to be reduced to below 0.7 bar, this valve is opened.

The system is controlled by the electronic circuit shown in figure 2.13. The circuit has been split up into different sections marked by the dotted lines, where each section has its own function.

Sections 1 and 2 of the circuit allow the bomb and seal pressure to be monitored, without affecting the control signals. Section 3 is an invertor, which changes the sign of the bomb pressure, for correct operation of the error amplifier (section 4). Section 4a is a summing amplifier, which compares (sums) the fluid pressure with the inverted bomb pressure to produce an error signal. An error signal is produced if the ratio of the bomb pressure to the seal pressure is different to the ratio of the resistors x and y (330/390). That is, the seal pressure is maintained at 85% of the bomb pressure. A time constant of 5 seconds is built in to damp the response of this circuit.

Section 4b is a unidirectional limiting amplifier to restrict the drive to section 9 to between 0 and 10 volts. Section 9 is the voltage to current convertor, which drives the proportional valve coil with constant current. This reduces the effect of valve coil temperature on the system performance.

A number of safety circuits have been built in for secure operation. Section 5 opens the on/off and forces the proportional valve open (via D2) if the seal pressure exceeds the bomb pressure and thus prevents the bomb being filled with oil. This may occur if the bomb is depressurised rapidly or the bomb pressure goes below the minimum operating range for the proportional control valve.

It was also necessary to make the proportional valve stay open (section 6), while the on/off valve was open and the bomb was pressurised. Without this, the

proportional control valve would attempt to increase the seal chamber pressure -which it would be unable to do while the on/off valve was open- by closing. In this situation, sudden closure of the on/off valve would cause the seal chamber pressure to exceed the bomb pressure, before the proportional valve could open.

In the case of a failure of the hydraulic pump, section 7 of the circuit would open the on/off valve, and force the proportional valve open via D2, when the seal pressure reached zero. This was to prevent the circuit being fooled into closing the proportional valve in an attempt to restore the seal chamber pressure. Restoration of the hydraulic pump supply in this case would again cause the seal chamber pressure to exceed the bomb pressure catastrophically.

With this system, the only time the seal pressure may exceed the bomb pressure would be during pressurisation of the combustion bomb, when the on/off valve has to be manually triggered to close. In this situation, care has to be taken not to close the on/off valve until the bomb pressure has exceeded 8 bar. This is because the proportional valve can only control the seal pressure when it exceeds 6 bar. Failure to do this would result in a small leakage of oil into the combustion bomb before the valve could open automatically again.

2.2.3 Single Shot Injection System

The basic (unmodified) single shot fuel injection system is described fully in reference (40), but a brief description of the system would help before describing the modifications.

The system is based around a CAV Minimec 6 element in line fuel pump (figure 2.14).Five of the elements have been disabled, and the remaining one is connected to the fuel injection nozzle by a length of standard fuel pipe. All governor and throttle linkages were removed and an extension bar connects the end of the fuel rack to an electric solenoid.

A 0.19 kW single phase induction motor drives the fuel pump via a vee belt, which connects to a flywheel on the end of the pump camshaft. Pump speed may be varied by altering the diameters of the pulleys. A small stud on the flywheel is used to trigger a signal in a magnetic pickup, which is used as a reference event for the control system.

With the solenoid de-energised, the fuel rack is held closed (zero fuel) by a spring. Thus, no injections will occur while the pump is running in this condition. To achieve a single injection, once the control system has been triggered, the sequence of events is as follows:-

1. The computer waits for the reference event from the pump pulley.
2. A preset delay occurs after this signal for synchronisation purposes.

3. The solenoid is energised and pulls the rack open.
4. The fuel element performs an injection.
5. The solenoid is de-energised so that the rack closes & only one injection takes place.

The amount of fuel that is injected may be controlled by the relative position of the solenoid to the fuel pump.

Fuel Injector and Cooling Jacket

The fuel injector is a CAV S-type. Under normal engine operating conditions, this type of nozzle would be mounted in a cooled cylinder head with a regular intermittent flow of fuel through the nozzle. In the combustion rig, the conditions are the complete opposite, in that the head is uncooled and there is no flow of fuel through the nozzle except for a single shot during tests.

Originally the injection nozzle was uncooled, but a satisfactory injection could only be obtained at low temperature conditions. A simple cooling jacket was therefore designed (figure 2.15), which was soldered to the outside of the nozzle holder. This only cooled the upper portion of the nozzle, but allowed the injector to give a better performance at higher air temperatures upto 500 C.

The cooling jacket design was subsequently improved (figure 2.16) so that it extended to the end of the nozzle and also allowed the cooling water to cool the nozzle directly. Flow control fins were incorporated,

which directed the water to the tip of the nozzle. This improved performance of the nozzle at even higher temperatures to a certain extent.

However, the injection was still not wholly satisfactory, so a different method of solution was also tried. Before an injection, the fuel in the fuel line is at low pressure. It was assumed that when the nozzle overheated, the increased vapour pressure of the fuel would force the fuel out of the line. An attempt at a fuel injection under these circumstances would only result in the fuel line being refilled with fuel instead.

The solution adopted was to increase the static fuel line pressure. Initially the inlet pressure to the fuel pump was increased to 5 bar, which indirectly increased the static fuel line pressure. This maintained the performance of the injector at slightly higher temperatures and resulted in the design of a continuous fuel line pressurisation system.

A schematic diagram of the system is laid out in figure 2.17. A tee junction has been incorporated in the fuel line, with a non return valve in the fuel pressurisation supply side. Spare components from a fuel pump element have been used for the non-return valve, which only allows fuel into the fuel line when there is a pressure gradient in that direction. During an injection the non-return valve, which has a travel of .075 mm, is automatically forced shut by the increase in fuel line pressure.

As no significant fuel flow was required, it was not necessary to use a high pressure fuel pump. Instead a simple differential piston arrangement was used, which is shown in figure 2.18. By applying 5 bar to the top of the large piston, a pressure of 60 bar may be generated under the smaller piston and therefore in the fuel line. The small bore piston chamber may be recharged with fuel by opening the inlet valve shown in the figure and pressurising the underside of the large piston using the air control valve. This system cured the remaining injection problem with no further poor injections occuring after its adoption.

2.2.4 Data Acquisition, Control and Instrumentation

General

At the heart of the high speed data acquisition and control system is a microcomputer, which controls the injection process and stores the resulting data. Alongside and independent of this exists the steady state instrumentation for reading temperatures, steady state pressures and shaft speed. Some of this equipment was extant at the beginning of this project and a full description of it may be found in reference (40).

Data Acquisition and Control

The microcomputer is a series 2 Commodore PET, which has been expanded from 8k to 32k RAM memory. The PET communicates through three interface cards as shown in figure 2.19.

An Analogics MP6812 analogue to digital converter (A-DC) is used in the data acquisition card along with a 6522 versatile interface adaptor (VIA). Sampling rate, number of samples and number of channels are controlled by the VIA.

The solenoid control card uses a 6522 VIA also and a 6840 chip containing three 16 bit timers. This card controls the solenoid energise synchronisation and duration for the fuel pump rack.

After each test the digital data stored in the PET may be displayed on the oscilloscope through the oscilloscope output card. The PET presents a section of the data from any one of the four channels (chamber pressure, needle lift, fuel line pressure and spare) to the cards VIA. A digital to analogue convertor (DAC) in the card converts the digital representation of the data sample into analogue form. One channel of the card outputs the x coordinate and the other outputs the y coordinate of the data.

Transducers (Transient)

There are three transducers which feed information into the high speed data acquisition system. The first is a Kistler 6121 quartz pressure transducer for measuring transient combustion chamber pressures. It incorporates a Polystable quartz element, which is reliable in ambient temperatures upto 350 C and may withstand flash temperatures of upto 2500 C. A cooled jacket is used, as the instrumented head temperature, where the transducer is located, may exceed 500 C.

Figure 2.20 shows the water cooled part of the tranducer, water being supplied at a pressure of 3 bar from the University cooling pond. An inner sleeve holds the transducer in place and produces a gastight seal with the head. The transducer signal is conditioned and amplified by a Vibrometer Charge Amplifier, type TA-3/C, which sends its output to the PET interface.

The two other transducers measure the important parameters concerned with the fuel injection. That is fuel line pressure and injection nozzle needle lift. Fuel line pressure is measured by a strain gauge type pressure transducer, which is positioned in the fuel line 3 cm from the injector body. Needle lift is measured by an induction type transducer which is located in an extension on top of the fuel injector body. Both transducer signals are conditioned and amplified by individual CAV amplifiers.

Transducers (Steady State)

Both combustion chamber and seal chamber pressures are measured by variable reluctance transducers (NEP type 1028). The combustion chamber transducer is connected to the supply line and has a range from 0 to 140 bar. The seal chamber pressure transducer has a range up to 70 bar.

Conditioning of the transducer outputs is by an SE 4000 system amplifier, which passes the two signals onto the circuit for controlling the seal chamber pressure. The combustion chamber pressure is displayed by a panel mounted DVM.

The swirl drum speed is measured through a sixty segment wheel, connected to the drum drive shaft (figure 2.1). This is used to induce signals in an Orbit magnetic pickup, which are converted into revolutions per minute by a digital display Orbit tachometer.

Under normal operating conditions, the gas temperature in the combustion chamber is measured by Cromel Alumel thermocouples, at three locations as shown in figure 2.21. Two of the thermocouple probes are unsheathed, the other being sheathed in stainless steel. The sheathed thermocouple gives a rough guide to the reliability of the more accurate unsheathed thermocouples. Thus a large discrepancy between the two readings would indicate a breakdown in the electrical insulation of the unsheathed thermocouples.

The unsheathed thermocouple design is shown in figure 2.22. In the araldited section, a small section of the porous thermocouple insulation has been removed. This was neccessary for an effective seal between the Araldite and thermocouple wire. The long length of 1/8th inch S.S tubing isolates the Araldite from the high combustion bomb temperatures.

The signal from thermocouple number 1 is used by the coil temperature control system for gas temperature control. The signals from thermocouples 2 and 3 are processed and displayed by an Ancom DTK-1000 digital thermometer via an Ancom MSR-12 twelve way switch.

The temperature of the inside surface of the cylinder head was required for a rough estimate of the heat transfer rate during combustion. This was measured by flush mounting a 3/8" bolt shown in figure 2.23, with a Cromel Alumel thermocouple soldered into the end. A temperature survey of the head was conducted by M. Balci (51), with five thermocouples in different locations. This showed that the mean head temperature could be given by a thermocouple positioned at a specific location. Therefore only one thermocouple is used to measure the mean head temperature and its signal is processed by the two Ancom instruments described in the previous section.

Heating Coil Temperature Measurement

Two stainless steel sheathed thermocouples are embedded in the heating coils. One of these feeds into the two Ancom instruments (section 2.2.n) for display on the panel mounted meter. The other signal is used by the air temperature control system to prevent the heating coils from overheating during warm up.

High Speed Camera

A Hycam 16 mm high speed camera is used to record fuel/air mixing and combustion, at frame rates upto 8000 fps. Speed control is effected by control of the input voltage with a Variac. The instantaneous frame rate may be obtained from timing marks strobed on to the film edge during filming.

Illumination of the combustion chamber was initially achieved by two 250 Watt projector lamps, but these were unable to produce enough light. Greater illumination was obtained subsequently from two M3 photo flash bulbs. They may only be used once to give a short burst of light, as shown in figure 2.24, but the intensity is 100 times greater than that of the projector lamps. Their effective duration is only 15 ms, but this is adequate to cover a full injection period.

A timing circuit, as shown in figure 2.25, synchronises the flash with the injection period. The delay for the flash, which is taken from the energisation signal for the fuel pump solenoid, is set by a potentiometer on the front of the circuit panel.

A high speed light meter was also built to help set the delay period for the flash and the exposure setting for the camera. The circuit diagram for this is shown in figure 2.26.

2.2.5 Air temperature control system

The original temperature control system, which is described in reference (40), used to control the temperature of the heating coils, but this was later switched to directly controlling the air temperature. Also the coils and power transformer were uprated from 1 to 3 1/2 kW capacity. As a result of this a system to prevent the coils from overheating was designed and built.

A thermocouple embedded in the heating coils, drives the circuit, which is shown in figure 2.27. If the heating coil temperature exceeds the value set on the panel mounted potentiometer, then the circuit triggers a relay to switch out the power transformer. The circuit also cuts out the power if the thermocouple becomes open circuit.

Absorption of heat by the seal oil supply, cooled pressure transducer and cooled injector, forced the uprating of the heating coils to 3 1/2 kW capacity. The original 10m of sheathed heating element, was replaced by 14m of sheathed heating element, but of greater current carring capacity. Peak continuous temperature operation for both these elements is 980 C.

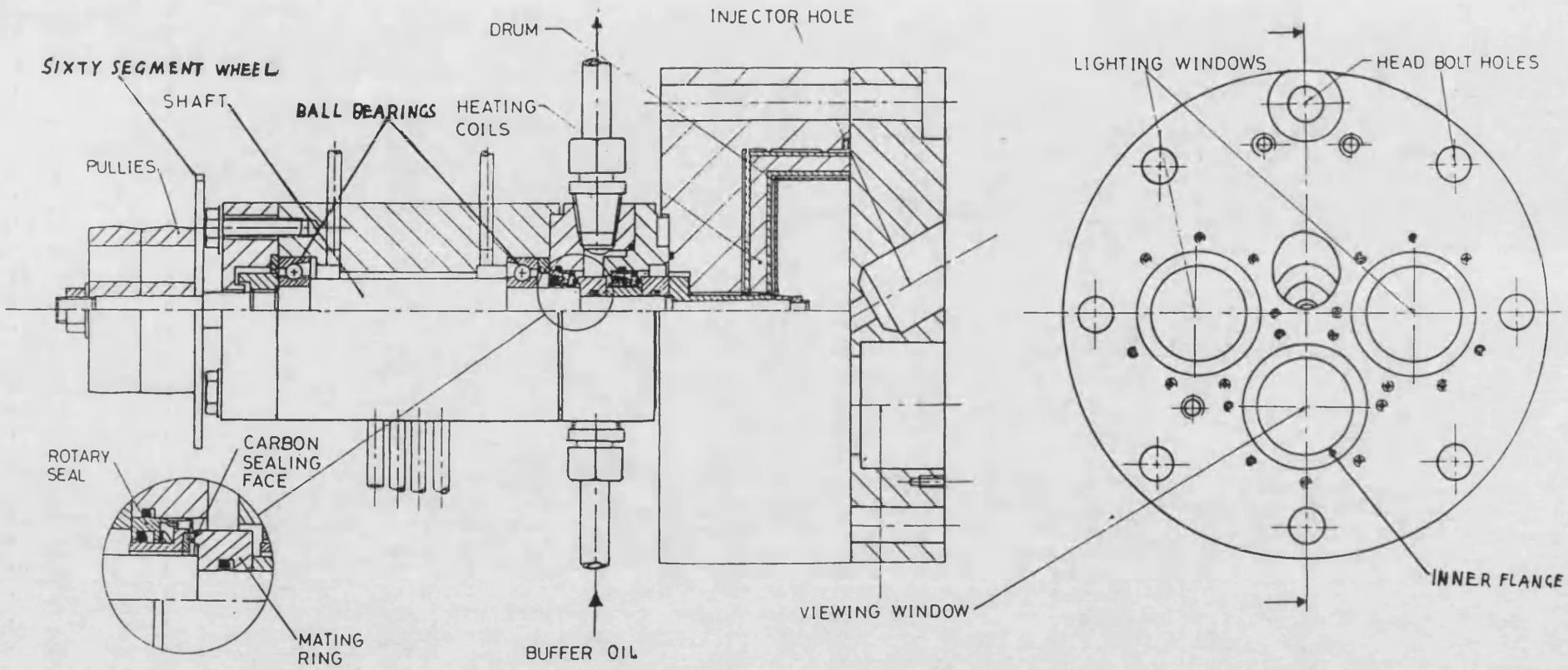

FIG. 2.1 SECTION OF COMBUSTION CHAMBER, DRUM DRIVE ASSEMBLY & OPTICAL HEAD

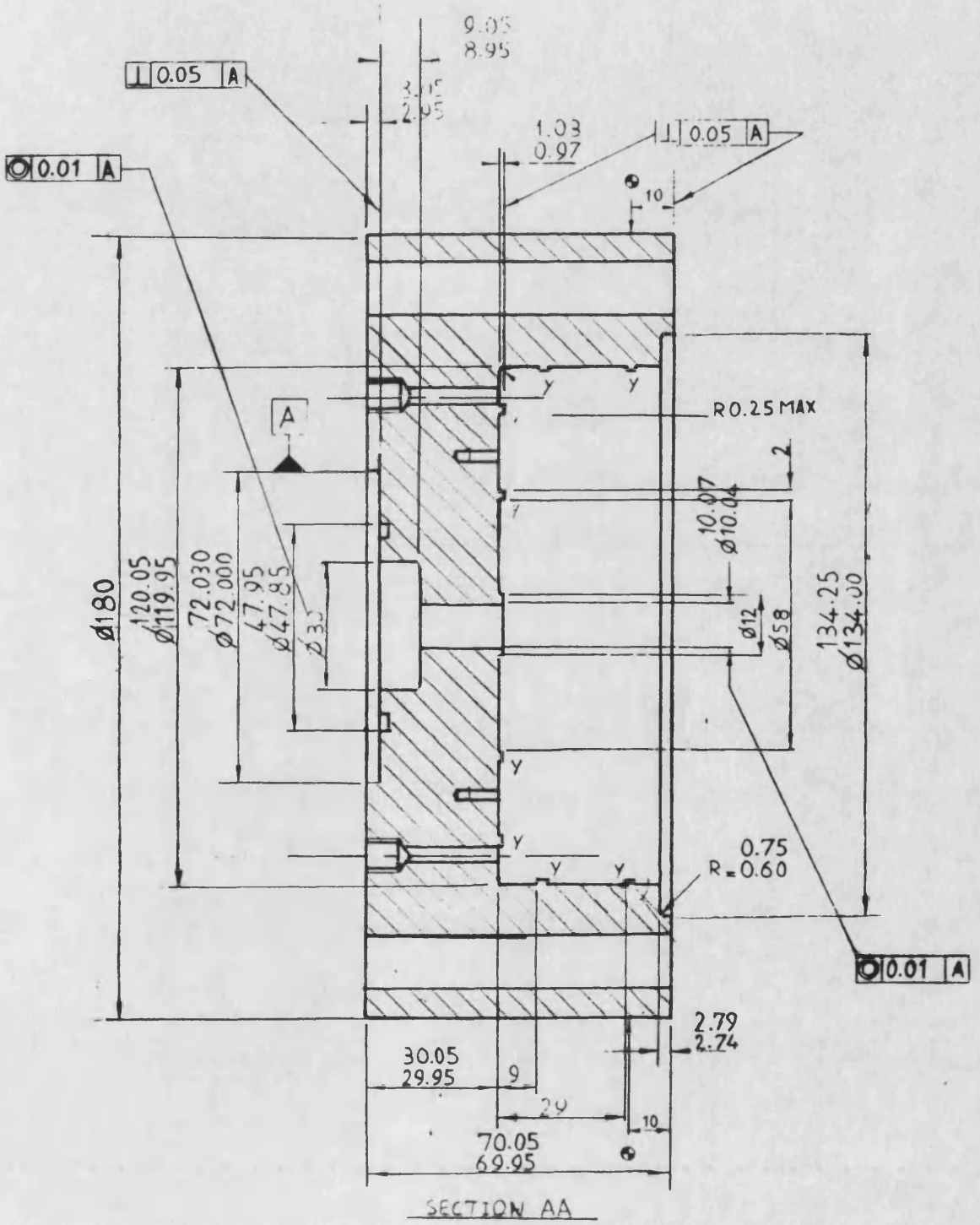

FIG. 2.2 COMBUSTION CHAMBER BLOCK

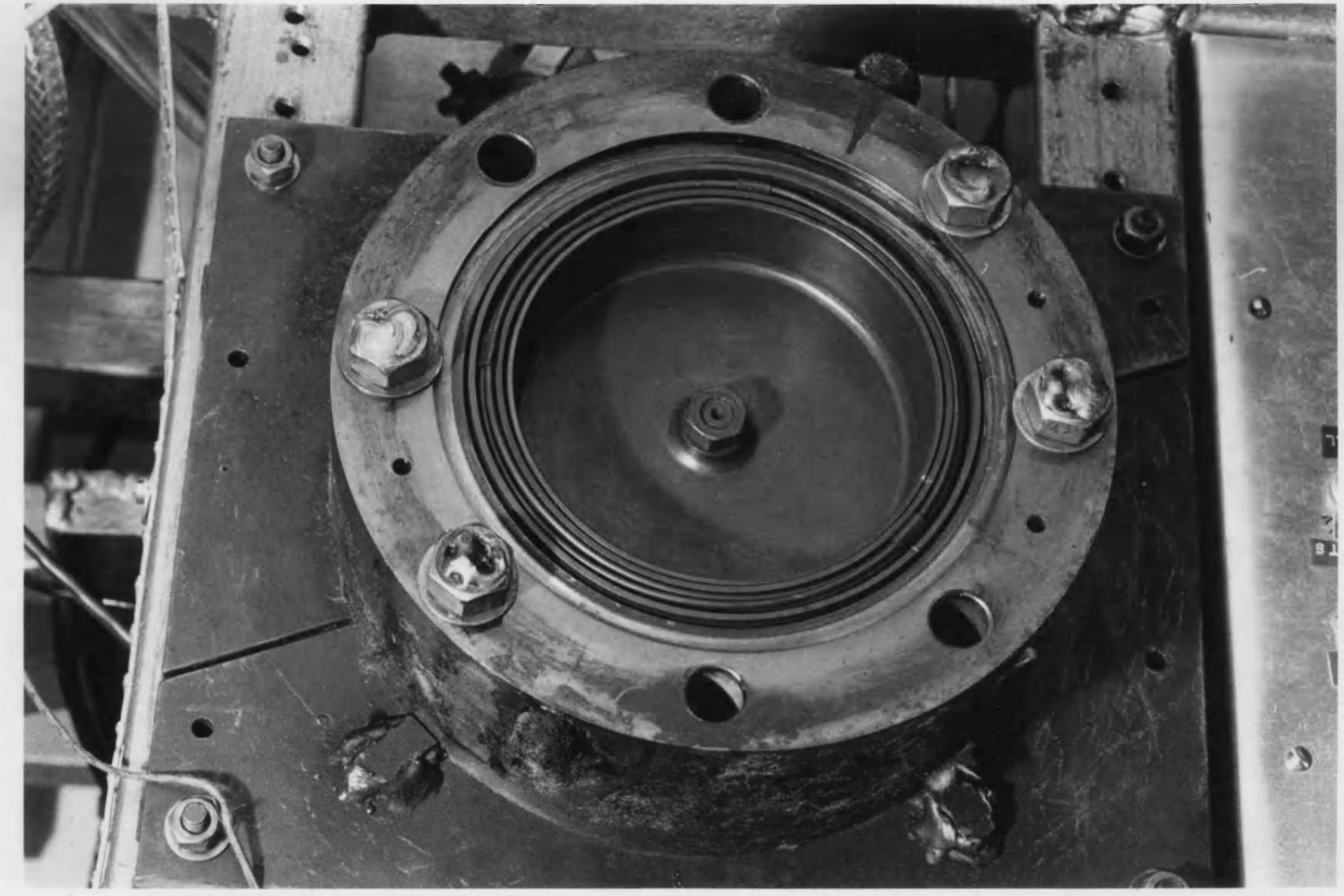

FIG. 2.3 HEATING COIL SUPPORT & SWIRL GENERATING DRUM

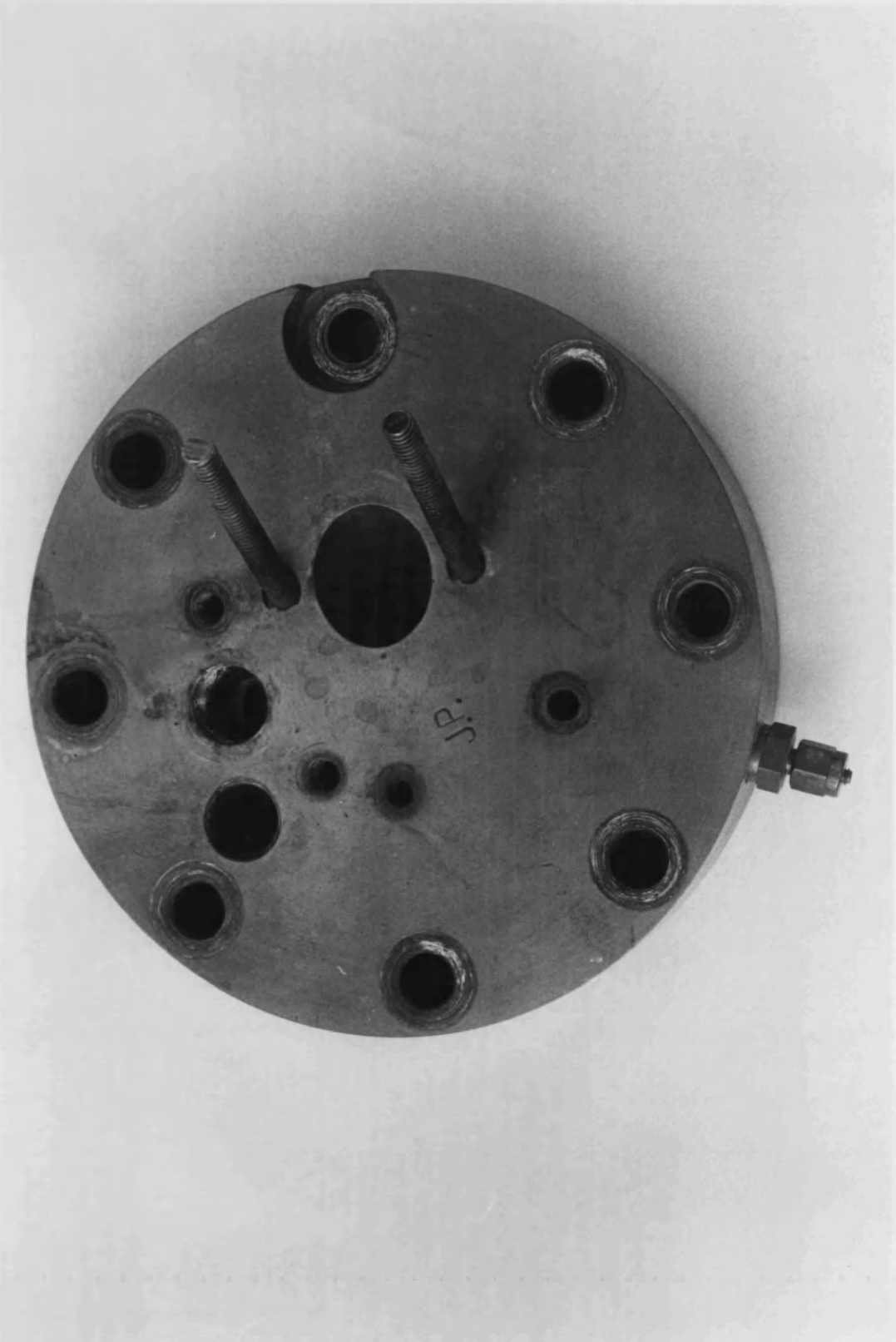

FIG. 2.4 INSTRUMENTED HEAD

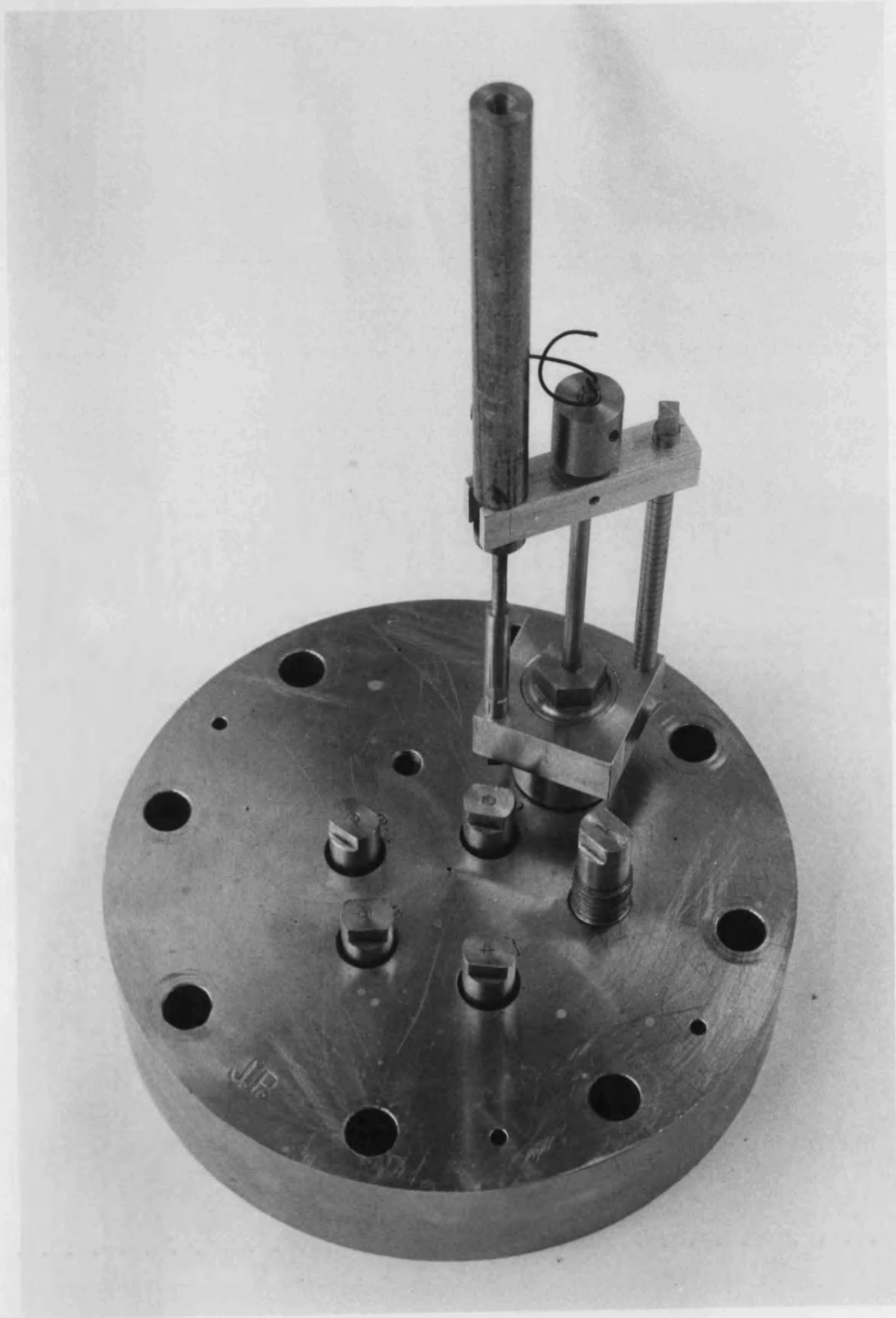

FIG. 2.5 ANEMOMETRY HEAD

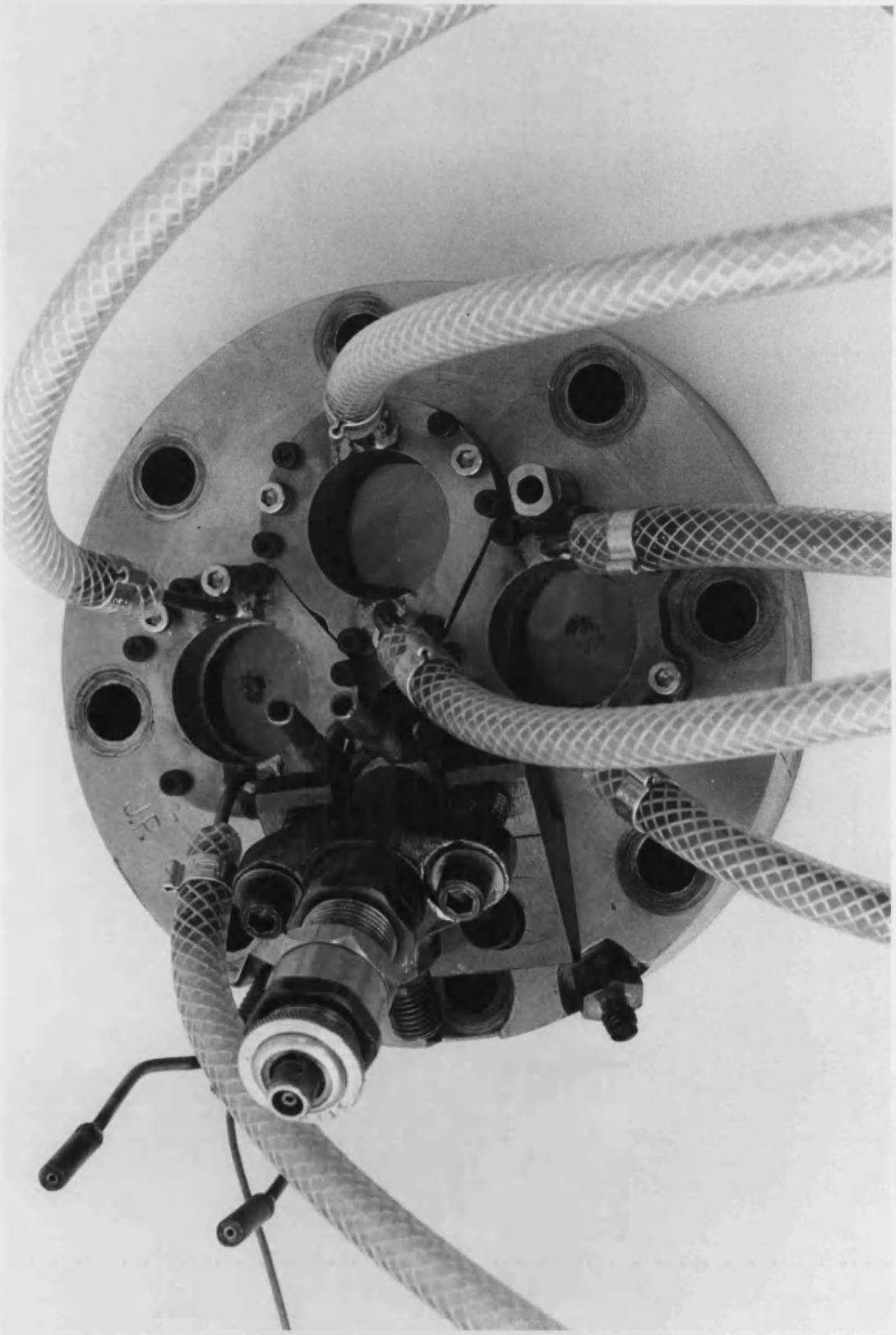

FIG. 2.6 OPTICAL HEAD

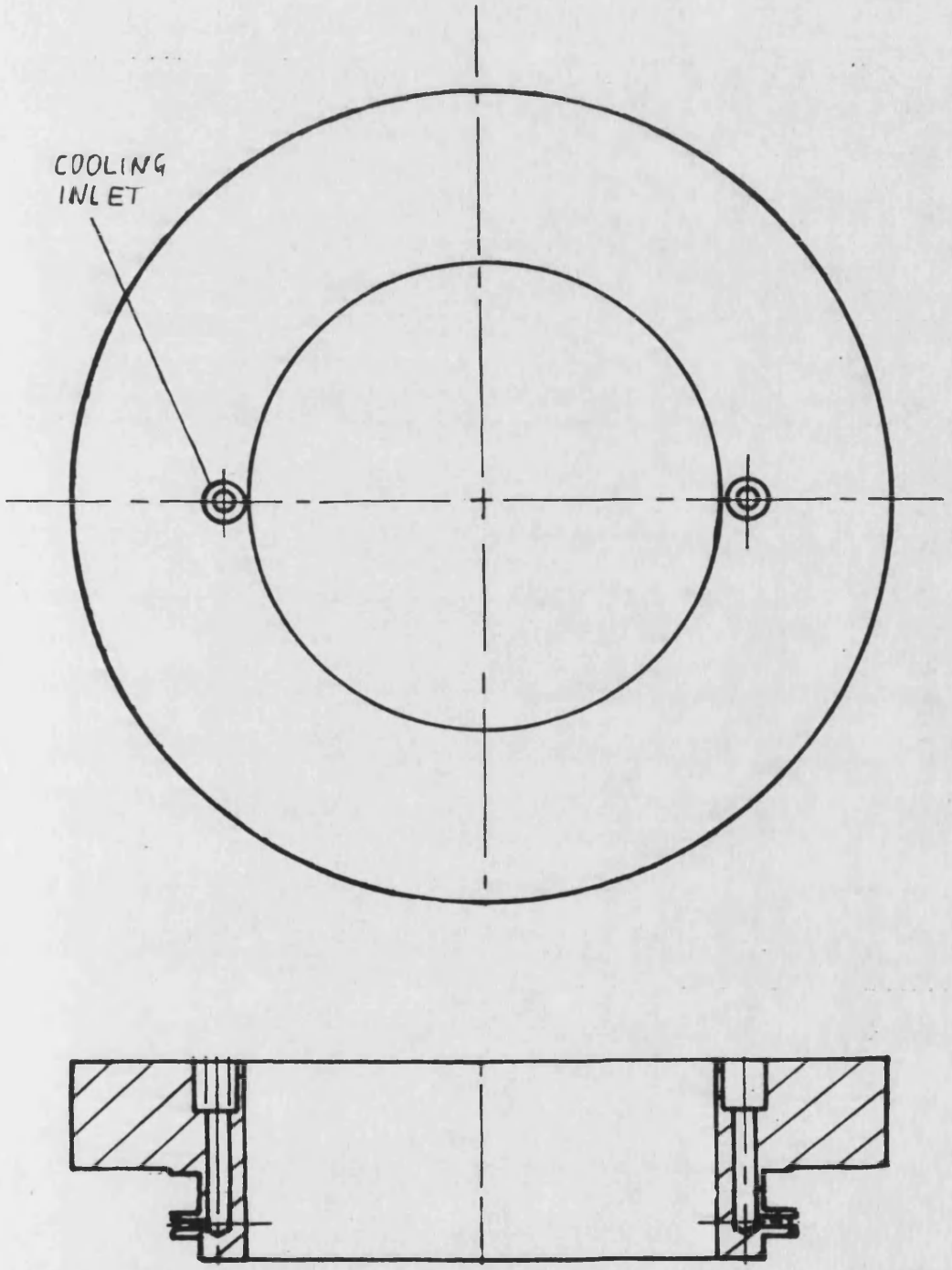

FIG. 2.7 CLAMPING RING FOR QUARTZ WINDOW

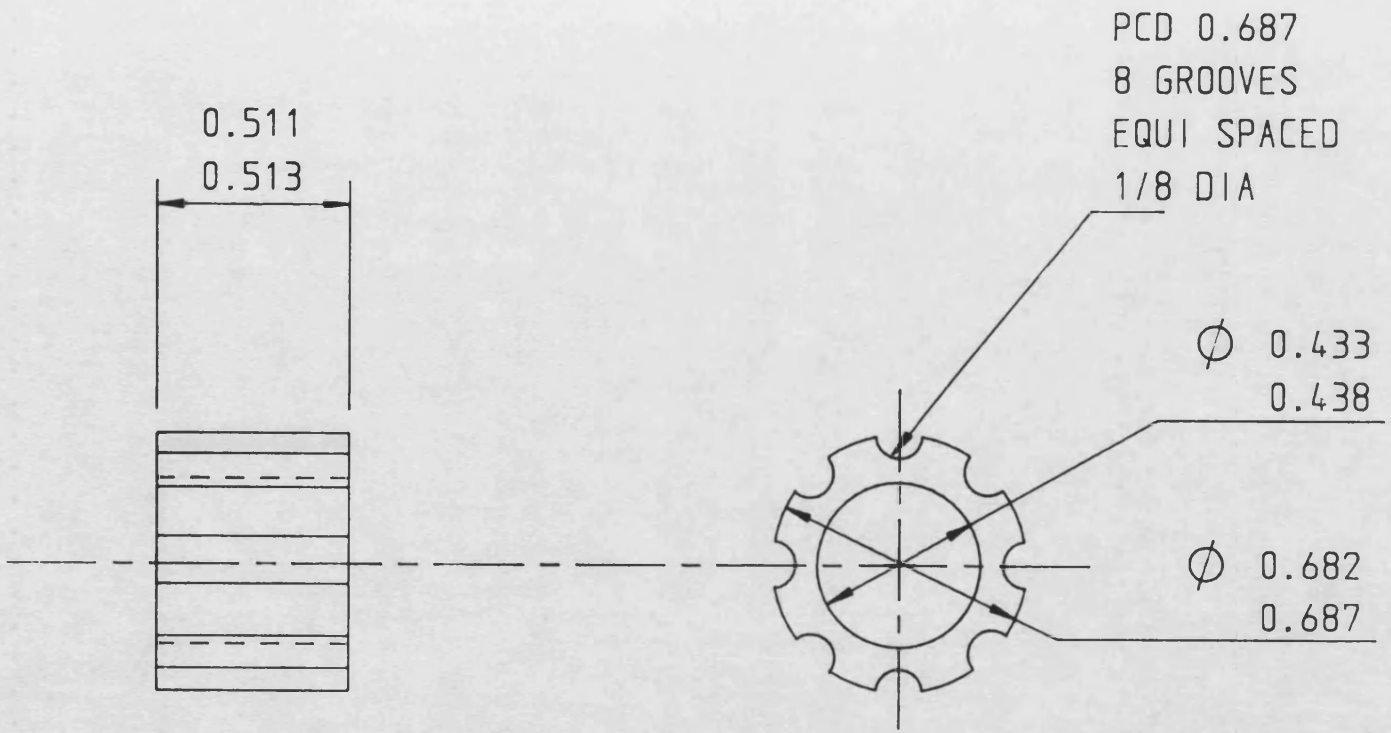

FIG. 2.8 COPPER SPACER

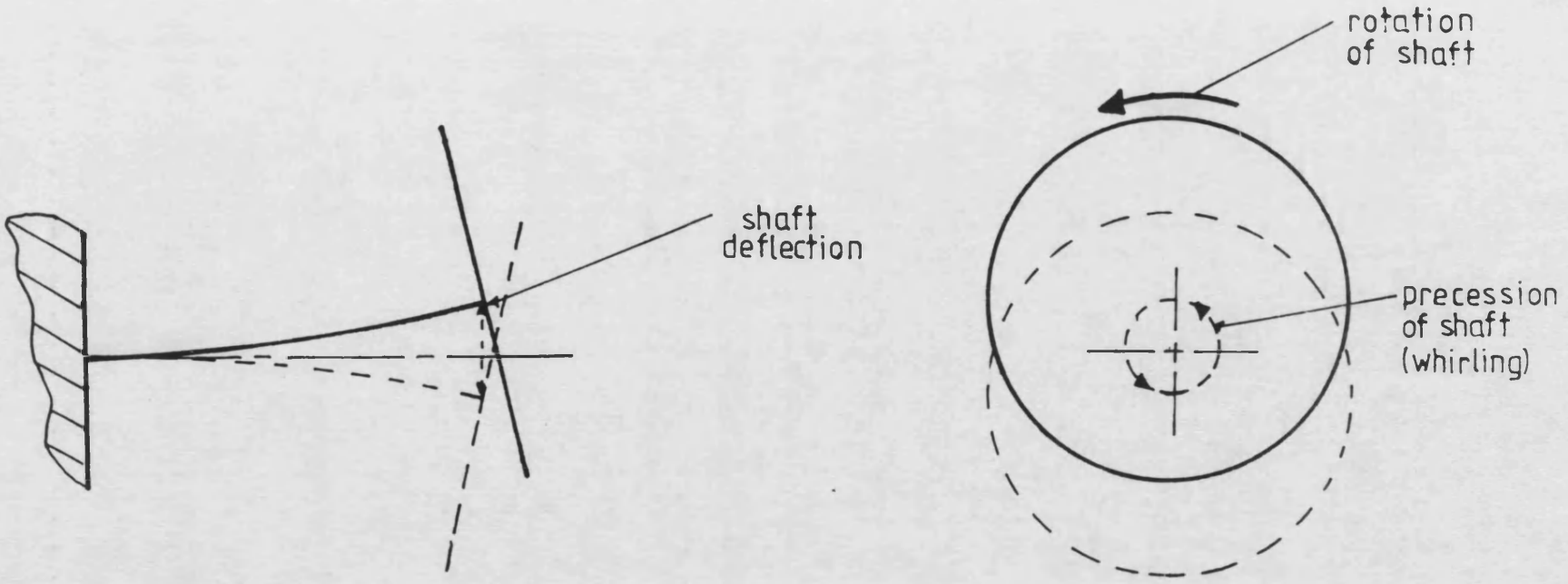

FIG. 2.9 EFFECT OF WHIRLING ON SHAFT

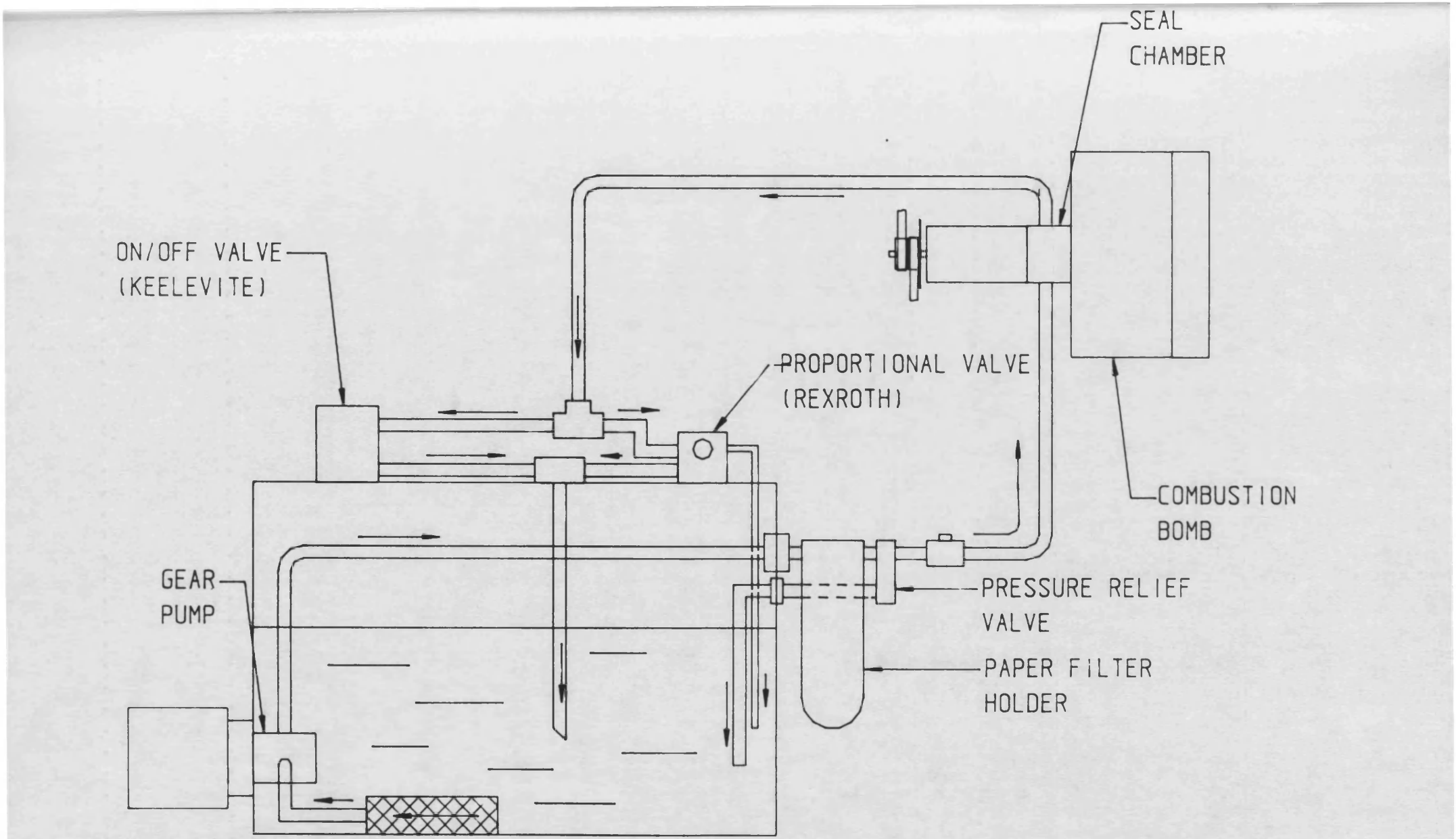

FIG. 2.10 HYDRAULIC CIRCUIT

FIG. 2.11 HYDRAULIC POWER PACK

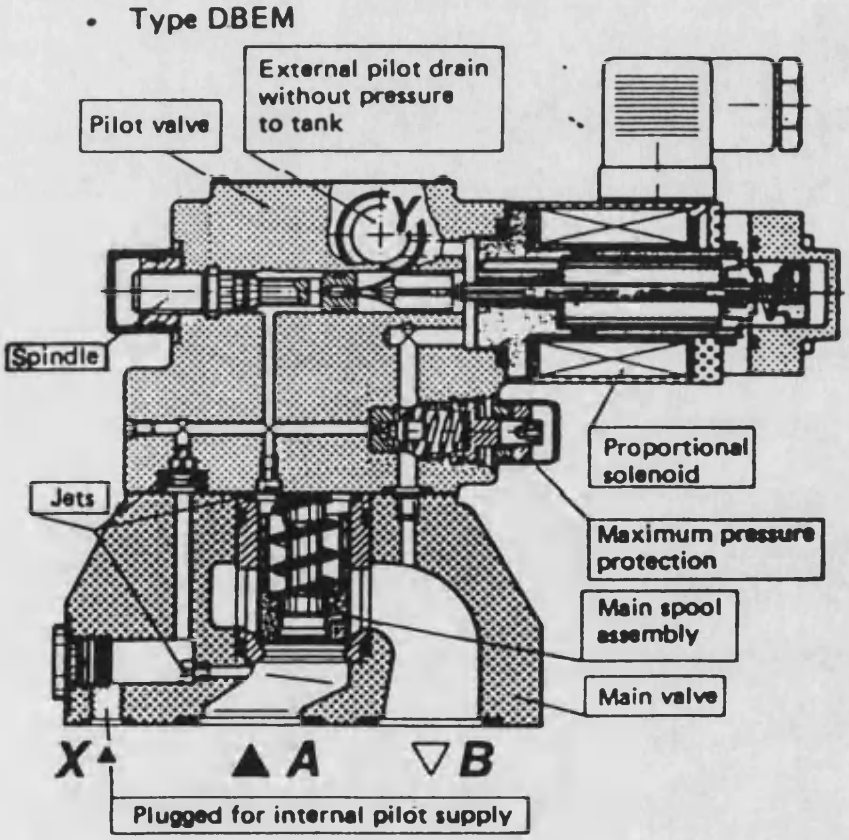

FIG 2.12 MANNESMANN REXROTH PROPORTIONAL CONTROL VALVE

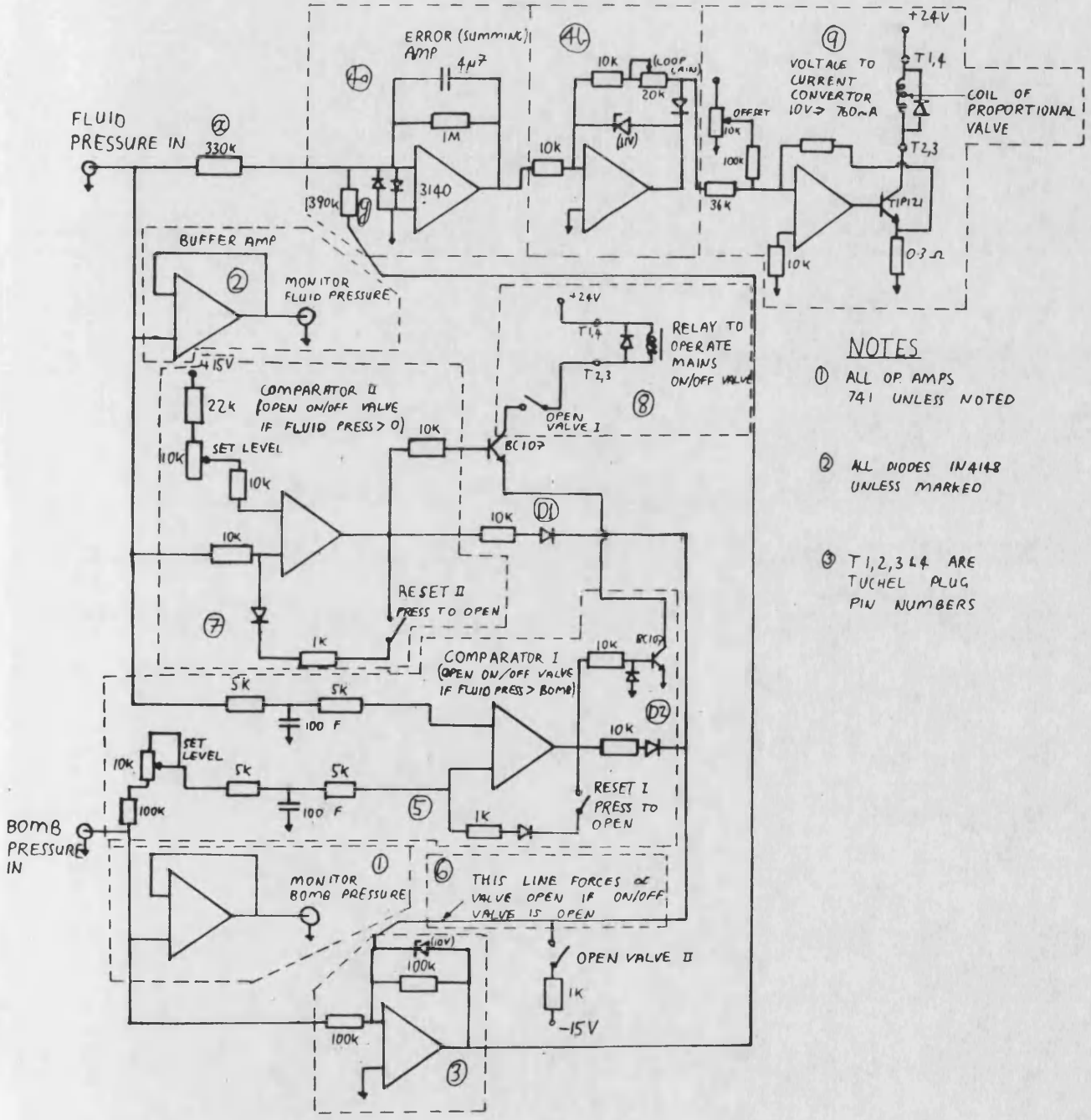

FIGURE 2.13 PRESSURE REGULATOR CIRCUIT

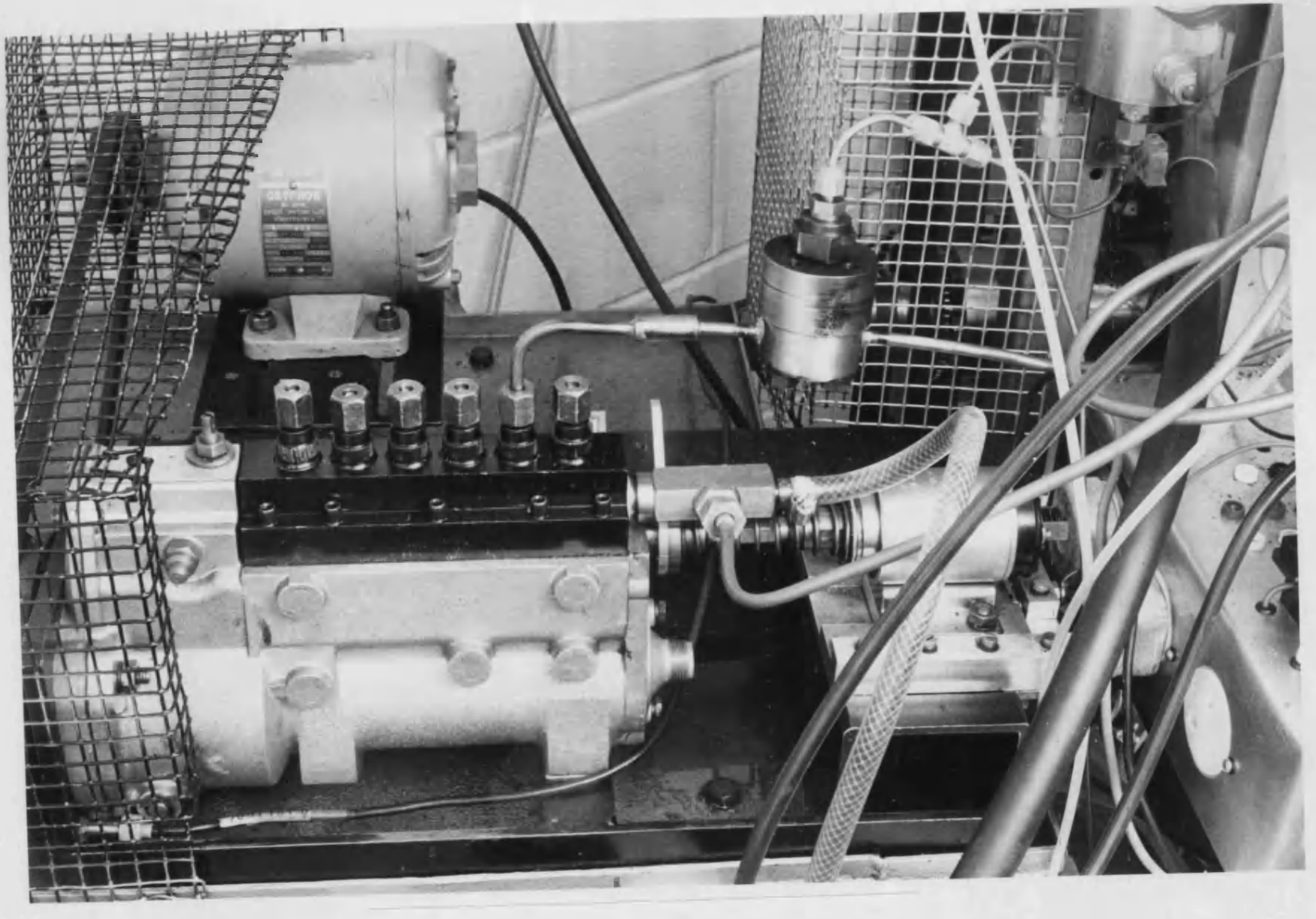

FIG. 2.14 FUEL PUMP & SOLENOID

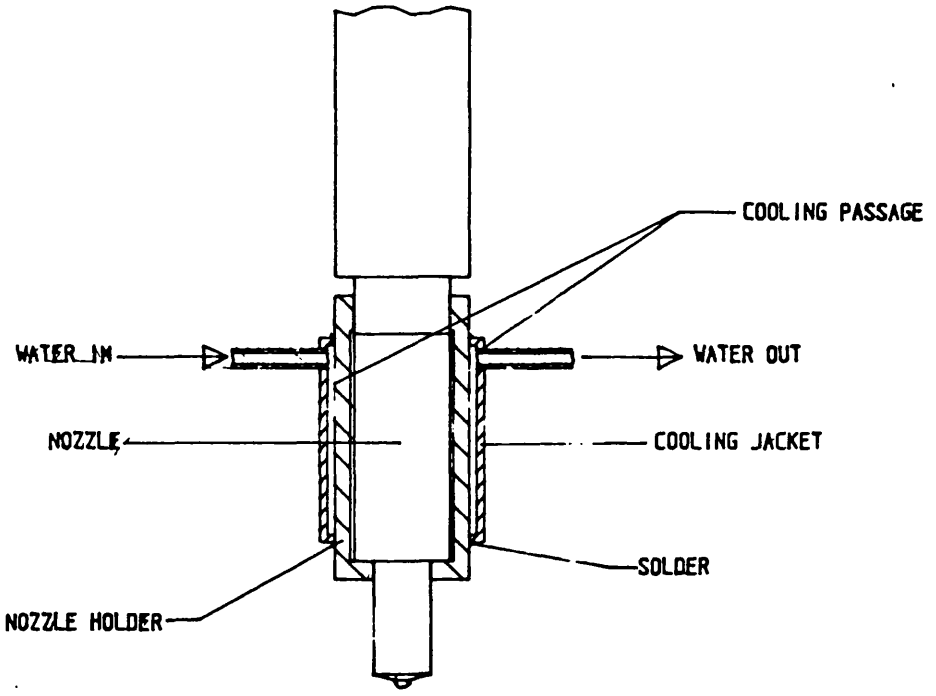

FIG. 2.15 OLD COOLING JACKET

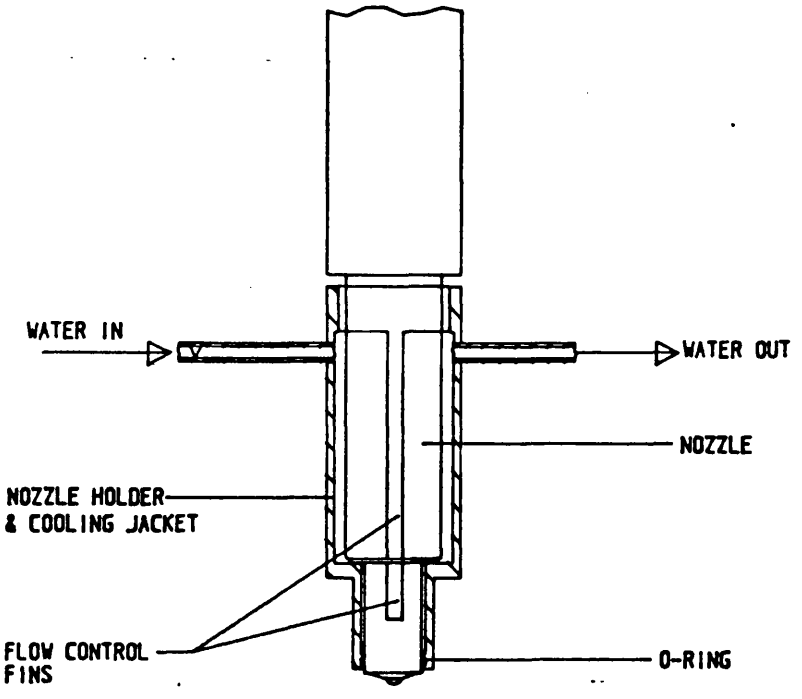

FIG 2.16 NEW COOLING JACKET

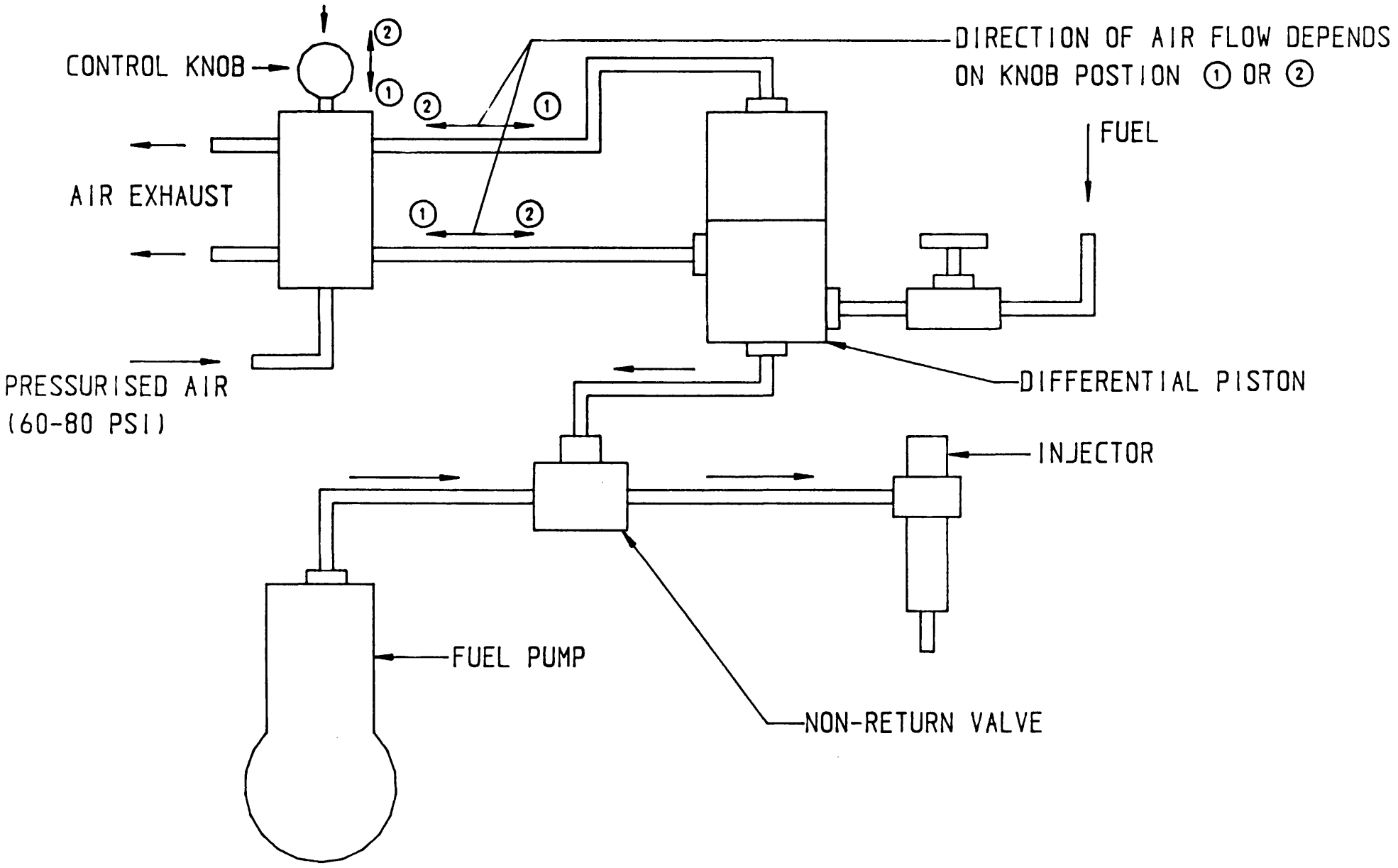

FIG 2.17 FUEL LINE PRESSURISATION SYSTEM

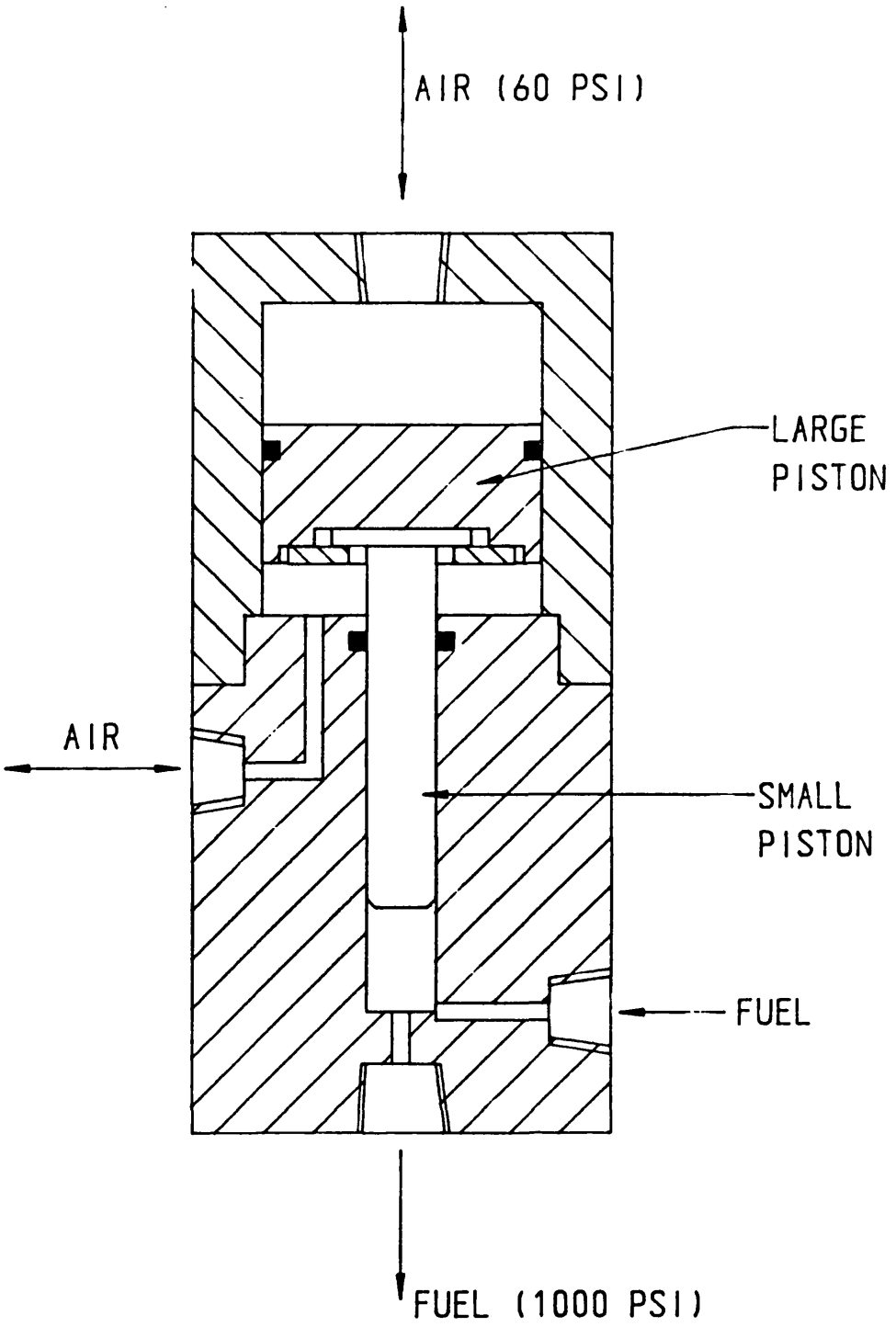

FIG. 2.18 DIFFERENTIAL PISTON

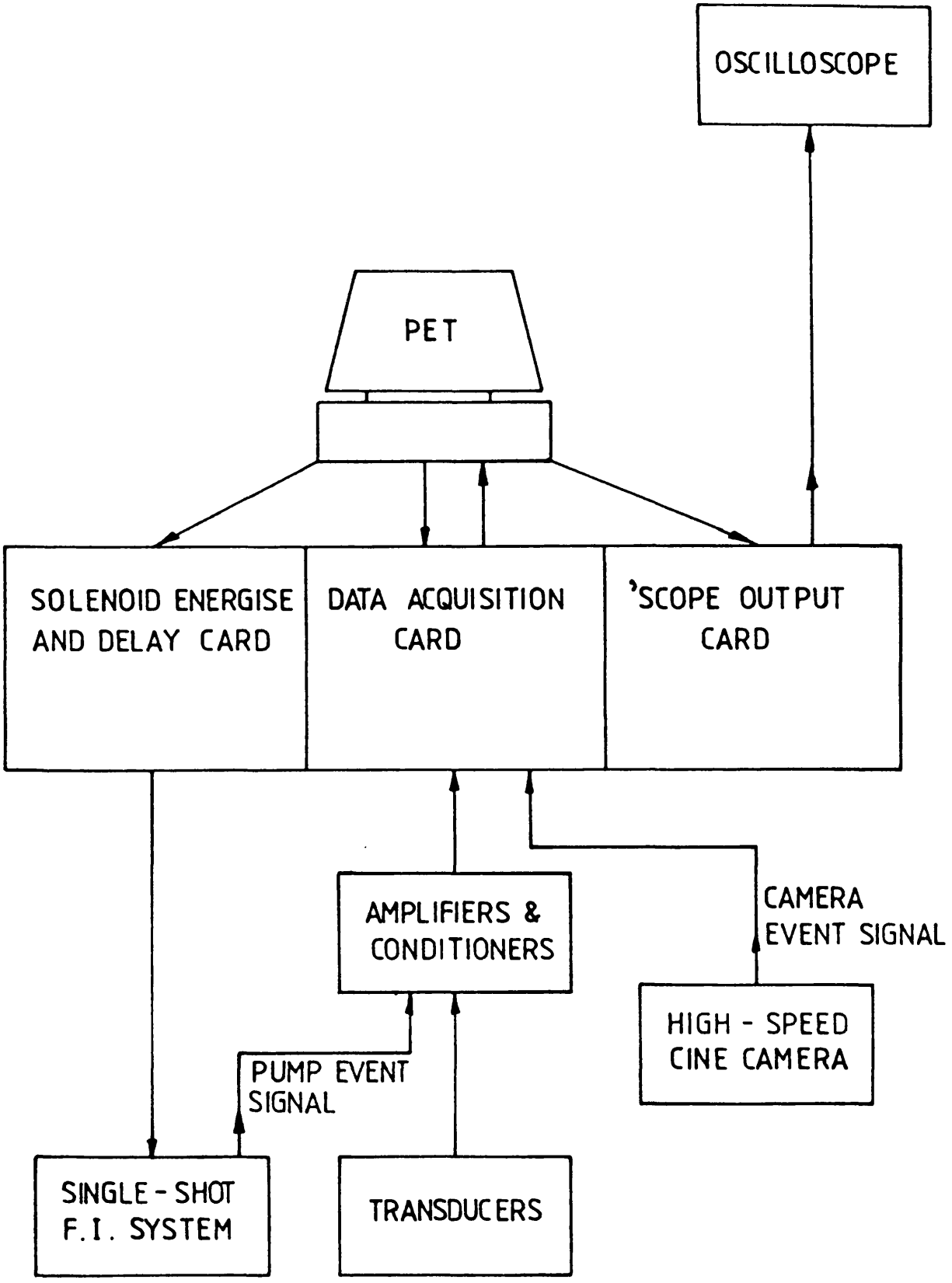

FIGURE 2.19 RIG CONTROL AND DATA ACQUISITION SYSTEM

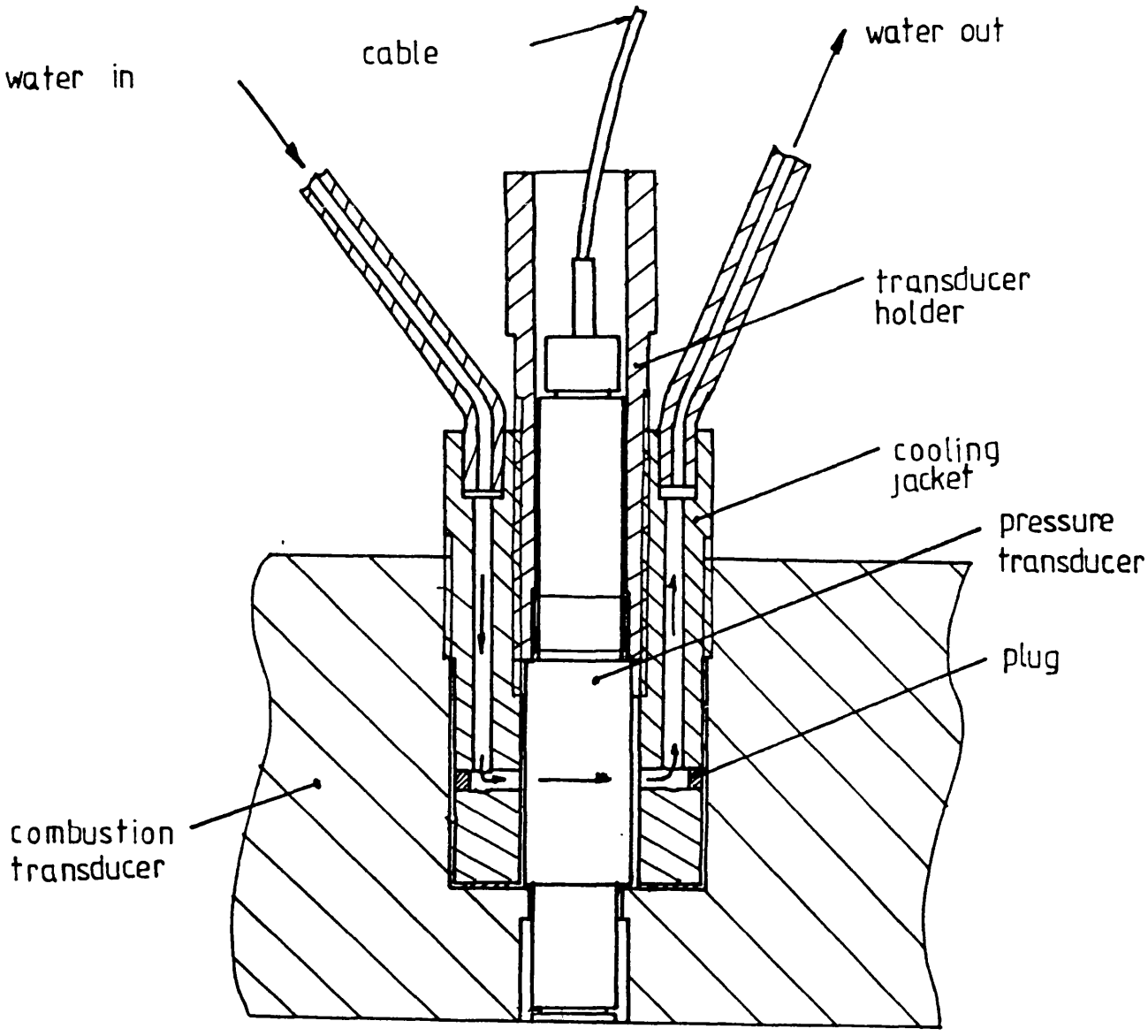

FIG. 2.20 PRESSURE TRANSDUCER COOLING JACKET

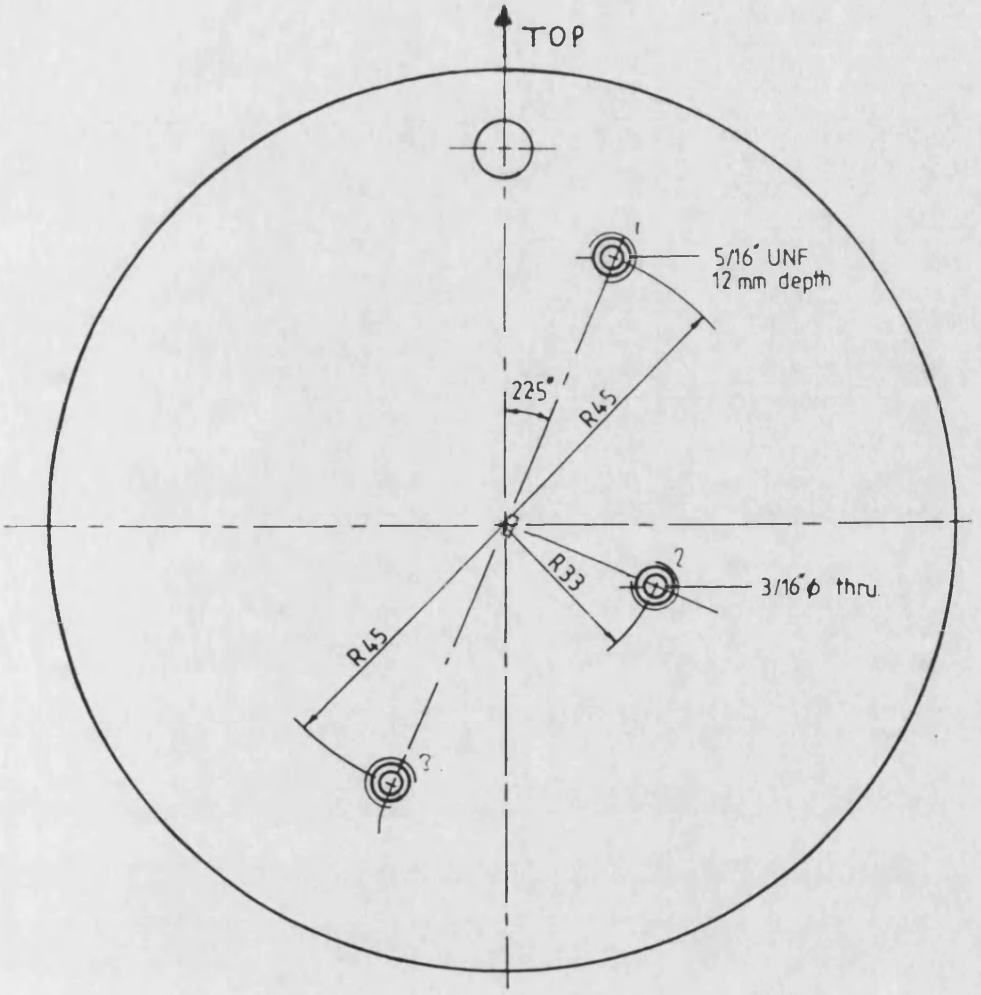

Figure 2.21 Location of thermocouples for gas temperature measurement.

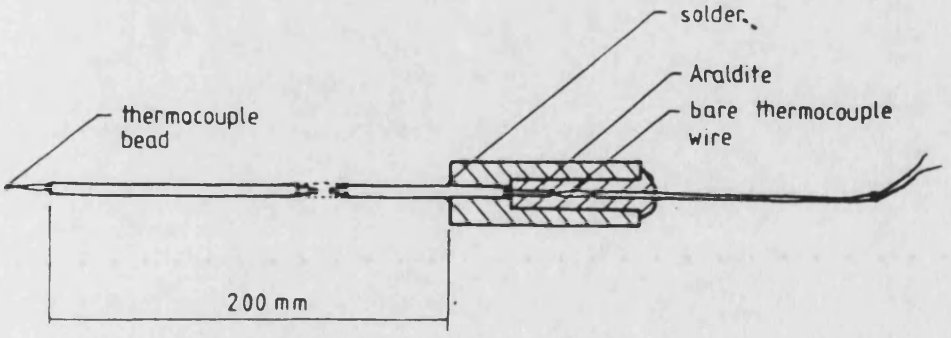

FIG 2.22 THERMOCOUPLE DESIGN FOR GAS TEMPERATURE MEASUREMENT

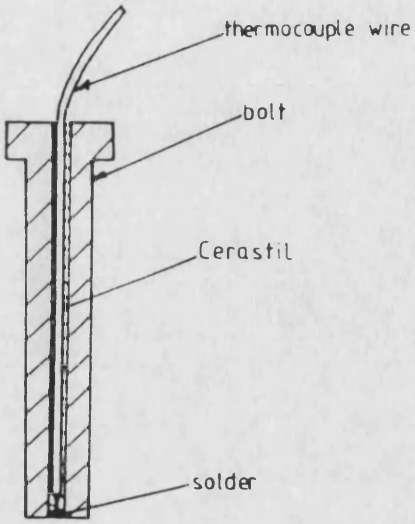

FIG. 2.23 THERMOCOUPLED BOLT FOR HEAD TEMPERATURE MEASUREMENT

Photo-Flash M3
Specification

Class	M
Colour of bulb	Clear
Total light output (lumens secs)	16000
Peak light output (megalumens)	1
Time to peak (milliseconds)	17
Duration above half peak (milliseconds)	15
Voltage range	3-45
Maximum bulb diameter (mm)	22
Maximum overall length (mm)	45
Bulbs per pack	6
Bulbs per outer container	180
Colour code	Red

Full Exposure Data is printed on every carton

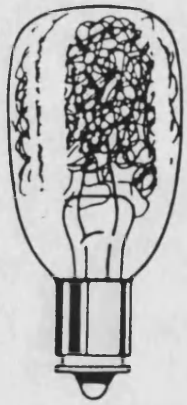

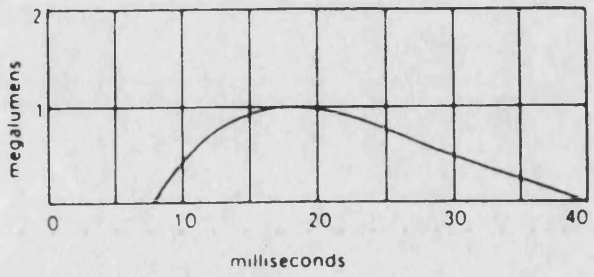

FIG 2.24 PHOTO FLASH BULB & SPECIFICATIONS

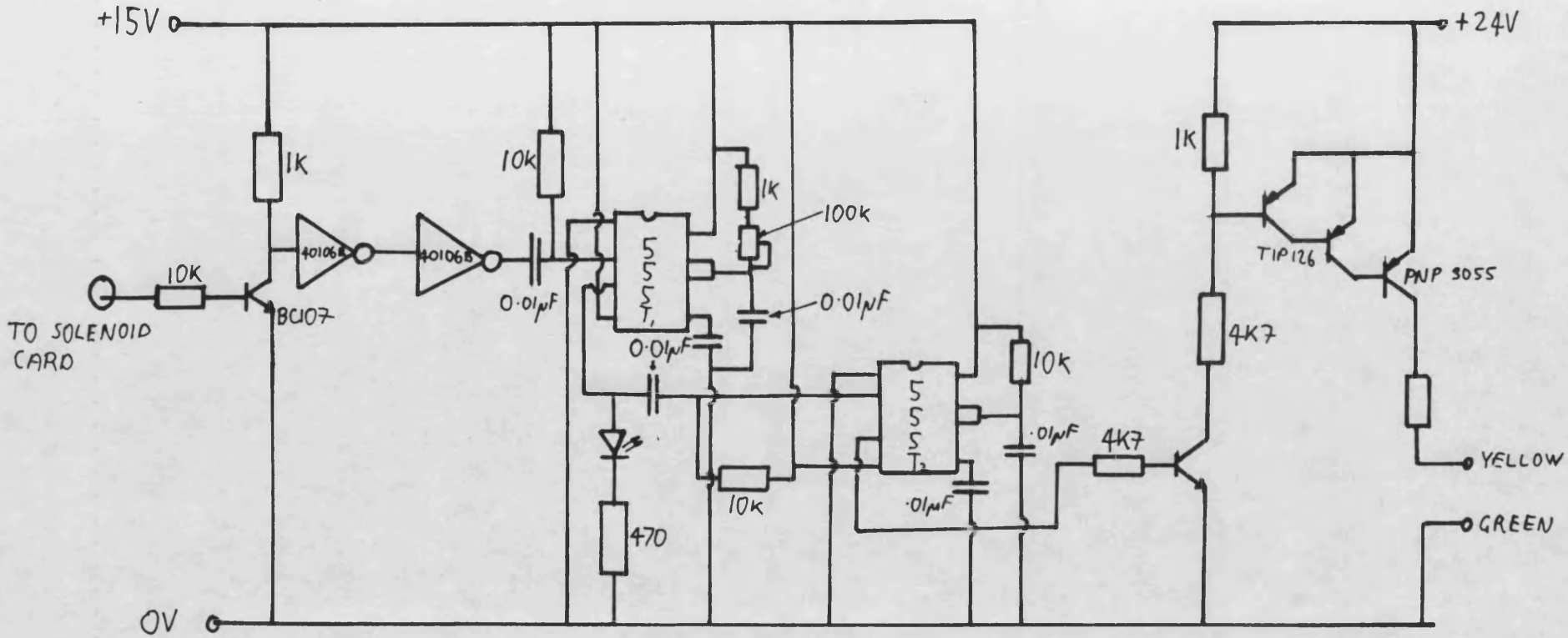

FIGURE 2.25 FLASH TRIGGER CIRCUIT

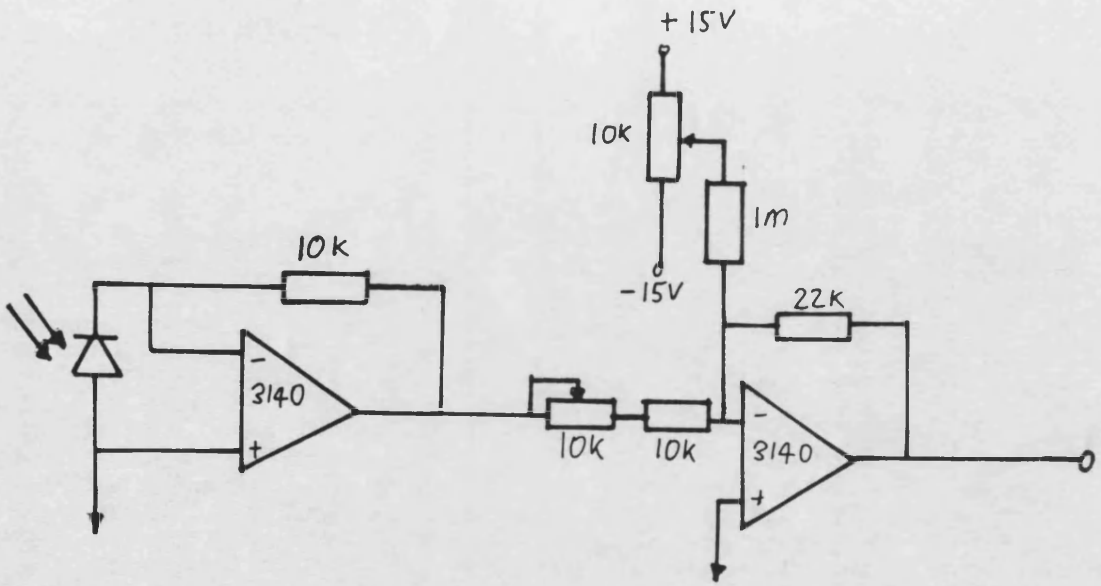

FIGURE 2.26 LIGHT METER

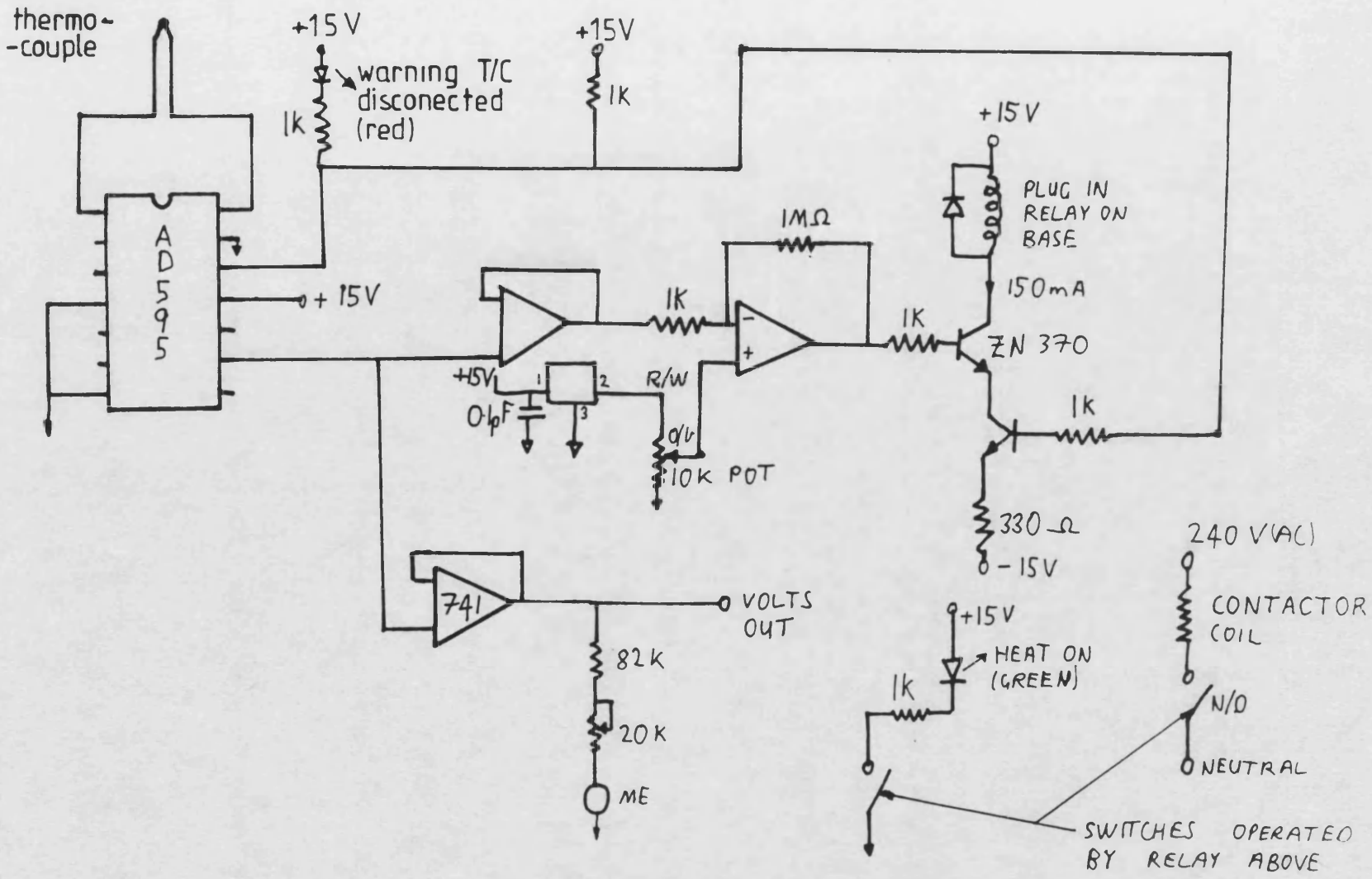

FIGURE 2.27 HEATING ELEMENT – O/TEMP. DETAIL

CHAPTER 3

Calibrations and Experimental Procedure.

Chapter 3: Calibrations & Experimental Procedure

3.1.a Calibration of Pressure Transducer

The steady state seal chamber & combustion chamber pressure transducers were calibrated against a dead weight tester. In both cases the output voltages of the transducer amplifiers were adjusted to read 6.9 volts for a pressure of 1000 psi gauge, which is equivalent to 1 volt per bar. Both transducers were periodically tested, but they proved to be very stable with time.

The piezo pressure transducer used for measuring transient pressures in the combustion chamber was periodically tested on a purpose built test rig, schematically illustrated in figure 3.1. Basically, this rig rapidly discharges a pre-set pressure applied to the pressure transducer, through a quick release ball valve. This negative step input of pressure is converted to an output voltage by the charge amplifier connected to the transducer & recorded on the peak hold DVM. From this, a calibration constant in terms of volts per bar is obtained.

The transducer had a non-linearity of 0.3% over its operating range. Also before & after each test series the calibration constant was checked, but the difference between each set of results never exceeded 0.7% during the whole test series.

3.1.b Fuel Quantity

The measurement of the fuel mass injected by the single shot fuel injection system was impeded, because of the small masses (0.1 gms) involved. A simple method would have been to repeat several injections into a container of known mass, measure the change in mass & obtain the mean mass per injection. However, this mass would not correspond to the mass injected into a pressurised chamber, because of the lack of back pressure on the nozzle.

A solution to this problem, illustrated in figure 3.2, was to measure the volume of fuel fed into the pump, rather than the mass injected. The fuel pump is supplied from a capillary tube, with an internal diameter of 1.2014mm. Volume fluctuations are damped out by the needle valve below the tube & the resulting pressure fluctuations are absorbed by a short length of reinforced plastic tube. An injection of fuel results in the level of fuel in the capillary tube dropping by an amount which should approximately correspond to the mass injected. This quantity should be less than the mass injected because of the minimal, but unavoidable leakage from the nozzle.

To obtain the mass of fuel injected, the fuel was injected into a container of known mass & the change in mass measured to a resolution of 0.1 milligrams. At the same time the drop in the capillary tube level was recorded. From these two figures, the relationship between the fuel mass injected & the drop in the level of the fuel was obtained.

Before calibrating the fuel injection system, the following precautions were taken to ensure repeatable results:-

1. The LP fuel system was bled to remove all traces of air.

2. The fuel pump was warmed up to a stable temperature by running it for an hour.

3. Several test injections were made to remove any air from the HP fuel pipe.

4. The initial fuel level in the capillary tube was started at the same height before each test to reduce the effects of gravity on the system.

An example series of injections is shown in table 3.1. These produced a mean ratio between the mass injected & the mass predicted (from the capillary tube) of 1.0424 with a standard deviation of 0.0246 (2.36%). This deviation is quite acceptable in comparison to the variation in the mass of fuel burnt, as predicted by the heat release analysis program.

3.1.c Thermocouples

It is well established that physical gas temperature measurement at high temperatures may be influenced by the effects of radiation and conduction. Therefore a theoretical analysis of the error between the actual gas temperature & the thermocouple reading was done. The problem was considered as shown in figure 3.3,

where the thermocouple bead is attached to a side wall by two thin wires. The gas passes over the bead & wires with a velocity related to the swirl level. Also the bead & wires receive & emit radiation to two walls at temperatures T_2 & T_3. The angle factor was considered to be 2/3 for the hot wall & 1/3 for the cold wall (bomb head). E_0 was taken to be the emissivity for all surfaces. By applying the principle of conservation of energy the following equations were derived:-

$$\frac{d^2T_1}{dx^2} = BT_1 + CT_1^4 + D \qquad - 3.1$$

where $$B = \frac{L_p h_w}{k A_1} \qquad - 3.2$$

$$C = \frac{L_p E_0 \sigma}{k A_1} \qquad - 3.3$$

$$D = -\frac{L_p}{kA_1}\left[h_w T_2 + E_0\sigma\left(\alpha_2 T_2^4 + \alpha_3 T_3^4\right)\right] \qquad - 3.4$$

Let

$$T_1 = y_1 \qquad - 3.5$$

& $$\frac{dT_1}{dx} = y_2 \qquad - 3.6$$

Therfore substituting 3.5 & 3.6 into 3.1, and 3.5 into 3.6 gives:-

$$\frac{dy_2}{dx} = By_1 + Cy_1^4 + D \qquad - 3.7$$

$$\frac{dy_1}{dx} = y_2 \qquad - 3.8$$

The boundary conditions for these equations were as follows:-

at $x=0$ $\quad T_1=T_3$

at $x=L_w$ $\quad T_1=T$

where

$$T=\left[A_b E_o \sigma\left(\alpha_2 T_2^4+\alpha_3 T_3^4\right)-2kA_1\left(\frac{dT_1}{dx}\right)_L-h_b A_b\left(T-T_a\right)\right]^{1/4} \qquad - 3.9$$

These derived equations were used in a simple numerical computer program, to give the temperature reading error for the thermocouple under different conditions.

The relationship of most interest was between the level of swirl & the thermocouple temperature error. The greatest errors in measurement are most likely at

high temperatures & low swirl levels. Therefore the temperature errors were computed at various swirl levels for the following constant conditions:-

Air temperature	- 973 K
Hot wall temperature	- 1073 K
Cold wall temperature	- 873 K
Thermocouple location radius	- 0.045 m
Diameter of bead	- 0.803 mm
Diameter of wire	- 0.203 mm
Length of wires	- 0.15 m
Gas Pressure	- 35 bar
E_σ	- 0.7

The results for this analysis are shown in figure 3.4 & show that the maximum error will be 4 C above the the actual air temperature at the minimum swirl level of 100 rad/s. This error reduces to 1.5 C at 1000 rad/s.

All the experiments were done at swirl levels above 100 rad/s. Also, in this analysis, the air temperature used was 100 C above the maximum temperature attained experimentally, which will increase the radiation errors. Since the errors will be at their maximum under these conditions, it seems reasonable to consider that the actual experimental temperature errors will be within acceptable limits.

3.2 Experimental Procedure

A strict experimental procedure was followed to produce repeatable & controlled results. Generally this procedure was the same whatever the type of test. For an optical test, there was the additional operating procedure for operating the camera & lighting. Similarily, certain procedures would be excluded such as the heating coil operation in a cold test or the swirl control in a quiescent test.

What follows therefore, is a comprehensive description of the experimental procedure including all operations, some of which were unnecessary depending on the type of test.

3.2.a Initial Start Up Routine

1. Check solenoid battery is charged & full. Also check the oil levels in the seal lubrication tank, the bearing lubrication tank & the fuel tank.

2. Turn on all the instrumentation & load the control program into the PET computer.

3. Open the valve on the gas bottle and pressurise the combustion chamber & check that the drum shaft seals are working.

4. Turn on the seal lubrication pump & check the seal chamber pressure is less than 10 psi on the low pressure gauge (to prevent oil leakage into the combustion chamber). Close the valve to the low pressure gauge.

5. Turn on the injector & piezo-electric pressure transducer cooling water supply plus the associated low flow alarm.

6. Switch on the heating coil control circuit & select the desired air temperature.

7. Allow the instrumentation to warm up & stabilise for at least 1 hr.

8. Mount the camera on its frame & connect up the three power & control cables.

9. Turn on the fuel supply & bleed any air from the fuel pump.

10. Turn on the low pressure air supply & open the inlet valve to the fuel pressurisation system. Retract the differential piston, by pushing in the air control spool valve to prime the pressurisation system. Close the inlet valve & pressurise the fuel system by pulling out the spool valve.

11. Switch on the solenoid battery power supply.

3.2.b General Test Procedure

1. Select the calibration mode on the PET & adjust the bit readings for the fuel line & needle lift to approximately 10.

2. Increase the pressure in the bomb to 10 bar & press the valve reset switch for the seal pressurisation system. This will close the bypass valve, which will allow the buffer oil to be pressurised.

3. Increase the bomb pressure to the required value using the pressure regulator on the gas bottle, while leaving the gas inlet valve open.

4. Switch on the fuel injection pump.

5. Switch on the swirl motors & bring them upto the required speed. If the swirl speed is to exceed 2500 rpm, turn on the bearing lubrication system. The swirl motors will need an occasional adjustment to keep them at the correct speed.

6. Select the test mode on the PET computer & input the control parameters for the injection process and data acquisition. (See 3.2.c for a description of the parameters.)

7. Allow the air and coil temperatures to stabilise & note their values. At the same time, note the swirl speed & the initial fuel line pressure.

8. Place the flash bulb holders in their respective window holes. (See 3.2.d for the camera & lighting set up.)

9. Shut the gas inlet valve & allow the bomb pressure to drop slowly to the exact pressure required for the test. While this is happening, the other conditions should be monitored constantly to make sure that they do not alter.

10. Unground the pressure transducer & start the camera, which should trigger the injection process & flash bulbs after the pre-set delay. If the camera is not being used, the injection process may be triggered manually by the switch on the control panel.

11. Turn off the power for the camera, which should have stopped after the film has finished.

12. Slow down the swirl motors & switch off the power supply along with the bearing lubrication system.

13. Open the exhaust valve & allow the pressure to drop slowly. (The bypass valve for the seal pressurisation system should open automatically when the bomb pressure goes below 8 bar.)

14. Remove the photo-flash bulb holders & eject the spent bulbs.

15. Examine the data from the PET, which should be displayed on the oscilloscope. A section from channel 1 (fuel line pressure) will be visible & this may be scanned by using the '<' & '>' keys. Channel 2 (needle lift) & channel 3 (chamber pressure) may also be examined by pressing keys '2' or '3' respectively.

16. If the data is satisfactory, it may be loaded onto a tape via the PET's inbuilt tape deck. This data may then be transferred to the main frame computer via another PET at a later time.

17. Turn out the room lights while the film is unloaded from the camera.

18. Purge the bomb by closing the exhaust valve & pressurising the bomb to 20 bar before reopening the exhaust valve. This should be repeated.

19. Clean out the camera with the airline & remove any film deposits adhered to the film gate.

3.2.c PET data acquisition & control parameters

When the test mode is selected on the PET computer, a table is displayed, which asks for a set of control parameters to be input. A reproduction of the display is shown in figure 3.5, with an example set of parameters. These control the injection process & the data acquisition. the first parameter, solenoid delay, sets the delay in milliseconds between the fuel pump reference signal & the solenoid

energisation. On the fuelpump flywheel there is a small stud, which induces a reference signal for the angular position of the camshaft in an Orbit magnetic pickup. The second parameter sets the energisation period for the solenoid.

The third parameter sets the delay between the reference signal & the start of the data acquisition. This prevents useless data being recorded, before the injection stroke of the pump. Parameter four sets the number of data input channels, upto a maximum of four, although no more than three have ever been used (fuel line pressure, needle lift and chamber pressure). Parameter five controls the number of samples to be recorded per channel upto a maximum of 999 each. The sample interval is set by the sixth parameter & the minimum for this is 30 microseconds. With three channels, this means that each channel would be sampled every 90 microseconds.

3.2.d Camera & Lighting set-up

The camera is focused & aligned, using the original projector lamps & the desired frame rate is pre-set by adjusting the voltage setting of the Variac. The input voltage set on the Variac determines the peak frame rate that the camera will reach. The f-stop, which is dependent on the frame rate, shutter setting & lighting is set simply by the lense ring. Loading of the film may be done with the lights on, but great care needs to be taken to ensure that the film follows the correct path through the camera as shown

by the diagram on the inside cover of the camera. Before the camera is closed, the timing strobe, which records on the edge of the film, should be checked & the viewfinder hole closed.

Two new photoflash bulbs should be fitted into their holders & the holders fitted into their respective windows just before the film is run. This is to protect the plastic coated bulbs from the hot combustion bomb. The delay period for the flash bulbs is set in relation to the pump speed and the event which is to be recorded. This is adjusted by the potentiometer situated on the front panel of the flash circuit. A full description of the camera and its operating procedure is included with the camera.

	Change in fuel level (cm)	Predicted mass a (gm)	Change in tin mass b (gm)	(a-b) (mgm)	% error	ratio b/a
	12.4	.1141	.1163	-2.183	-1.83	1.019
	11.6	.1141	.1174	-3.280	-2.80	1.029
	11.6	.1068	.1159	-9.14	-7.89	1.086
	11.9	.1095	.1163	-6.78	-5.83	1.062
	12.4	.1141	.1156	-1.48	-1.28	1.013
	12.0	.1104	.1139	-3.464	-3.04	1.031
	12.3	.1132	.1148	-1.603	-1.40	1.014
	12.0	.1104	.1167	-6.264	-5.37	1.057
	12.0	.1104	.1165	-6.064	-5.21	1.055
	11.8	.1086	.1149	-6.305	-5.49	1.058
mean c	-	.1112	.1158	-4.656	-3.519	1.0424
standard deviation d	-	2.585 e-3	1.045 e-3	2.598 e-3	1.790	.0246
(d/c)*100 (%)	-	2.33	.901	55.0	50.9	2.36

Table 3.1 Example of calibration results for fuel measurment system.

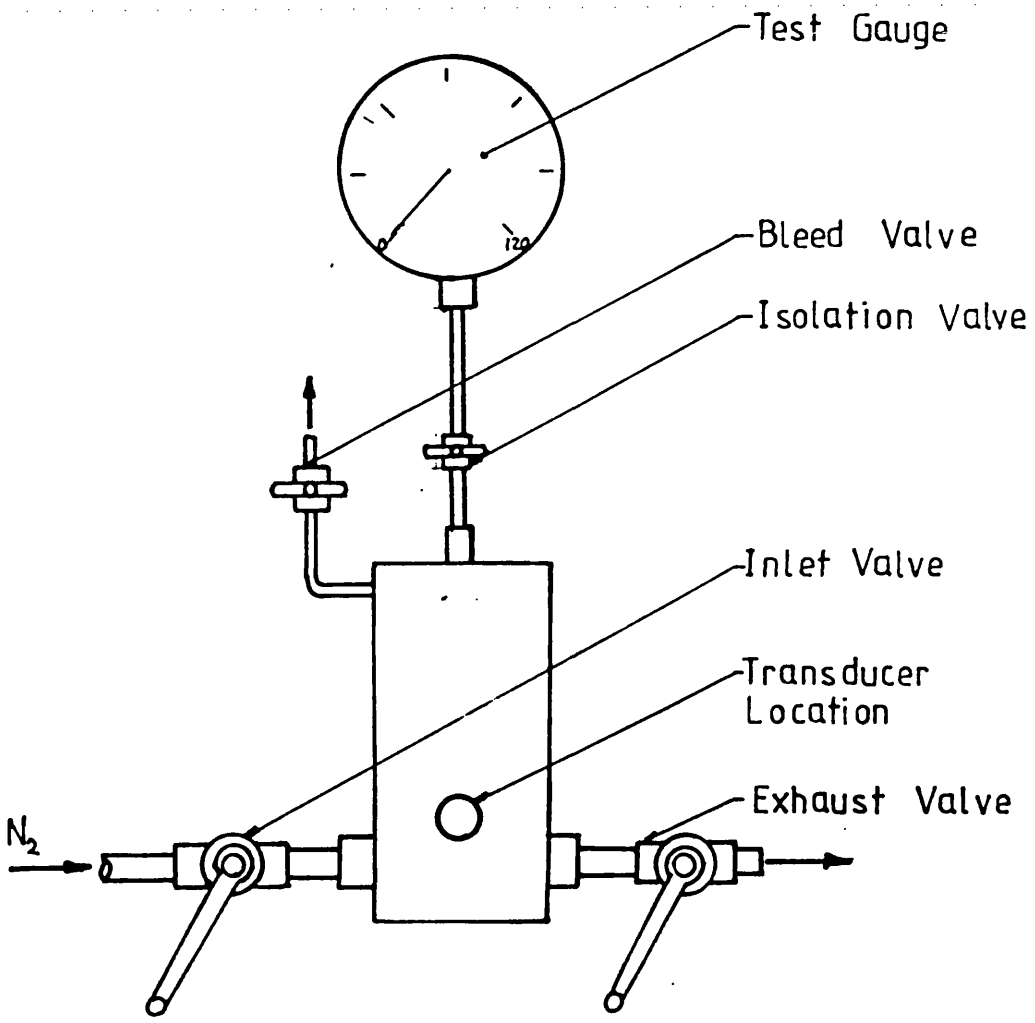

Figure 3.1 Piezo pressure transducer test rig.

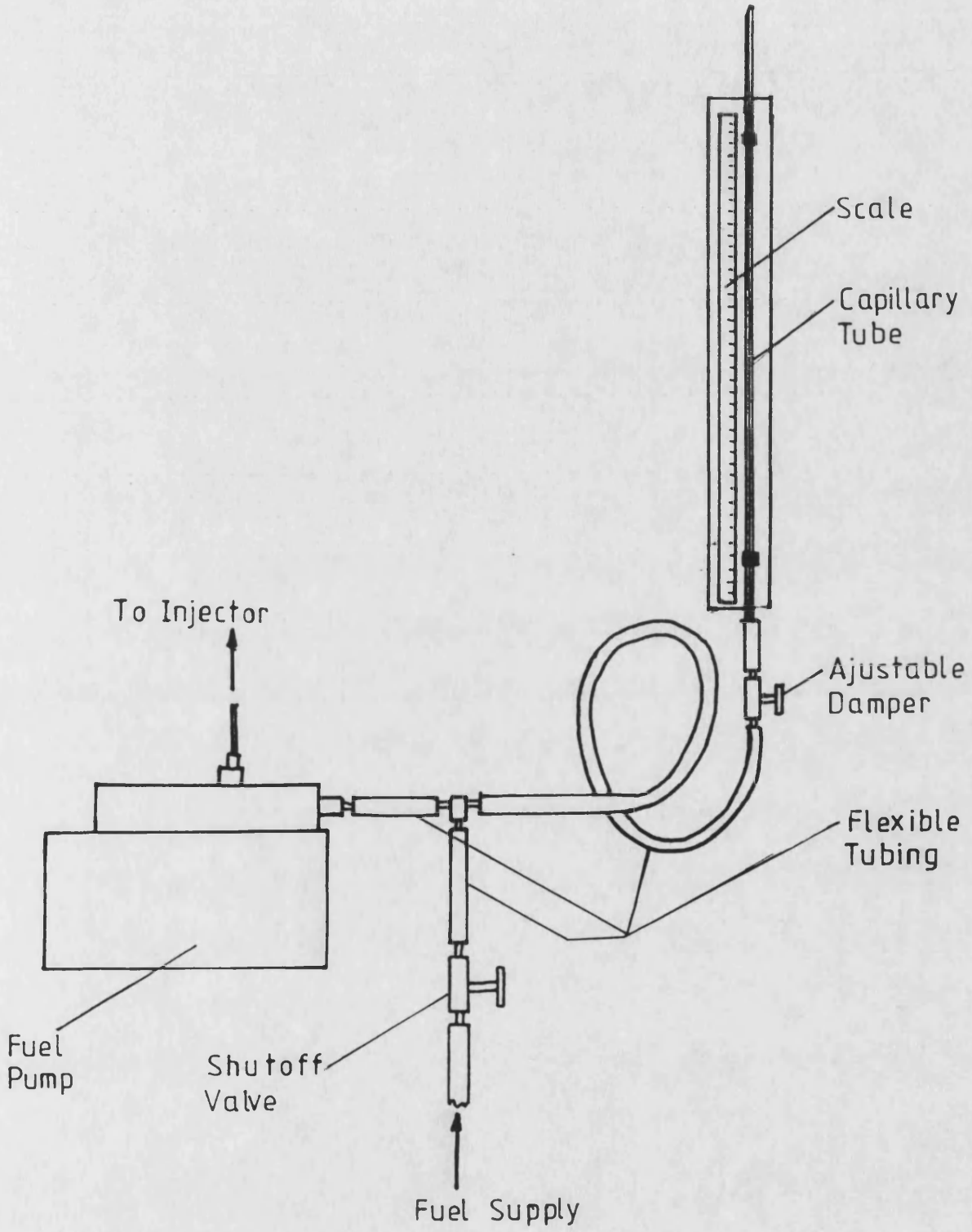

Figure 3.2 Fuel injection measurement system.

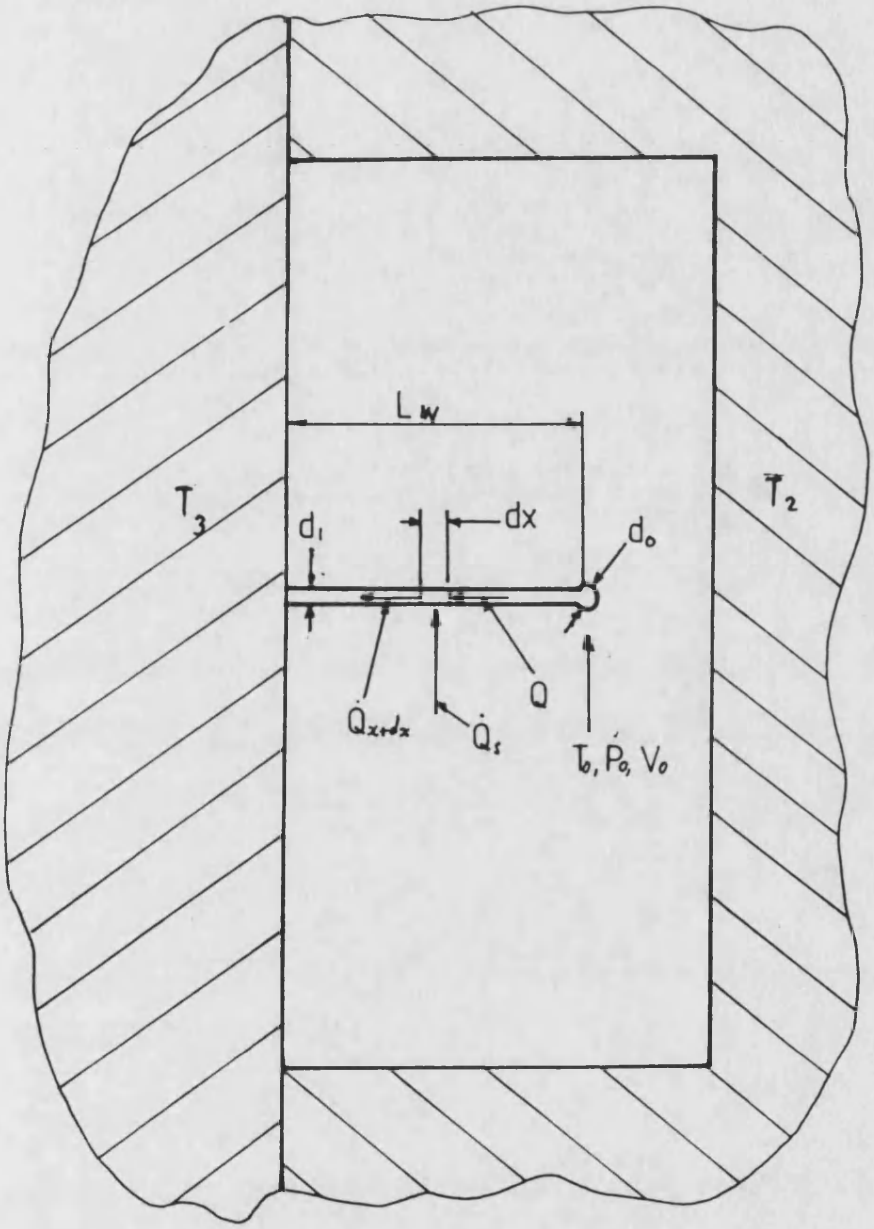

Figure 3.3 Thermocouple bead heat transfer problem.

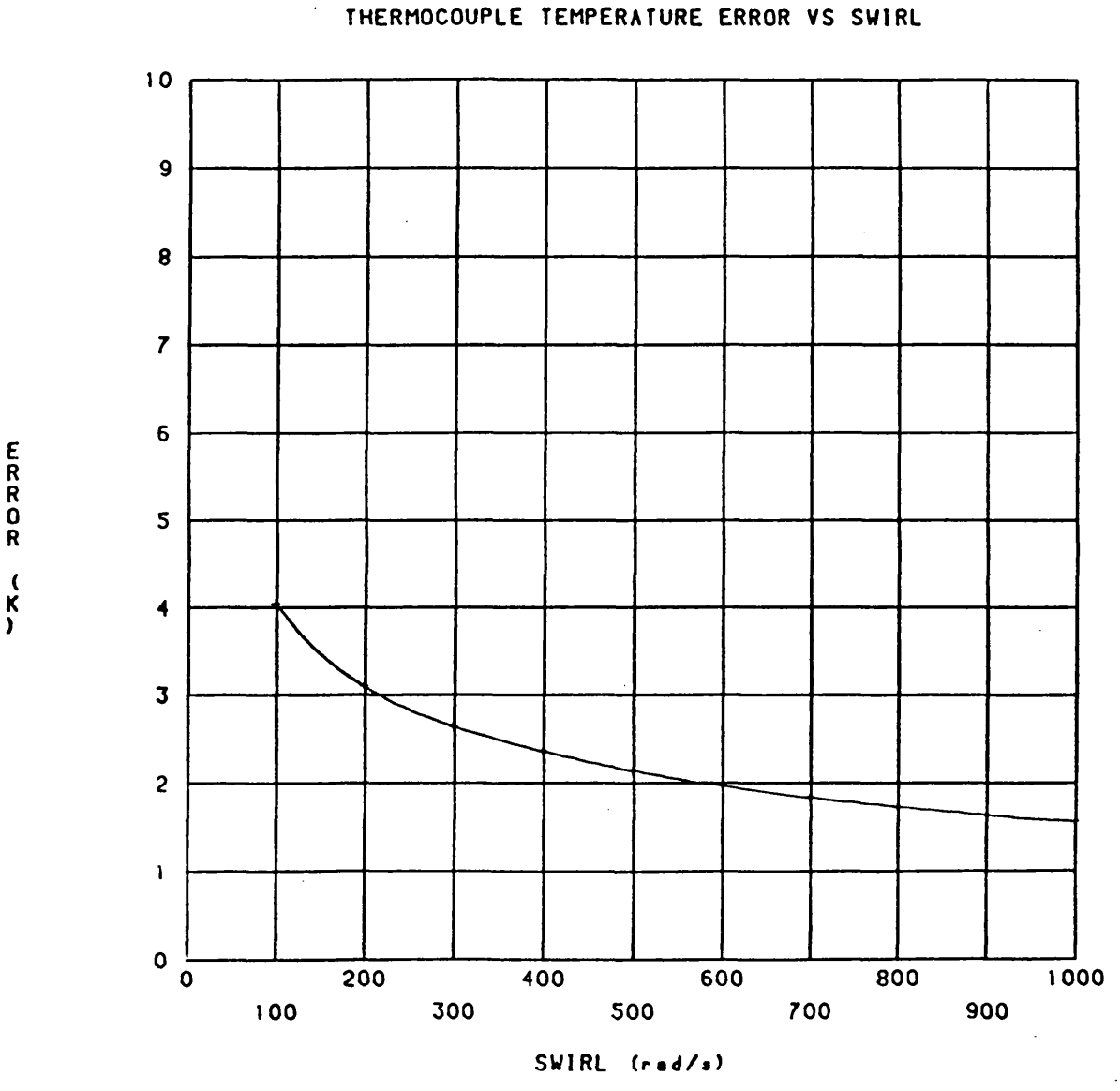

Figure 3.4 Gas temperature error for thermocouple at different swirl levels.

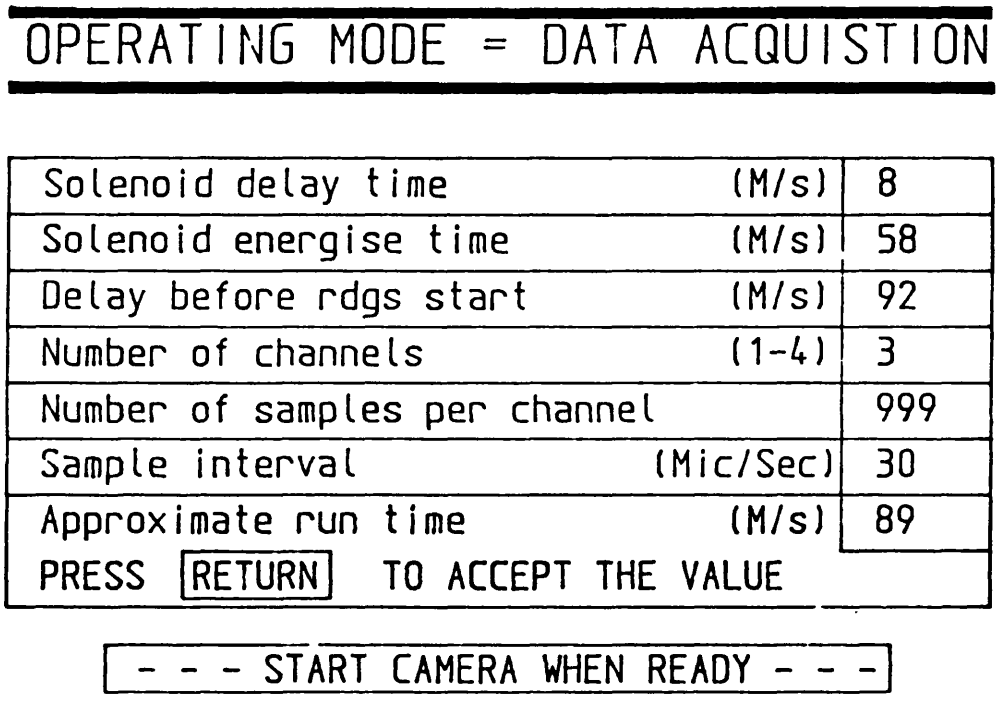

Figure 3.5 Reproduction of PET data acquisition and control display.

CHAPTER 4

Experimental results and Discussion - Optical Tests.

Chapter 4: Experimental Results & Discussion - Optical Tests

4.1 Cold Injections into Nitrogen

Although injections of fuel into hot Nitrogen would have been more representative of engine conditions, evaporation of the fuel would have made the visualisation of the spray boundaries impossible. Filming techniques such as Schlieren photography, which would have highlighted the spray boundaries, require backlighting, which would not be possible owing to the design of the combustion bomb. Thus a short series of fuel injections into cold Nitrogen were filmed, with diffusive (side) lighting.

Figure 4.1 shows the nozzle/combustion chamber configuration, along with the spray trajectory for a straight jet & the lighting arrangements. The nozzle used in the injector was a CAV 3 holed nozzle, type HL130S26C175P3, with enlarged injection hole (from 0.26 mm to 0.46 mm).

Five acceptable B & W films were made & the injection diagrams for these are shown in figures 4.2 to 4.6. The films were analysed at UMIST by Dr J P Packer on a film analyser, to produce spray boundary profiles for successive frames. The profiles were superimposed on to single diagrams to produce composite pictures of spray growth. These five composite pictures are illustrated in figures 4.7 to 4.11. The profiles have been numbered so as to illustrate the sequence of frames from the start of injection.

Listed in table 4.1 are the conditions & parameters for each test, including both the drum swirl speed & the estimated air swirl speed. The estimated swirl speed for the air is based on the hot wire anemometry work done by J P Packer (40). This showed that the slip between the air & drum (with the anemometry head fitted) was such that the level of swirl at all conditions was only 45% of the drum swirl speed. The air swirl speed with the optical head fitted can only be estimated from this linear correlation. Thus the maximum air swirl speed, attained in test 28, was approximately 7875 rpm (drum swirl 17,500). Even at this level of swirl, the spray easily reached the wall (figure 4.11) & was only partially deflected.

An examination of the relationship between the fuel spray, combustion chamber & swirl in dimensionless terms helps to explain this behaviour. Way (39) derived a dimensionless group of variables, which may be used to match injection equipment to a combustion chamber. This work was developed from a hydraulic analogy of the fuel spray & air mixing process, using a technique of water injection into water. Two dimensionless parameters were derived. The first parameter being for penetration, which related the penetration of the spray to the chamber size & the second was for the level of swirl. The dimensionless parameter for penetration was as follows:-

$$\phi P = \left[\frac{h_c f_i}{d.NH}\right]^{1/2} \qquad - 4.1$$

where f_i - mass fraction: ratio of mass injected to mass in chamber.

h_c - height of chamber.

d - injector nozzle hole diameter.

NH - number of injector holes.

And the dimensionless parameter for swirl is:-

$$\phi S = 6.RPMS.t_i \qquad - 4.2$$

where RPMS - swirl rate (rpm).

t_i - injection period.

The ratio between these two defines the relative effect of swirl to penetration. ie:-

$$\phi R = \frac{\phi S}{\phi P} \qquad - 4.3$$

Way found that the maximum mixing rate occurred at around ØR=400. Below 400, excessive wall impingment occurred & above this under penetration occurred. He also found that optimum mixing in the water rig corresponded to optimum mixing in an engine with dimensionally similar combustion chamber & injector.

Using this technique, the maximum ØR ratio achieved for the films was 232 (test 28), which explains the small deflection & excessive wall impingement of the fuel sprays.

The quantitative analysis of films of this type is limited to jet penetration, deflection (trajectory) & cone angles. As the swirl level was too low to achieve any significant deflection of the spray, & it was also difficult to determine the jet centreline, no measurement of the tangential deflection was made. Also the limited number of films & the visual masking of the initial spray region, meant that the spray cone angle could not be measured to an acceptable level of accuracy. Thus analysis has been limited to spray penetration & the effect of swirl on the spray. The spray penetration results have been compared with four fairly recently derived penetration correlations, including the one used in the Shahed et al (31) combustion model. These correlations are as follows:-

1) Taylor & Walsham (52)

$$s = 0{\cdot}641.d.\left[\left(\frac{t}{d}\right).\left(\frac{\Delta P}{\rho_a}\right)^{1/2}\right]^{0.64}\left(\frac{L}{d}\right)^{0.18} \quad (m) \quad - 4.4$$

where d - nozzle orifice dia (m)
s - penetration (m)
t - time (s)
ΔP - effective injection pressure
ρ_a - chamber air density
L - nozzle hole length

This correlation was developed from cold bomb tests, with single gas oil injections into Nitrogen.

2) Dent J C (53)

$$s = 2{\cdot}649\left[\left(\frac{\Delta P}{\rho_a}\right)^{1/2}.t.d\right]^{1/2}\left(\frac{530}{T_g}\right)^{1/4} \qquad - 4.5$$

where T_g - temperature of gas (K)

This correlation was developed from both hot and cold bomb methods, but some limits were set on its use, which are as follows:-

$2 \leqslant (L/d) \leqslant 4$ & $t > 0.5$ ms

3) Fujimoto et al (54)

$$s = 27{\cdot}1.\bar{V}_o^{1/2}.t^{0{\cdot}38}.\gamma_a^{(0{\cdot}09.\log t - 0{\cdot}41)}.d^{1/2} \qquad (m) \qquad - 4.5$$

where $\bar{V}_o$ - mean discharge velocity at the nozzle outlet (m/s)

γ_a - specific weight of the charge (kg/m^3)

The limits for this correlation were as follows:-

$180 \leqslant \bar{V}o \leqslant 250$ m/s

$1.2 \leqslant \gamma_a \leqslant 122$ kg/m^3

$0.89 \leqslant p \leqslant 98.9$ bar

$2.83 \leqslant T_g \leqslant 960$ K

As the initial velocity ($\bar{V}_o$) of the fuel spray in these tests was unknown, the equation used by Chiu, Shahed & Lyn (31) was used to estimate this parameter.

4a) Chiu, Shahed & Lyn (31)

$$s = Ft^{0.6} \qquad \text{(m)} \qquad - 4.7a$$

$$\text{where} \quad F = \frac{6{\cdot}429.d^{0.5}.(\rho_f/\rho_d)^{0.4}}{(1+\rho_a/\rho_{atm})^{0.85}} \cdot \left(\frac{\rho_a}{\rho_{atm}}\right)^{0.5} . (\Delta p)^{0.25}$$

& ρ_{atm} - density of atmosphere (kg/m^3)
ρ_d - density of diesel fuel (kg/m^3)
ρ_f - density of reference fuel
(840 kg/m^3)
Δp - effective injection pressure (N/m^2)

Unlike the three previous equations, Chiu, Shahed & Lyn developed an expression to reduce the radial penetration (predicted for a straight jet) in swirl. ie:-

4b) $$s_\omega = s\left[1-0{\cdot}35\left(\frac{s_\omega.Q_a}{Q_j.d}\right)^{0.44}\right] \qquad \text{(m)} \qquad - 4.7b$$

where $Q_a = \rho_a\left(s_\omega\right)^2 w^2$ (momenta of air)
$Q_j = \rho_f \bar{V}_o^2$ (momenta of fuel)
S_ω = radial penetration in swirl (m)
w = swirl rate (rad/s)

These four correlations have been plotted against the results obtained from the films & are shown in figures 4.12 to 4.16. Chiu et al's correlation has been plotted both with & without the swirl modification, for comparison. Although the other equations do not include the influence of swirl, it seems reasonable to consider them, because of the

relatively low swirl rates & short spray paths. Any discrepancies between the experimental results & correlations due to swirl should be restricted to spray penetrations close to the wall.

The Taylor et al correlation (equation 4.4) underpredicted for all the filmed conditions, particularily for the initial spray penetration. The error between the two reduces at large penetrations. Hay & Jones (55) found that this correlation underpredicts for nozzle hole diameters greater than 0.51 mm, which is only slightly larger than the nozzle hole (0.46 mm) used in the filmed tests. As the nozzle hole size is close to this limit, a slight underprediction of the spray penetration might be expected.

Dent's correlation (equation 4.5) drastically overpredicted for all conditions, but in this case the experimental conditions were outside the limits of use set for the equation: i.e. The experimental nozzle hole length to diameter ratio (L/d) equalled 1.74, whereas the limits set for the equation were between 2 & 4. (A low ratio would produce a bushier spray with less penetration than expected.)

Fujimoto et al's correlation (equation 4.6) generally produced the worst underpredictions, particularily at large penetrations & low swirl levels. Although again, one of the experimental conditions was outside the limits of use set for the equation. The largest experimental nozzle velocity (Vo) was only 141 m/s, as calculated by Chiu et al's correlation, which is well below the minimum limit of 180 m/s set for the

equation. These low predictions could of course have been due to low estimates of the initial spray velocity by Chiu et al's equation.

Chiu, Shahed & Lyn's equation (4.7a) produced the closest predictions for the spray penetrations for all the conditions, but tended to overestimate for large penetratins & at high swirl levels. With the modification for swirl (equation 4.7b) included in the equation, the correlation underpredicted for large penetrations & all swirl levels. The explanation for this may be as follows: The two correlations (4.7a & 4.7b) were derived from an experimental bomb shown in figure 4.17, which is similar to the one described in this thesis, except for the method of swirl generation. Therefore the predictions for spray penetration should be close, at low swirl levels, because of the similarity between experimental conditions.

Their method of swirl generation would have produced swirl tending towards constant velocity (ie V = wr = constant, figure 4.18), whilst the bomb described in this thesis will tend to produce solid body rotation (ie w = constant, figure 4.19). Thus their sprays will have been subject to higher initial gas velocites, for any given mean swirl level, which will have reduced the penetration. Their correlation will therefore overestimate the effect of solid body swirl (w=constant, figure 4.19) on the spray penetration.

Overall, none of these four correlations could be described as general or universal in their application. Although equation 4.7a (Shahed et al)

produced the closest predictions, this is probably due to the similarity between experimental conditions under which both the films were produced and the correlation was derived. All the correlations place different emphasis (if any) on different parameters. For example, Taylor et al's correlation is the only one which includes a term for nozzle hole length (L). This parameter is important in determining the hardness or bushiness of the spray. A large L, relative to the nozzle hole length will produce a hard spray with greater penetration. Fujimoto et al's correlation partly bypasses the parameter for nozzle hole length, by requiring the initial nozzle velocity to be specified ($\bar{V}_o$), but in an engine this may only be determined theoretically.

4.2 Combustion Films

All the combustion films except one were shot using colour film. The colour film had the advantage of making combustion more distinguishable from the general background lighting, but unfortunately the film base was not very strong. This restricted the maximum reliable frame rate, at which the film could be shot, to 4000 frames per second (fps). The black & white combustion film had a tough Ester-AH base & could therefore be shot at the maximum frame rate for the camera of 9000 fps. The speed restriction (fps) on the colour film, gave poor resolution in terms of time between frames.

Furthermore, the cooling of the window seals reduced the maximum pre-ignition temperatures so that the ignition delay was approximatly the same duration as the injection duration. Thus the following analysis of the films has been restricted to a qualitative description of the combustion process.

Fourteen combustion films were shot & developed in total. The first nine were used to set the exposure & lighting for the camera & also for system development. The rest of the films were shot at conditions which approached those which might be expected in a diesel engine. The pre-ignition conditions & camera settings for these films are set out in table 4.2.

The films were again processed on the film analyser mentioned in the previous section to produce spray boundary & combustion profiles for successive frames.

These composite pictures for spray & combustion growth are shown in figures 4.20 to 4.24.

It was difficult to determine the exact source of ignition within the combustion chamber, because of the relatively long period between each frame compared to the spread of combustion during the pre-mixed phase. This is most clearly illustrated in figure 4.21, which shows the profiles of the only quiescent combustion film. In frame 7 there was no visible combustion (although there could have been outside the view through the window) & in frame 8 combustion has spread to cover 1/3 of the viewing area. Generally though, in the other films, the approximate source of ignition could be determined.

In all the films of combustion with swirl (figures 4.20,4.22 4.23 & 4.24), ignition occurred on the downwind boundary of the spray & close to the wall. However, in test 534 (figure 4.24), there was a small but separate ignition source on the upwind side of the spray. From the relative sizes of the two ignition centres, it nevertheless seems likely that the downwind ignition source started earlier. The location of the ignition source is important in explaining the effect of swirl on ignition delay described in the next chapter.

Also of interest, were the relationships between the films & the pressure/time records. The most interesting of these was the difference between the ignition delay in terms of pressure rise & combustion illumination. In all cases the illumination delay was upto 0.4 milliseconds longer than the pressure rise

delay. This has also been observed by Henein & Bolt (56). This discrepancy mainly arises from the low luminosity of pre-mixed combustion, which would be swamped by the light from the flash bulbs. Also the non-luminous preflame reactions have an influence.

Figure 4.25 shows the pressure/time record for film 533 (figure 4.23). The relationship between the film & this pressure record was as follows: For the first 2.25 milliseconds after ignition, the combustion flame was bright white, turbulent & expanding across the combustion chamber. The transition between the premixed combustion & diffusion combustion was not distinguishable. From 2.25 to 5 ms, when the rate of pressure rise was decreasing up to the peak pressure, the flame was still bright white, but the intensity of combustion was reducing. At 5ms the chamber pressure had reached its peak, but the white flamed combustion was still fairly vigorous & continued up until 7.5 ms, although the pressure was dropping slightly. From 7.5 to 10 ms the pressure & the rate of combustion were rapidly decreasing until the last vestige of white flame had dissappeared at 10 ms. Finally combustion tailed off from 10 ms to 15 ms, when all visible flame had disappeared.

To put this into perspective, a 15 ms combustion in a diesel engine running at 2000 rpm corresponds to 180 degrees of crank angle, which is rather long. This may partly be explained by the low level of turbulence generated by the bomb & the low initial pressures & temperatures when compared with an engine. These will reduce the micro mixing rate. Also in real terms, the time to consume 99% of the fuel in

the bomb is approximately 6 ms according to the heat release analysis. To burn 95% of the fuel takes approximately 5 ms.

General Test conditions

Frame rate	-	6000fps
Time between frames	-	160 us
Air & fuel temperature	-	293 K

Camera Settings

Event mark	-	60 ft
Shutter	-	1/10
f-stop	-	4

Test No.	Chamber (N_2) Pressure (bar)	Drum Swirl Rate (rev/sec)	Air Swirl Rate (rev/sec)	Injection Duration (ms)	Mean Inj. Pressure (bar)
24	45	10,000	4,000	1.84	200
25	55	10,000	4,500	2.40	275
26	55	0	0	2.28	265
27	55	15,000	6750	2.48	300
28	55	17,500	7875	2.40	290

Table 4.1 Initial conditions & results for films of fuel injections into cold nitrogen.

Test No.	Frame Rate (fps)	Air Press. (bar)	Air Temp. (°C)	Drum Swirl Rate (rev/sec)	Air Swirl Rate (rev/sec)	Ignition Delay* (ms)	Injection Pressure (bar)	Injection Duration (ms)
530	4,000	35	519	10,100	4,545	1.95	250	2.00
531	4,000	35	507	2,000	900	1.92	240	1.50
532	4,000	35	522	15,000	6,750	-	230	1.50
533	4,000	55	506	10,000	4,500	2.19	290	2.40
534	6,000	55	513	10,000	4,500	2.19	290	2.50

* Ignition delay taken from pressure trace
(One faulty pressure trace)

table 4.2 Initial conditions & results for films of combustion.

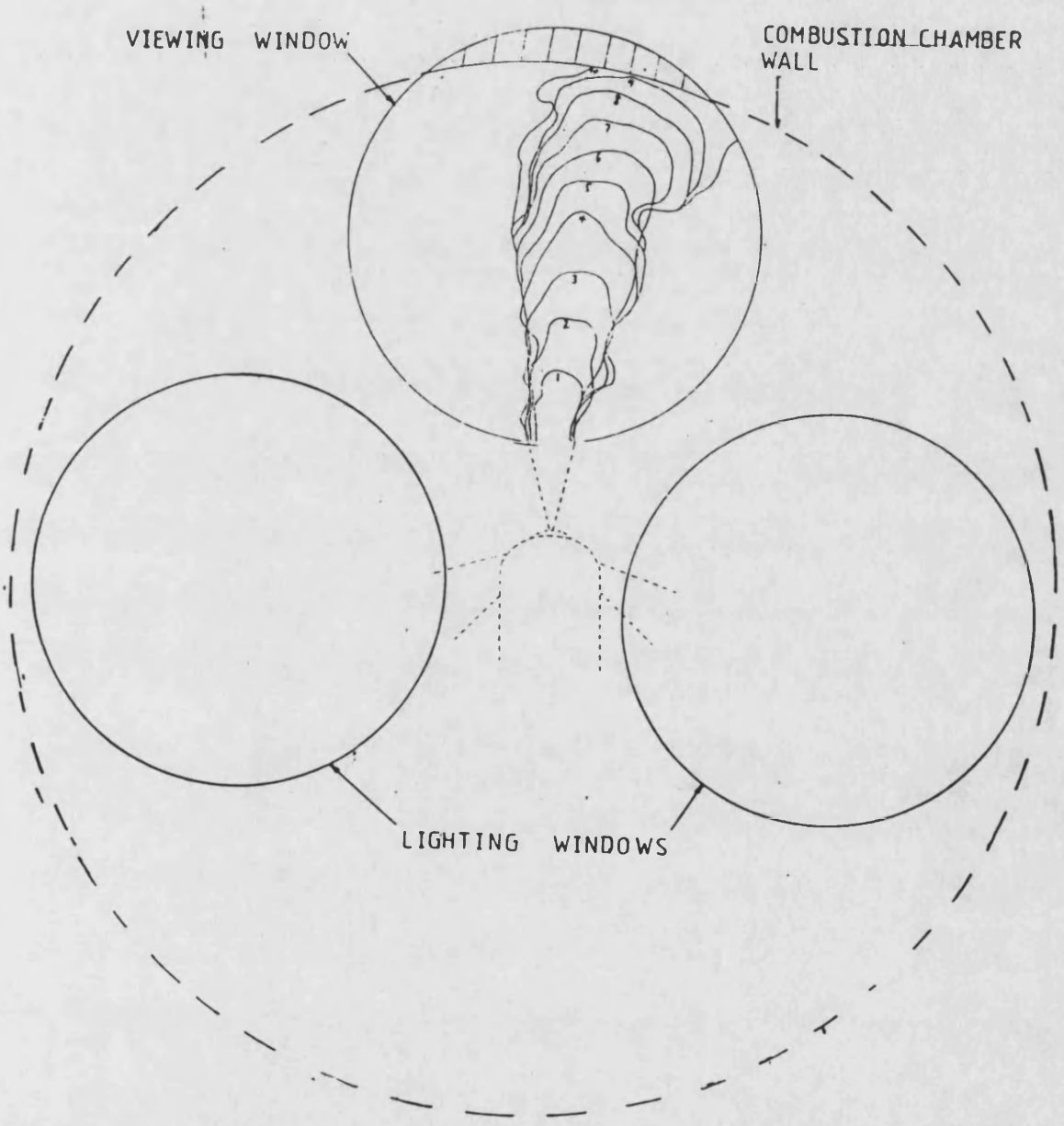

Figure 4.1 Nozzle combustion chamber configuration along with spray trajectory and lighting arrangements.

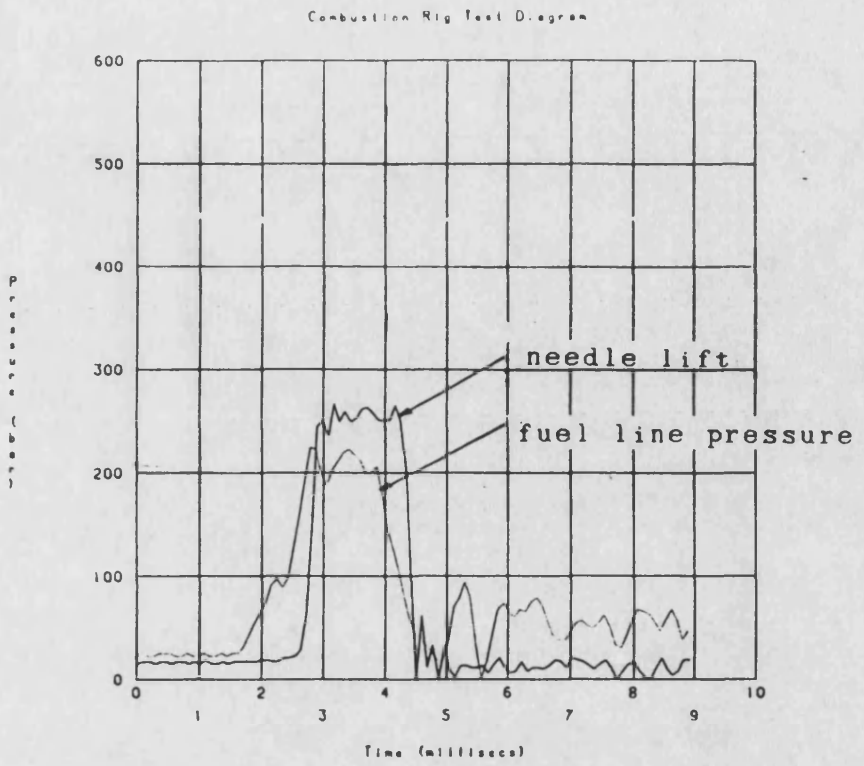

Figure 4.2 Injection diagram for monochrome film of fuel injection into cold nitrogen. Test 524: p=45 bar, N_{-}=10,000 rpm

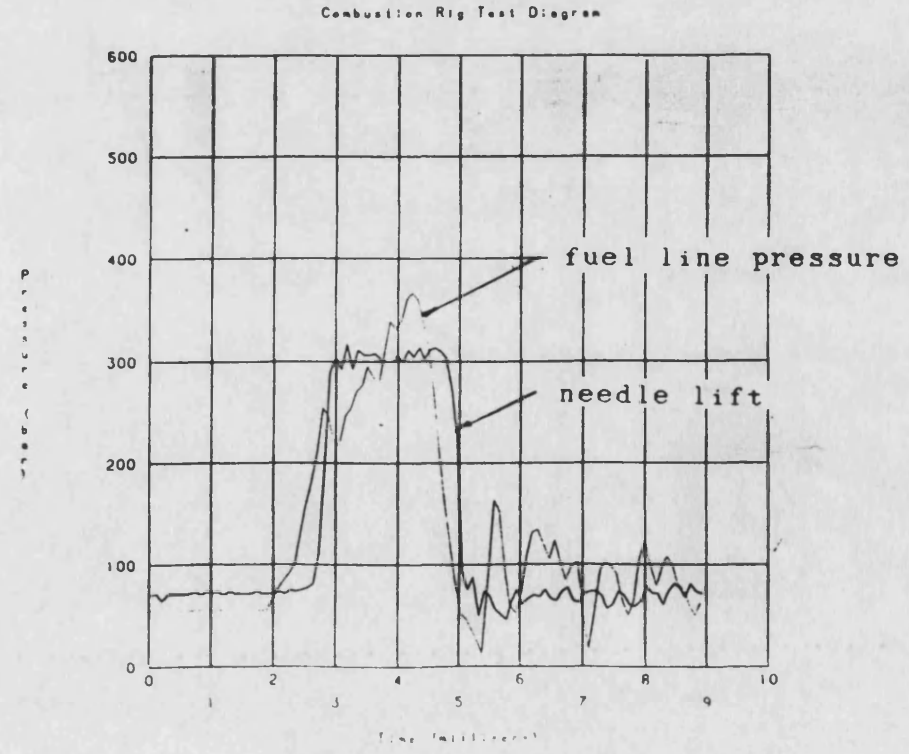

Figure 4.3 Injection diagram for monochrome film of fuel injection into cold nitrogen Test 525: p=55 bar N_{-}=10,000 rpm

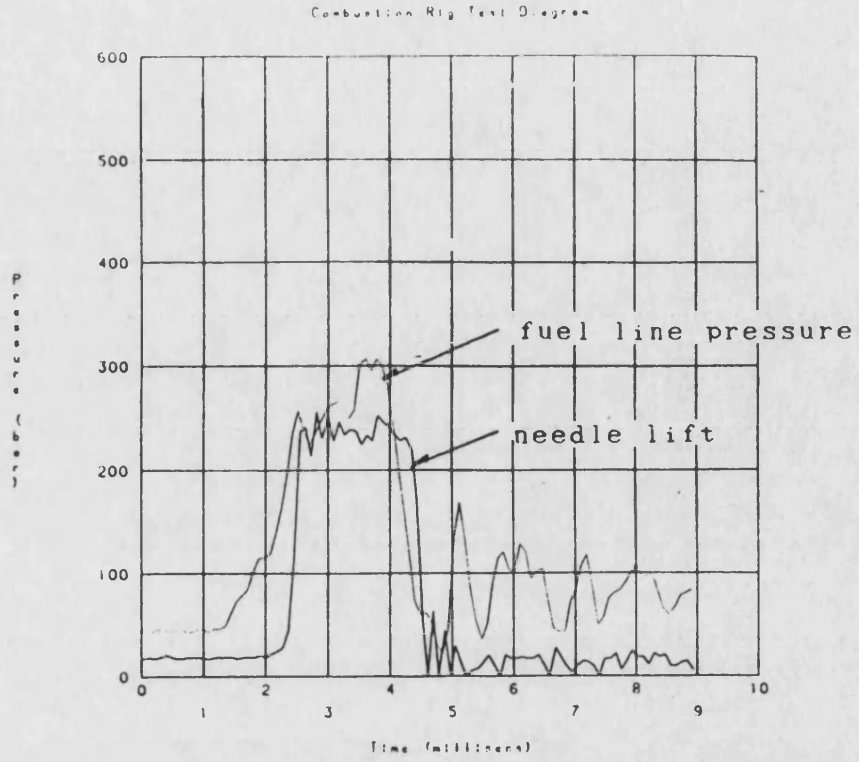

Figure 4.4 Injection diagram for monochrome film of fuel injection into cold nitrogen
Test 526: p=55 bar, N_w=0 rpm

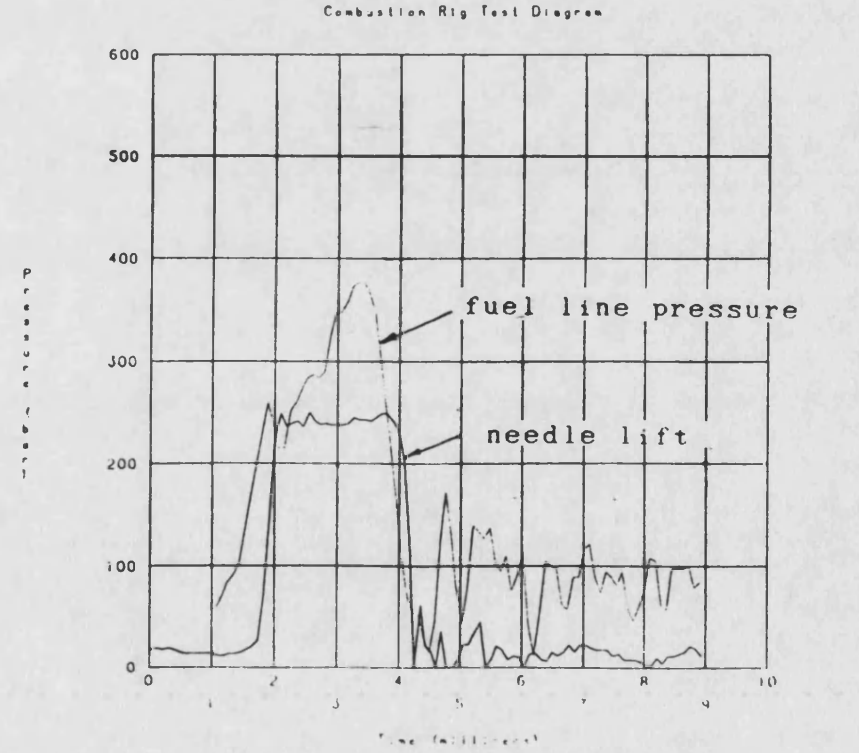

Figure 4.5 Injection diagram for monochrome film of fuel injection into cold nitrogen
Test 527: p=55 bar, N_w=15,000 rpm

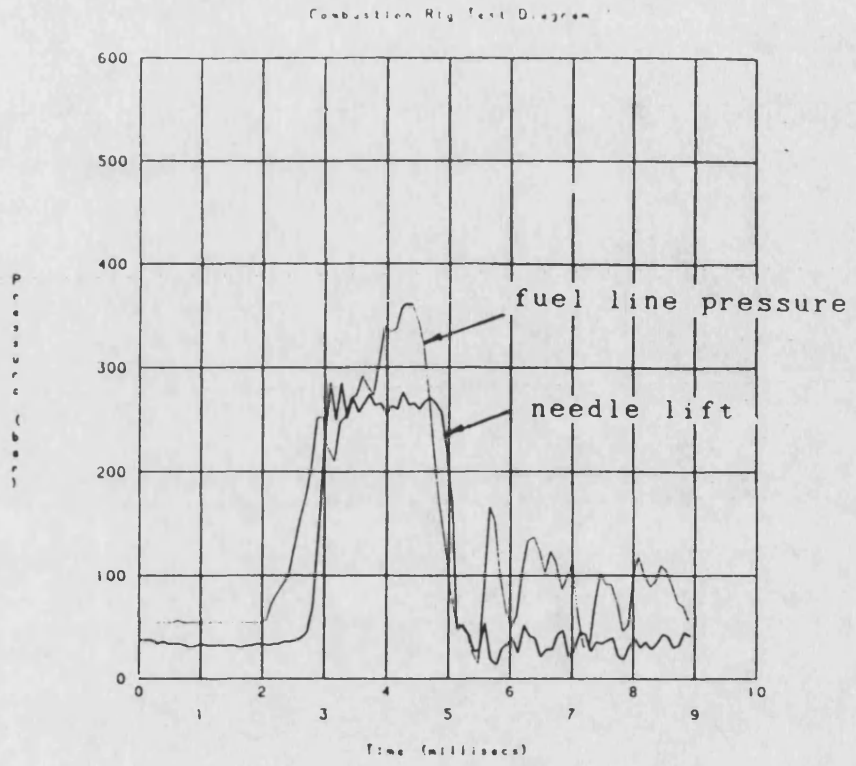

Figure 4.6 Injection diagram for monochrome film of fuel injection into cold nitrogen
Test 528: p=55 bar, $N_{\blacksquare}$=17,500 rpm

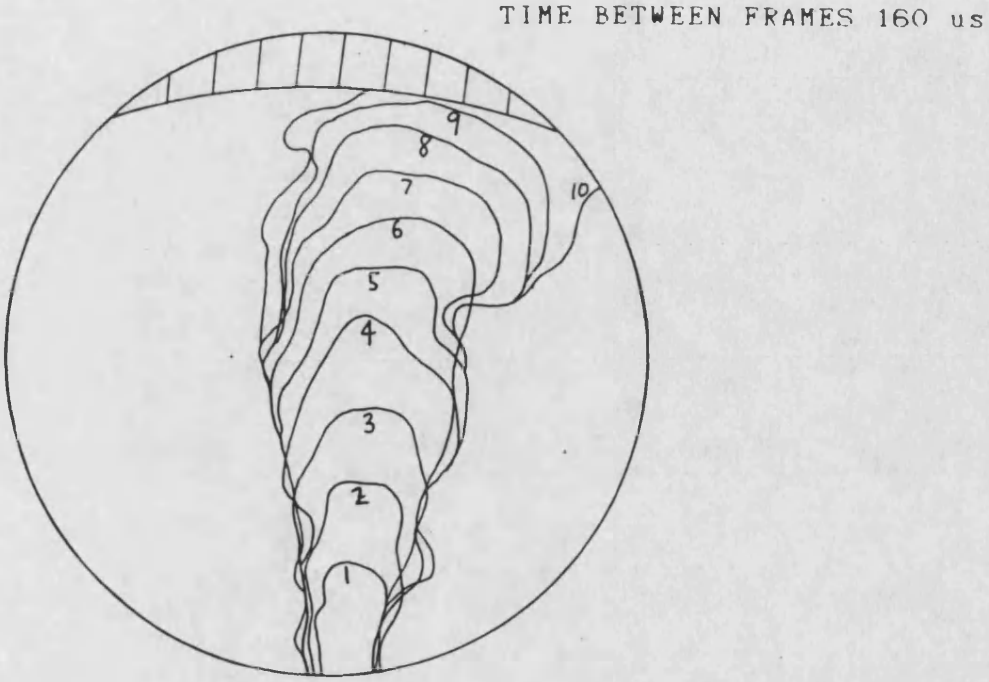

Figure 4.7 Spray trajectories for fuel injection into cold nitrogen.
Test 524: p=45 bar, N_e=10,000 rpm

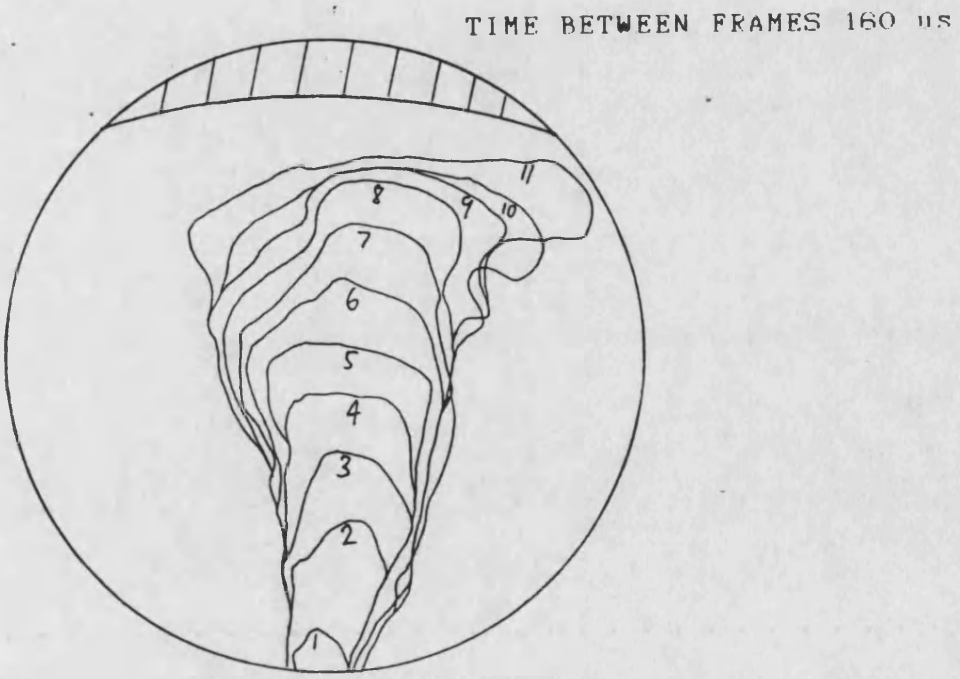

Figure 4.8 Spray trajectories for fuel injection into cold nitrogen
Test 525: p=55 bar, N_e=10,000 rpm

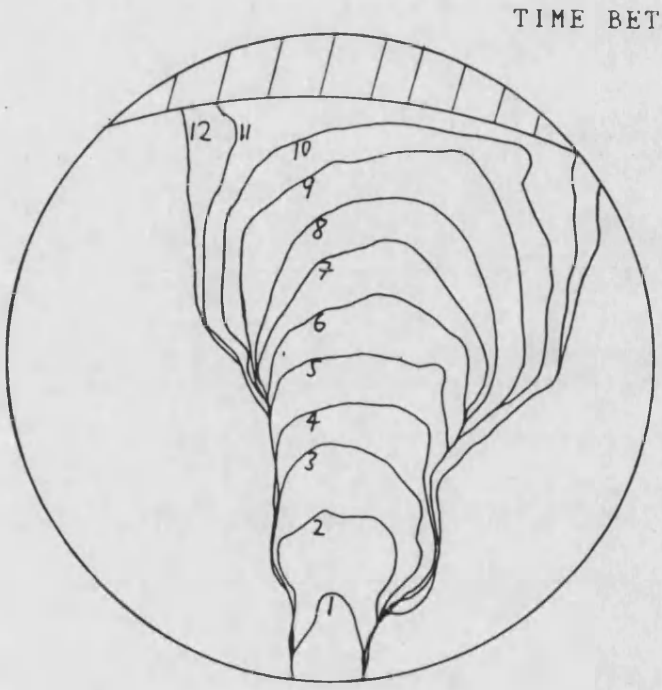

Figure 4.9 Spray trajectories for fuel injection into cold nitrogen.
Test 526: p=55 bar, N_r=0 rpm

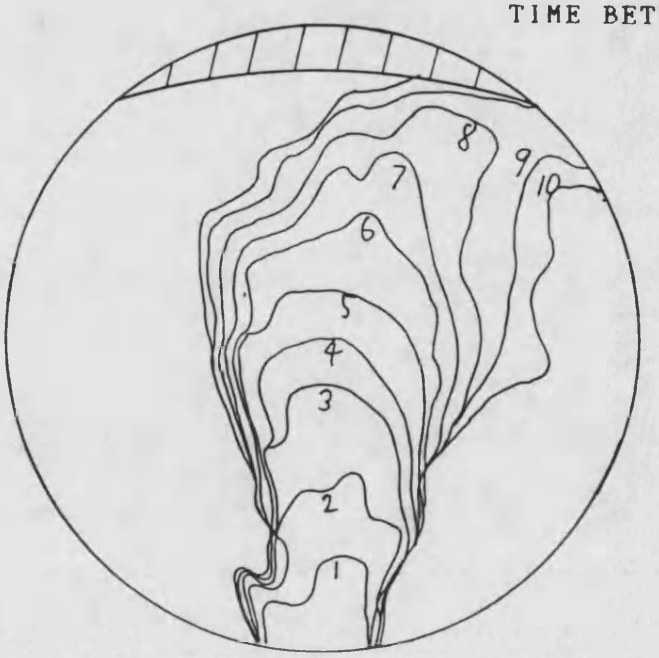

Figure 4.10 Spray trajectories for fuel injection into cold nitrogen.
Test 527: p=55 bar, N_r=15,000 rpm

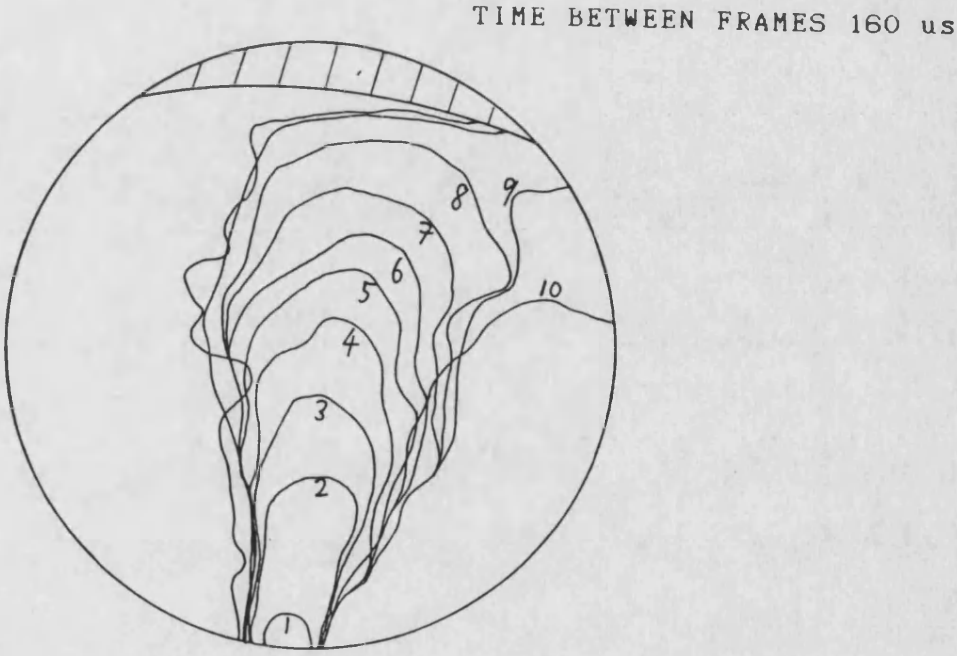

Figure 4.11 Spray trajectories for fuel injection into cold nitrogen.
Test 528: p=55 bar, N_w=17,500 rpm

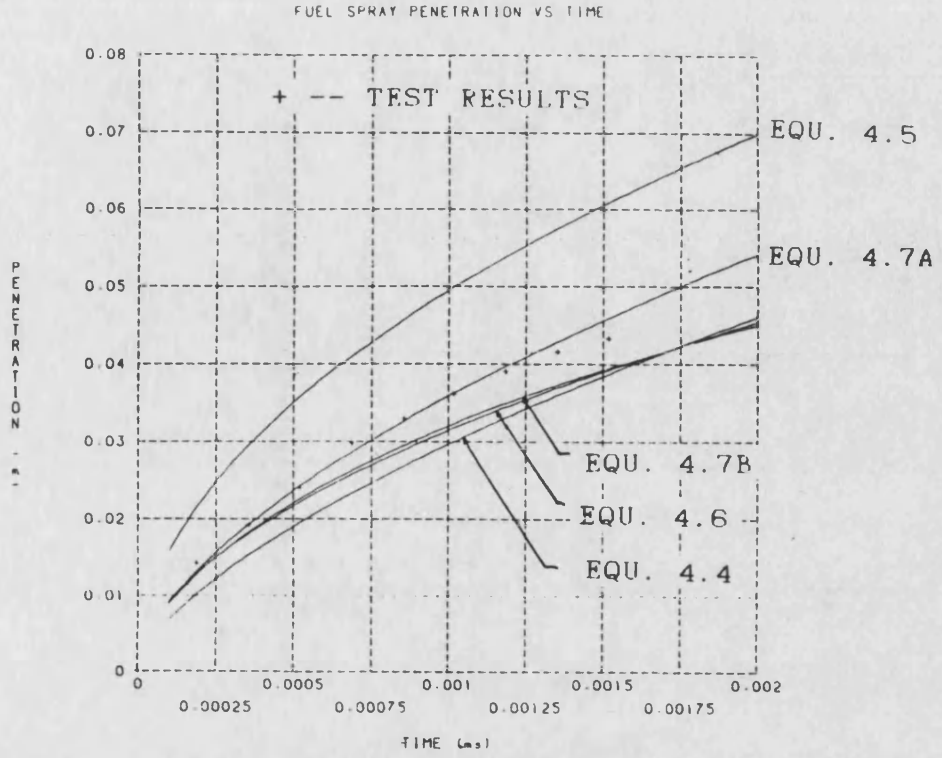

Figure 4.12 Comparison of spray penetration results with correlations.
Test 524: p=45 bar, N_e=4,500 rpm

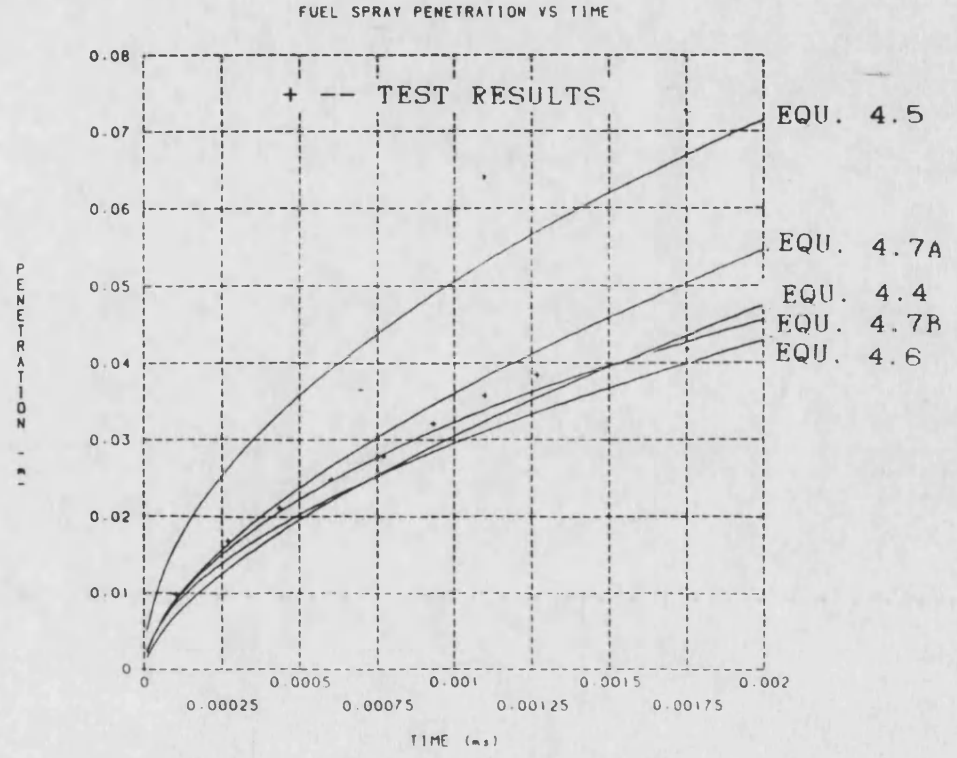

Figure 4.13 Comparison of spray penetration results with correlations.
Test 525: p=55 bar, N_e=4,500 rpm

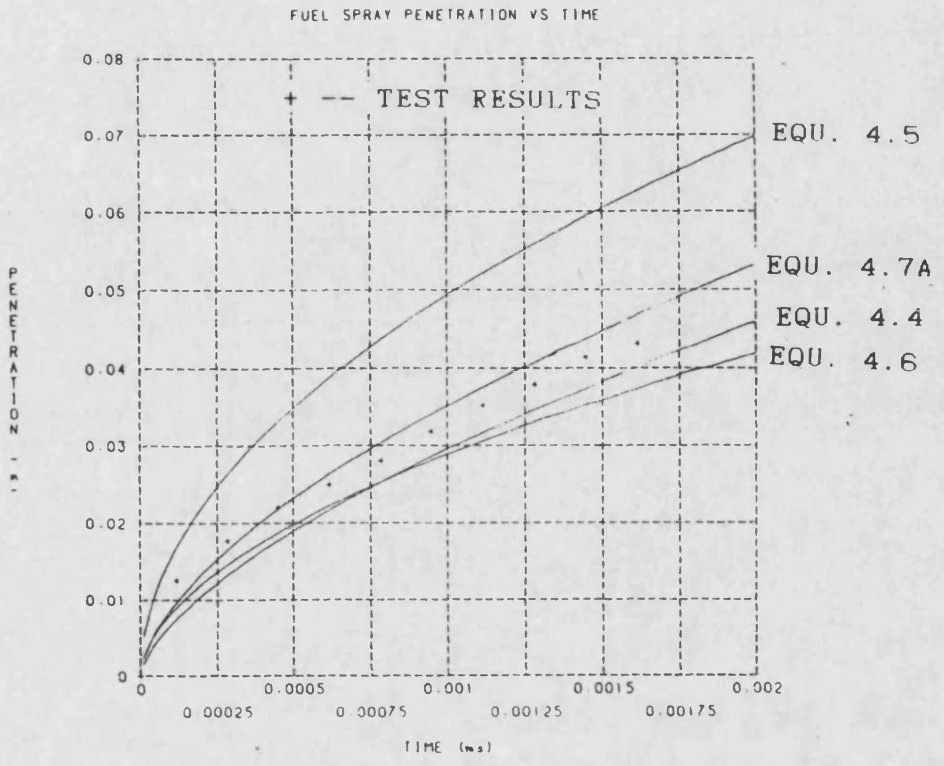

Figure 4.14 Comparison of spray penetration results with correlations.
Test 526: p=55 bar, N_w=0 rpm

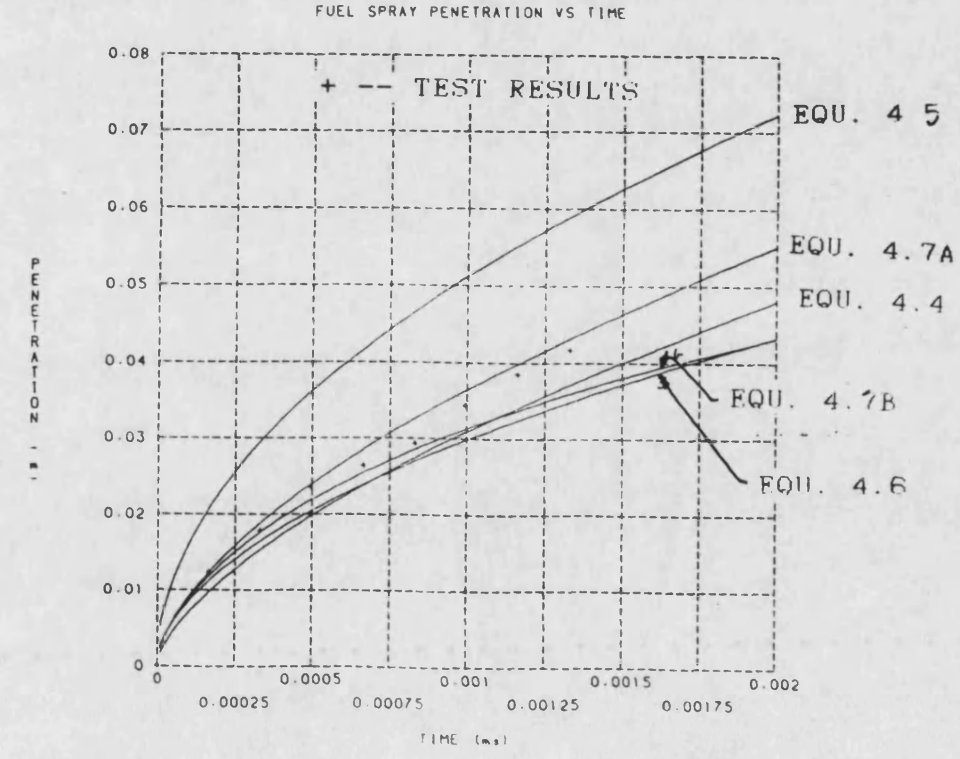

Figure 4.15 Comparison of spray penetration results with correlations.
Test 527: p=55 bar, N_w=6,750 rpm

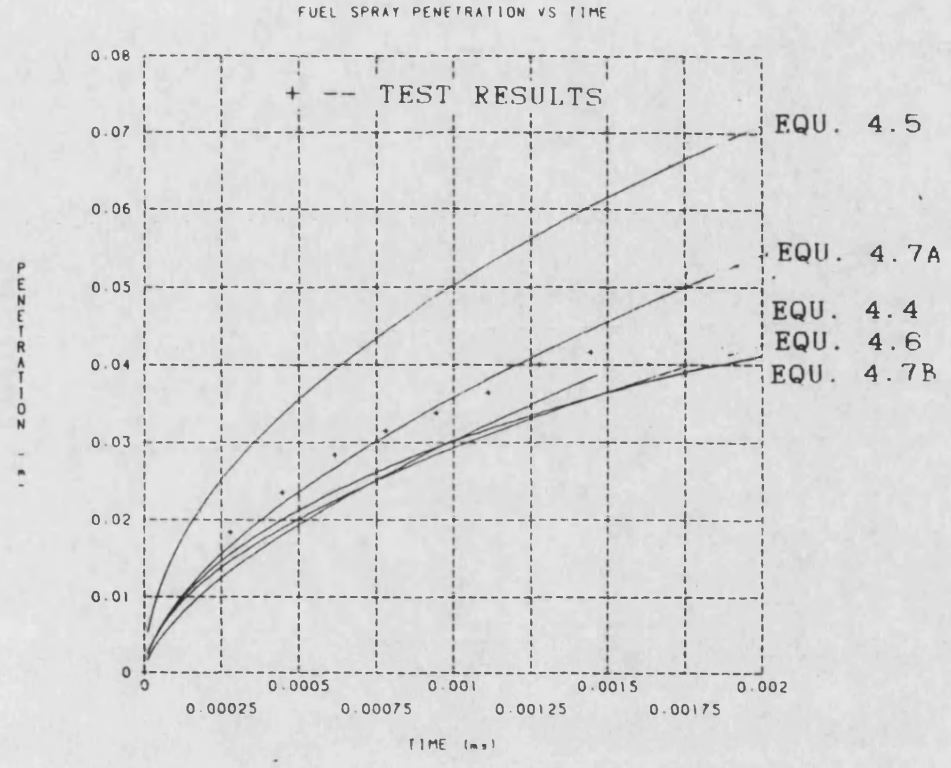

Figure 4.16 Comparison of spray penetration results with correlations.
Test 528: p=55 bar, N_p=78750 rpm

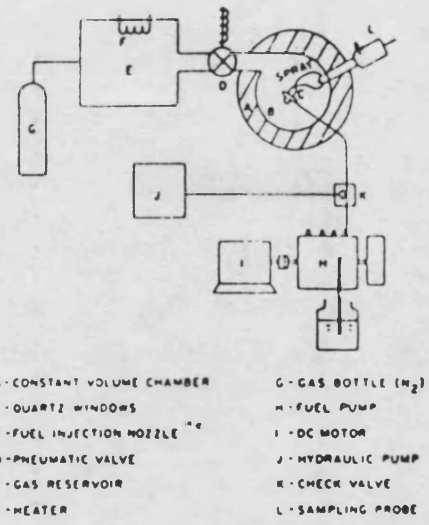

Figure 4.17 Chiu, Shahed and Lyn (31) combustion bomb.

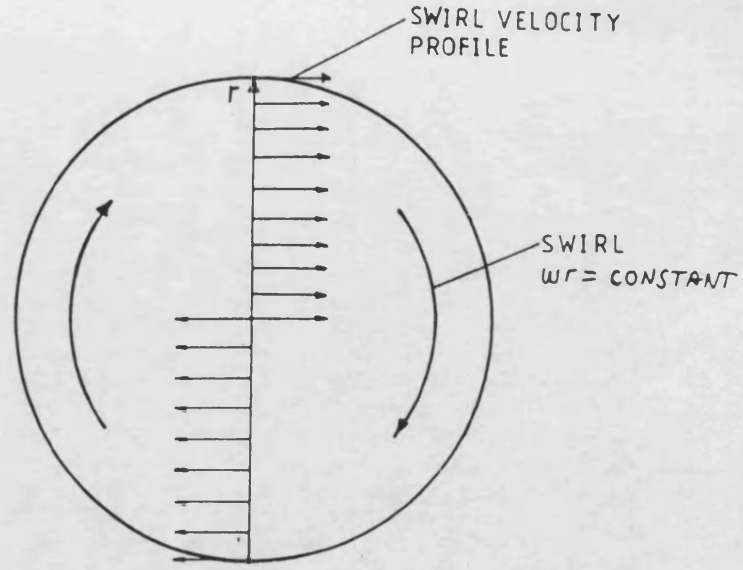

Figure 4.18 Constant velocity swirl.

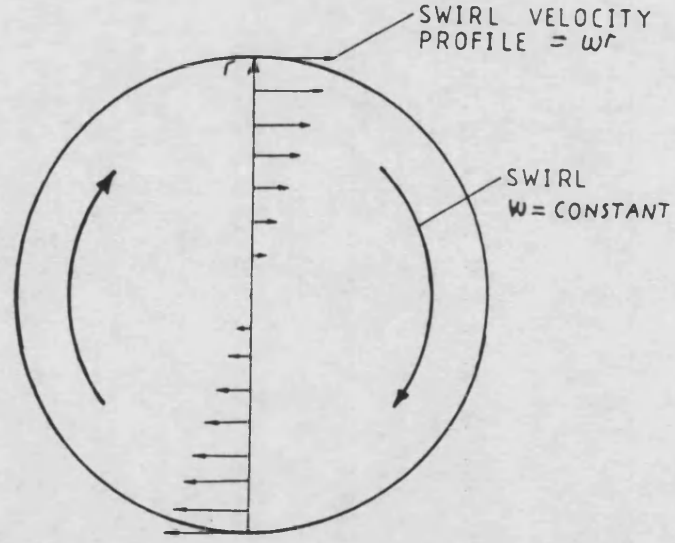

Figure 4.19 Solid body rotation.

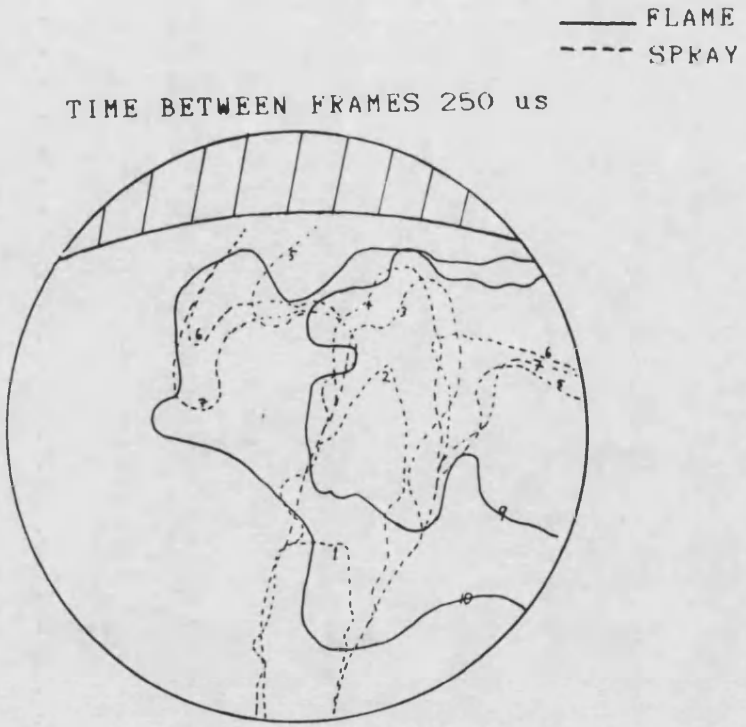

Figure 4.20 Composite spray and combustion profiles.
Test 530: p=35 bar, T=519 C, N_e=4545 rpm

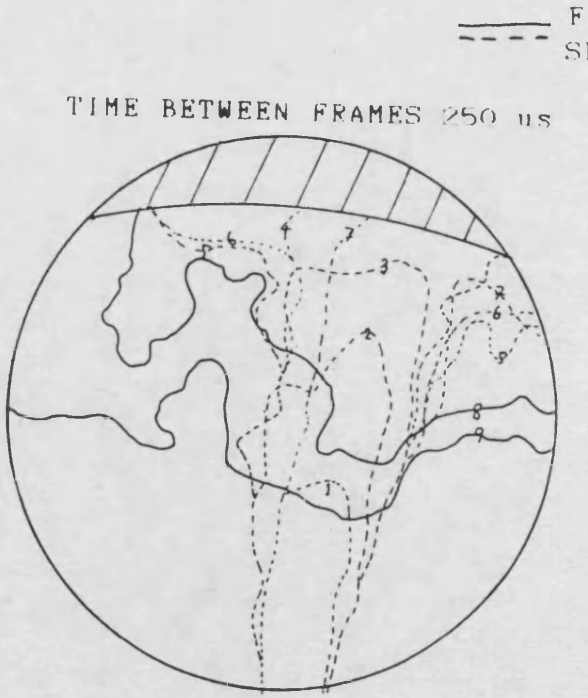

Figure 4.21 Composite spray and combustion profiles.
Test 531: p=35 bar, T=507 C, N_e=900 rpm

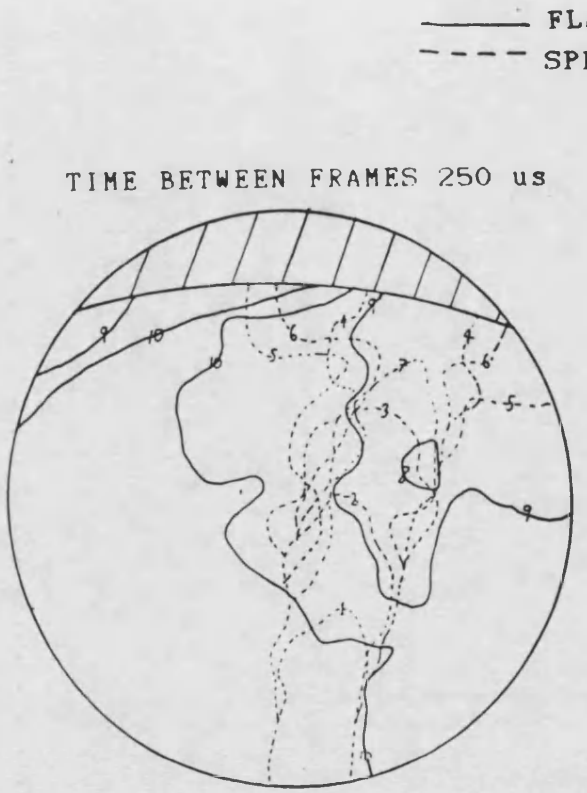

Figure 4.22 Composite spray and combustion profiles.
Test 532: p=35 bar, T=522 C, N_e=6750 rpm

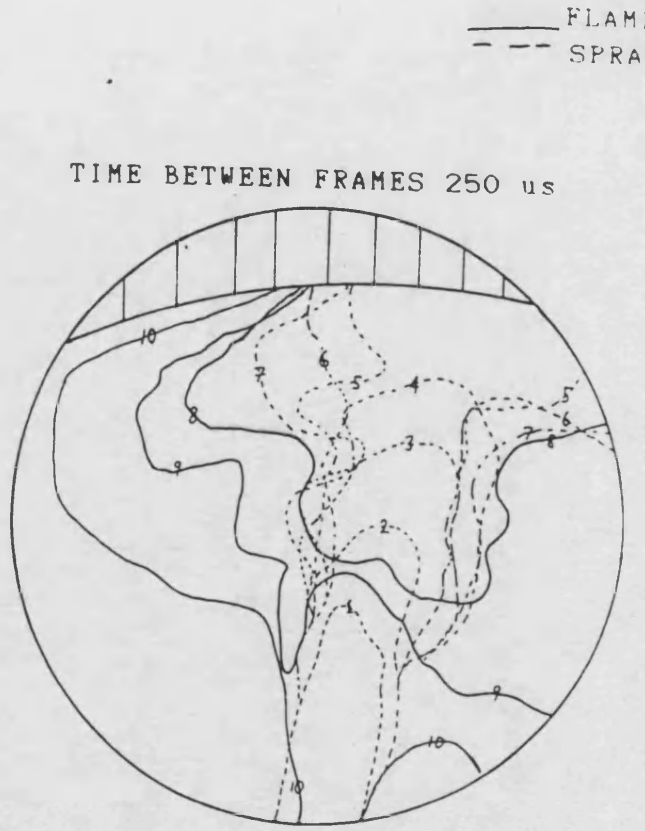

Figure 4.23 Composite spray and combustion profiles.
Test 533: p=55 bar, T=506 C, N_e=4500 rpm

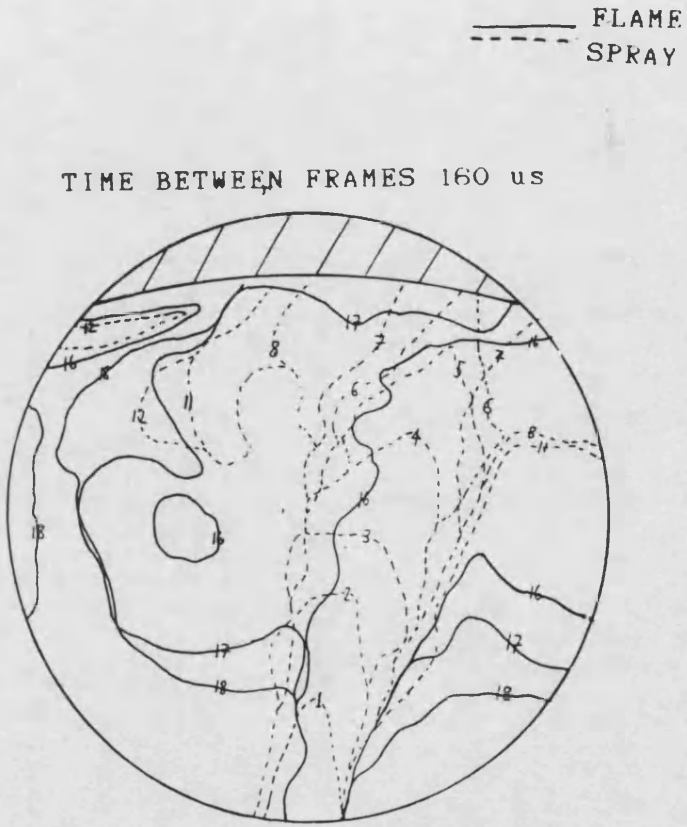

Figure 4.24 Composite spray and combustion profiles. Test 534: p=55 bar, T=513 C, N=4500 rpm

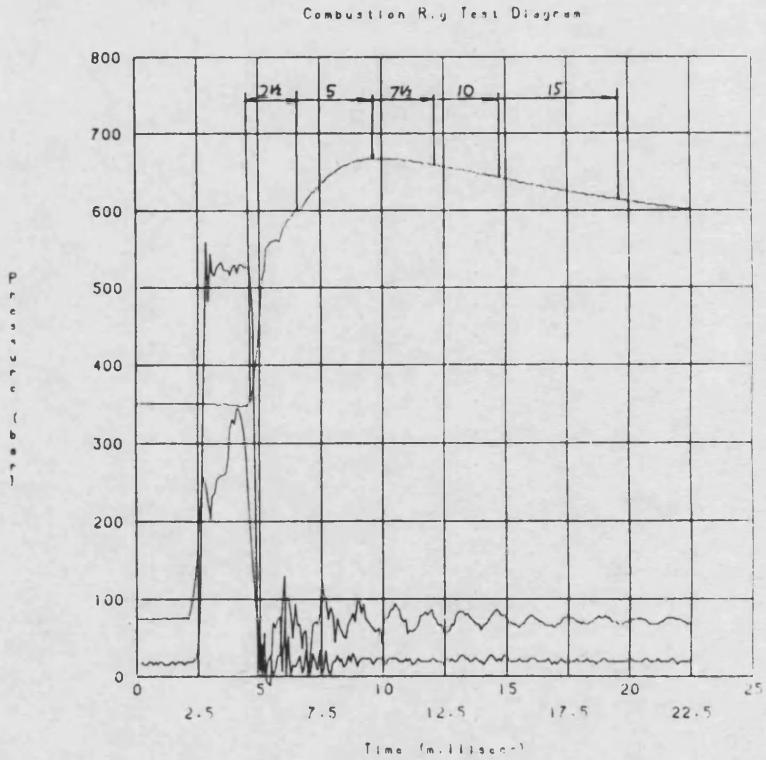

Figure 4.25 Pressure vs time record for test 533 (p= bar, T=506 C, N=4500 rpm

CHAPTER 5

Experimental Heat Release Results and Discussion.

Chapter 5: Experimental Heat Release Results & Discussion

5.1 Presentation of some typical results

Although a large amount of the experimental time was spent on the development of the combustion rig, the principle purpose of this work was to study a comprehensive range of combustion conditions. In the short time available, after the implementation of the swirl generating system & between system modifications, 79 conditions were studied. The pre-injection conditions covered most of the following combinations of pressures, temperatures & swirl:-

Pressures (bar) - 35, 45, 55

Temperature (k) - 773, 873

Swirl (rpm) - 1000 to 10000, 15000, 20000

The full range of test conditions is tabulated in table 5.1.

Two typical analysed tests will be presented as an example of the experimental information obtained from the combustion rig.

The first example (test no. 182) was undertaken at a pre-injection chamber pressure of 55 bar, a nominal gas temperature of 500 C & a drum swirl rate of 10000 rpm. Figure 5.1 is a reproduction of the data

obtained from the combustion rig. No scale is included for the needle lift, while the chamber pressure is 1/10 of the scale for the fuel line pressure.

The slight pressure drop during the ignition delay is caused by the evaporation of the fuel. As can be seen, the ignition delay (2.64 ms) is longer than the injection duration. The ignition delay was taken from the point of first needle lift to the time where the chamber pressure equalled the initial chamber pressure. This criterion for ignition delay was chosen because it gave a more clearly defined point of ignition than one based on the point of first pressure rise. The ignition delay was calculated from a numerical print out of the data.

After the ignition delay, there is a rapid & large initial pressure rise, followed by a small & shallow rise to a peak pressure of 83.3 bar. The pressure drop after the peak is predominantly caused by loss of heat from the gas by heat transfer to the chamber walls. A pressure curve of this shape is typical of a pre-mixed dominated combustion, produced by an ignition delay longer than the injection duration.

It seems intuitively sensible to assume that the rapid and random fluctuations in chamber pressure superimposed on the main trend are caused by inherent combustion generated shock waves. Therefore a curve fit of the data is necessary to smooth out these pressure fluctuations as well as the steps in the digital information to obtain a mean chamber pressure.

Figure 5.2 shows the result of a cubic spline curve fit of the chamber pressure using the computer program 'data_fit.fortran' (57). A section which is 176 data points long, has been fitted, using 20 knots. The knots are closely spaced around the section of rapid pressure rise to obtain a close curve fit & therefore an accurate measurement of the maximum rate of pressure rise.

The first derivative of the curve fit, otherwise known as the rate of change of pressure, is illustrated in figure 5.3. This shows that the peak dp/dt reached was just over 3.0e9 Pa/s.

Figures 5.4 to 5.7 show the curves for pressure, temperature, burning rate & mass fraction respectively, which were generated by the heat release program (57). As stated earlier, the heat release model is based on a homogeneous single zone model & thus the combustion chamber temperature is the estimated mean. The local flame temperatures reached will have been much higher.

The large spike in the burning rate diagram again illustrates the dominance of the pre-mixed phase during the combustion. 51.3 gm/s was the peak burning rate achieved as shown in table 5.2. There was very little diffusion burning (mixing controlled burning), & it appears that the duration of this phase was effectively only 3 ms. The mass fraction diagram shows that the proportion of fuel burnt during the pre-mixed phase was 90% with the remaining 10% being

burnt during the diffusion phase. These would have been poor results if they had been produced by an engine.

The second example (test no.215) was also undertaken at a pre-injection chamber pressure of 55 bar & a drum swirl rate of 10000 rpm, but the nominal gas temperature was 100 C higher at 600 C. In this case the ignition delay of 1.2 ms is shorter than the injection duration. Naturally this results in a much shorter rapid pressure rise phase, as shown in figure 5.8, due to the shorter time available for pre-mixing of the fuel & air, and a correspondingly larger diffusion phase.

The curve fit of the chamber pressure, shown in figure 5.9, was also done over 176 data points with 20 knots. The first derivative from this, plotted in figure 5.10, shows that the peak dp/dt has been reduced by 30% & a second diffusion peak is now present.

A comparison of the plots generated by the heat release program for this test with the first example (5.11 to 5.14) shows that the mean peak temperature reached was over 150 C higher. Also the pre-mixed burning rate, which is related to the dp/dt curve, has been reduced by 30%. The diffusion phase of combustion is quite different, from the first example with a duration over 3 times longer at 10 ms. From the mass fraction diagram, the proportion of fuel burnt during the pre-mixed phase in now only 25% with the remaining 75% being consumed during the diffusion phase.

The second example above shows that the combustion bomb can reproduce the conditions found in a DI diesel engine. This is most clearly illustrated by the burning rate diagram (figure 5.13), which is of the same shape & form as would be produced by a normally aspirated DI diesel engine.

5.2 Heat Release Analysis

The results produced by the heat release analysis for all the tests are given in table 5.2. Results under the heading 'max. burning rate: diffusion', have only been included, when there was a significant amount of diffusion type burning as illustrated in figure 5.13. No heading is included for calculated mass of fuel burnt, mainly because at present there are no heat transfer correlations which could accurately predict the amount of energy lost through heat transfer.

5.2.a Effect of Pressure and Temperature on Ignition Delay

In figure 5.15, ignition delay data (taken from table 5.2) has been plotted against pressure for three pre-ignition conditions, which were as follows:-

1. T=500 C; N_s=5000 rpm

2. T=600 C; N_s=5000 rpm

3. T=600 C; N_s=10000 rpm

As the tests were limited to three pressures (35,45 & 55 bar) & a maximum of 13 data pts for any condition, only the linear trend of ignition delay against pressure has been shown. As expected, the ignition delay decreases with pressure. However, it should also be noted that there is a reduction in the ignition delay at the higher swirl levels.

Also, as expected, the ignition delay decreases with temperature. Three conditions have been analysed, the results of which are shown in table 5.2 and figure 5.16. The pre-ignition conditions were as follows:-

1. p=35 bar; N_s=5000 rpm

2. p=35 bar; N_s=15000 rpm

3. p=55 bar; N_s=5000 rpm

The effects of pressure & temperature on the ignition delay have been extensively studied by many workers (eg ref. 5,24,42,6,22,43), some of whom have produced ignition delay correlations. In figure 5.17 two such correlations by Stringer (58) & Wolfer (59) along with experimental results from this work have been plotted against pressure. The experimental conditions were a nominal air temperature of 600 C & a swirl level of 10,000 rpm. The Stringer ignition delay equation is as follows:-

$$id = \frac{1}{p_a^{n'}\left(B'T-K\right)} \qquad - 5.1$$

where 'p_a' is in atmospheres & 'T' is in Kelvin.

The values for n' B' & K for the two fuels are as follows:-

Fuel	Pressure exponent n'	Temperature coefficient B'	Constant K
Diesel	0.83	216.0e-6	150.6e-3
Avtur	0.83	175.0e-6	124.4e-3

Wolfer used apparatus similiar to the combustion bomb described in this thesis to obtain his experimental results, from which he produced the following correlation:-

$$id = \frac{0.44}{p^{1.19}} \exp\left(\frac{4650}{T}\right) \qquad - 5.2$$

where id - ignition delay (ms)
p - absolute pressure before injection (bar)
T - air temperature

An analysis of the results, displayed in figure 5.17 (condition 3 above) produced an index of 0.78 for the pressure term in the Wolfer equation. That is:-

$$id = \frac{0.44}{p^{0.78}} \exp\left(\frac{4650}{T}\right) \qquad - 5.3$$

This shows that the influence of pressure on ignition delay is reduced in comparison to Wolfer's results.

The effect of pressure on ignition delay compares quite well with the results produced by Stringer & Wolfer. Differences between the experimental results & the correlations may be attributed to the use of different fuels as well as possible errors in the measurement of the gas temperature. This has been discussed in section 3.1.c. It has also been shown by Lyn & Valdmanis (5) that slight differences in ignition delay may be produced by altering the spray characteristics. They found that the ignition delay would decrease with increasing nozzle opening pressure as shown in figure 5.18. The reduction in ignition delay was ascribed to the increased injection velocity.

Although the effect of temperature on the ignition delay was only investigated at two temperatures, the results compare quite favourably with those of other workers. To show this, Stringer's & Wolfers equations have again been plotted in figure 5.19 along with the results from this work & the results from reference (5).

5.2.c Effect of Swirl on Ignition Delay

Unlike the effects of pressure & temperature on the ignition delay, the effect of swirl on the ignition delay was not so obvious. Figures 5.20 to 5.25 show the effects of swirl on ignition delay for all six combinations of pressure (35,45 & 55 bar) and temperature (500 & 600 C). Unfortunately the general scope of the tests resulted in a limited number of ignition delay results for each condition & thus with the random variation of ignition delay, it was not

always possible to produce a statistically significant result for some conditions.

At the higher temperature condition (600 C), a least squares straight line curve fit (figures 5.23,5.24 & 5.25) shows that the ignition delay decreases as the swirl increases. This appears to be true for all pressures at a temperature of 600 C. On the other hand, at the low temperature conditions of 500 C, this trend is only apparent at the pressure of 35 bar (figure 5.20). At 45 bar & 55 bar the ignition delay appears to be almost independent of swirl.

The results at 45 bar & 55 bar are quite anomalous considering the other conditions. If the ignition delay does decrease with swirl, then one explanation may come from the differences between the two test series. That is the swirl tests from 10,000 to 20,000 rpm were done separately & at a later date to the low swirl tests (0 to 10,000 rpm). If the overlapping tests at 10,000 rpm are compared, the slight changes in experimental conditions become apparent. For example, at a nominal air temperature of 500 C and an initial chamber pressure of 45 bar, the following readings were made:-

a. low swirl test series: tests at 10,000 rpm.

coil temp. C	ignition delay ms	swirl rpm *1000	nominal air temp. C	pressure bar	head temp. C
678	2.46	10	500	45	390
663	2.55	10	500	45	391

b. high swirl test series: tests at 10,000 rpm

coil temp. C	ignition delay ms	swirl rpm *1000	nominal air temp. C	pressure bar	head temp. C
610	2.82	10	500	45	427
632	2.64	10	500	45	411

On average, the coil temperature is lower & the head temperature is higher in the 2nd test series than in the first, although the air temperatures were nominally the same. The spare air thermocouple also gave the same reading in both test series. The differences in coil temperature have obviously influenced the ignition delay. There is no obvious reason for the different coil temperature readings, apart from changes in the experimental technique or apparently minor changes to the combustion rig.

Ignoring the two anomalous results (500 C at 45 & 55 bar), the reduction in ignition delay at the higher swirl levels may partly be due to the increased head temperature. Figure 5.26 shows how the head temperature increases with swirl due to the greater heat transfer at the same nominal air temperature. An examination of figure 5.27, which shows the location of the air temperature probe, reveals how the head temperature may influence the air temperature close to the nozzle. Thus an increased head temperature at high swirl levels, probably means that the fuel spray experiences a higher initial air temperature, then it would at lower swirl levels.

Lyn & Valdmanis (5) have also shown that the ignition delay decreases with increased swirl. Their results were produced from an IDI engine, in which the swirl level in the pre-chamber was controlled by altering the throat diameter. The swirl level was calculated from the maximum air velocity in the throat. Schlieren photography indicated that the issuing velocity from the throat was much the same as the peripheral velocity in the chamber.

In total four air swirl speeds were examined as tabulated below:-

Engine speed (rpm)	Swirl velocity	
	Chamber A2 (modified throat)	Chamber A3
300	55	25
1000	180	85

Their ignition results are shown in figure 5.28 for various compression temperatures. The effects of swirl were most noticeable at the low compression temperatures.

Assuming that the ignition delay is affected by swirl, then how does swirl achieve this effect? An examination of some models of ignition, which have been postulated might assist in the understanding of the effect.

Wakil et al (6) studied two models, the first of which considered the evaporation of a droplet in a quiescent infinite atmosphere. It was shown that a stoichiometric mixture at a low temperature is first formed at the droplet surface as shown in figure 5.29. As the droplet heats up, the stoichiometric mixture moves away from the surface of the droplet & the stoichiometric temperature increases. The physical delay is defined as the time required for the stoichiometric mixture to reach a spontaneous ignition temperature.

As an aside, the ignition delay is generally considered to consist of two parts. The first part being the physical delay, which is the time for a combustible mixture to form. the second part, being the chemical delay, which is the time for the chemical reaction to become explosive.

Calculations showed that under typical running conditions for a diesel engine, the physical delay would be less than 0.1 ms as shown by figure 5.30. However, Lyn (60) showed experimentally that the physical delay is very much longer than this, by a factor of 10.

The second model suggested by Wakil et al, considered a group of droplets, which are allowed to come into thermal equilibrium with a limited amount of air. The equilibrium temperature would be dependent on three parameters, 1) the initial temperature of the liquid fuel, 2) the initial temperature of the air & 3) the mass ratio of the fuel to the air. This is illustrated in figure 5.31 for decane. Below the

saturation temperature, liquid fuel is still present and above the saturation temperature is the superheat region, which consists entirely of vapour & air.

The time to reach adiabatic saturation depends upon the original fuel/air ratio. For example figure 5.32. shows how fast two fuel/air ratios approach the saturation condition. A rich fuel/air ratio approaches equilibrium conditions faster than a weaker fuel air/ratio.

It should be noted that ignition will only occur when the fuel/air mixture is between the inflamability limits & above the self ignition temperature. This situation will occur towards the outer part of the fuel spray. It is also essential that the vapour/air mixture should be sustained within these limits long enough for the chemical delay to lapse before it is over diluted. This view of ignition, which was discussed in the introduction, is also supported by Lyn & Valdmanis (5).

This returns us to the question of how swirl can affect the ignition delay. When the fuel spray is injected into the crosswind (swirl), the mixing of the fuel with the air is enhanced (24,31) so that thermal equilibrium is approached more quickly than would be under quiescent conditions. Also a recirculating area is established behind the jet as it is distorted into the classical horseshoe shape (61,62). In this way a large zone with a vapour/air mixture between the inflammability limits & above the autoignition temperature is formed on the downwind side of the spray. It is held in this state long

enough for ignition to occur. The turbulent recirculation may also assist in the reduction of the ignition delay.

Photographic studies (9,32,63) have shown that ignition starts in the downstream region of the spray as illustrated in figure 5.33, which was taken from this work (see previous chapter).

5.2.d Effect of Pressure and Temperature on Peak burning rate

Figures 5.34 to 5.36 show that the maximum burning rate tends to decrease as the pressure is increased. Although at T=500 C & N_S=5000 rpm, the maximum burning rate may reach a minimum value as shown by the cubic curve fit in figure 5.37.

The effect of temperature on the peak burning rate is more positive. Figures 5.38 to 5.40 clearly show that the maximum burning rate decreases with temperature.

Pressure & temperature not only control the maximum burning rate directly, but also indirectly, by controlling the ignition delay. A shorter ignition delay obviously means that less pre-mixed fuel and air is available for immediate combustion.

The direct influence of pressure & temperature on the maximum burning rate may be seen in the ideal Arrhenius formula for chemical reaction rate (64). ie:-

$$R_a = Kp^2 m_A m_B T^{-3/2} \exp\left(-E_a/RT\right) \qquad (kg/m^3 s) \quad - 5.4$$

Where $K = SN_a^2 d_m^2 M_A \left(R/M^*\right)^{1/2} \left(M/R\right)^2$

and
- S - Steric factor
- N_a - Avogardo's constant
- d_m - diameter of molecule
- M_A - molecular weight of specie A
- R - gas constant
- M^* - Reduced mass of molecule
- $\bar{M}$ - mean molecular weight
- m_A - mass fraction of A
- m_B - mass fraction of B
- T - temperature K
- p - pressure
- E_a - Activation energy

In realistic terms this may be simplified to:-

$$R_A = C_1 p^{C_2} m_{fu}^{C_3} M_{ox}^{C_4} \exp\left(-C_5/T\right) \qquad - 5.5$$

as the collision controlled reaction of the previous equation is only an idealisation of what actually occurs.

From this it can be seen that the reaction rate increases substantially with pressure depending on the constant C_2. The reaction rate is also steeply dependent on temperature. On the other hand, the

amount of pre-mixed fuel available for burning decreases with pressure & temperature due to the shorter ignition delay, although the reduction in pre-mixed fuel is partly offset by the increased mixing rates associated with increased pressure & temperature.

Thus, at low pressures (35 to 45 bar), the reduction in maximum burning rate with pressure is due to the reduction of the ignition delay having a greater effect than the increased pressure. At higher pressures, the reduction in ignition delay is not so significant & is offset by the effect of pressure in the reaction rate equation. This transition is more noticible at the lower pre-ignition temperatures as illustrated in figure 5.34 & 5.41.

Although tests at only two temperatures were done (500 & 600 C), it seems likely that the reduction in maximum burning rate with temperature is controlled by the reduction of ignition delay with temperature. This may be seen from a comparison of figure 5.16 with figures 5.38 to 5.40. The initial gas temperature should have little effect on the peak flame temperature & the reaction rate once combustion has started. That is, at the low temperature condition with the long ignition delay, the amount of pre-mixed fuel available for combustion is higher. Therefore the flame temperatures (& pressure) will be greater, along with the peak burning rate, than at the high temperature, short ignition delay condition.

5.2.e Effect of Swirl on Peak Burning Rate

At 500 C, the maximum burning rate increased with swirl at all three test pressures (35, 45 & 55 bar). This is clearly shown by the plots in figures 5.42, 5.43 & 5.44. This effect was not apparent at the 600 C test conditions. At the pressures of 35 & 45 bar, the peak burning rate seemed to be almost independent of the swirl rate as displayed by figures 5.45 & 5.46. While at 55 bar, the peak burning rate decreased with increasing swirl, although this trend was only very slight as can be seen from figure 5.47.

Figure 5.48 has all these six test conditions combined onto one graph.From this, it appears that the influence of swirl on the peak burning rate is related to the severity of the initial conditions; ie as the temperatures and pressures increase there is a transition from the peak burning rate increasing with swirl to the peak burning rate either being unaffected by the level of swirl or decreasing slightly with swirl.

Swirl influences the peak burning rate in two opposing ways. It increases the mixing rate & thus the amount of pre-mixed fuel available for pre-mixed combustion. It has also been demonstrated that it may decrease the ignition delay & thus the time available for the generation of pre-mixed fuel.

Figure 5.48 clearly illustrates the dominant influences at various conditions. At low pressure & temperature (35 bar, 500 C), when the ignition delay is long, the dominant influence is the effect of

swirl on the mixing rate. In this case the peak burning rate increases with pressure. As the conditions become more severe (55 bar, 600 C) there is a gradual transition where the reduction in ignition delay becomes more dominant. At the initial conditions of 55 bar & 600 C it appears that the peak burning rate decreases with swirl.

It should be pointed out though that the effect of swirl on ignition delay is not entirely due to the swirl, but partly its influence on the experimental apparatus (see section 5.2.c).

Thus the reduction in ignition delay may only reduce the effects of the increased mixing rates at the higher swirl levels. That is, in reality, at the most severe condition (55 bar, 600 C), the peak burning rate may still increase slightly with increasing swirl.

It should also be pointed out that these results were produced at swirl levels which are below the overswirled condition. In the case of overswirl, when the fuel is retained in the centre of the combustion chamber, the peak burning rate may or may not decrease with increasing swirl.

5.2.f Third Stage of Combustion (mixing controlled)

At 500 C, there was not a significant quantity of diffusion burning. All or most of the fuel was consumed during the pre-mixed phase, because of the long ignition delay. At 600 C, the ignition delay was

always shorter than the injection duration. Thus there was always some diffusion (mixing) controlled burning.

Figures 5.49 & 5.50 both show that the diffusion burning rate increases with increasing pressure. The increased amount of diffusion burning with increased pressure stems from the shorter ignition delay & also the increased mixing rates (65). The reduction in ignition delay at higher temperatures is also the cause of the increased diffusion burning with increased temperature. This assumes that the fuel mixing rate has passed its peak by the time the diffusion stage of combustion has started. If the ignition delay, in both cases, were to be shorter than the time to reach the peak mixing rate, then there would be no significant effect on the level of the peak diffusion burning rate.

As stated earlier, there was no significant diffusion burning at 500 C, therefore the effect of swirl on the peak diffusion burning rate, was only examined at 600 C. Figures 5.51 to 5.53 all show that the peak diffusion burning rate increases with swirl. Again this effect may be attributed to the shorter ignition delay at high swirl levels, which reduces the amount of fuel burnt during the pre-mixed stage & thus increases the amount of fuel available for diffusion burning. Also the increased mixing rates associated with swirl increases the diffusion burning rate.

When the ignition delay is slightly longer than the injection duration, the amount of diffusion burning may decrease with swirl. This is because of the

increased mixing rates associated with swirl & the resulting increase in pre-mixed burning.

Again it should be pointed out that overswirled conditions were not achieved although several investigations have found that overswirling suppresses all combustion stages & therefore diffusion combustion.

Test No.	Pressure bar	Air Temp. main °C	secondary °C	Surface Temp. coil °C	head °C	Drum Swirl rpm
133	35	500	524	725	232	2000
134	35	500	512	714	255	4000
135	35	500	510	584	294	6000
136	35	500	513	623	383	6000
137	35	500	511	558	407	9000
138	35	500	510	565	412	8000
139	35	500	513	581	407	7000
140	35	500	521	687	333	3000
141	35	500	515	645	376	5000
142	35	500	512	592	412	9000
170	45	500	494	673	366	4600
171	45	500	497	675	315	1400
172	45	500	495	678	390	10000
173	45	500	494	677	362	5500
174	45	500	498	660	309	1000
175	45	500	495	663	391	10000
180	55	500	492	684	356	5000
181	55	500	503	675	353	1400
182	55	500	496	657	409	10000
183	55	500	498	670	400	5000
184	55	500	500	670	357	1100
185	55	500	500	678	385	10000

Table 5.1 Experimental conditions for heat release tests.

Test No.	Pressure bar	Air Temp. main °C	secondary °C	Surface Temp. coil °C	head °C	Drum Swirl rpm
190	35	600	591	782	452	5000
191	35	600	596	752	435	1400
192	35	600	593	773	494	10000
193	35	600	593	762	478	5000
194	35	600	594	740	443	1400
195	35	600	593	772	496	10000
200	43.5	600	595	755	451	2150
201	45.4	600	595	740	408	10000
202	45	600	596	751	481	10000
203	45	600	596	744	463	5000
204	45	600	596	736	448	1800
205	45	600	597	732	493	9930
210	55	600	597	734	484	5000
211	55	600	598	729	455	2000
212	55	600	596	711	498	10000
213	55	600	598	737	486	5000
214	55	600	599	718	465	2400
215	55	600	597	715	509	10000
216	55	600	599	715	457	2400
220	35	500	495	595	413	15000
221	35	500	496	588	414	15000
222	35	500	497	612	430	19000
223	35	500	496	611	429	19800

Table 5.1 (cont.) Experimental conditions for heat release tests.

Test No.	Pressure bar	Air Temp. main °C	Air Temp. secondary °C	Surface Temp. coil °C	Surface Temp. head °C	Drum Swirl rpm
230	45	500	497	603	439	14950
231	45	500	502	610	425	15000
232	45	500	499	624	411	20000
233	45	500	498	610	427	10000
234	45	500	497	591	430	20000
235	45	500	494	631	392	5260
236	45	500	495	632	411	10000
240	55	500	496	603	420	15000
241	54	500	497	576	438	19400
242	55	500	495	595	424	15000
243	54	500	496	584	433	20000
250	35	600	602	733	507	15000
251	35	600	605	757	471	5000
252	35	600	605	758	487	10000
253	35	600	603	730	507	15000
254	35	600	608	751	485	5000
255	35	600	606	750	491	10000
260	45	600	602	722	524	15000
261	45	600	608	757	498	5000
262	45	600	598	758	497	10000
263	45	600	600	713	524	15000
264	45	600	603	741	494	5000
265	45	600	600	748	502	10000

Table 5.1 (cont.) Experimental conditions for heat release tests.

Test No.	Pressure bar	Air Temp. main °C	Air Temp. secondary °C	Surface Temp. coil °C	Surface Temp. head °C	Drum Swirl rpm
270	55	600	601	693	530	15000
271	55	600	602	740	500	5000
272	55	600	601	735	512	10000
273	55	600	601	702	530	15000
274	55	600	604	752	500	5000
275	55	600	601	744	515	10000
280	35	600	601	737	500	15000
281	35	600	605	745	481	5400
282	35	600	601	761	487	10000
290	35	655	656	755	506	5500

Table 5.1 (cont.) Experimental conditions for heat release tests.

Test No.	Air Swirl Rate (rad/s)	Ignition Delay (ms)	Max. Burn. Rate (gm/s)	Calc. mass of fuel burnt.(mg)	Peak. Press. (bar)	Peak Temp. Mean (K)	Max Burning Rate: Diff. (gm/s)
133	94	3.36	76.07	67.5	61.76	1347	-
134	188	3.00	87.95	85.9	62.15	1356	-
135	283	3.27	89.60	93.0	62.46	1362	-
136	283	2.91	86.41	87.0	60.22	1315	-
137	424	2.76	84.24	94.6	59.60	1300	-
138	377	2.73	62.98	88.7	59.53	1298	-
139	330	2.91	68.31	83.9	58.70	1281	-
140	141	3.00	83.87	69.3	62.94	1371	-
141	236	2.82	95.60	83.4	63.63	1385	-
142	424	2.64	66.79	90.0	58.46	1277	-
220	707	2.55	147.6	68.8	67.05	1458	-
221	707	2.46	140.6	68.1	66.72	1452	-
222	896	2.55	200.5	70.0	69.18	1509	-
223	933	2.73	161.9	76.0	69.45	1508	-

Table 5.2a Results from heat release analysis.
Initial air pressure - 35 bar
Initial air temperature - 773 K

Test No.	Air Swirl Rate (rad/s)	Ignition Delay (ms)	Max. Burn. Rate (gm/s)	Calc. mass of fuel burnt.(mg)	Peak. Press. (bar)	Peak Temp. Mean (K)	Max Burning Rate: Diff. (gm/s)
170	217	2.73	55.4	50.3	73.79	1255	-
171	66	2.55	33.1	45.7	71.27	1213	-
172	471	2.46	49.6	50.7	72.09	1226	-
173	258	2.73	51.2	47.7	72.70	1237	-
174	47	2.64	39.0	41.2	68.98	1175	-
175	471	2.55	72.3	51.6	72.88	1242	-
230	705	2.64	141.4	72.9	80.90	1376	-
231	707	2.82	83.8	57.1	74.40	1265	-
232	942	2.73	87.8	65.0	77.29	1313	-
233	471	2.82	71.5	51.5	71.37	1214	-
234	942	2.73	88.0	57.9	72.86	1239	-
235	248	2.82	43.8	40.5	68.86	1175	-
236	471	2.64	53.2	44.8	69.73	1186	-

Table 5.2b Results from heat release analysis.
Initial air pressure -- 45 bar
Initial air temperature - 773 K

Test No.	Air Swirl Rate (rad/s)	Ignition Delay (ms)	Max. Burn. Rate (gm/s)	Calc. mass of fuel burnt.(mg)	Peak. Press. (bar)	Peak Temp. Mean (K)	Max Burning Rate: Diff. (gm/s)
180	236	2.64	55.2	50.5	84.11	1173	-
181	66	2.28	38.2	45.3	81.80	1144	-
182	471	2.64	51.5	50.0	83.34	1162	-
183	236	2.73	58.8	44.2	80.24	1119	-
184	52	2.55	30.3	36.6	76.76	1072	-
185	471	2.64	69.1	49.2	82.56	1151	-
240	707	2.64	76.0	55.9	83.67	1167	-
241	914	2.55	92.2	61.0	83.86	1191	-
242	707	2.01	36.9	48.8	77.97	1088	-
243	942	2.55	86.6	60.7	83.52	1185	-

Table 5.2c **Results from heat release analysis.**
Initial air pressure - 55 bar
Initial air temperature - 773 K

Test No.	Air Swirl Rate (rad/s)	Ignition Delay (ms)	Max. Burn. Rate (gm/s)	Calc. mass of fuel burnt.(mg)	Peak. Press. (bar)	Peak Temp. Mean (K)	Max Burning Rate: Diff. (gm/s)
190	236	1.65	25.7	39.3	55.61	1371	6.8
191	66	1.83	33.7	36.2	55.31	1365	5.2
192	471	1.65	30.9	43.1	55.58	1370	9.4
193	236	1.83	33.0	41.7	56.53	1394	7.2
194	66	1.92	41.5	39.2	56.76	1399	7.4
195	471	1.65	33.0	47.9	57.09	1406	10.0
250	707	1.56	42.8	61.7	62.09	1521	10.8
251	236	1.83	38.5	49.9	60.42	1483	7.9
252	471	1.65	41.0	58.0	61.34	1514	11.3
253	707	1.47	44.3	62.7	61.19	1498	11.3
254	236	1.83	43.0	49.2	59.77	1469	8.8
255	471	1.65	37.8	56.7	60.32	1479	12.0
280	707	1.56	40.3	61.8	60.99	1494	11.5
281	254	1.74	39.0	50.0	59.92	1471	8.5
282	471	1.65	34.5	57.7	61.72	1513	12.0
290*	259	1.47	25.4	53.6	60.81	1583.3	12.0

*Test at an initial air temperature of 928 K

Table 5.2d **Results from heat release analysis.**
Initial air pressure - 35 bar
Initial air temperature - 873 K

Test No.	Air Swirl Rate (rad/s)	Ignition Delay (ms)	Max. Burn. Rate (gm/s)	Calc. mass of fuel burnt.(mg)	Peak. Press. (bar)	Peak Temp. Mean (K)	Max Burning Rate: Diff. (gm/s)
200	** 243	1.74	36.7	49.4	69.09	1371	8.0
201	* 101	1.74	29.6	49.1	72.75	1382	7.0
202	471	1.47	37.7	60.5	73.19	1404	11.1
203	236	1.65	28.3	52.2	72.41	1387	9.0
204	85	1.83	33.5	49.8	72.11	1386	7.5
205	468	1.38	32.4	56.4	72.28	1385	10.0
260	707	1.29	33.9	68.1	74.70	1429	17.0
261	236	1.56	34.0	53.7	73.43	1407	12.0
262	471	1.38	30.2	56.7	73.30	1404	13.5
263	707	1.20	35.8	64.3	73.76	1412	15.0
264	236	1.47	36.5	55.7	73.81	1413	13.0
265	471	1.47	30.3	59.0	73.38	1405	14.0

**Initial air pressure - 43.5 bar

*Inital air pressure - 45.4 bar

Table 5.2e Results from heat release analysis.
Initial air pressure - 35 bar
Initial air temperature - 873 K

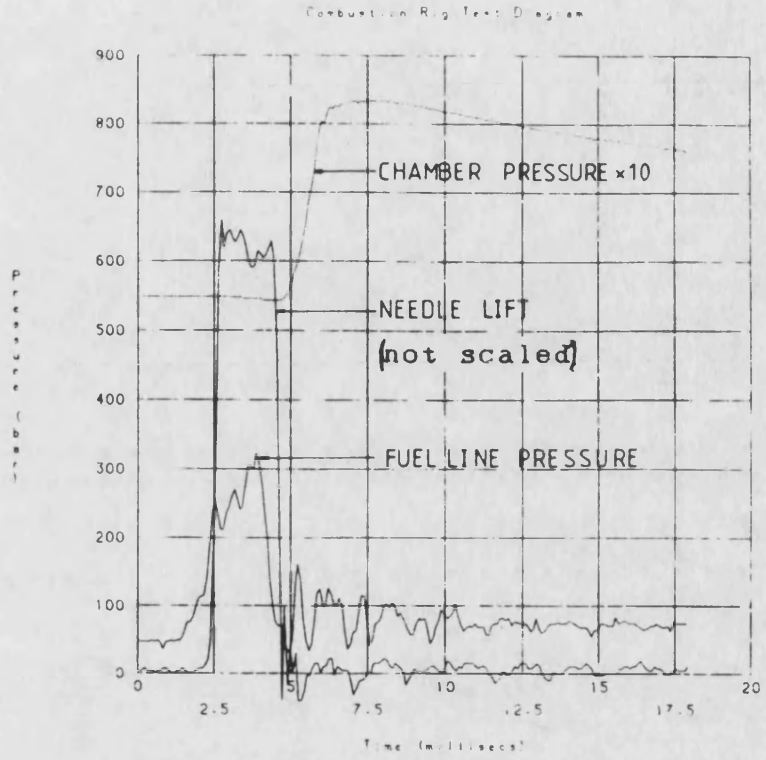

Figure 5.1 Combustion Rig Test diagram. Test 182 (p=55 bar, T=773 K)

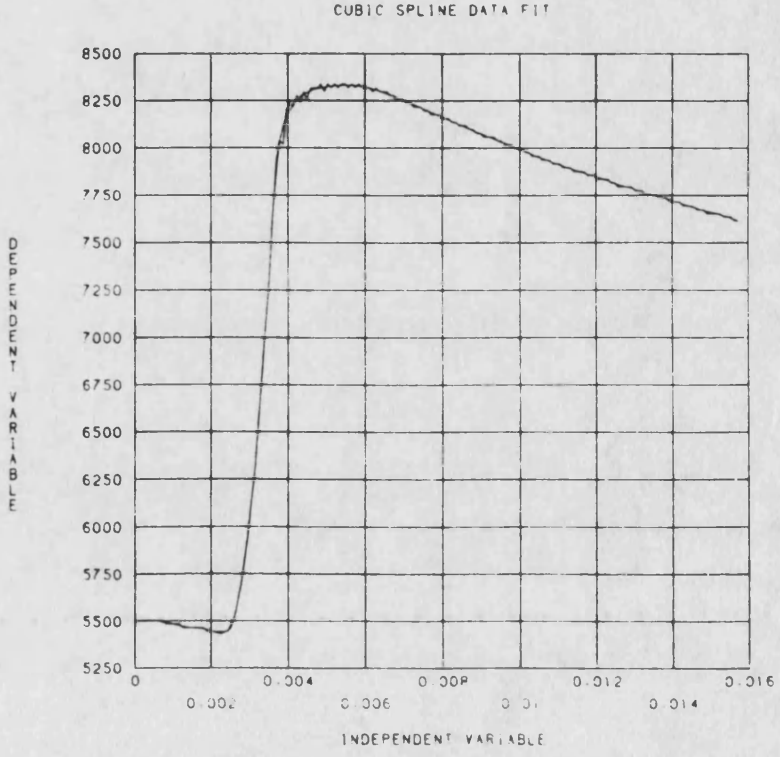

Figure 5.2 Cubic spline curve fit. Test 182 curve fit experimantal data

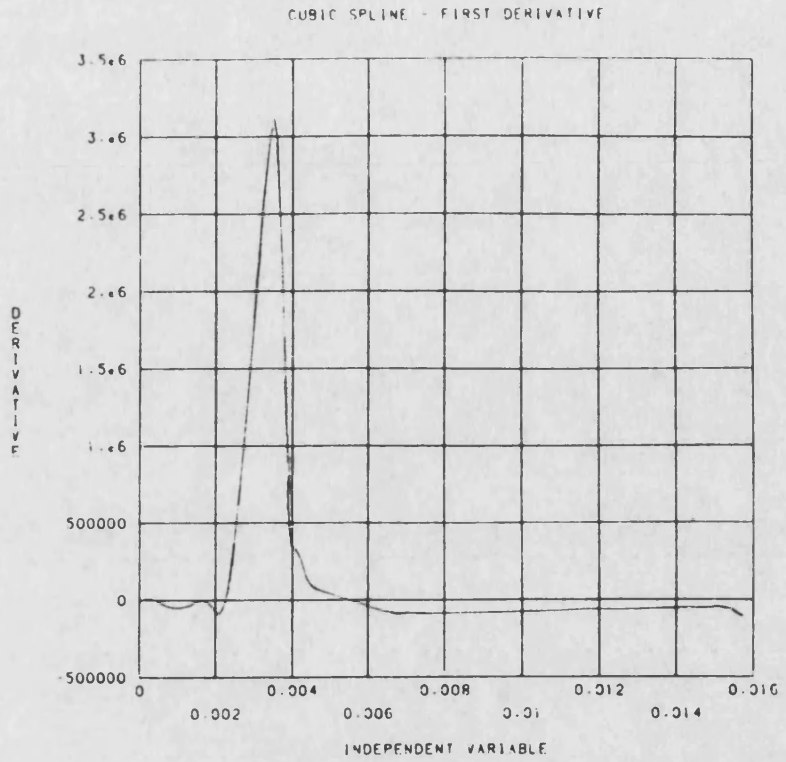

Figure 5.3 Cubic spline first derivative. Test 182 (dp/dt)

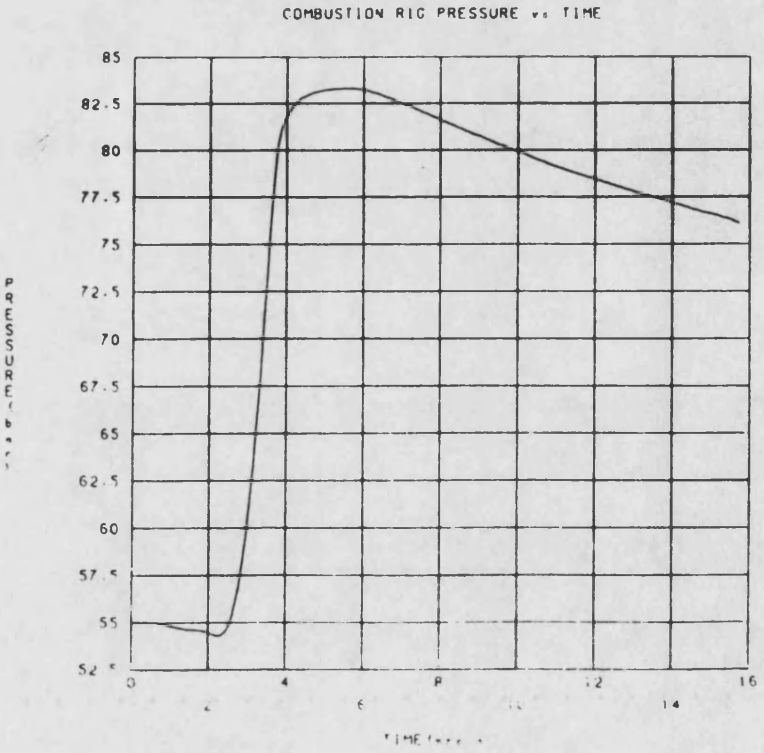

Figure 5.4 Smoothed pressure curve produced from heat release analysis. Test 182

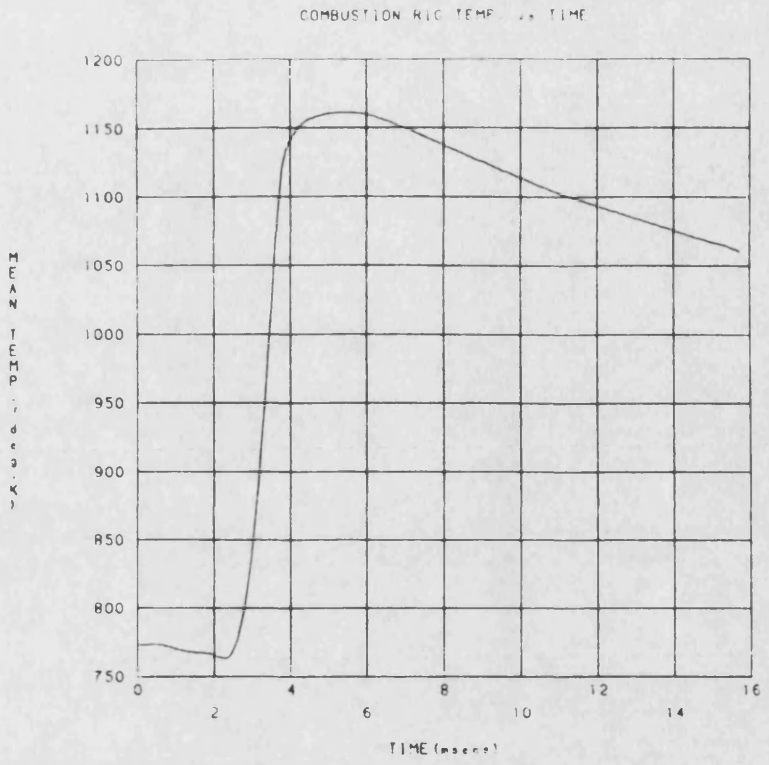

Figure 5.5 Mean chamber temperature produced from heat release analysis. Test 182

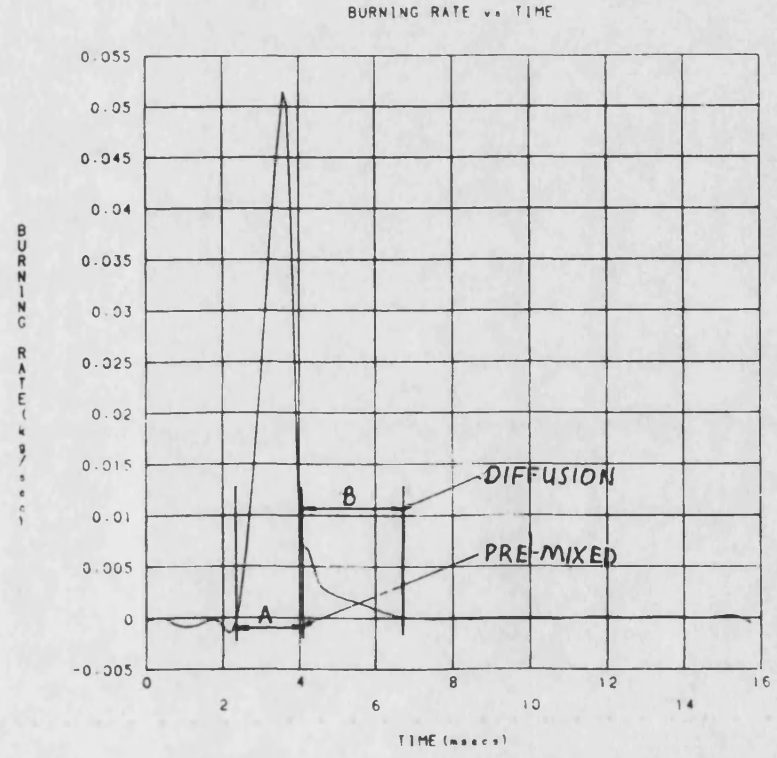

Figure 5.6 Burning rate diagram produced from heat release analysis. Test 182

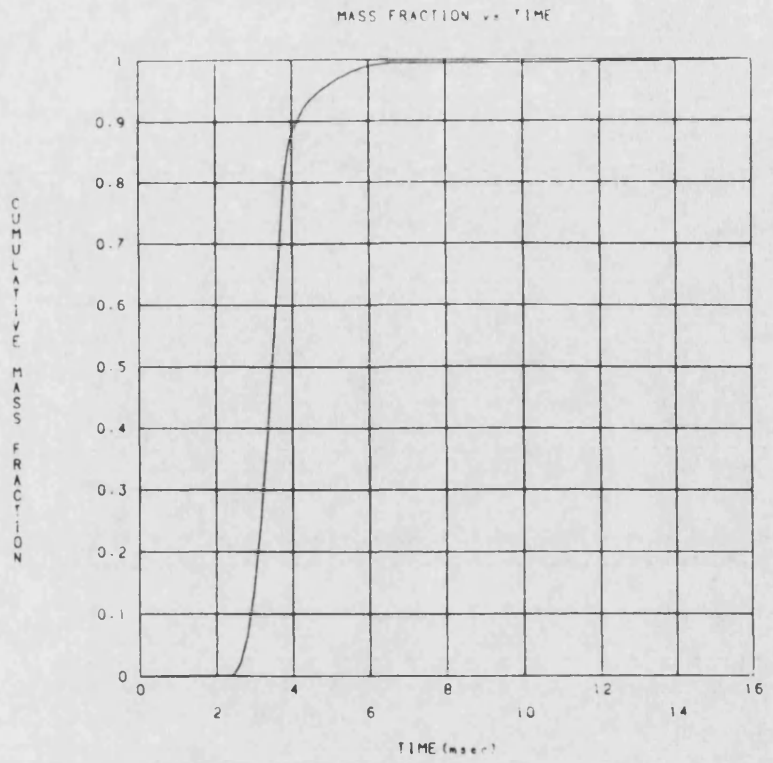

Figure 5.7 Mass fraction vs time produced from heat release analysis. Test 182

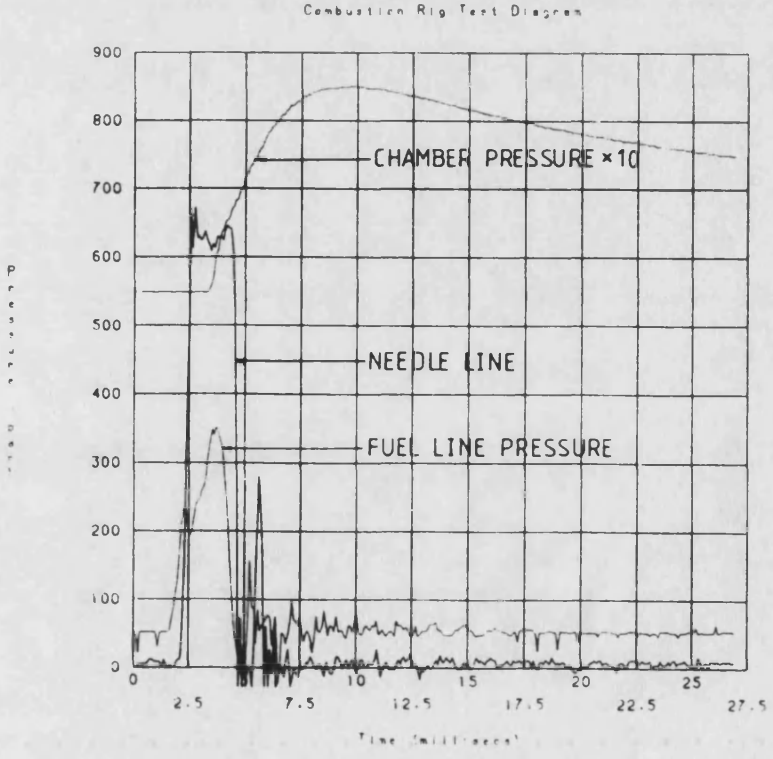

Figure 5.8 Combustion Rig Test diagram. Test 215 (p=55 bar, T=873K)

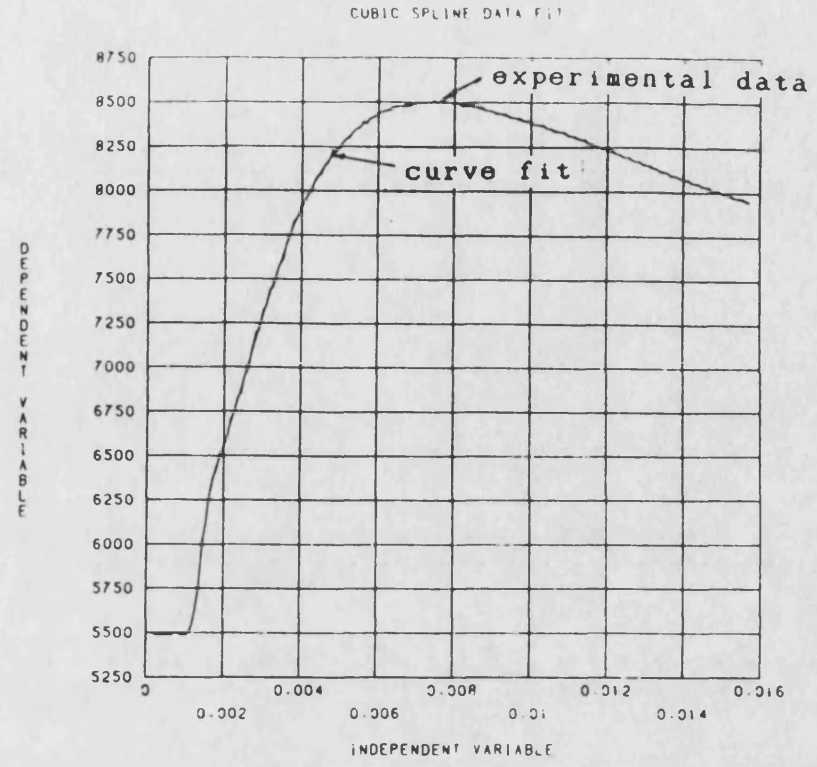

Figure 5.9 Cubic spline curve fit. Test 215

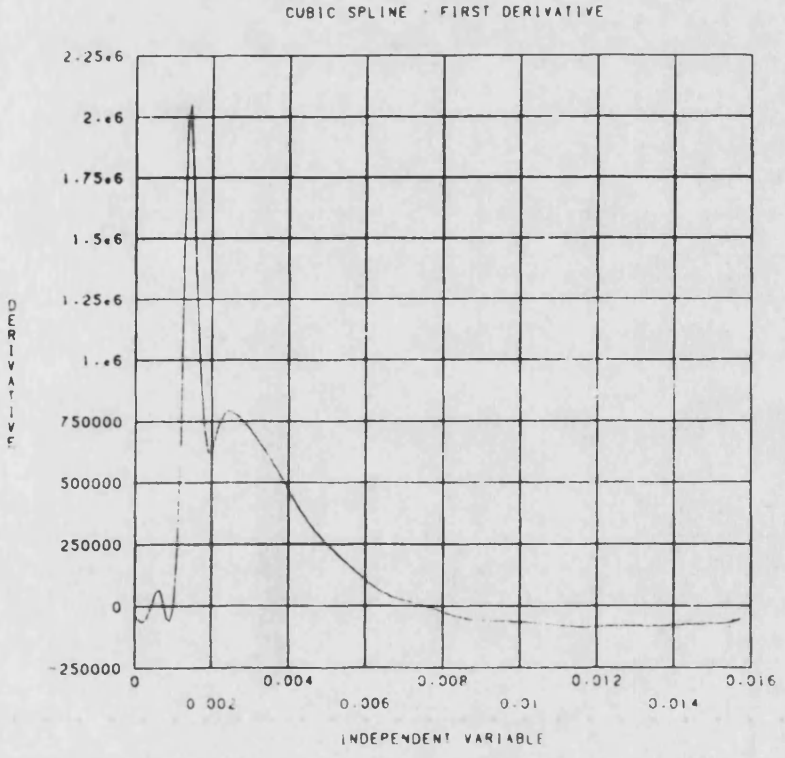

Figure 5.10 Cubic spline first derivative. Test 215

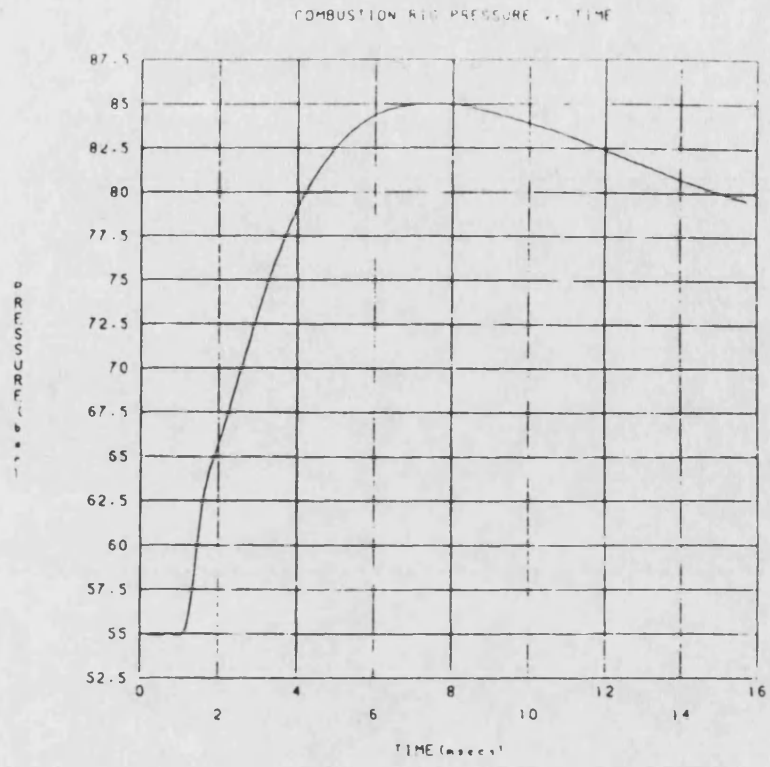

Figure 5.11 Smoothed pressure curve. Test 215

Figure 5.12 Mean chamber temperature. Test 215

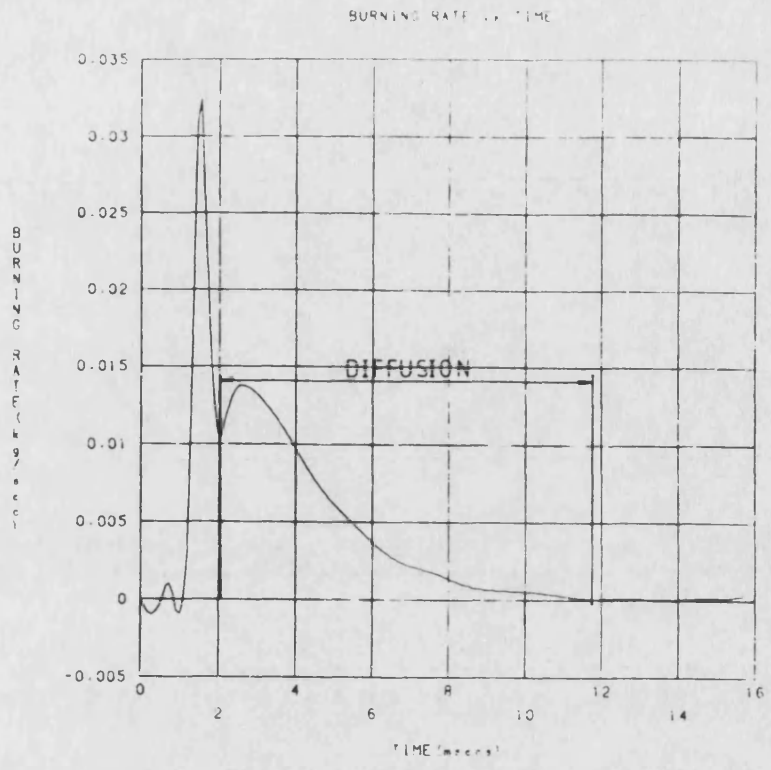

Figure 5.13 Burning rate diagram. Test 215

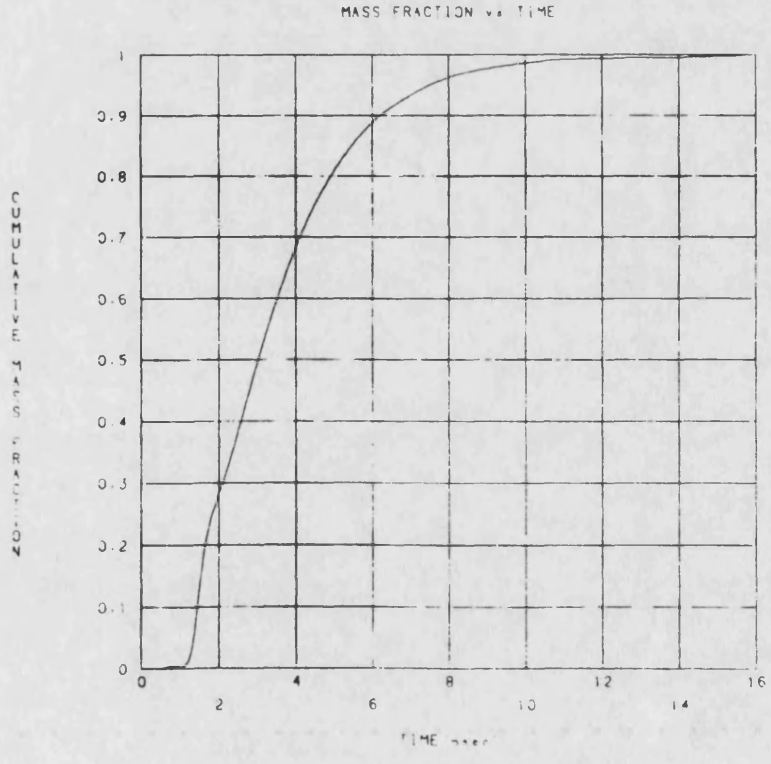

Figure 5.14 Mass fraction vs time. Test 215

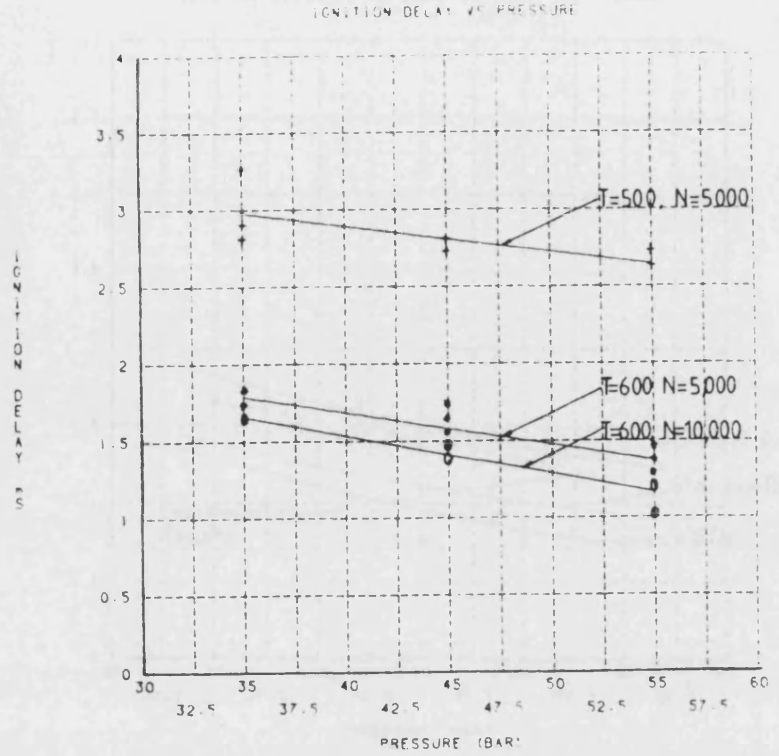

Figure 5.15 Ignition delay vs pressure for three conditions

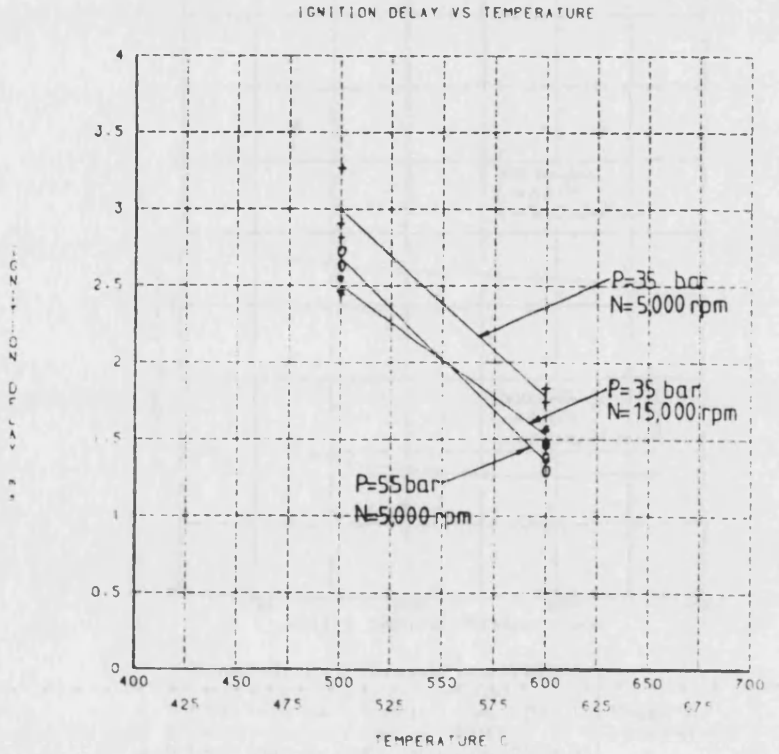

Figure 5.16 Ignition delay vs temperature for three conditions

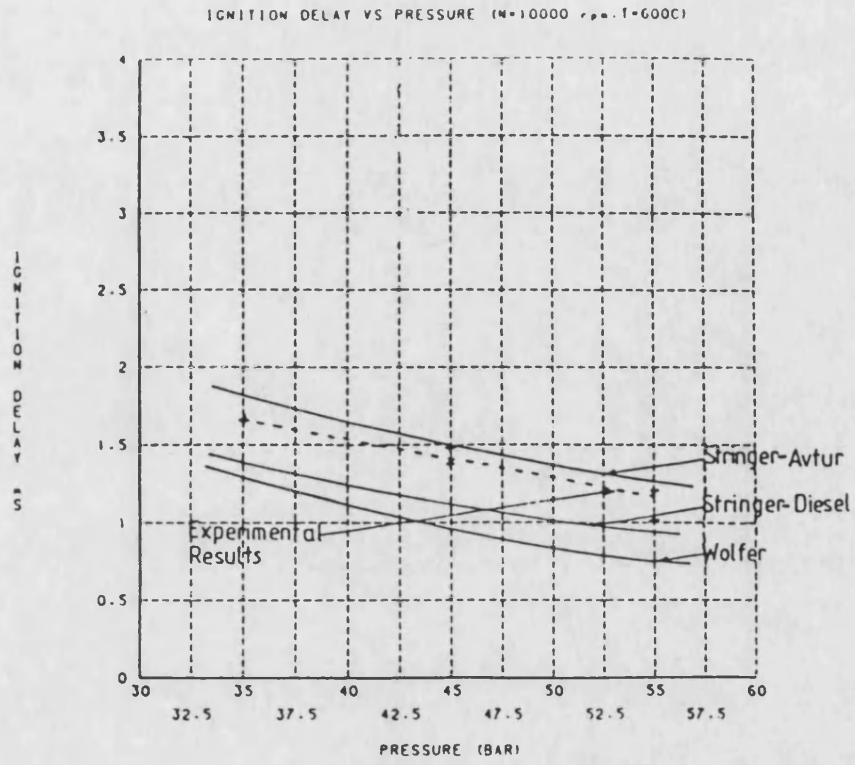

Figure 5.17 Ignition delay vs pressure. Comparison with two experimental correlation

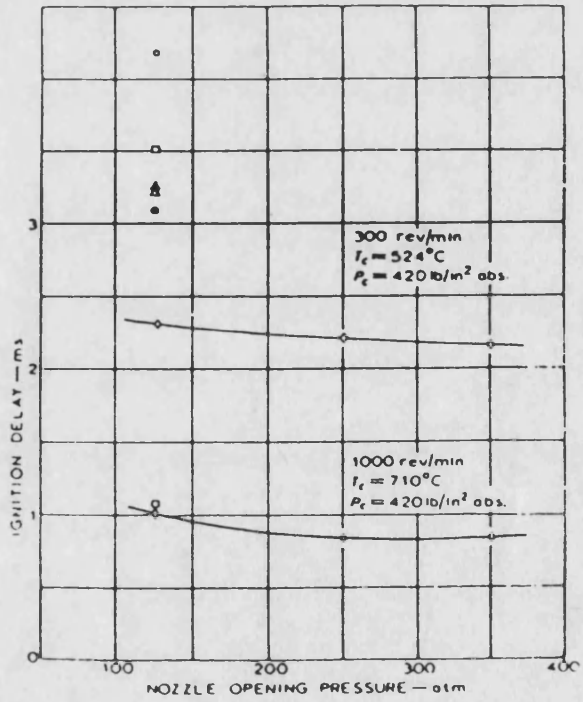

Figure 5.18 Effect of nozzle opening pressure on ignition delay (5).

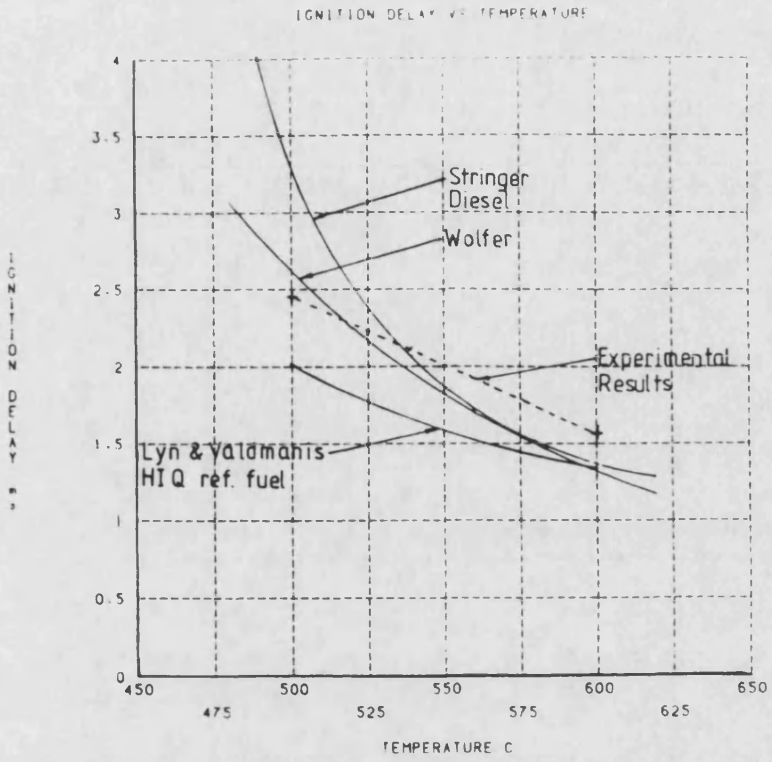

Figure 5.19 Ignition delay vs temperature. Comparison with experimental correlations. (p=35 bar, drum swirl=15,000 rpm)

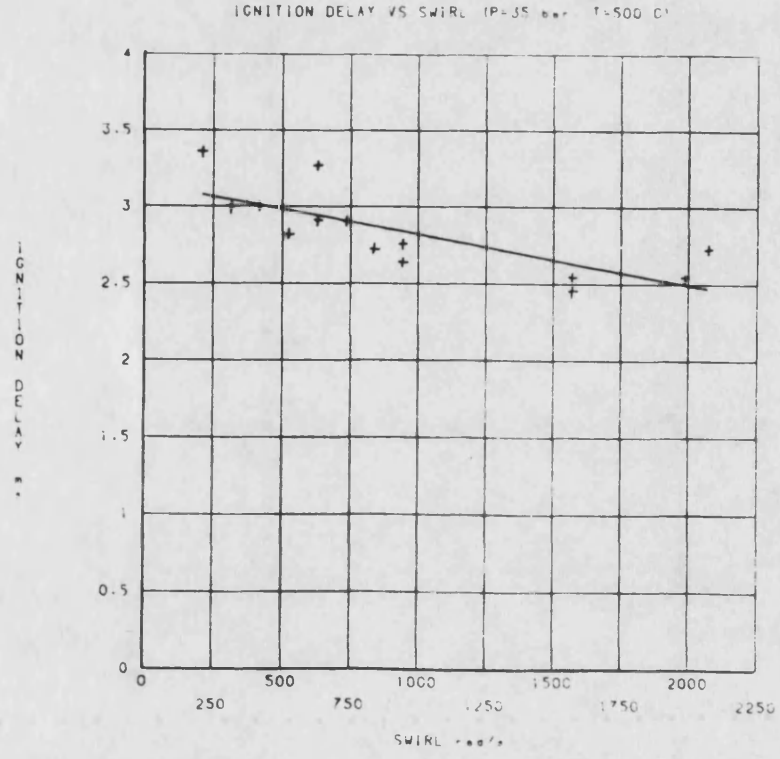

Figure 5.20 Ignition delay vs drum swirl rate. (p=35 bar, T=500 C)

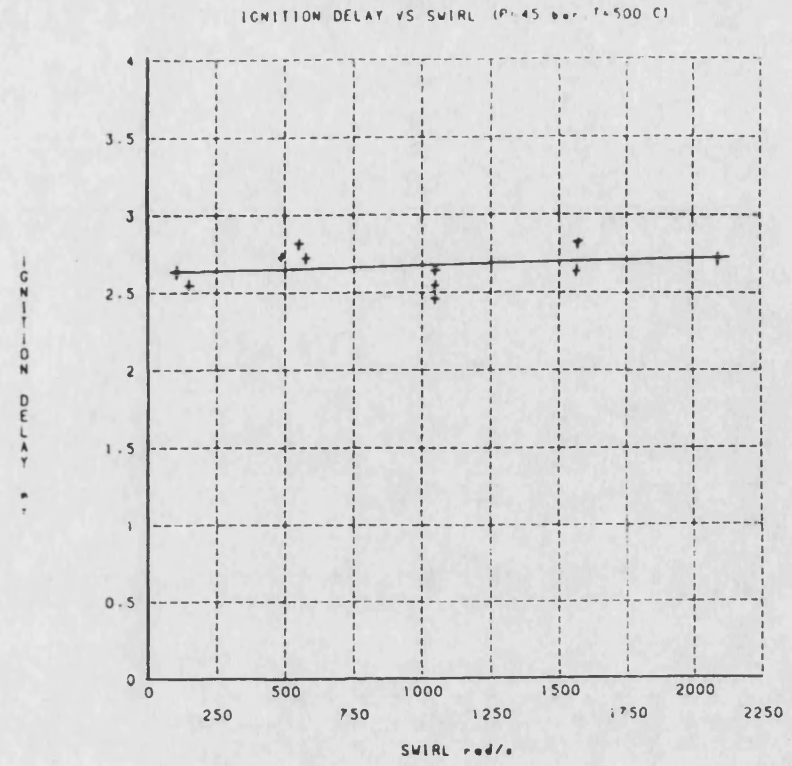

Figure 5.21 Ignition delay vs drum swirl rate.
(p=45 bar, T=500C)

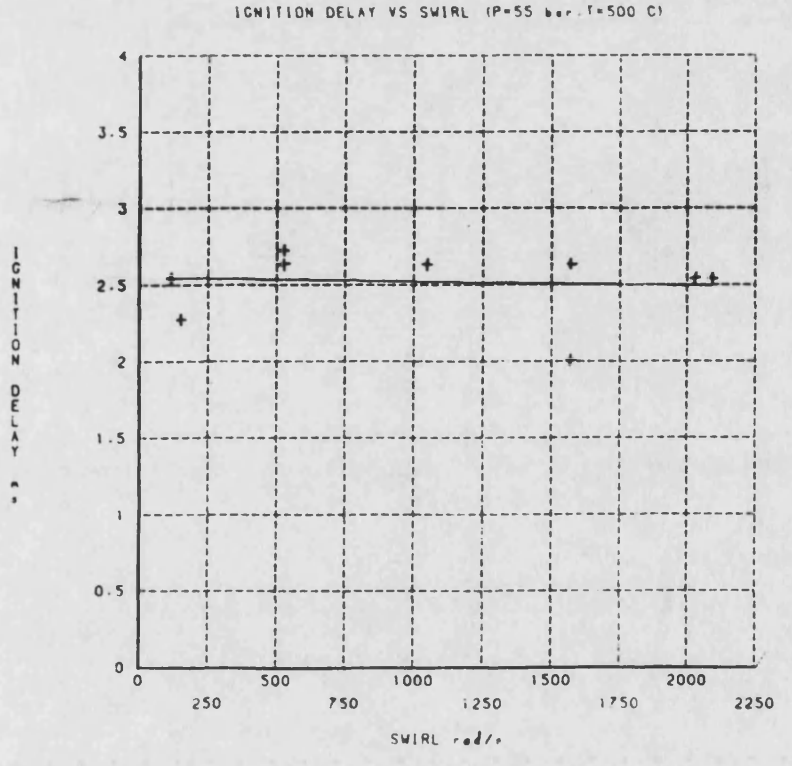

Figure 5.22 Ignition delay vs drum swirl rate.
(p=55 bar, T=500 C)

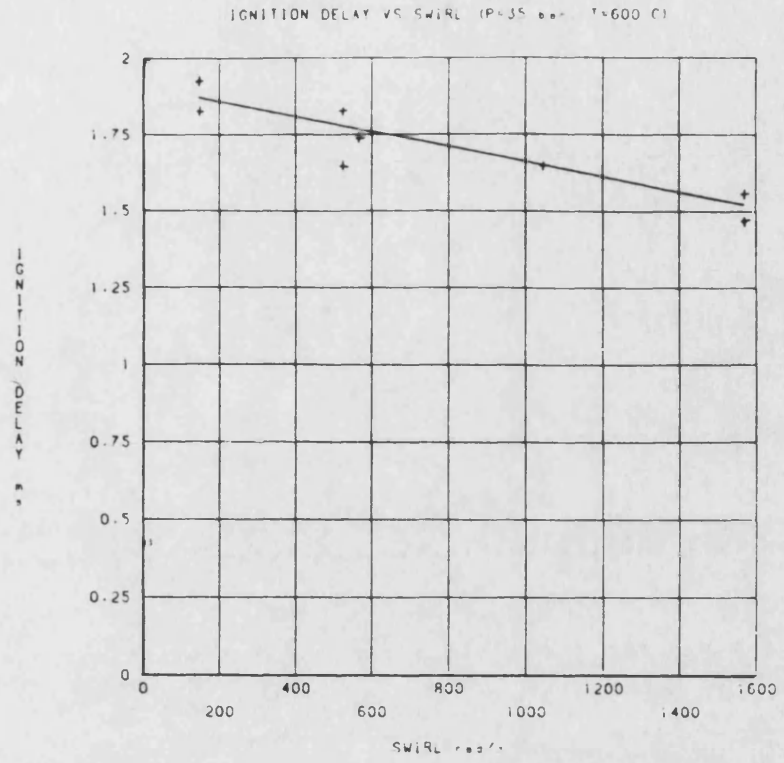

Figure 5.23 Ignition delay vs drum swirl rate.
(p=35 bar, T=600C)

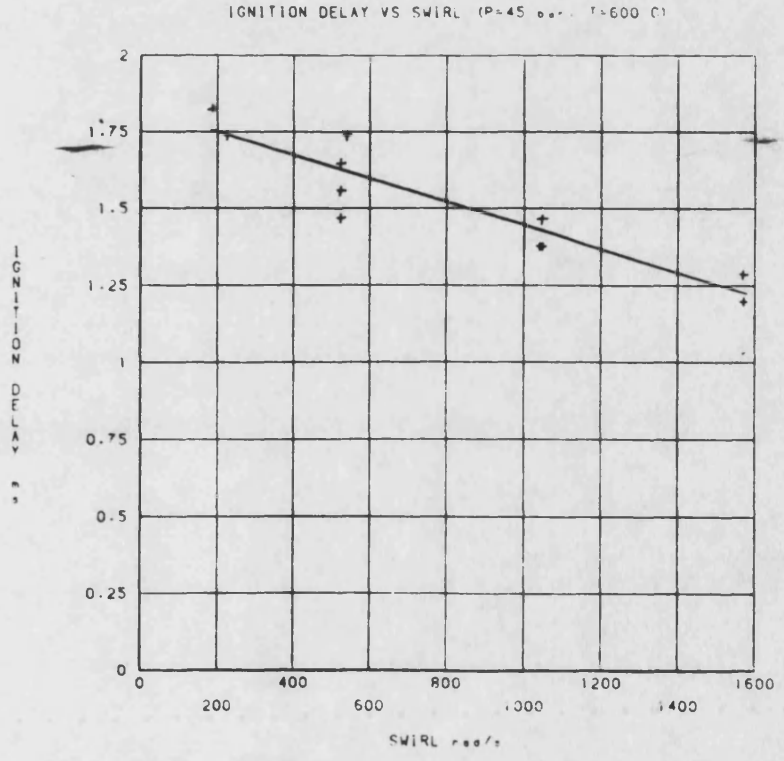

Figure 5.24 Ignition delay vs drum swirl rate.
(p=45 bar, T=600 C)

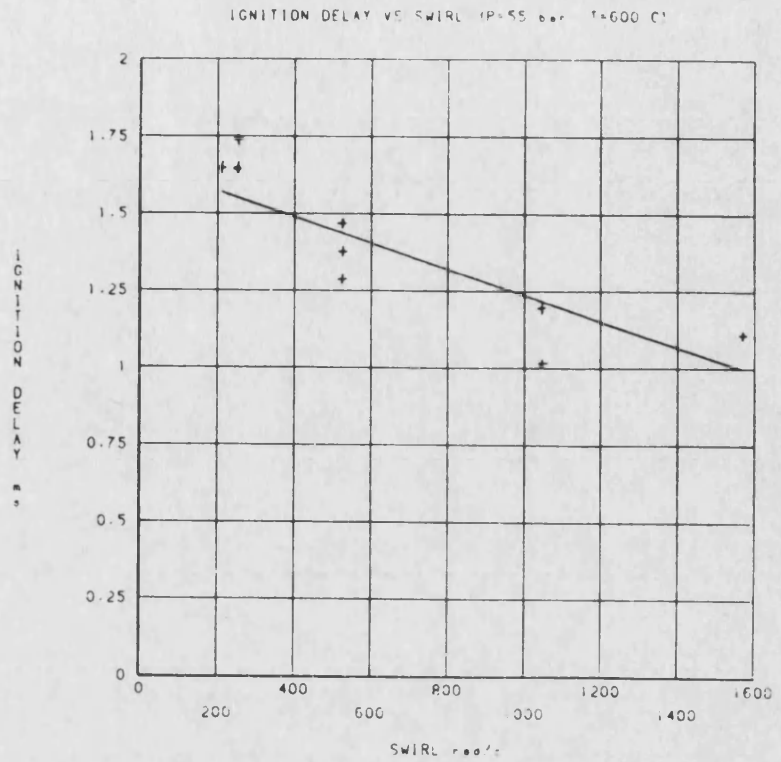

Figure 5.25 Ignition delay vs drum swirl rate. (p=55 bar, T=600C)

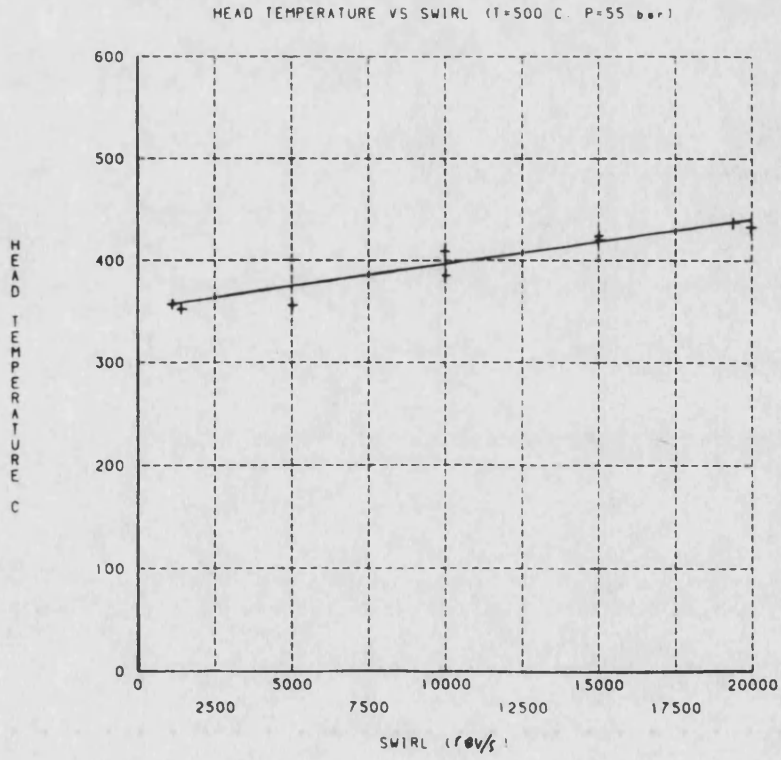

Figure 5.26a Mean Combustion chamber head temperature vs drum swirl rate. (p=55 bar, T=500 C)

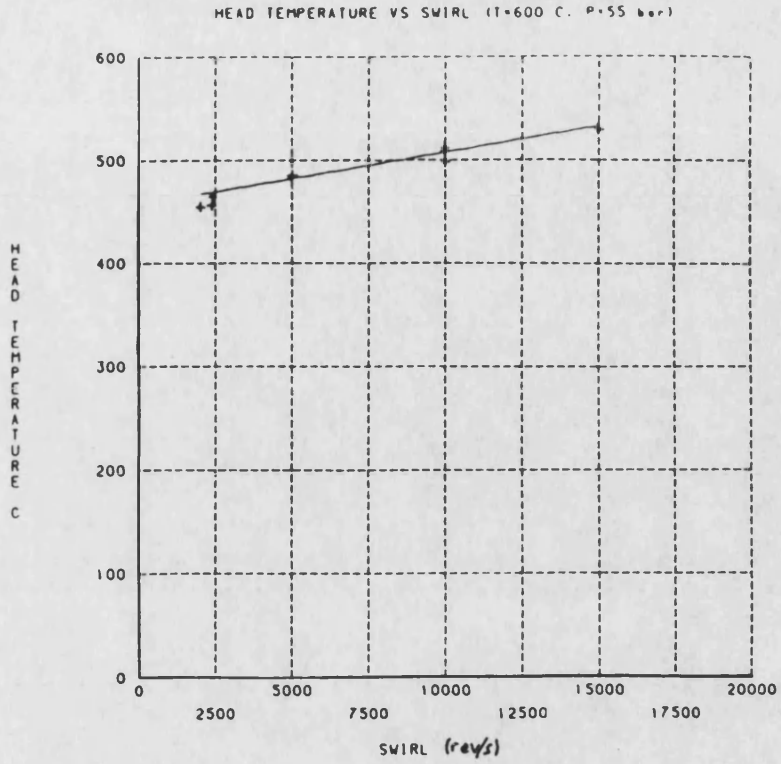

Figure 5.26b Mean Combustion chamber head temperature vs drum swirl rate. (p=55 bar, T=600 C)

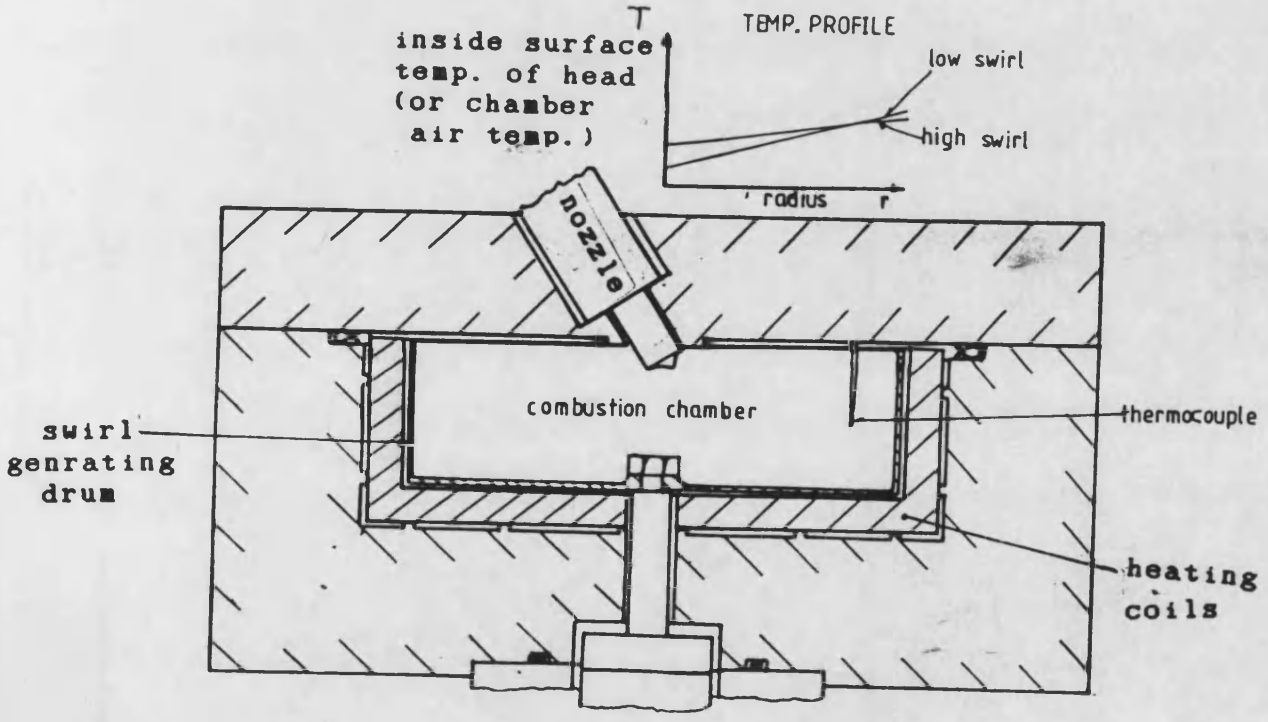

Figure 5.27 Cross-section of combustion chamber, which shows how the swirl rate may influence the head & gas temperature profiles.

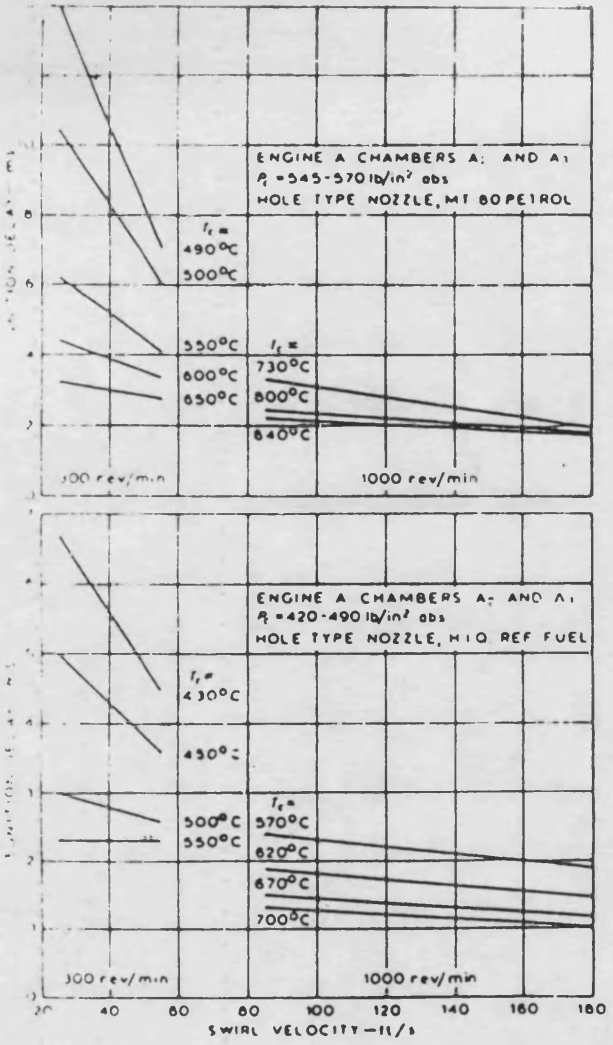

Figure 5.28 Effect of swirl rate on ignition delay in an IDI diesel engine. Taken from reference (5).

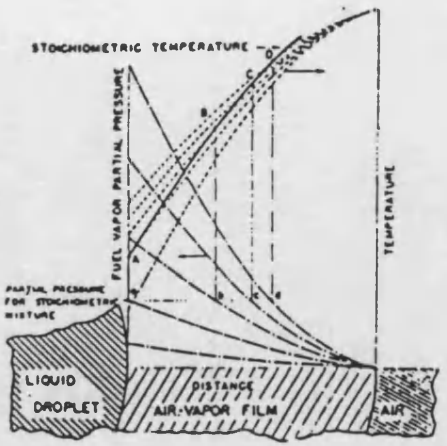

Figure 5.29 Development of stoichiometric-mixture temperature history in air-vapour film at droplet surface (6).

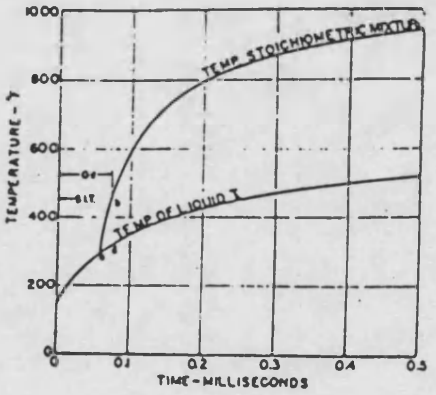

Figure 5.30 Physical delay for vapour-air mixture surrounding liquid droplet (decane) to reach self ignition temperature (6).

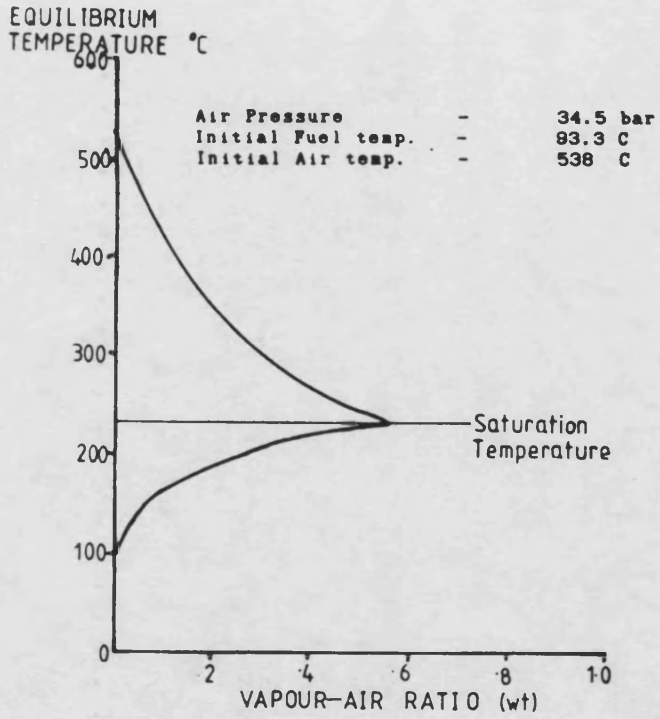

Figure 5.31. Adiabatic saturation temperature versus fuel/air ratio by weight at adiabatic saturation conditions.

(Taken from ref. 6)

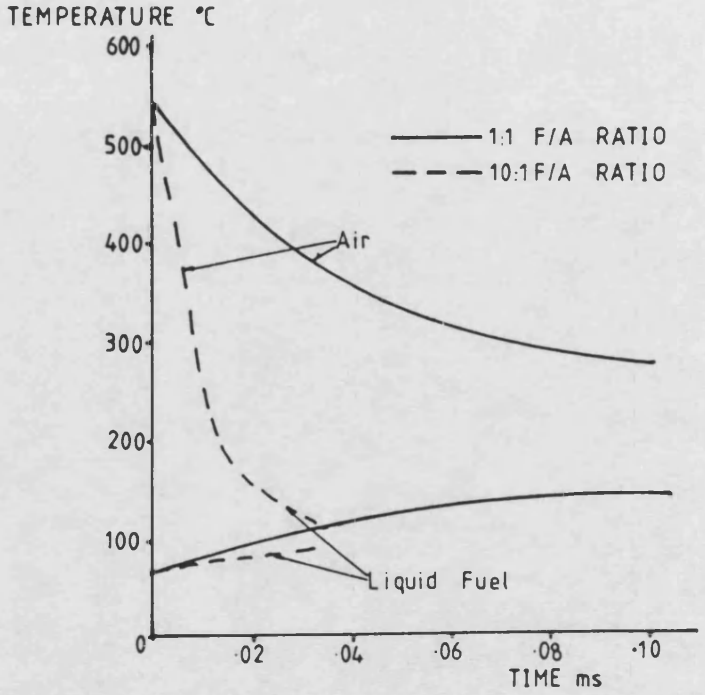

Figure 5.32 Effect of fuel/air ratio on rapidity of approach to adiabatic saturation conditions. Decane with fuel air ratios of 1:1 & 10:1 by weight. Drople size - 25 um (6)

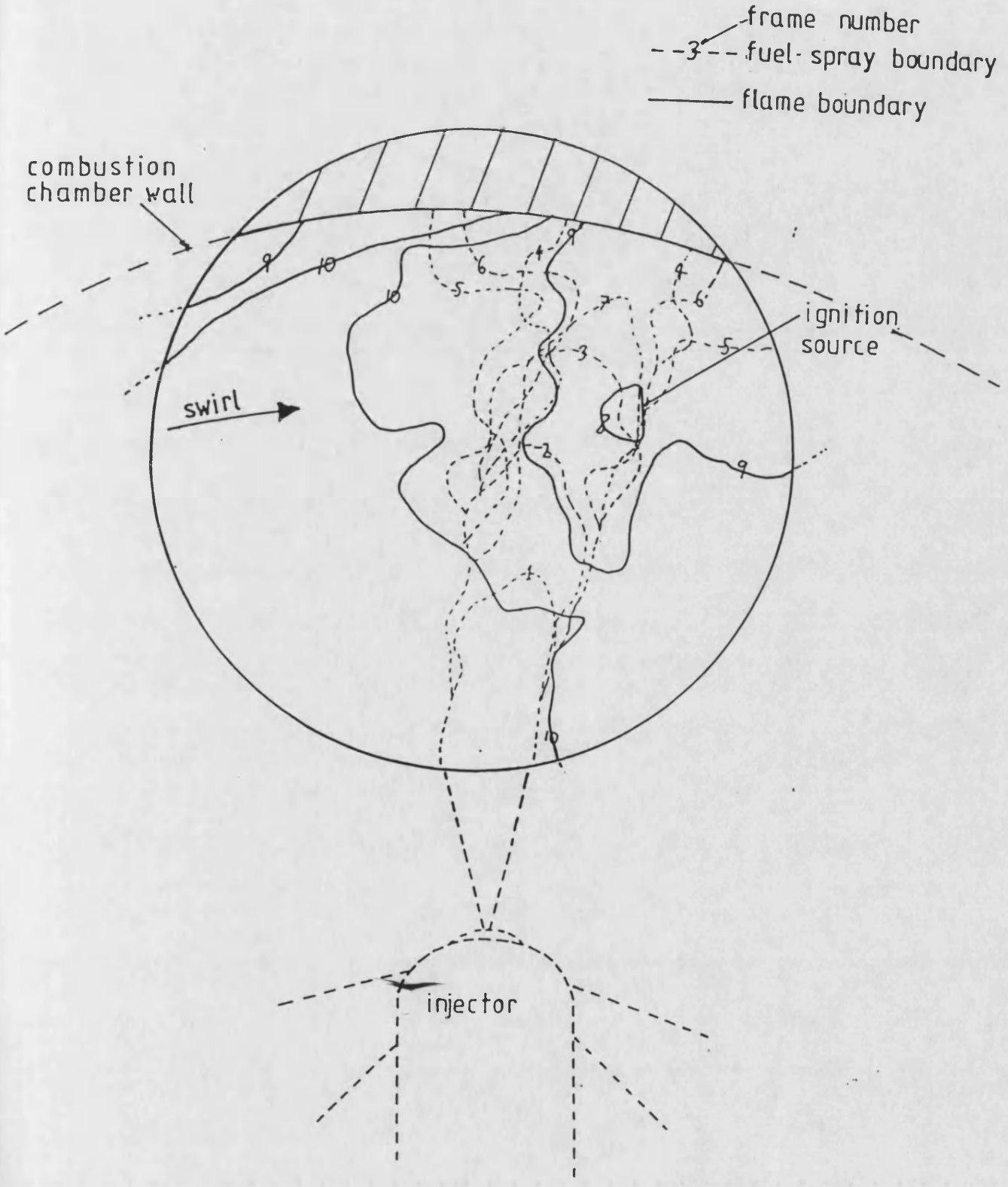

Figure 5.33 Ignition source in downwind side of fuel spray in swirl (Test 532: p=35 bar, T=522 C, air swirl=6750 rev/s)

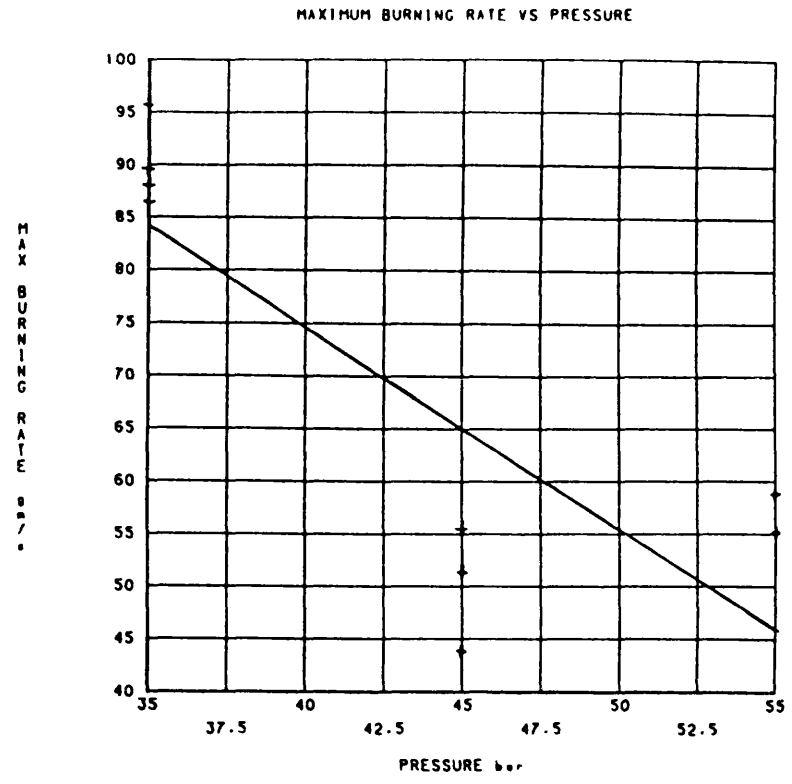

Figure 5.34 Effect of pressure on maximum burning rate. (T=500 C, drum swirl=5000rpm)

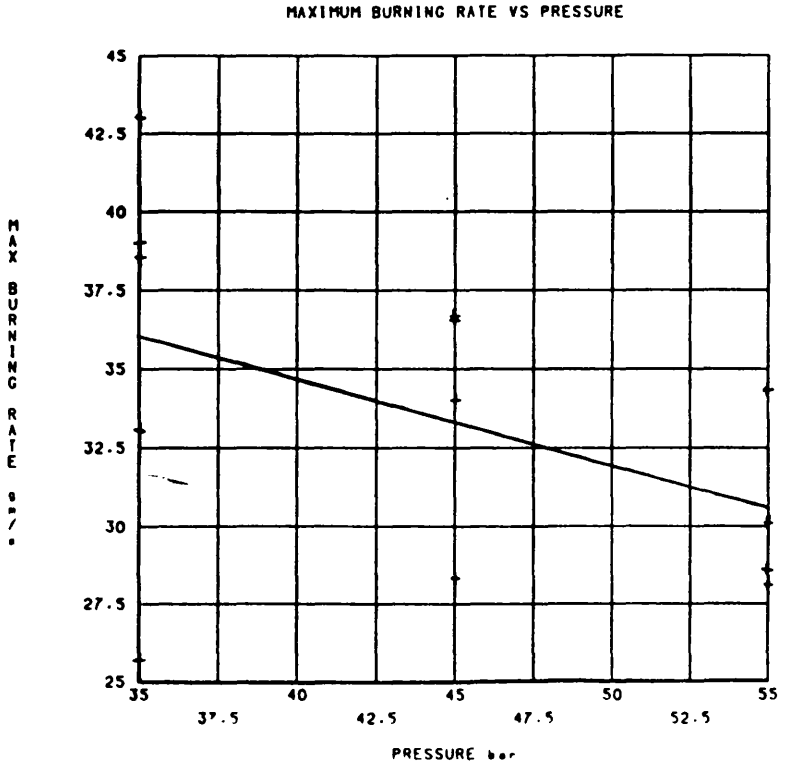

Figure 5.35 Effect of pressure on maximum burning rate. (T=600 C, drum swirl=5000rpm)

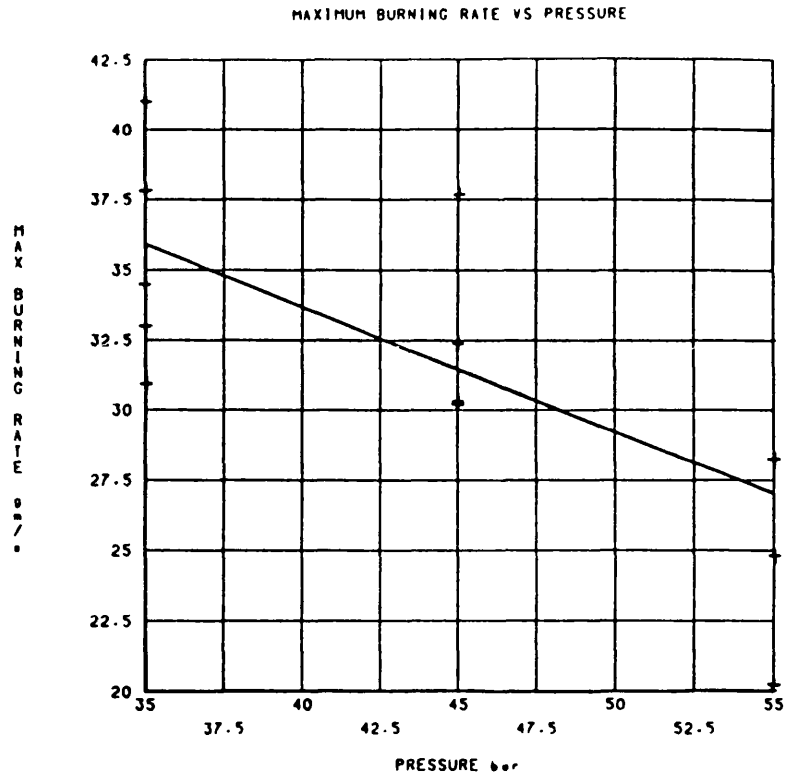

Figure 5.36 Effect of pressure on maximum burning rate. (T=600 C, drum swirl=10000rpm)

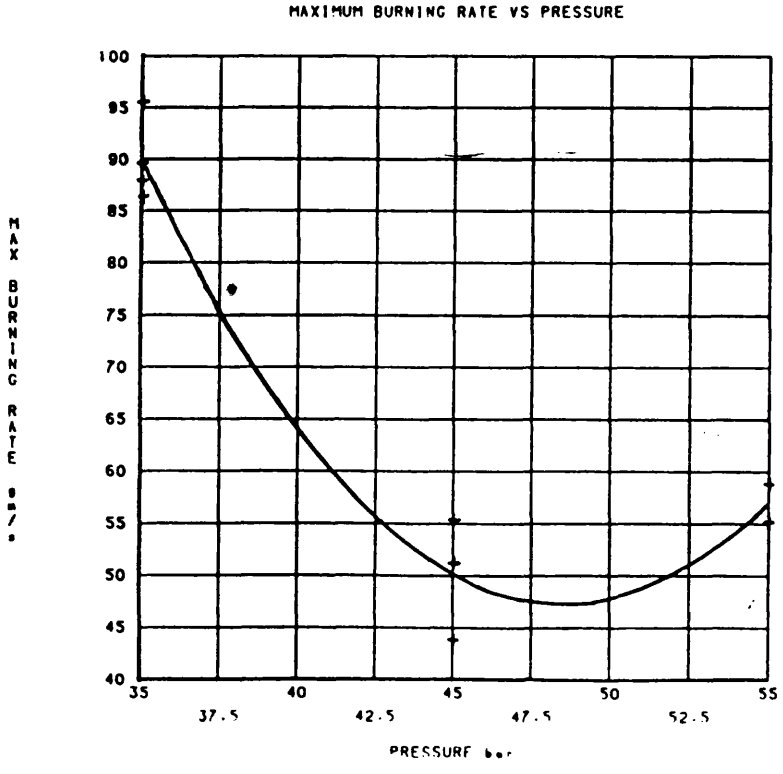

Figure 5.37 Effect of pressure on maximum burning rate. (T=500 C, drum swirl=5000rpm)

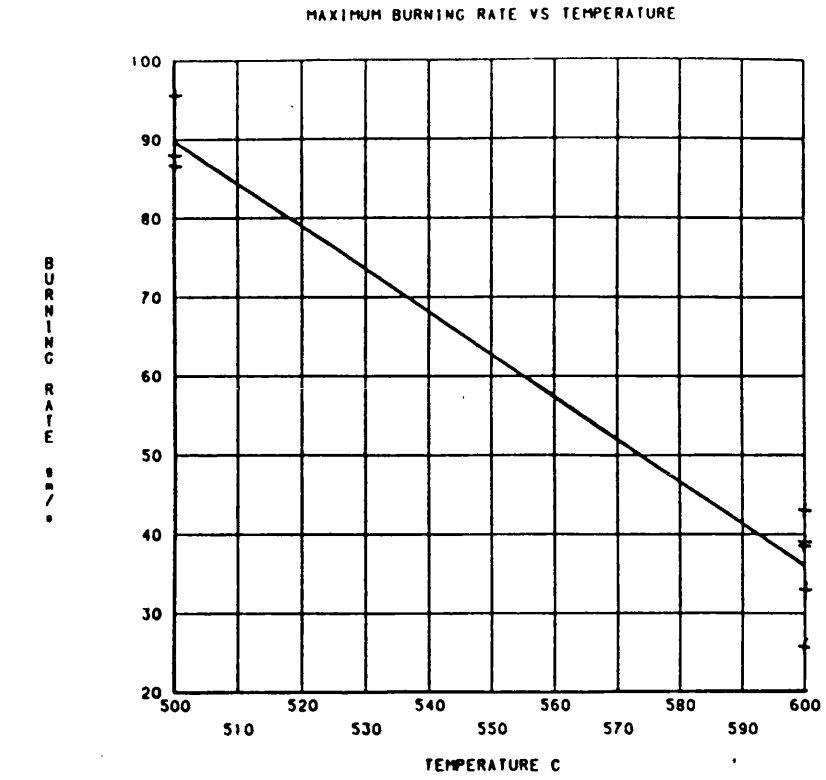

Figure 5.38 Effect of temperature on maximum burning rate. (p=35 bar, drum swirl=5000rpm)

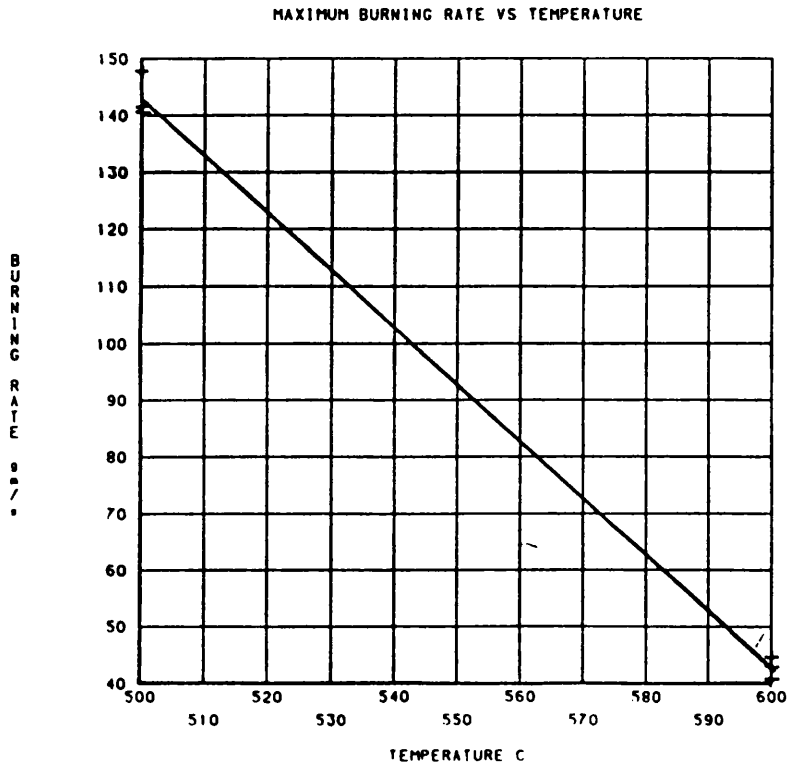

Figure 5.39 Effect of temperature on maximum burning rate. (p=35 bar, drum swirl=15000rpm)

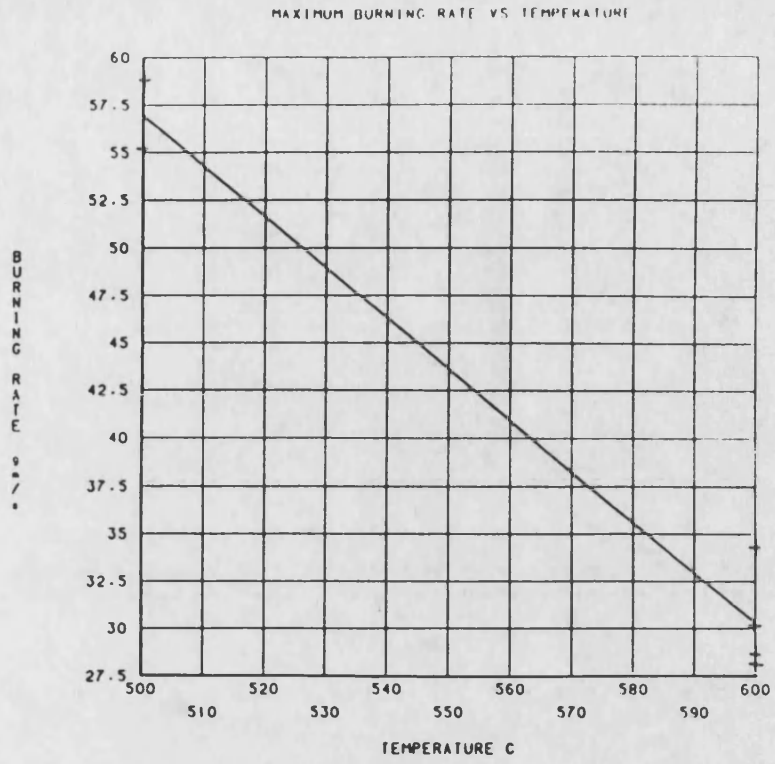

Figure 5.40 Effect of temperature on maximum burning rate. (p=55 bar, drum swirl=5000rpm)

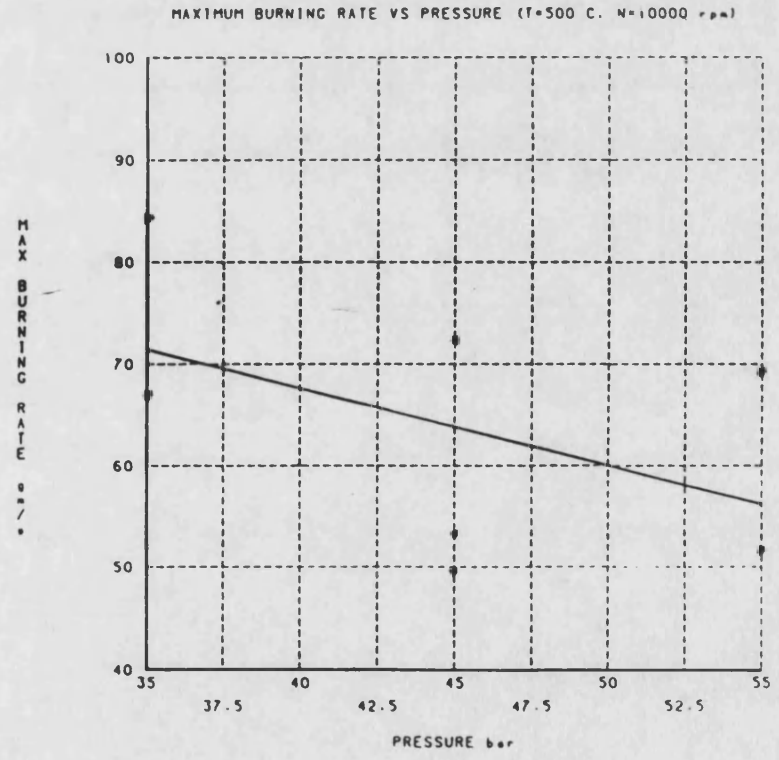

Figure 5.41 Effect of pressure on maximum burning rate. (T=500 C, drum swirl=10000rpm)

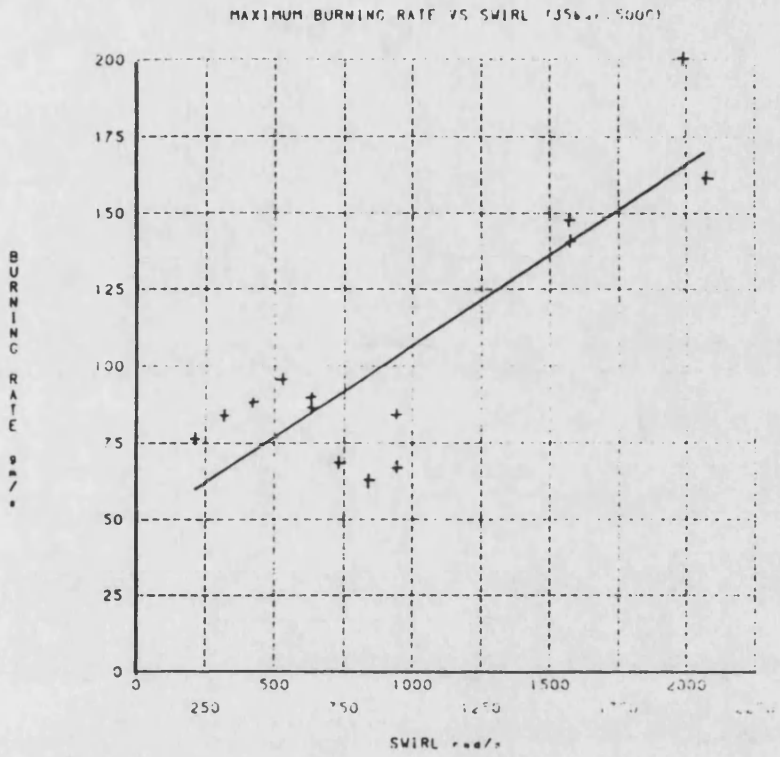

Figure 5.42 Effect of swirl on maximum burning rate. (p=35 bar, T=500 K)

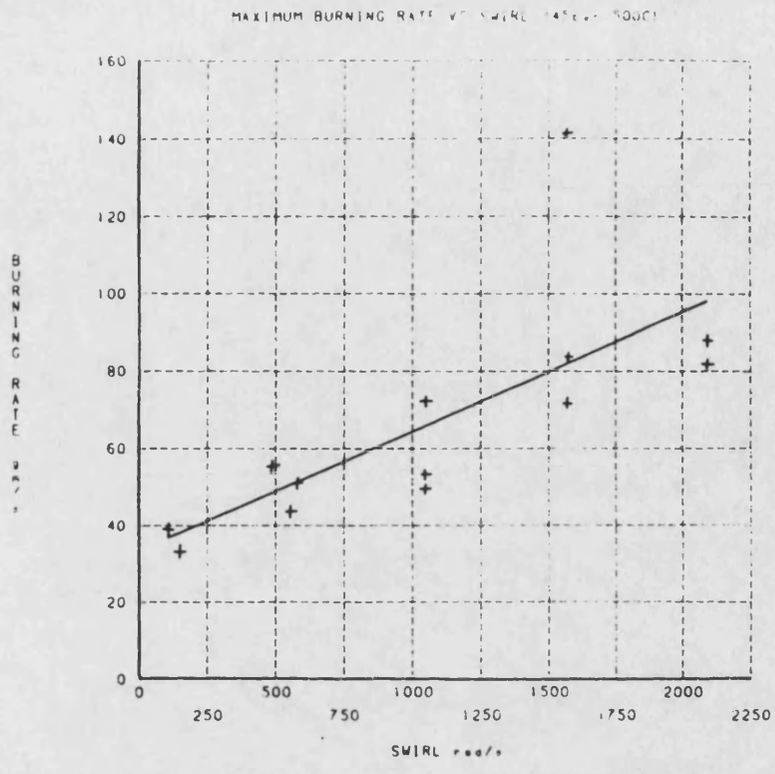

Figure 5.43 Effect of swirl on maximum burning rate. (p=45 bar, T=500 C)

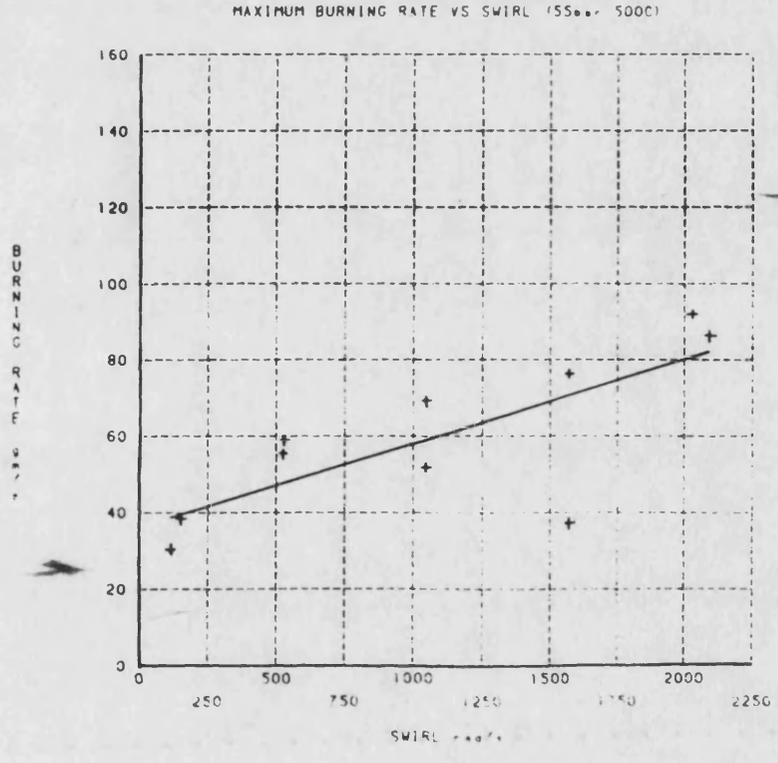

Figure 5.44 Effect of swirl on maximum burning rate. (p=55 bar, T=500 C)

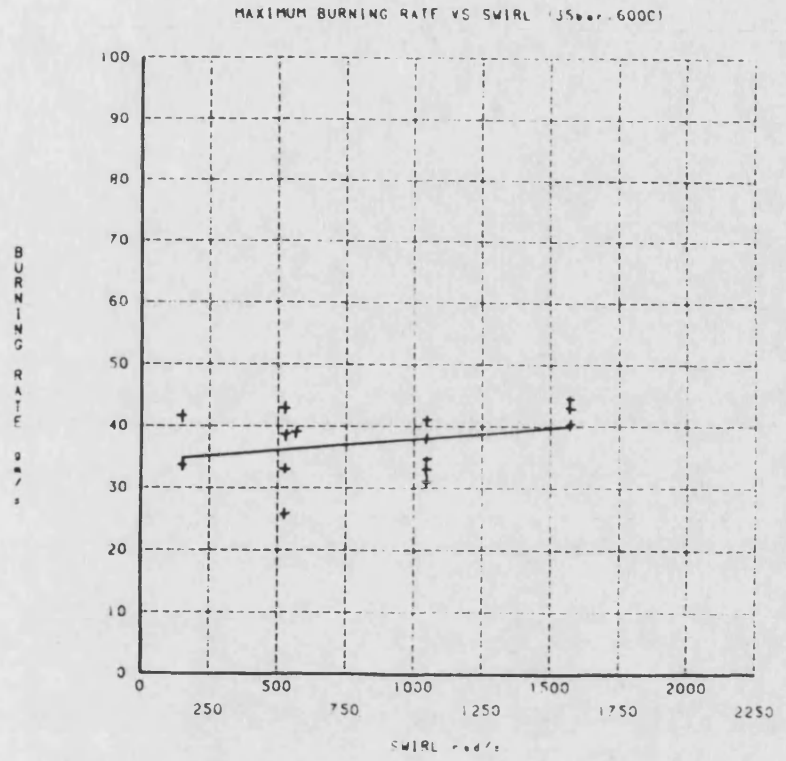

Figure 5.45 Effect of swirl on maximum burning rate. (p=35 bar, T=600 C)

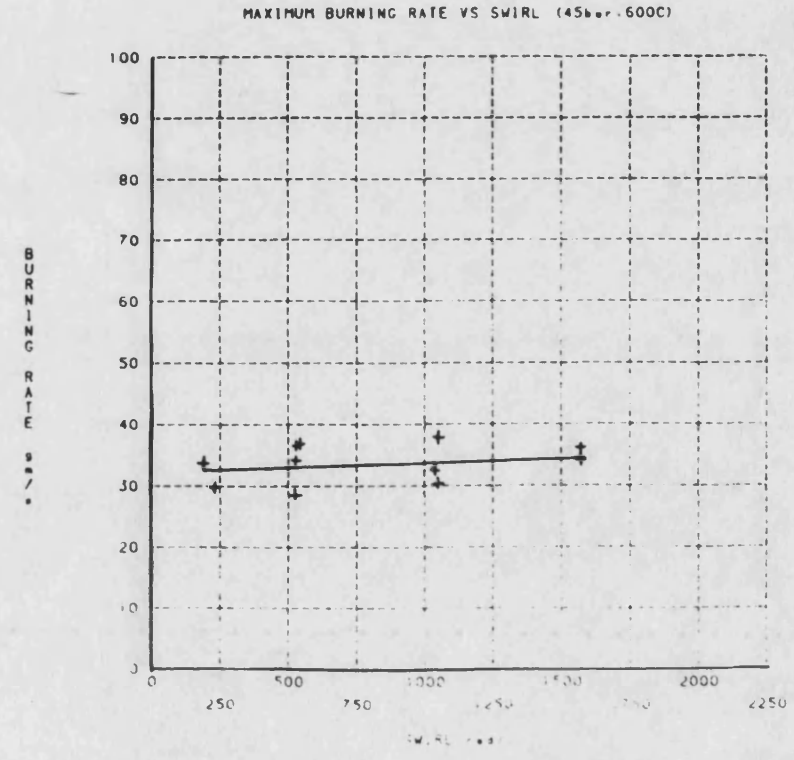

Figure 5.46 Effect of swirl on maximum burning rate. (p=45 bar, T=600 C)

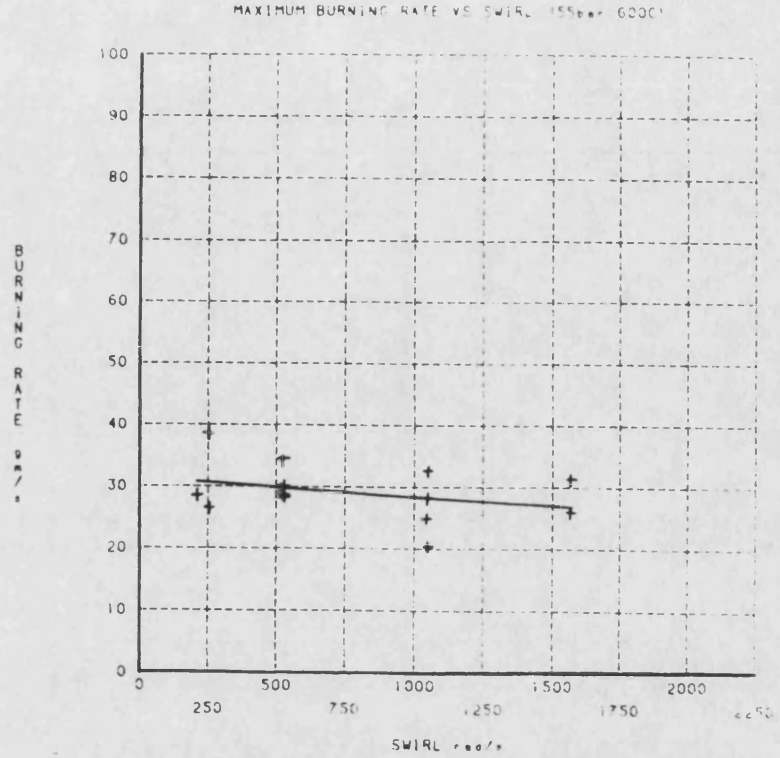

Figure 5.47 Effect of swirl on maximum burning rate. (p=55 bar, T=600 C)

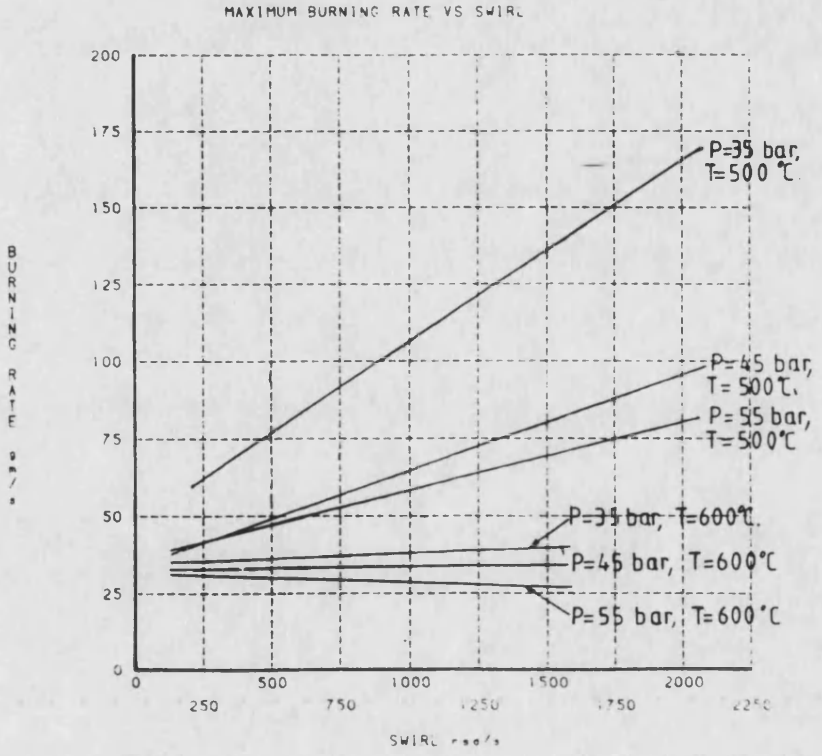

Figure 5.48 Comparison of maximum burning rate vs swirl at conditions of different severity. (from p=35 bar & T=500 C to p=55 bar & T=600 C)

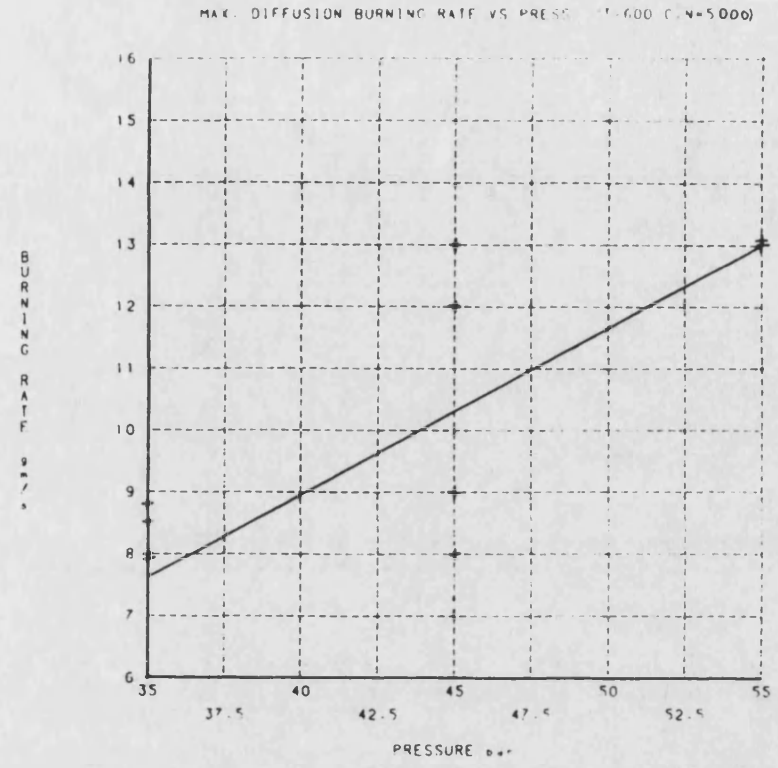

Figure 5.49 Effect of pressure on maximum diffusion burning rate. (T=600 C, drum swirl=5000 rpm)

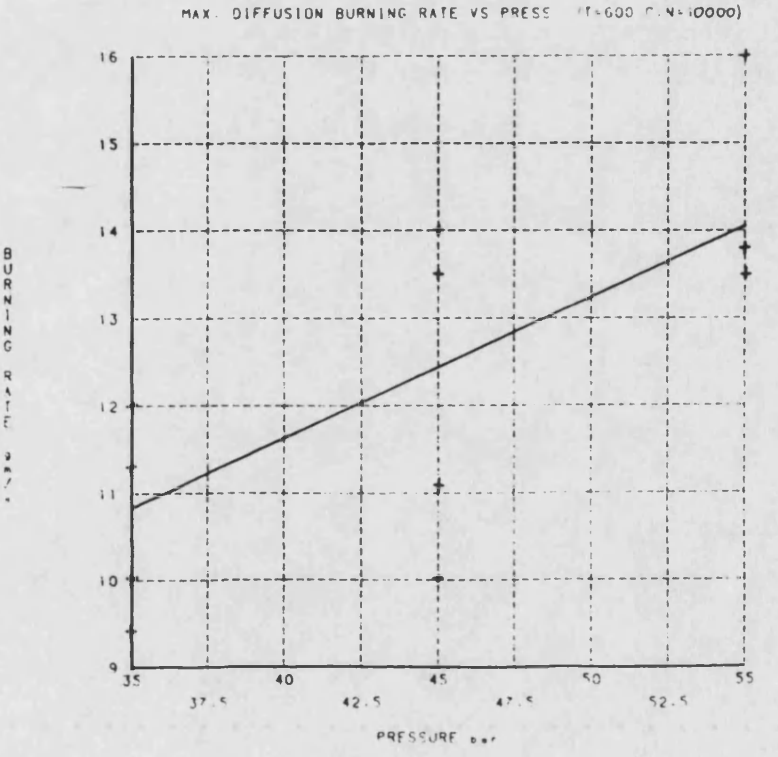

Figure 5.50 Effect of pressure on maximum diffusion burning rate. (T=600 C, drum swirl=10000 rpm)

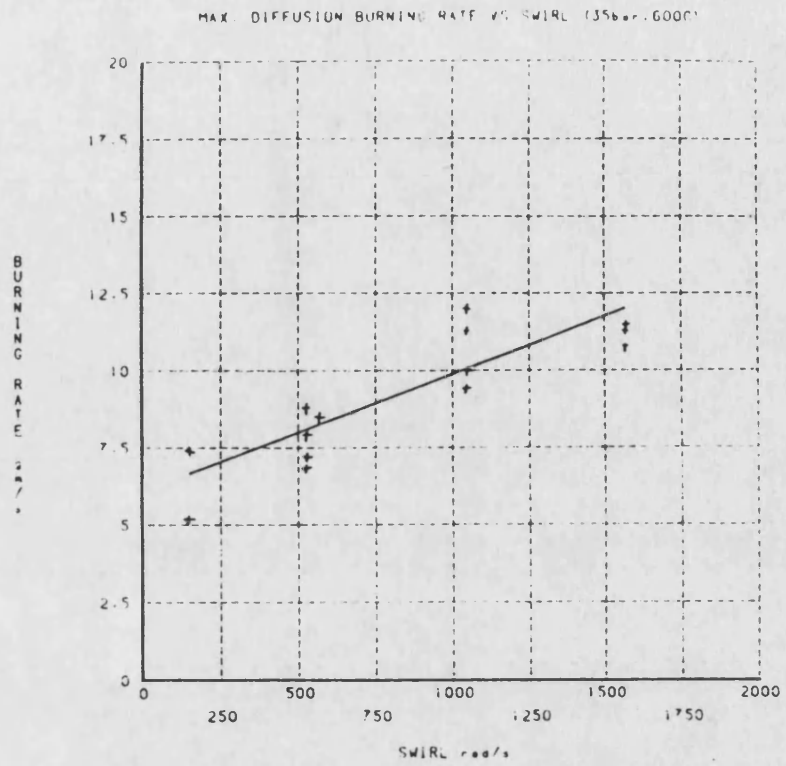

Figure 5.51 Effect of swirl on maximum diffusion burning rate. (p=35 bar, T=600 C)

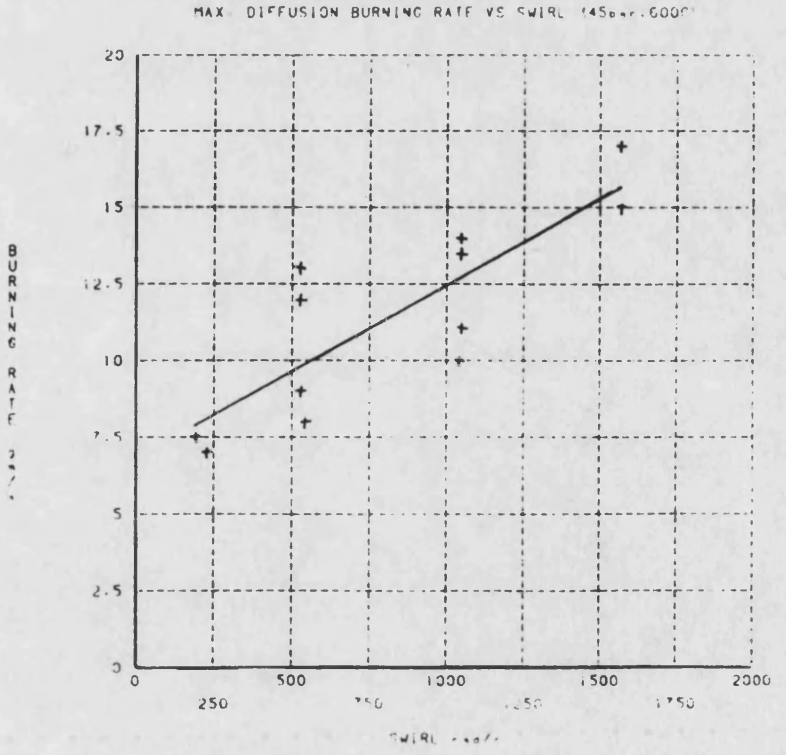

Figure 5.52 Effect of swirl on maximum diffusion burning rate. (p=45 bar, T=600 C)

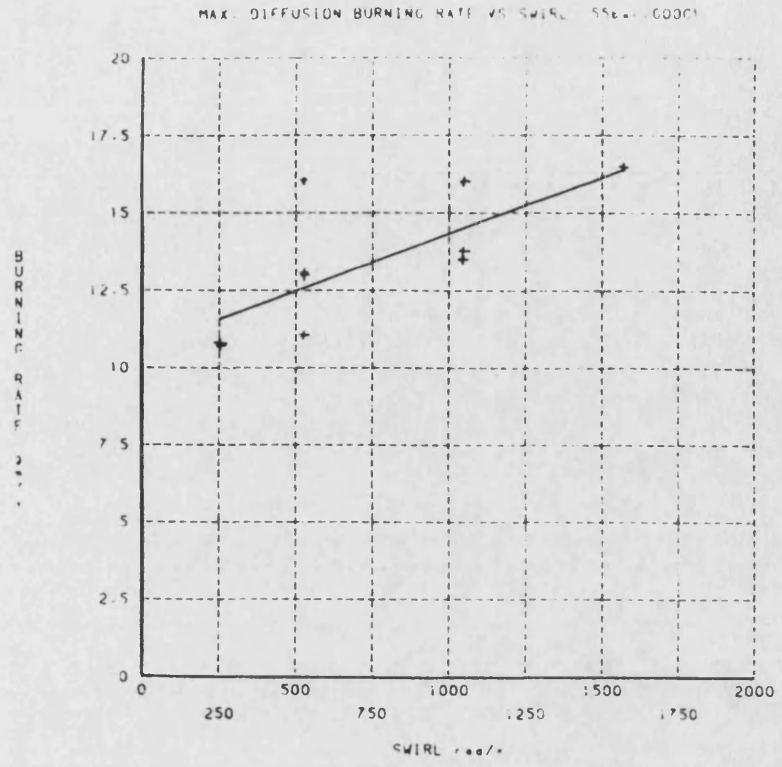

Figure 5.53 Effect of swirl on maximum diffusion burning rate. (p=55 bar, T=600 C)

CHAPTER 6

Combustion Model.

Notation

For chapters 6 and 7

$a_{i,k}$	-	coefficient k for specie i in thermodynamic property equation
act	-	activation energy
A	-	empirically derived constant in Annand equation
b	-	spray half width of circular spray (m)
b_{max}	-	spray half width of jet front (m)
b_f	-	burnt fraction (mass burnt/mass injected)
b_1	-	leading edge width of spray (m)
b_2	-	trailing edge width of spray (m)
b_3	-	perpendicular half width of spray (m)
B	-	empirically derived constant in Annand equation
C	-	fuel concentration withein spray (mass of fuel/mass of fuel+air)
C_A	-	empirically derived constatn in Annand equation (W/m^2K^4)
C_d	-	coefficient of discharge from an orifice
C_m	-	centreline concentration within spray
C_p	-	specific heat capacity at constat P (J/kg K)
C_{st}	-	stoichiometric concentration
C_v	-	specific heat capacity at constant volume (J/kg K)
d	-	nozzle diameter (m)
d_b	-	diameter of combustion chamber (m)
d_n	-	equivalent nozzle diameter (m)

D	-	fuel droplet diameter (m)
D_o	-	initial fuel droplet diameter (m)
E	-	activation energy (J/kgmol)
(fk)	-	time dependent constant added to jet centreline concentration equation after fresh air depletion
F	-	intermediate variable in tip penetration correlation
h	-	absolute specific enthalpy (J/kgmol)
hoi	-	absolute specific enthalpy of specie i at absolute zero (J/kgmol)
H	-	absolute enthalpy (J)
k	-	thermal conductivity (W/m K)
k_p	-	empirical coefficient
k_s	-	Steric factor
K	-	empirical coefficient
K'	-	empirical coefficient
m	-	dimensionless empirical index
M_{fz}	-	mass of fuel in zone (kg)
M_i	-	mass of injected fuel (kg)
Mol_i	-	number of moles of specie i
M_u	-	mass of unburnt fuel (kg)
n	-	number of fuel droplets
N	-	engine speed (rev/min)
p	-	pressure (N/m^2)
P_a	-	chamber pressure (N/m^2)
P_{inj}	-	injection pressure (N/m^2)
P_o	-	partial pressure of oxygen (N/m^2)
q	-	heat transfer rate (W)
Q	-	total heat transfer (J)
Q_a	-	momenta of air
Q_j	-	momenta of spray
r	-	radius from centre of combustion chamber (m)

R	–	gas constant (J/kg K)
R_b	–	burning rate of fuel (kg/s)
Re	–	Reynolds number
R_{mol}	–	universal gas constant (J/kgmol K)
R_p	–	preparation rate of fuel (kg/s)
s	–	tip tangential displacement (m)
t	–	time (s)
tim	–	time since start of injection (s)
t0	–	time for jet to form (s)
T	–	gas temperature (K)
T_m	–	mean temperature (K)
T_w	–	wall temperature (K)
T_z	–	zone temperature (K)
U	–	absolute internal energy (J)
V	–	velocity within spray (m/s)
V_m	–	centreline velocity within spray (m/s)
V_o	–	spray velocity at nozzle exit (m/s)
V_z	–	zone volume (m^3)
w	–	air swirl (rad/s)
$\varkappa$	–	dimensionless index
x	–	radial penetration of spray (m)
x_1	–	tail radial position (while injection is in progress: $x_1=0$) (m)
x_b	–	tip penetration for straight jet (m)
xtw	–	radial tip penetration of spray in swirl (m)
xx	–	axial position in jet front between 0 and xxx (m)
xxx	–	length of jet front (m)
y	–	perpendicular distance from spray axis (m)
y/b	–	normalised perpendicular position within spray
$y/b(\phi_1,x)$	–	integral limit; function of ϕ_1 and x

$y(\phi_i, x)$	-	integral llimit; perpendicular distance from spray axis, function of ϕ_i and x
$\alpha(t)$	-	time dependent function in axial concentration equation
Δt	-	injection duration (s)
ρ_a	-	density of air (kg/m^3)
ρ_{atm}	-	density of atmosphere (kg/m^3)
ρ_{az}	-	density of air in zone (kg/m^3)
ρ_s	-	density of reference fuel (840) (kg/m^3)
ρ_f	-	density of fuel (kg/m^3)
μ	-	viscosity of air (kg/m s)
ϕ_z	-	equivalence ratio (C/C_{st})

Subscripts

a	-	air
c	-	core
f	-	fuel vapour
i	-	specie
L	-	liquid
mol	-	molar
T	-	total
z	-	zone

Chapter 6 Combustion Model

6.1.a Basis of Model

Many research workers have produced models of the combustion process in diesel engines, none of which have been entirely satisfactory. This has mainly been due to the complex physical and chemical mechanisms, which are involved in the combustion of the heterogeneous fuel/air mixture, not least those associated with turbulent gas flows.

An integral jet mixing model, which may be applied to sprays in swirl, has been developed at Bath. This was based on the model by Adler & Lyn (61) as implemented by J P Packer (40) & extended by M Wilson (45). In its present form it includes variable density non-isothermal jets with phase change. Eventually, it is hoped that the combustion phase can be added to this jet mixing model.

However, recognising that a model including combustion was highly desirable in the context of this present thesis previous combustion models were studied to ascertain if they could be used as a basis for modelling the processes in the high swirl bomb. These endeavours resulted in the development of a model based on the works of Shahed, Chiu & Lyn (31,46). Before desrcibing this model in detail & examining the reasons for its choice, some of the other models will be described. The descriptions will only cover the fundamental bases of the various models.

6.1.b Single Zone Models

The simplest models are based on a homogeneous distribution of fuel & air, heat release & temperature within the chamber. Variations between these models, are primarily found in the method of describing or ascertaining the heat release rate.

In the Whitehouse & Way model (66), the combustion relations are based on the rate of preparation of fuel from droplets, ie a droplet based model. Initially the combustion is controlled by chemical kinetics, but the rate is small as the initial temperature is low. As the temperature rises the burning rate increases until reduced again by lack of prepared fuel. This mechanism of pre-mixed burning is shown in figure 6.1. The diffusion stage of the combustion is considered to be controlled by the rate at which unburnt fuel is prepared & is based on a function, which relates droplet diameter, mass of fuel & oxygen available. ie:-

$$R_p = K.M_i^{1-x} M_u^{x} P_o^{m} \qquad - 6.1$$

where R_p - Preparation rate of fuel.
M_i - Mass of injected fuel.
M_u - Mass of unburnt fuel.
P_o - Partial pressure of O_2.
x - dimensionless constant.
m - dimensionless constant.
K - empirical coefficient.

Also:-

$$M_i = n.\rho_f.\tfrac{1}{6}.\pi D_o^3 \qquad - 6.2$$

$$M_a = n.\rho_f.\tfrac{1}{6}\pi D^3 \qquad - 6.3$$

where n - No. of fuel droplets.

ρ_f - density of fuel.

D - Fuel droplet diameter.

D_o - Initial droplet diameter.

The constants x & m must be found empirically together with the constant K, which is dependent on fuel injection characteristics, air movement & combustion chamber shape.

Equation 6.1 represents a physical preparation rate of fuel for burning not only during the diffusion phase, when the physical preparation rate R_p is equal to the burning rate R_b, but also during the pre-mixed phase when R_p has to be taken in conjunction with chemical kinetics, represented by the activation energy 'act'.

Pre-mixed burning is controlled by an Arrhenius based burning rate equation, which incorporates the fuel preparation rate. ie:-

$$R_b = K' P_o \int \left(R_p - R_b\right).d\theta.e^{-act/T} \qquad - 6.4$$

where R_b - Rate of burning.

K - Empiracal coefficient.

P - Partial pressure of O .

N - Engine speed.

T - Gas temperature.

R_p - Rate of fuel preparation.

$e^{-act/T}$ - Arrhenius burning rate function.

$d\theta$ - Crank angle interval

Basically the integral $\int (R_p - R_b).d\theta$ defines the amount of fuel available for combustion.

Other less sophisticated droplet based models have been developed in references (67),(68).

Other models, which relate the heat release rate to the fuel injection rate or characteristics are described in references (69) & (70). Reference (69) is a simple model developed just to obtain pressures & rate of change of pressures.

Reference (70) is slightly more sophisticated, but produces similar end results. The heat release rate is based on functions controlled by six empirically defined parameters. These are used in equations to determine fuel evaporation rate (parameter C_1), fuel burning rate (C_2), burned mixture dilution rate (C_3), heat release rate (C_4), heat release mixture ratio (F), & Specified increment in mixture ratio Δf for each crank angle interval.

6.1.c Two zone models.

In an attempt to produce a more realistic heterogenous model, researchers have split the combustion space into two zones (71,72); ie a burning zone (fuel spray) & non burning zone. The two zone model gives a crude approximation to the temperature within the combustion zone, which may assist in the estimation of nitrous oxide (NO_x) formation by less empirical means than the single zone models.

In the model from reference (72), both the preparation rate & reaction rate equations (6.1 & 6.4) are taken from the previously described Whitehouse & Way single zone model. The main improvement over the single zone model is the distinction made between the two zones with respect to temperature & composition

6.1.d Four zone models.

An example of a four zone model is that by Baluswamy (73), which extends the two zone model, so that the jet consists of three zones instead of one, ie an unburnt fuel zone, a stoichiometric burning zone & a product air zone plus the remaining non-burning zone as shown in figure 6.2.

Combustion is again based on the Whitehouse & Way model (66). The model should give a better estimation of temperatures within the zones than the two zone models & therefore should be able to provide a better base for the realistic estimation of pollution.

6.1.e Multizone Models.

Multizone models are a logical extension of the previously described models & have been developed with the desire to more precisely describe the conditions within the combustion chamber.

A general study of the available literature has revealed two different types of zoning method. The first method separates the fuel into individual packets, which have trajectories depending on their radial position relative to the axis of the jet (74,75,76). As an example, a model produced by Meguerdichian & Watson (75) will be briefly described.

Method 1

The fuel spray is considered as a jet of two dimensional form, which is described by three empirically derived mathematical functions. Two of these are Abramovich profiles (36) for velocity & concentration which are as follows:-

$$\frac{V}{V_m}=\left(1-\left(\frac{y}{b}\right)^{1.5}\right)^2 \qquad \text{- velocity} \qquad \text{- 6.5}$$

$$\frac{C}{C_m}=\left(1-\left(\frac{y}{b}\right)^{1.5}\right) \qquad \text{- concentration} \qquad \text{- 6.6}$$

The third is a tip penetration equation for a straight jet taken from Hay & Jones (55) which is:-

$$\frac{x_t}{d_n} = 2{\cdot}28\left(\frac{V_o.t}{d_n}\right)^{1/2} \qquad - 6.7$$

The zone division pattern imposed on the jet moves with the same motion as the jet. The zones are split into concentric layers of equal fuel mass & therefore different widths ($\_Y_k$) (figure 6.3). Zones near the 'half velocity' line of the jet (eg zone 3 in figure 6.3) are thinner than the zones at the boundary or centreline, because the fuel masses are proportional to:- (from equ. 6.6)

$$\text{fuel mass } \alpha \int_{y_1}^{y_2} \left(1-\left(\frac{y}{b}\right)^{1.5}\right)\left(\frac{y}{b}\right).dy \qquad - 6.8$$

This is clearer if the integrand is plotted against the jet width as in figure 6.4.

The velocities of the zones are made equal to:-

$$V_k = [(2k-1)/10] * (\text{centreline velocity}) \qquad - 6.9$$

where k refers to the zone postion relative to the jet boundary shown in figure 6.3, the total number being five.These zone velocities approximate to the Abramovich profile. Also the half radius zones move with the same velocity as the jet tip. As the centreline zones (eg layer 5 in figure 6.3) approach the jet front, they move across to the outside of the jet and settle as slow moving zones. This motion can

be seen in figure 6.5 for the jet front. This pattern does not truly represent the complex motion at the jet front.

Burning of the zones between the rich and lean limits of inflammability is calculated from an Arrhenius type burning rate equation as follows:-

$$\frac{dR_{bz}}{dt} = k_s \rho_{az} \cdot (1 - b_z)(1 - \phi_z b_z) \exp(-E/R T_z) \qquad - 6.10$$

where k_s - steric factor
ρ_{az} - density of air in zone z
b_z - burnt fraction (mass burnt/ mass injected)
ϕ_z - equivalence ratio (C/C_{st})
E - activation energy
R - gas constant
T_z - zone temperature

Method 2

The other of method of zoning, as used by Shahed, Chiu & Lyn (31,46), has a system of expanding zones with iso-equivalence ratio boundaries. The main principles of the model are as follows:

The spray is treated as a turbulent gaseous jet & experimental correlations are used for spray tip & tail penetrations, spray widths & spray-swirl interaction.

The fuel/air distribution along the centreline of the jet is described by a time dependent hyperbolic function. ie:-

$$C_m = 1/(\alpha(t).x+1) \qquad - 6.11$$

Across the jet a normal distribution is assumed:-

$$C/C_m = 1-(y/b)^{1.5} \qquad - 6.12$$

$\alpha(t)$ is determined by using the principle of mass conservation. ie The mass of fuel distributed in the spray must equal the mass of fuel injected up to that point. In mathematical terms, this is:-

$$\int_0^t \frac{dM_i}{dt}\,dt = 2\Pi \int_{X_L}^{Xt}\int_0^{b(x)} C\rho y\,dy.dx \qquad - 6.13$$

By substituting for C & ρ, $\alpha(t)$ may be obtained by applying an iteration technique to the above equation.

At the moment of ignition, the pre-mixed vapour is split into several zones of different fuel/air ratio between the rich & lean limits of inflammability shown in figure 6.6. The mass of fuel in each zone is determined from an equation similar to the previous one. ie:-

$$M_{rz} = 2\Pi \int_{x_L}^{x_t}\int_{y(\phi_{i+1},x)}^{y(\phi_i,x)} C\rho y\,dy.dx \qquad - 6.14$$

The fuel masses in each burning zone are made equal & kept constant. The iso-equivalence ratio boundaries ($y(\phi_i,x)$, figure 6.6) are calculated from equations (6.11), (6.12) & (6.13) in conjunction with equation (6.14).

As time progresses, further jet penetration occurs & air is entrained into the core & burning zones from the air zone. This air dilutes the burning zones & allows more fuel to cross the rich limit of inflammability to create a new zone. A new zone is considered complete once it has filled to a fuel mass equal to one of the original burning zones. Thereafter new zones are created until all the fuel in the core has crossed the rich limit of inflammability.

The burning zones are considered to shift instantaneously to their equilibrium state at their respective fuel/air ratios. The combustion rate is therefore controlled by the rate at which fuel crosses the rich limit of inflammability.

6.1.f choice of Combustion Model

The choice of multizone combustion model was based on the adaptability of the combustion phase to the Bath jet mixing model (45). Two different types of combustion models were considered. The first was Meguerdichian & Watson's (75) & the second was Shahed, Chiu & Lyn's (31,46).

The method of zoning used in Meguerdichian & Watson's model is such that it defines the jet geometry. That is a change in jet profiles (eg figure 6.2 & 6.3) could not be easily accommodated by the zoning method used. It is difficult to visualise how the method of zoning described in the previous section could be applied to a jet in swirl with a distorted profile.

On the other hand the Shahed, Chiu & Lyn model could be easily applied to any deflected 2 dimensional jet. This model could also be applied to a 3 dimensional jet, but the computational difficulty would be substantially increased. The zone boundaries are mapped onto the jet in the same way as contour lines are generated on a map. The zoning method does not affect the jet mixing model except through the effects of combustion on pressure.

Therefore a model based on the Shahed, Chiu & Lyn concept was developed with the possibility that the combustion phase of the model could be adapted to the Bath jet mixing model. The model produced & described in the next section was not an exact copy of the Shahed, Chiu & Lyn model, but was based on the same principles.

6.2 Outline Description of Model

6.2.a Spray Mixing Model

The main function of the spray mixing model was to provide a realistic basis for the combustion model. Therefore there was no necessity for the spray model to be particularily sophisticated. The main requirement was a temporal & spatial description of the fuel & air within the spray. This was achieved simply by using empirical equations for spray tip penetration, width & trajectory as used in the Shahed model.

Tip penetration

The tip penetration for a fuel spray in quiescent air is based on an experimental correlation taken from Chiu, Shahed & Lyn (31), which is:-

$$x_t = F.t^{0.5} \qquad - 6.15$$

where

$$F = 6.429.\frac{d^{0.5}\left(\rho_f/\rho_d\right)^{0.4}.\left(\rho_a/\rho_{atm}\right)^{0.5}\left(P_{inj}-P_a\right)}{\left(1+\left(\rho_a/\rho_{atm}\right)\right)^{0.25}} \qquad - 6.16$$

For a fuel spray in swirl the tip penetration (x_t) in the radial direction is reduced. This is achieved by adjusting the above equation by the following relation to give the radial penetration in swirl.

$$xtw = x_t \cdot \left(1 - 0.35 \left(\frac{xtw \cdot Q_a}{Q_j \cdot d}\right)^{0.44}\right) \qquad - 6.17$$

where Q_j and Q_a are the momentum for the fuel & air respectively, and:-

$$Q_a = \rho_a \cdot xtw^2 w^2 \qquad - 6.18$$

$$Q_j = \rho_f \cdot V_o^2 \qquad - 6.19$$

Initial Jet Velocity

The initial jet velocity is based on the equation for discharge from an orifice, which is as follows:-

$$V_o = C_d \left[\frac{2(P_{inj} - P_a)}{\rho_a}\right]^{0.5} \qquad - 6.20$$

where the coefficient of discharge (C_d) is taken to be 0.62.

Spray Axis & Trajectory

For a spray in swirl, the tangential displacement of the tip from the nozzle axis is given by the following relation:-

$$S = \left[\frac{Q_a}{Q_j}\right]\left[\frac{xtw}{d}\right]^{2.217} \qquad - 6.22$$

Adler & Lyn (77) have shown that the trajectory of a transient fuel spray follows the axis of an equivalent steady state jet. Therefore the spray axis (locus of maximum fuel concentration) is assumed to correspond to the tip trajectory.

Tail Movement

At the end of injection, the spray detaches from the nozzle to form a tail. It is assummed that the tail travels at half the equivalent tip velocity in the same position ie:-

$$x_1 = \left(\tfrac{1}{2}\right)\left[F\left(t-\Delta t\right)^{0.6}\right] \qquad - 6.22$$

Where F is taken from the tip penetration equation & Δt is the injection duration. This equation is taken from reference (31), although it is not based on an experimental or theoretical analysis. ie: the behavior has been assumed to be of this form. They found that very little effect on the mixing rate was produced by adjusting the constant (1/2) in the equation from 0.25 to 1.0. Therefore it seems reasonable to use this equation until an experimental correlation may be substituted for it.

Shape of the Cross-Section within the Main Body of the Spray

For a jet injected into quiescent air, the cross-section is of circular form, with axisymetric distribution of properties. In swirling air, the axisymetric circular cross-section of the jet has been shown to distort into a horse shoe shape as

shown in figure 6.7. As it is extremely difficult to describe mathematically or to use this complex shape, the jet is simplified so that the cross-section is circular, but with a modified area.

The jet is first simplified so that the jet cross-section is a combination of two half elipses as shown in figure 6.8. The leading edge width 'b_1' has been shown experimentally (31) to be equal to the half width of an equivalent straight jet. Also the trailing edge width 'b_2' has been shown to grow faster than 'b_1' where the relationship between the two is as follows:-

$$b_2 = b_1(1+0.0016.R_e^{0.66}) \qquad - 6.23$$

where Reynolds number, R_e, is defined by:-

$$R_e = 2\Pi.\rho_a.r.w.d/\mu \qquad - 6.24$$

μ - viscosity of air
d - injector nozzle diameter
w - air swirl (rpm)
r - radius from centre
ρ_a - density of air

The leading edge width 'b_1' is obtained from Prandtl's mixing-length theory for the growth rate of a straight jet (36). That is:-

$$\frac{db}{dx} = \frac{k_\rho}{2}\left(1+\frac{\rho_a}{\rho_j}\right) \qquad - 6.24a$$

The constant 'k_p' has been shown experimentally (31) to be equal to 0.24.

The spray half width 'b_s' is obtained theoretically from Prandtl's mixing length theory to give:-

$$b_s = b_1 + 0.11x.(\rho_a/\rho_j) \qquad - 6.25$$

x - radial penetration of jet front

This two half ellipse spray cross-section is further simplified by transforming it into a circular cross-section of an equal area. This is shown in figure 6.9, where the spray width is obtained from the following equation:-

$$b = \left(b_s \frac{(b_1 + b_2)}{2}\right)^{0.5} \qquad - 6.26$$

The effect of swirl on the spray is to increase the spray radius relative to the straight jets radius and thus enhance the air entrainment rate.

Shape of Spray Front

Although Chiu, Shahed & Lyn treated the jet front as a flat blunt body, the classical bell shaped formation has been adopted. The length of the jet front is defined by the following correlation:-

$$xxx = x_* . t0/tim \qquad - 6.27$$

where:-

$$t0 = 5.2 d_n / V_o \qquad - 6.28$$

& d_n is the equivalent nozzle diameter for a dense jet & has been defined by reference (77) to be:-

$$d_n = d.\left(\rho_f/\rho_a\right)^{0.5} \qquad - 6.29$$

The jet half width as a function of axial position is described by the following equation:-

$$b_{xxx} = b_{max}(1-(xx/xxx)^{1/2})^{2/3} \qquad - 6.30$$

Concentration Distribution

The fuel/air distribution along the jet as stated earlier in equation 6.11 is described by a time dependent hyperbolic function (figure 6.11) ie:-

$$C_m = \frac{1}{(\alpha(t).x+1)} \qquad - 6.31$$

$\alpha(t)$ is a function of time only & is determined by applying the principle of mass conservation to the jet. That is the mass of fuel distributed in the spray must equal the mass of fuel injected upto that time.

Across the jet a normal distribution as found experimentally by Abramovich (36) is used. ie:-

$$C/C_m = 1-(y/b)^{1.5} \qquad - 0 \geqslant y \geqslant b \qquad - 6.32$$

This equation is extended to include the jet front, where b_x is substituted for b.

Conservation of Fuel Mass

As stated earlier, the mass of fuel injected must equal the mass of fuel distributed within the spray. In mathematical terms this is:-

$$\int_0^t \frac{dM_f}{dt}\,dt = 2\Pi \int_{x_t}^{x_t} \int_0^1 \left(b.C.\rho\frac{y}{b}\right).d\left(\frac{y}{b}\right).dx \qquad - 6.33$$

The local density within the jet is found from the combined equations of state for the fuel vapour and air to give:-

$$\rho = \frac{P_a}{\left[(1-C)R_a + CR_f\right].T} \qquad - 6.34$$

After substituting equations (6.31), (6.32) & (6.34) into equation 6.33 above, $\alpha(t)$ may be determined through numerical iteration. The numerical iteration technique used was Patterson's method (78), as implemented in NAG routine d01daf. Once $\alpha(t)$ is known, the fuel/air distribution at that instant of time may be described by equations (6.31) & (6.32).

Mixing After Fresh Air Depletion

No information could be found on jet mixing after fresh air depletion under these conditions. Therefore a model with no experimental or rigorous theoretical basis for these conditions was assumed. The assumed model does, however, reduce the mixing rate & redistributes the fuel so that the mixture moves

towards a homogeneous state. This at least, qualitively models what actually happens after fresh air depletion.

Both the jet centreline & boundary concentrations are increased, where the boundary concentration is equal to zero before fresh air depletion. Fresh air depletion is reached when the the mass of air in the fuel spray exceeds the original mass of air in the chamber. ie:-

error=(mass of air injet)-(mass in chamber) - 6.35

where:- error is positive after fresh air depletion.

To reduce the mass of air in the jet, the boundary concentration is increased (thus decreasing the jet width) by some small arbitrary amount. This gives a new error between the mass of air in the jet & the original air mass in the chamber. From this a new estimate for the boundary concentration may be determined by using the following equation:-

$$C_3 = C_1 + \left[\frac{error_1 (C_2 - C_1)}{error_1 - error_2}\right] \qquad -6.36$$

This method is illustrated in figure 6.12.

Decreasing the jet width would clearly decrease the mass of fuel within the jet, if the same

concentration profiles were used. Therefore a constant (fk) is added to the jet centreline concentration (equ. 6.31) thus:-

$$C_m=(fk) + \frac{1}{(\alpha(t)x+ 1)} \qquad - 6.37$$

The value of (fk) is obtained iteratively using a similar technique to the one used above to obtain the new jet boundary concentration.

Adjusting the concentration profiles will affect the mass of air in the jet. Therefore the jet boundary concentration C & the constant (fk), will need alternate re-adjustment until both conditions for air & fuel mass are satisfied.

6.2.b Zoning

At the point of ignition the jet is split into; a fuel rich core above the inflammability limit of the fuel; 'n' combustion zones of equal fuel mass, but decreasing equivalence ratio; an air zone which includes the fuel below the lean limit of inflammability. This is illustrated in figure 6.13a, where the initial number of burning zones is three. Properties within the zones are considered uniform & the boundaries to the zones are of constant fuel/air ratio. That is the boundaries follow iso-equivalence ratio contours.

Initially (first step), the iso-equivalence ratio boundaries of the burning zones are unknown, apart from the boundary between the rich core & the inner

burning zone, & the boundary between the air zone & the outer burning zone. These two known boundaries are set at the rich & lean equivalence ratios respectively. Furthermore, the mass of fuel in the core, the mass of fuel in the air zone & the mass of air in all the remaining zones are unknown. The fact that the air zone contains fuel is due to the choice of the value of the outer burning zone boundary equivalence ratio (figure 6.13a), usually taken as 0.5, which inevitably leaves some fuel outside in the so-called air zone.

These unknown conditions are determined from the following equations:-

$$\text{mass of fuel in zone} = 2\Pi \int_{x_i}^{x_t} \int_{\frac{y}{b}(\phi_i, x)}^{\frac{y}{b}(\phi_{i+1}, x)} b^2 C \cdot \rho\left(\frac{y}{b}\right) \cdot d\left(\frac{y}{b}\right) \cdot dx \qquad - 6.38$$

$$\text{mass of air in zone} = 2\Pi \int_{x_i}^{x_t} \int_{\frac{y}{b}(\phi_i, x)}^{\frac{y}{b}(\phi_{i+1}, x)} b^2 (1-C) \rho\left(\frac{y}{b}\right) d\left(\frac{y}{b}\right) \cdot dx \qquad - 6.39$$

C & ρ are determined from equation 6.31, 6.32 &6.34. The function $\frac{y}{b}(\phi_i, x)$ may be obtained from equation 6.31 & 6.32 to give:-

$$\frac{y}{b}(\phi_i, x) = \left(1 - C_i(\alpha(t)x + 1)\right)^{2/3} \qquad - 6.40$$

Once the mass of fuel in the air zone is determined, it remains constant, although any future modifications should allow entrainment of some of the fuel back into the burning zones.

As time progresses, further air is entrained into the jet & new zones are created as prepared fuel & air crosses the rich limit of combustion. A new zone is created once enough fuel has crossed the rich limit of combustion. Although the masses of fuel within the burning zones are fixed once they are formed, they are continuously diluted by entrained air.

At each step the unknown boundary conditions & masses are determined from equations 6.38 & 6.39. There is one difference between the initial zoning step & subsequent steps. At the first step the fuel mass in the air zone is unknown, but its upper equivalence ratio boundary is known (lean limit). In the subsequent steps the situation is reversed. ie The mass of fuel in the air zone is known, but the upper equivalence ratio of that zone is unknown.

New zones are created until the fuel rich core is consumed. This zoning process from beginning to end is illustrated in figure 6.13a, 6.13b & 6.13c.

Combustion & Chemical Equilibrium

Combustion is imposed on top of the zoning model. At each step, the burning zones are considered to instantaneously shift to their chemical equilibrium state at their respective fuel/air ratios. Thus the combustion rate is controlled by the rate of air

entrainment into the burning zones & the rate at which fuel crosses the rich limit of combustion to form a new zone. The newly created burning zone goes from an unburned state to chemical equilibrium. Subsequently it follows chemical equilibrium as the zones fuel/air ratio becomes weaker through entrained air.

As yet the pre-mixed combustion phase is not modelled. The height of the pre-mixed spike is controlled by the mass of fuel & air prepared during the ignition delay & an arbitrarily chosen step length.

Chemical equilibrium is based on 12 species, which are H_2O, H_2, OH, H, N_2, NO, N, CO_2, CO, O_2, O & Ar. The equilibrium distribution of these species can be fully described by the following seven reactions:-

1) $H_2 \rightleftharpoons 2H$
2) $O_2 \rightleftharpoons 2O$
3) $N_2 \rightleftharpoons 2N$
4) $2H_2O \rightleftharpoons 2H_2 + O_2$
5) $2H_2O \rightleftharpoons 2OH + H_2$
6) $CO_2 + H_2 \rightleftharpoons H_2O + CO$
7) $2H_2O + N_2 \rightleftharpoons 2H_2 + 2NO$

These reactions occur in both directions. Chemical equilibrium occurs when all these reactions are balanced, so that the species concentrations are constant. This balance is a function of pressure, temperature & fuel/air ratio.

When the fuel/air ratio in a zone is on the rich side, there will be a relatively large proportion of CO & OH species. These species will convert to CO_2 & H_2O, when further air is entrained into the zone, producing further chemical energy release.

The numerical procedure for the solution of these equilibrium equations was taken from reference (73). Provision has been made in this numerical procedure for the freezing out of NO fractions, so that NO pollution may be predicted.

6.2.d Heat Release

The overall energy release is derived by applying the principle of energy conservation to each zone. That is:-

Absolute change of internal energy	=	The external work done by the zone	+	Heat trans. from the zone	+	Absolute enthalpy of flow

$$\Delta U = \int_1^2 p.dv + \Delta Q + \Delta H \qquad - 6.41$$

For a burning zone going from state 1 to 2 (figure 6.14), there is: 1) an inflow of enthalpy from the entrained air $\Delta M_a h_a$, 2) an outflow of heat & work ΔQ & ΔW. This equals the change in absolute internal energy, ΔU, between states 1 & 2.

The equation of state:-

$$pV_z = mRT \qquad - 6.42$$

is used to calculate the volume changes of each individual zone. Clearly the sum of all the individual zone volumes should equal the total chamber volume. ie:-

$$\sum_{z=n}^{n} V_z = \text{Chamber Volume} \qquad - 6.43$$

This equality may be satisfied by adjusting the chamber pressure at each step.

Heat Transfer

It should be pointed out that the model being described here is for a unique constant volume bomb. Therefore the estimation of heat transfer is particularly difficult, as little work has been done in this area. At present, any heat transfer correlation will only give an indication of the heat transfer trends.

Heat transfer through radiation is particularly important in diesel engines, because of the luminescence of diffusion type combustion. For this reason, an Annand type correlation has been used, which is as follows (79):-

$$q = A\left(\frac{k}{d_b}\right) R_e^{\beta}\left(T - T_\omega\right) + C_a\left(T^4 - T_\omega{}^4\right) \qquad - 6.44$$

The coefficients A, B & C were arbitarily taken to be the same as those quoted by Annand for a four stroke diesel engine. These were as follows:-

$A = 1*10$ kg^{B}/m^{3B}

$B = 0.7$

$C_a = 3.27*10$ $W/m^{2}K^{4}$

For simplicity, the viscosity & density terms in the Reynolds equation (R_e) are based on the properties of air in the air zone. Air density is calculated from the ideal gas law & air viscosity is calculated from the following simple correlation:-

$$\mu = 4.73*10^{-7} . T^{0.645} \qquad - 6.45$$

The velocity term in the Reynolds equation is based on the swirl drum peripheral velocity. Also the thermal conductivity 'k' is calculated from the Prandtl equation for air , which is assumed to be a constant of 0.7. ie:-

$$Pr = 0.7 = \frac{\mu C_p}{k} \qquad - 6.46$$

The mean chamber gas temperature was used in the heat transfer correlation & was obtained from the following equation:-

$$T_m = \text{Mean temp.} = \frac{\sum(\text{zone masses} \times \text{zone temp})}{\sum(\text{zone masses})} \qquad - 6.47$$

The heat transfer is then distributed between the zones as a function of zone mass & temperature. ie:-

$$\text{zone H.T.} = \frac{(\text{zone mass} \times \text{zone temp.})}{\sum(\text{zone mass} \times \text{zone temp.})} \times \text{total H.T.} \qquad - 6.48$$

Thus the distribution of heat transfer is biased towards zones at a higher temperature.

Enthalpy of Flow between Zones

The enthalpies associated with the mass flows across zone boundaries needs to be accounted for in the zone energy balances. For the fuel core there are three sources of enthalpy, which are as follows:-

1) The injected fuel, whose initial enthalpy is based on liquid fuel at room temperature. ($dm_f h_f$)

2) The fuel & air used to create a new zone where the enthalpy is based on the mean core temperature. ($dm_p h_p$)

3) The influx of entrained air from the air zone. The initial enthalpy is based on the air zone temperature. ($dm_a h_{a1}$)

In mathematical terms this is:- (see figure 6.13b

$$\frac{dmha}{dt} + \frac{dm_f h_{f1}}{dt} - \frac{dm_p h_{fc}}{dt} \qquad - 6.49$$

For the air & burning zones where the fuel masses remain constant, only the enthalpy associated with the entrained air needs to be taken account of. Thus for the burning zones the enthalpy of flow is:-

$$\frac{dm_{a}h_{ai}}{dt} \qquad - 6.51$$

Where the initial enthalpy is based on the air zone temperature. For the air zone the enthalpy of flow is:-

$$- \frac{dm_{at}h_{ai}}{dt} \qquad - 6.51$$

Where the mass of air, dm_{aT}, is equal to the sum of all the masses entrained into the other zones.

Gas Properties

The gas properties for any combination of the 12 species of combustion, including air, are worked out by the subroutine 'prop'. This program is based on work from Benson RS (80), where the thermodynamic properties, calculated from spectroscopic data, have been fitted. For the enthalpy of any particular specie, the polynomial is of the following form:-

$$H_i = Mol_i\left[R_{mol}\sum_{k=1}^{k=5}\left(a_{i,k}.T^k\right) + ho_i\right] \qquad (J) - 6.52$$

where H_i - Total enthalpy of specie.

Mol_i - No. of moles of specie i

R_{mol} - Universal gas const.

$a_{i,k}$ - Coefficient k for specie i.

T - Temperature (K)

hoi - Enthalpy of specie i at absolute zero.

The total enthalpy for a combination of different species is the sum of the polynomials. ie:-

$$H=\sum_{i=1}^{i=N} Mol_i\left(R_{mol}\sum_{k=1}^{5} a_{i,k}T^k + hoi\right) \qquad J - 6.53$$

Similarly the specific heat at constant pressure may be derived from the differential thus:-

$$C_{pmol}=\frac{1}{Mol}\left[\frac{dH}{dT}\right] \qquad - 6.54$$

$$C_{pmol}=\frac{R_{mol}}{Mol}\left[\sum_{K=1}^{5}\sum_{k}\left(Mol_i . a_{i,k}\right)T^{k-1}\right] \qquad - 6.55$$

J/kgmol K

Briefly the polynomial for absolute internal energy is:-

$$U=R_{mol}\left[\sum_{k=1}^{5}\sum_{i=1}^{N} Mol.\, a_{i,k}T^k-\sum_{i=1}^{N} Mol_i\, T\right]_N+\sum_{i=1}^{N} Mol_i\, hoi \qquad - 6.56$$

J

& the specific heat at constant volume is:-

$$C_{Vmol} = C_{\rho mol} - R_{mol} \qquad - 6.57$$

J/kgmol K

The coefficients, $a_{i,k}$ for the polynomials are tabulated in table 6.1.

Fuel properties

Fuel properties were based on the compound n-Tridecane with the chemical formula $C_{13}H_{28}$. Gas properties for the fuel in vapour form are also calculated by the subroutine 'prop'. The above polynomials are used, but the coefficients were obtained from a curve fit of the TRC (Thermodynamic Research Centre) Hydrocarbon Projects (81) tabulated data. This curve fit is shown in figure 6.15 & the polynomial coefficients are also tabulated in table 6.1.

The initial enthalpy of the fuel in liquid form was also based on the data from the TRC Hydrocarbon Project.

6.3 Computing Scheme

The computing scheme reflects the path followed in its development. Jet mixing is modelled by the main program whereas the combustion phase, which was modelled separately, is a subprogram to this. In total there are 6 subroutine subprograms, one of which is NAG routine d01daf (82), & six function subprograms. All six function programs are used by the NAG routine. The computing network for the main program & the 12 subprograms is illustrated in figure 6.16. The program listings may be obtained from reference (83).

6.3.a Main Program: Jet mixing (figure 6.17)

The simplicity of this empirically based model is clearly demonstrated in the flow diagram shown in figure 6.17. Apart from the radial tip & tail penetration the jet description involves sequential solution of straightforward algebraic equations.

A Newton type method is used for the determination of the radial tip penetration in swirl. That is:-

$$xtw_{NEW} = xtw_{OLD} - \frac{f(xtw)}{f'(xtw)} \qquad - 6.58$$

where f(xtw) comes from equations 6.15 & 6.16. ie:-

$$f(xtw) = x_* \left(1 - 0.35 \left(\frac{xtw^3 \cdot \rho_a \cdot w^2}{Q_j \cdot d} \right)^{0.44} \right) - xtw \qquad - 6.59$$

The differential f'(xtw) is as follows:-

$$f'(xtw) = -0.462 . x_{st} . xtw^{0.32} \left(\frac{\rho_a . w^2}{Q_j d} \right)^{0.44} - 1.0 \qquad - 6.60$$

At each step the first estimate for xtw is taken as the tip penetration (x_{st}) for a straight jet. The method is also used for the determination of the tail penetration.

Alcalc (figure 6.18)

This subroutine, which is called by the main program, is used to determine the function $\alpha(t)$ in equation 6.31. $\alpha(t)$ is a time dependent function & is used in the axial concentration profile equation 6.31.

Again a Newton type method is used to find $\alpha(t)$, although the differential function, f'(x), is not determined directly. From equation 6.33 the function f(x) is:-

$$f(x) = 2\pi \int_{x_t}^{x_t} \int_{0}^{l} b^2 C \rho \left(\frac{v}{b}\right) d\left(\frac{v}{b}\right) . dx - \int_{0}^{t} \frac{dMf}{dt} . dt \qquad - 6.61$$

f(x)=(mass of fuel in jet)-(mass injected)

The qualitative relation of this function with α is plotted in figure 6.19. By determining the value of $f_1(\alpha)$ & $f_2(\alpha)$ for two similar values of α_1 & α_2, the approximate value $f'(\alpha)$ may be determined. That is:-

$$f'(\alpha) = \frac{f_1 - f_2}{\alpha_1 \quad \alpha_2} \qquad - 6.62$$

Thus a better estimate for α would be:-

$$\alpha_3 = \alpha_1 - f_1\left(\frac{\alpha_2 - \alpha_1}{f_1 - f_2}\right) \qquad - 6.63$$

$$\alpha_3 = \left(\frac{\alpha_2 f_1 - \alpha_1 f_2}{f_1 - f_2}\right) \qquad - 6.64$$

This is repeated as shown by figure 6.19, until the function $f(\alpha)$ is close enough to zero:-

The integral from equation 6.33:-

$$\int_{x_1}^{x_t} \int_{0}^{y(x)} b^2 C\rho\left(\frac{r}{b}\right) d\left(\frac{r}{b}\right) . dx \qquad - 6.33$$

is solved by NAG routine d01daf & the mass injected is calculated by the main program from the fuel injection parameters.

NAG routine d01daf (82)

As stated earlier this is a standard routine implemented on multics & therefore no listing or flow chart has been produced.

Its function is to evaluate a double integral to a specified accuracy, by repeated application of the method described by Patterson (78). The integral is of the form:-

$$I=\int_{a}^{b}\int_{f_1(x)}^{f_2(x)} f(x,y).dy.dx \qquad - 6.65$$

Where a and b are constants & $f_1(x)$ & $f_2(x)$ are fuctions of the variable x. These are supplied by the user along with the integrand f(x,y). The external functions $f_1(x)$ & $f_2(x)$ correspond to the normalised functions P1 & P2 or P3 & P4 as shown in figure 6.20. The jet tip, 'xt', & the jet back, 'xl', replace the constants a & b respectively. Function subprogram fa, evaluates the integrand f(x,y) at any point (x,y).

On exit from d01daf, the estimate of the integral (equ. 6.33) is contained in the variable 'an', returned by d01daf.

Function Subprogram fa (figure 6.21)

This function evaluates $b=c\rho(y/b)$ at location x & (y/b) within the fuel jet & is used by NAG routine d01daf.

The jet half widths are only calculated at discrete x locations as shown in figure 6.22. Thus any half width between these locations has to be determined by interpolation.

For example, if NAG routine d01daf requires the value of the function $b=c\,(y/b)$ at location (x,y) & the x is between known locations xs(i-1) & xs(i). Then the half width at x will be as follows:-

$$b=b(i-1)+\left[\frac{b(i)-b(i-1)(x-xs(i-1))}{xs(i)-xs(i-1)}\right] \qquad - 6.66$$

Section A in the flow chart (figure 6.21) illustrates how the two xs(i) points, which immediatly abound location x are determined.

This function will also evaluate the integrand $b=(1-c)\rho(y/b)$, when the mass of air in a zone etc. is being determined.

Function Subprograms P1, P2, P3, & P4 (figure 6.23)

These functions are used by subroutine d01daf as the upper & lower limits of the inner integral (equ. 6.31). Functions P1 & P2 are constant & define the axis & boundary of the fuel jet respectively (figure 6.20). As the jet boundaries are normalised, P1 & P2 equal 0.0 & 1.0 respectively.

P3 & P4 define the outer & inner boundaries of a zone respectively at constant equivalence ratios (figure 6.20). Thus from equations 6.31 & 6.32:-

$$\text{function P4}=\frac{y_i}{b}\left(\phi_i,x\right)=\left[1-c_i\left(\alpha.x+1\right)\right]^{2/3} \qquad - 6.67$$

& function P3= $\frac{y_2}{b}\left(\phi_2, x\right) = \left[1 - c_{i-1}\left(\alpha x + 1\right)\right]^{2/3}$ - 6.68

where c(i) is the fuel concentration at boundary 'i'. Figure 6.23 shows the flowchart for function P4

Subroutine Zonc (figure 6.24)

This subroutine divides the jet, defined by the main program, into its zones at the point of ignition & calculates the resulting heat release.

On the first call to zonc, the pre-ignition zones & conditions are set up as illustrated in the flow diagram in sections A & B. The number of zones is controlled by a small section at the start of the program as illustrated by section F in the flow chart. This is followed by section G which uses the same Newton type iteration technique as used in the subroutine alcalc, to obtain the zone boundary equivalence ratio's. Section H defines the changes of masses & mols within each zone & the flow of enthalpy across zone boundaries. Gas properties, heat transfer & chemical equilibrium are dealt with in the following section I.

A double iteration loop is used to satisfy the energy conservation equation & volume constraint. Both these loops start at point C in the flow diagram & finish at points D & E respectively.

A new estimate for the zone temperature is made, by dividing the error from the energy conservation equation for each zone by the heat capacity for each zone. That is:-

$$T_{new} = T_{old} + \frac{\text{zone energy error}}{C_{pbz} \cdot Mol_z} \qquad - 6.69$$

where C_{pbz} is the molar specific heat capacity at constant pressure.

The chamber pressure is updated by using the ideal gas laws. ie:-

$$P_{new} = P_{old}\left(\frac{\sum \text{zone vol.}}{\text{Chamber vol.}}\right)^{\gamma} \qquad - 6.70$$

When both these conditions are satisfied, the fuel mass burnt & burning rate are calculated.

Subroutine Subprogram Prop. (figure 6.25)

In subroutine prop, the equation for enthalpy, internal energy & both specific heats (eqn's. 6.53 to 6.57) have been split up into common parts. eg. The expressions:-

$$\sum_{i=1}^{13} Mol_i hoi \quad \& \quad \left[\sum_{k=1}^{5}\sum_{i=1}^{13}\left(Mol_i a_{i,k}\right) T^k\right] \qquad - 6.71$$

are common to both equations 6.53 & 6.56 (enthalpy &

internal energy). Therefore these expressions need only be evaluated once in the determination of both enthalpy & internal energy.

Although this makes the program more complex, it does reduce the running time.

Function Subprogram rmf (figure 6.26)

This is a fairly straight forward function, which evaluates the mass of fuel (or air) within the fuel jet or a zone's boundaries. If the flag 'iair' equals 1 in the calling program, than the mass of air is determined. The mass required is partly determined by the NAG routine d01daf.

Subroutine Subprogram Pareq

This is based on a program written by Baluswamy (73) which evaluates the chemical equilibrium (see section 6.2.b) for 12 species.

Subroutine Subprogram Confin

This subroutine is called from zonc when the mass of air in the jet exceeds the mass of air in the chamber. It increases the jet boundary concentration from zero (thus decreasing the jet width) & the overall concentration profiles. These are adjusted until the mass of air in the jet equals the original air chamber mass & the mass of fuel in the jet equals the mass injected. The technique used is based on the description given in the section on mixing after fresh air depletion.

SPECIES	a	b	c	d	e	hoi (kJ/kgmol)
H_2	3.43328	-8.18100E-6	9.66990E-8	-1.44392E-11	0.00000	0.00000
CO	3.31700	3.76970E-4	-3.22080E-8	-2.19450E-12	0.00000	-1.13950E5
N_2	3.34415	2.94260E-4	1.95300E-9	-6.57470E-12	0.00000	0.00000
NO	3.50174	2.99380E-4	-9.58800E-9	-4.90360E-12	0.00000	8.99684E4
CO_2	3.09590	2.73114E-3	-7.88542 .E-7	8.66002E-11	0.00000	-3.93640E5
O	3.25304	6.52350E-4	-1.49524E-7	1.53897E-11	0.00000	0.00000
H_2O	3.74292	5.65590E-4	1.00187E-8	-1.81802E-11	0.00000	-2.39225E5
O	2.76403	-2.51427E-4	1.00187E-7	-1.38670E-11	0.00000	2.47071E5
N	2.49906	2.87441E-6	-2.44816E-9	6.15151E-13	0.00000	4.71650E5
H	2.50000	0.00000	0.00000	0.00000	0.00000	2.16239E5
A	2.50000	0.00000	0.00000	0.00000	0.00000	0.00000
OH	3.26140	2.9859E-4	-2.37450E-8	0.45660E-11	0.00000	3.86762E4
$C_{13}H_{28}$	33.498	-6.24300E-2	2.22240E-4	-2.0731E-7	6.7564E-11	-2.5213E5

table 6.1 Polynomial coefficients for thermodynamic property equations. Temperature range from 500 K to 3000 K. $C_{13}H_{28}$ temperature range from 200 K to 1000 K. (73)(81)

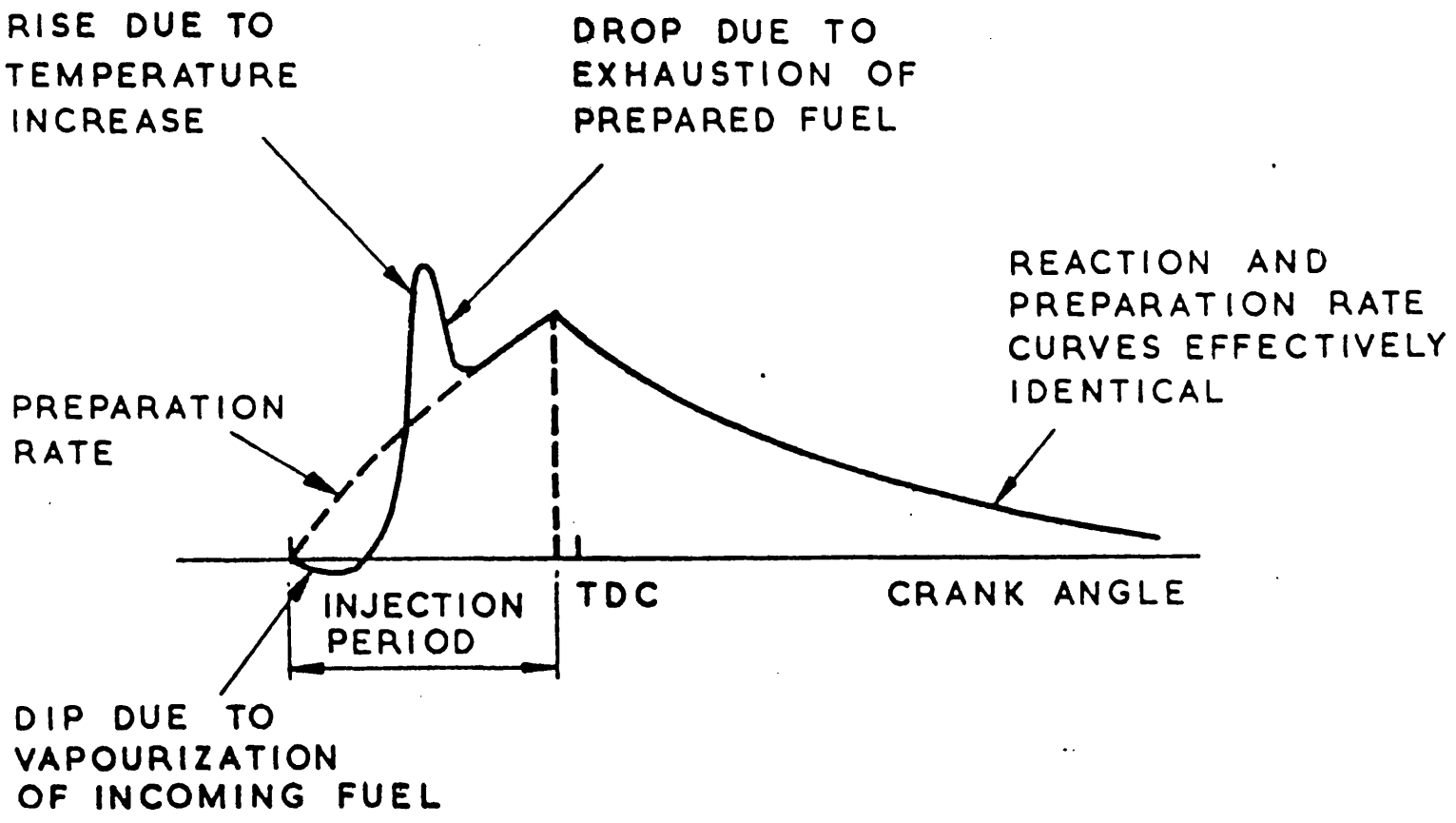

Figure 6.1 representation of pre-mixed burning. Taken from reference (66).

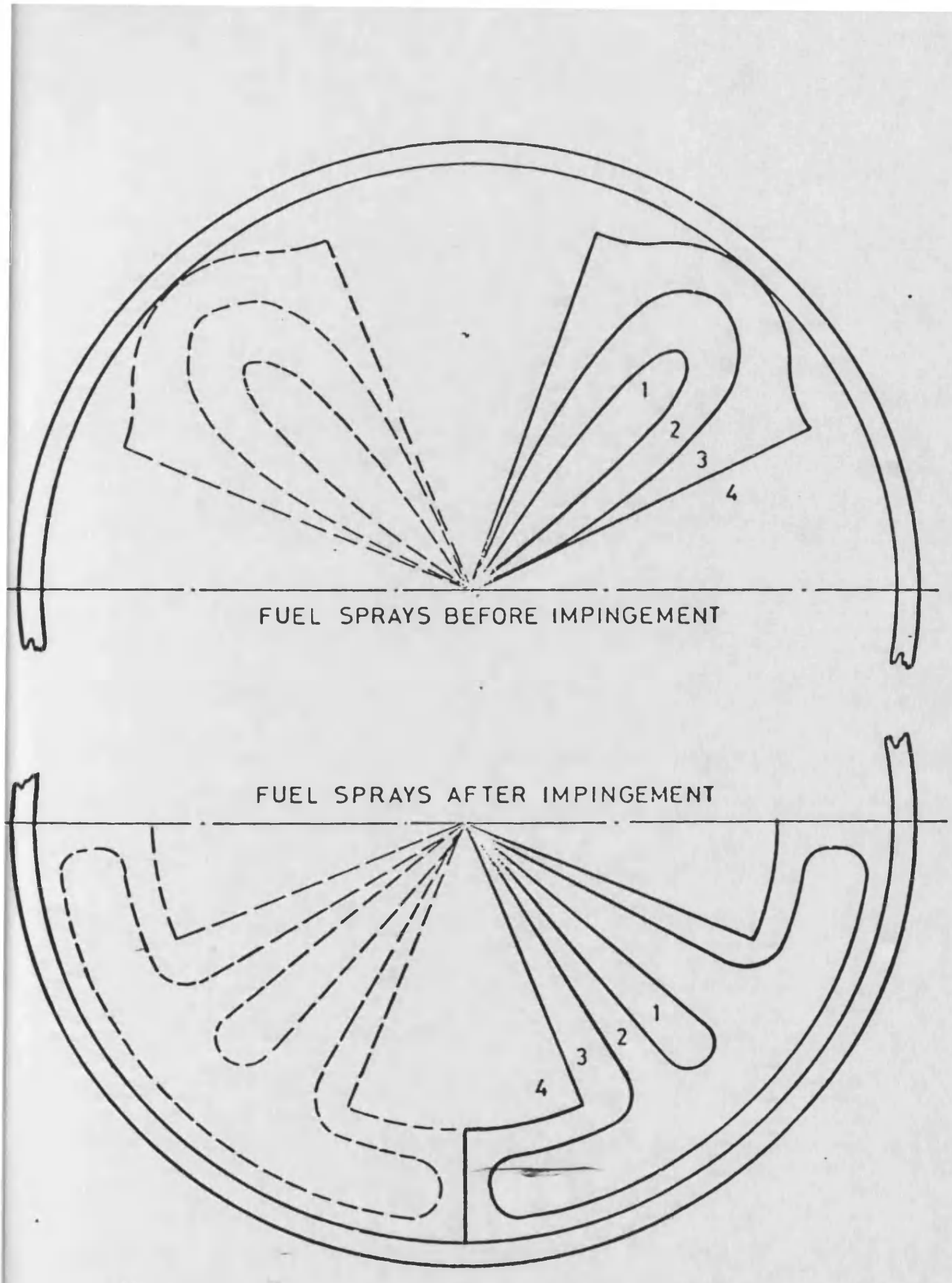

Figure 6.2 Four zone model by Baluswamy (73).

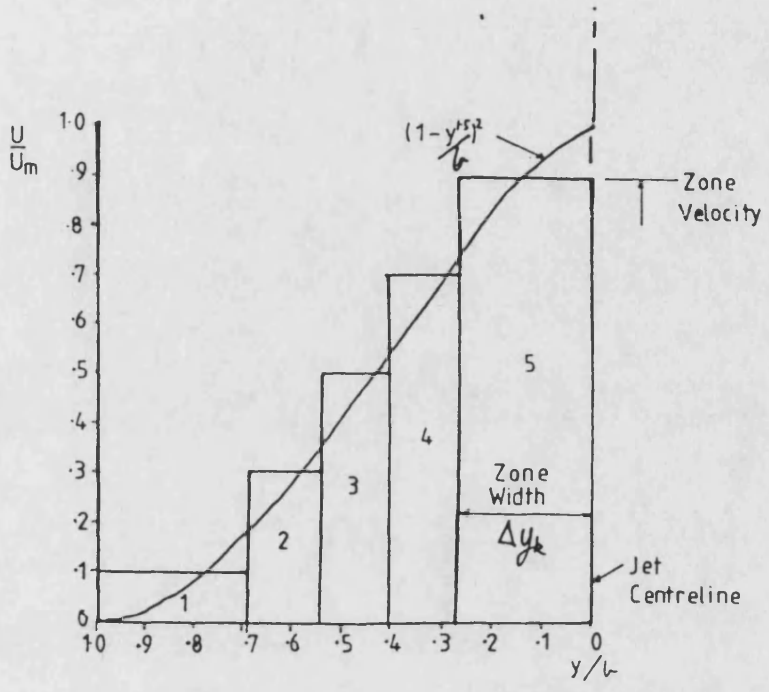

Figure 6.3 Zone division method in multi-zone model by Meguerdichian (75).

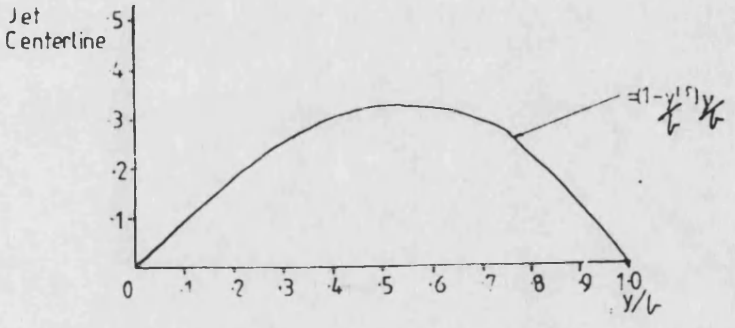

Figure 6.4 Fuel mass integrand plot for equation 6.8.

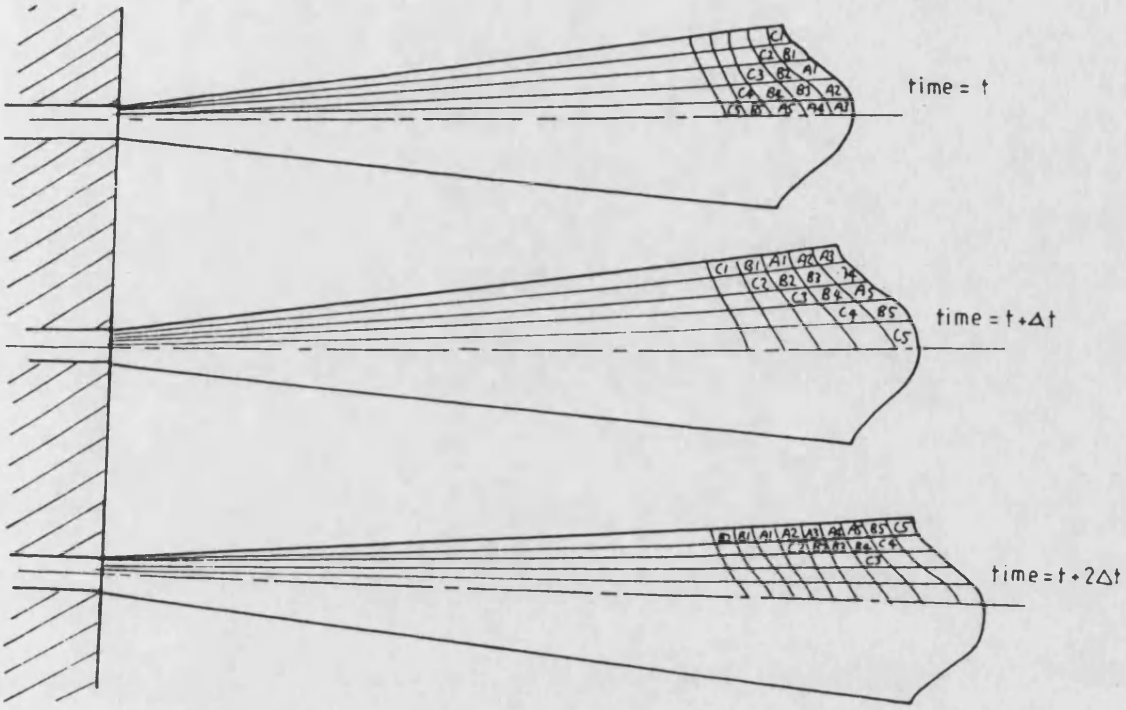

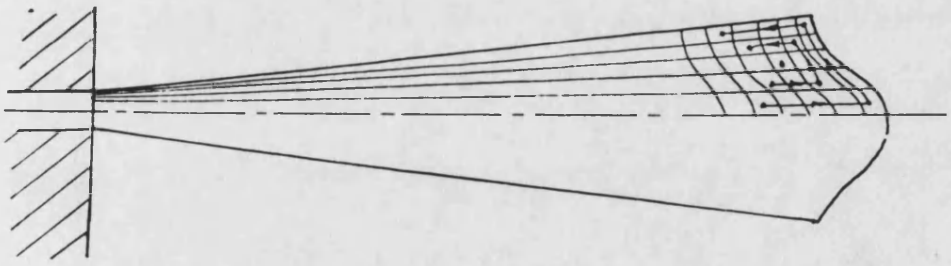

Figure 6.5 Zone motion in Mequerdichian model (75).

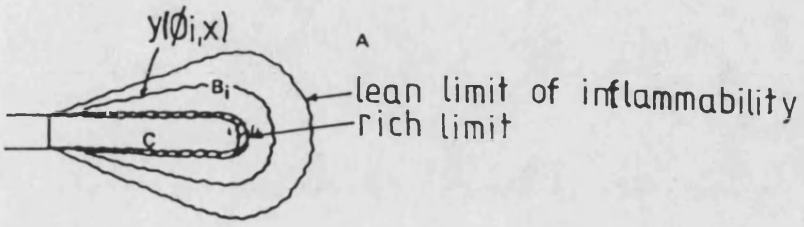

FRAME 1

INCIPIENT IGNITION IN 'n' ZONES

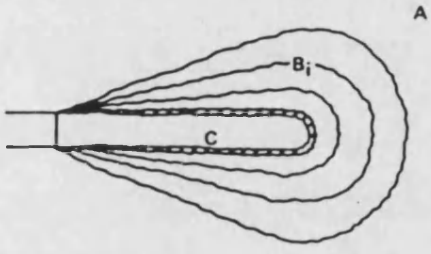

FRAME 2

CONTINUOUS ENTRAINMENT & MIXTURE PREPARATION

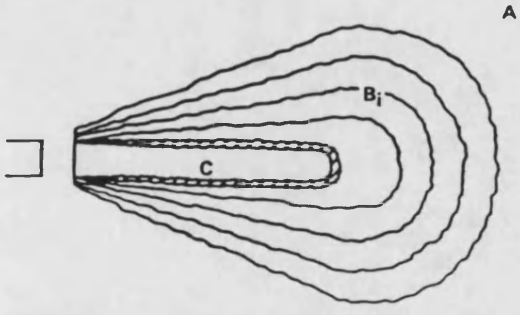

FRAME 3

END OF INJECTION, CONTINUOUS MIXING

Figure 6.6 Zoning method, evolution & air entrainment for model of Shahed, Chiu & Lyn (31.46).

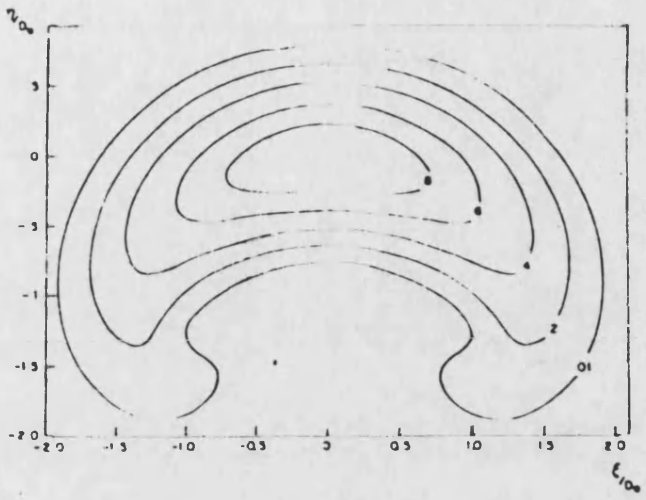

Figure 6.7 Cross-section of distorted jet in swirl (horseshoe shape) with lines of constant velocity.

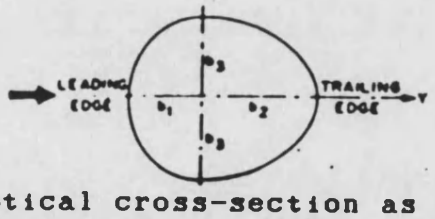

Figure 6.8 Eliptical cross-section as simplification of distorted jet (31).

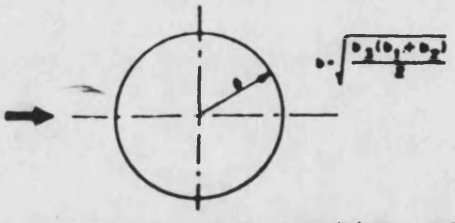

Figure 6.9 Axi-symmetric cross-section as simplification of figure 6.8 above (31).

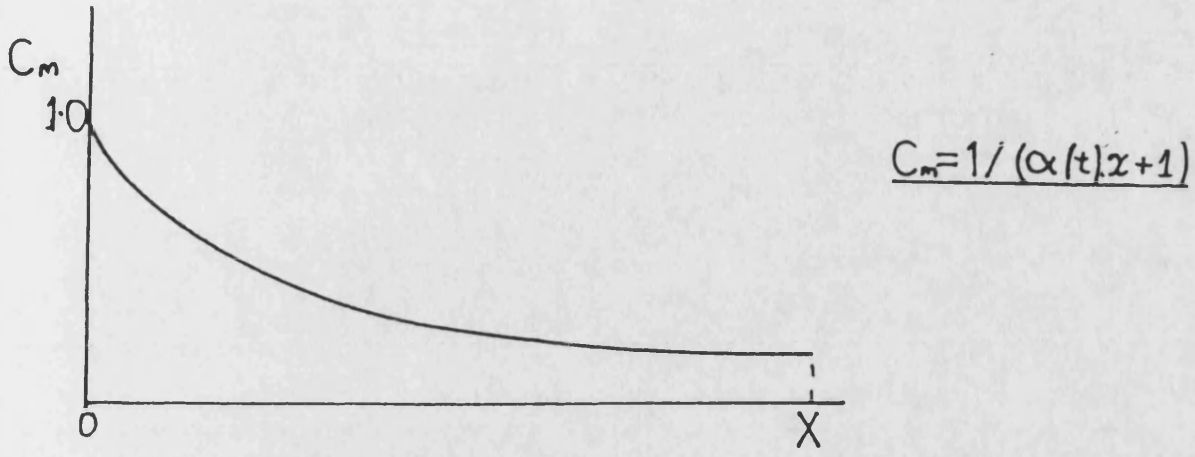

Figure 6.11 Fuel/air distribution along jet represented by hyperbolic function.

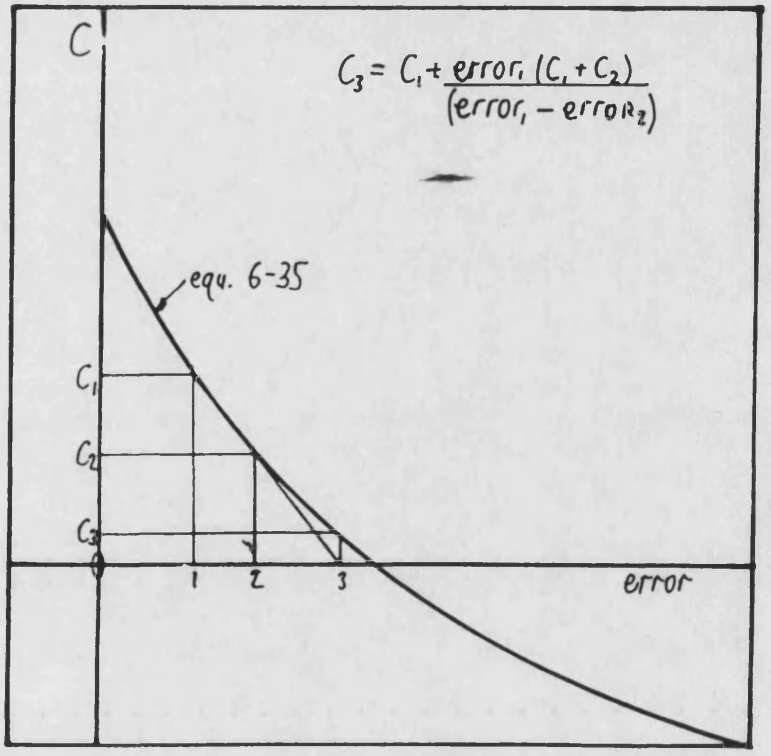

Figure 6.12 Newton type iteration technique used to find jet boundary equivalence ratio after fresh air depletion.

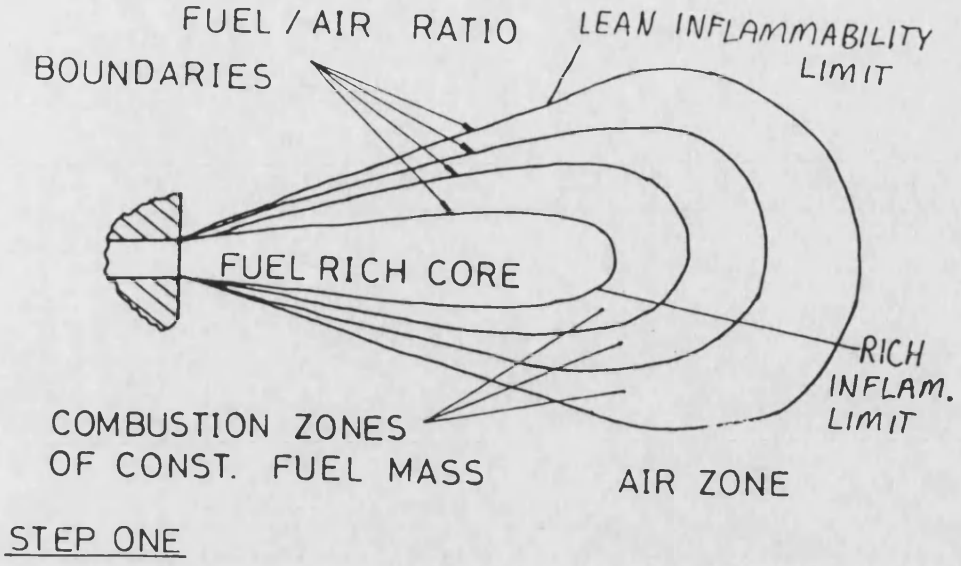

Figure 6.13a Initial zoning method for three burning zones.

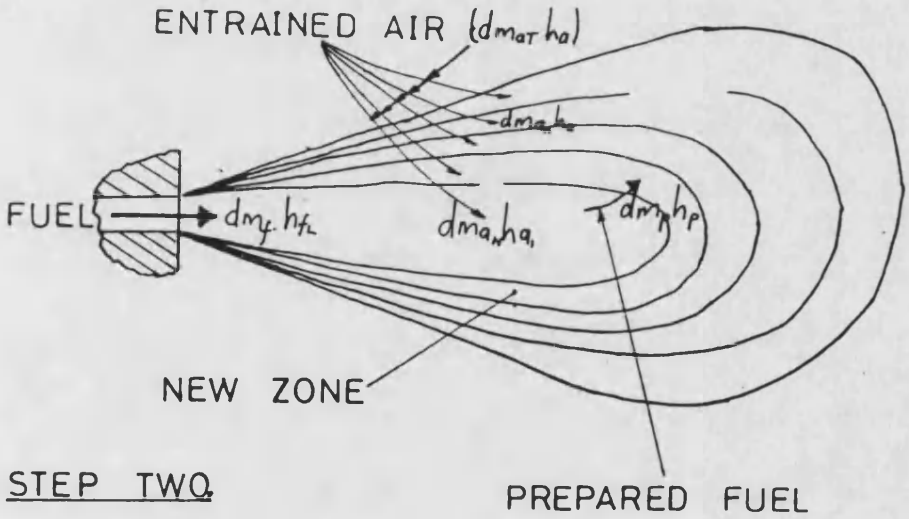

Figure 6.13b New zone created from prepared fuel & entrained air at next step.

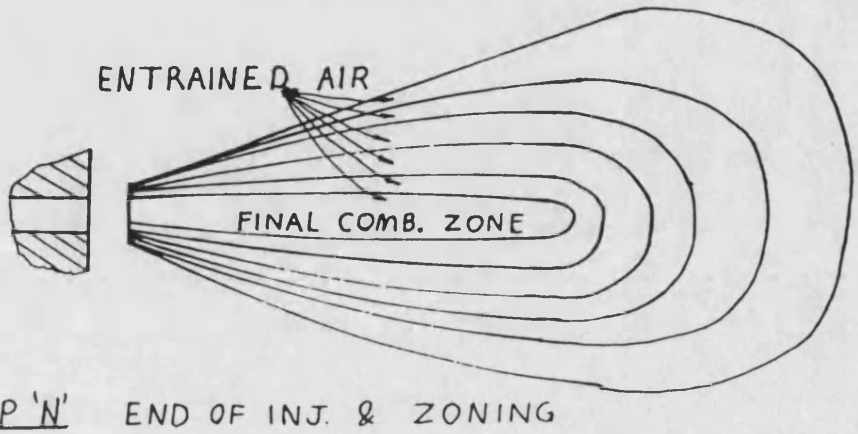

Figure 6.13c Final zone after end of injection (fuel rich core consummed).

The change of absolute internal energy	=	The external work done by zone	+	Heat transfer from the zone	+	Absolute enthalpy of flow
ΔU		$\int p.dv$		ΔQ		ΔH

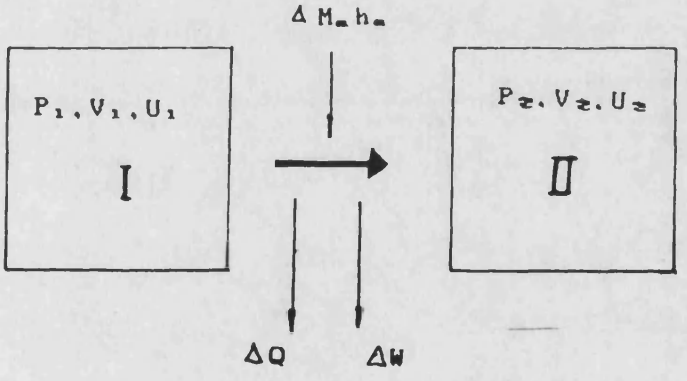

Figure 6.14 Energy balence for zone going from state I to state II.

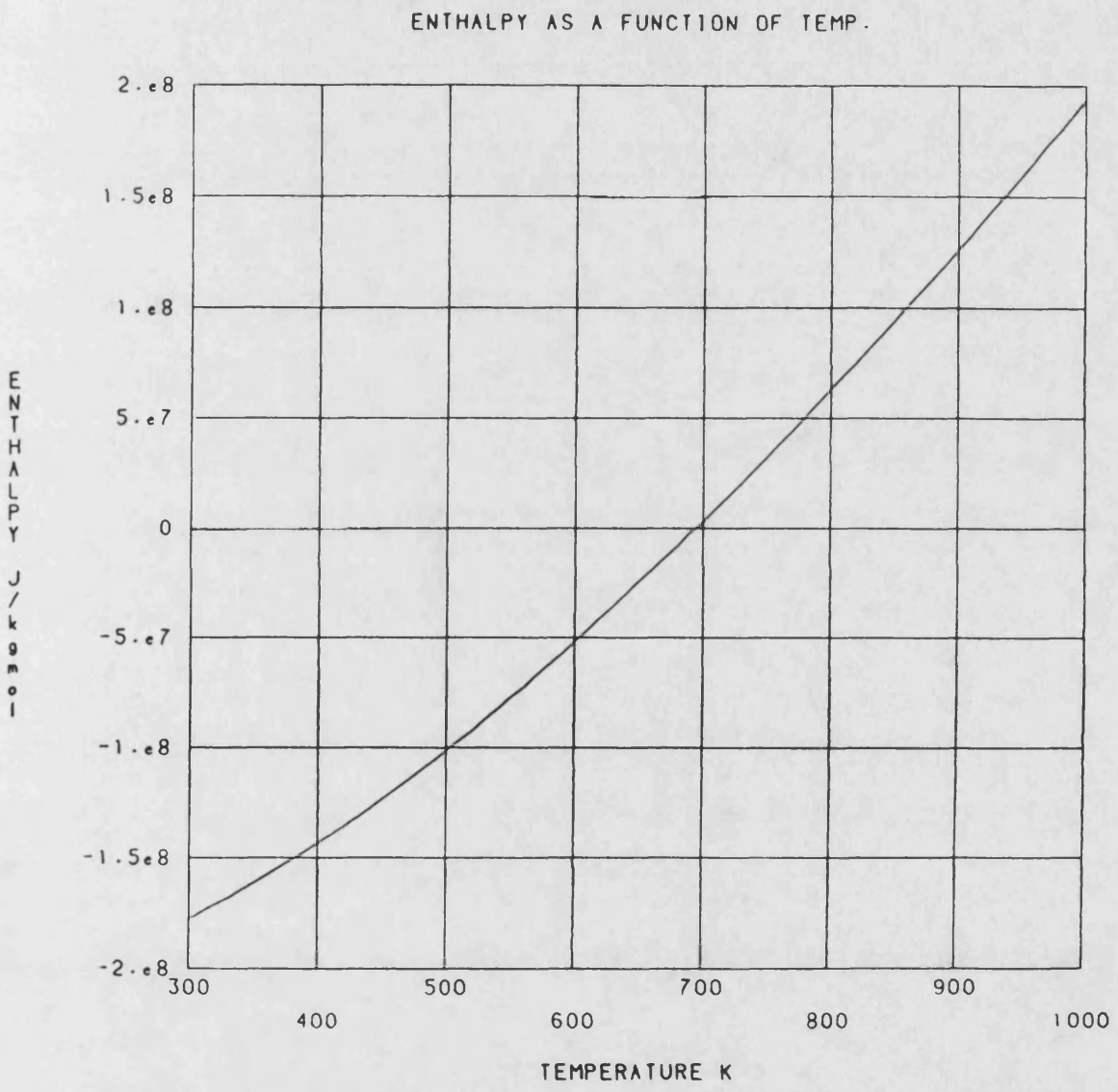

Figure 6.15 Enthalpy of $C_{13}H_{28}$ as function of temperature (81).

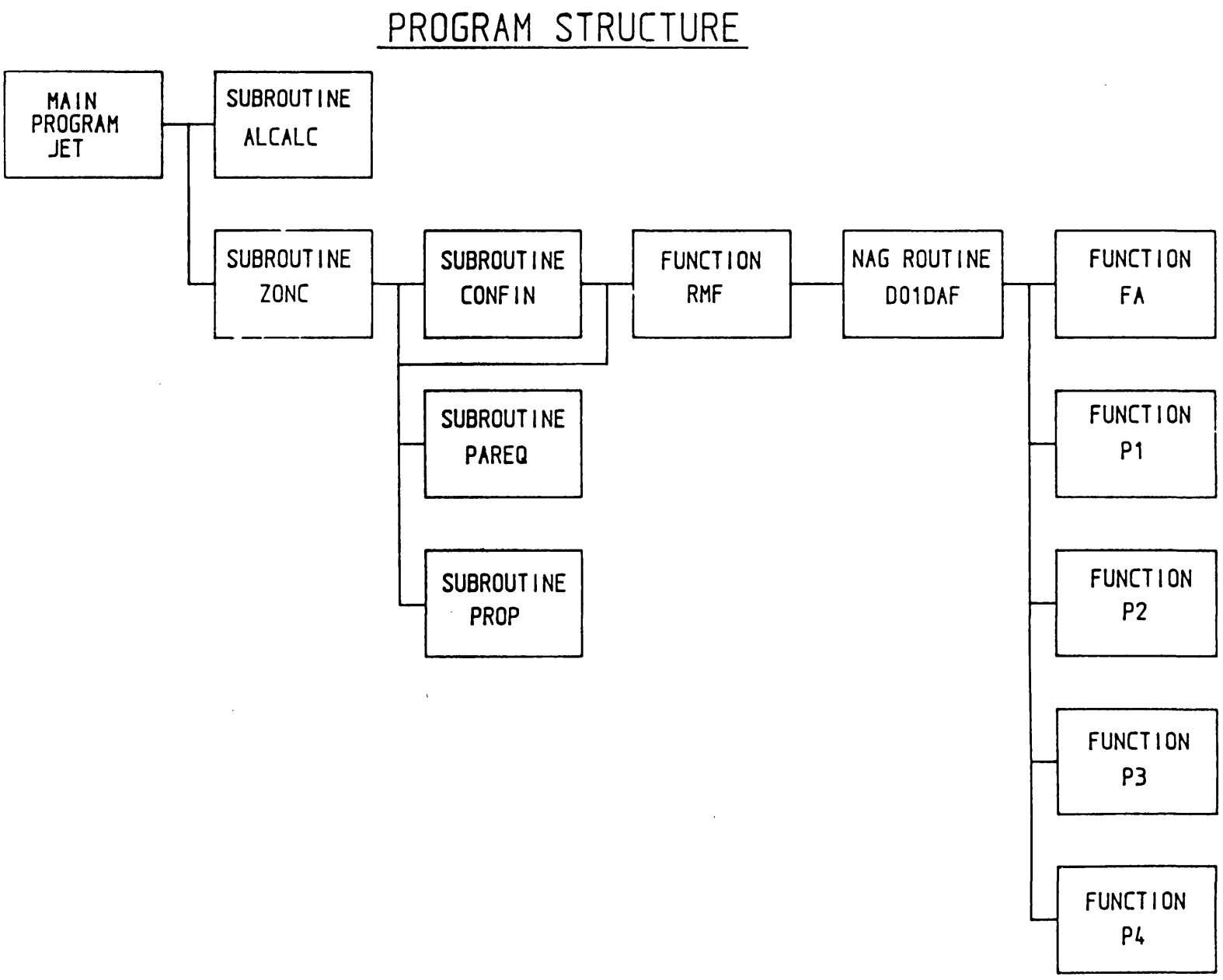

Figure 6.16 Program structure for combustion program

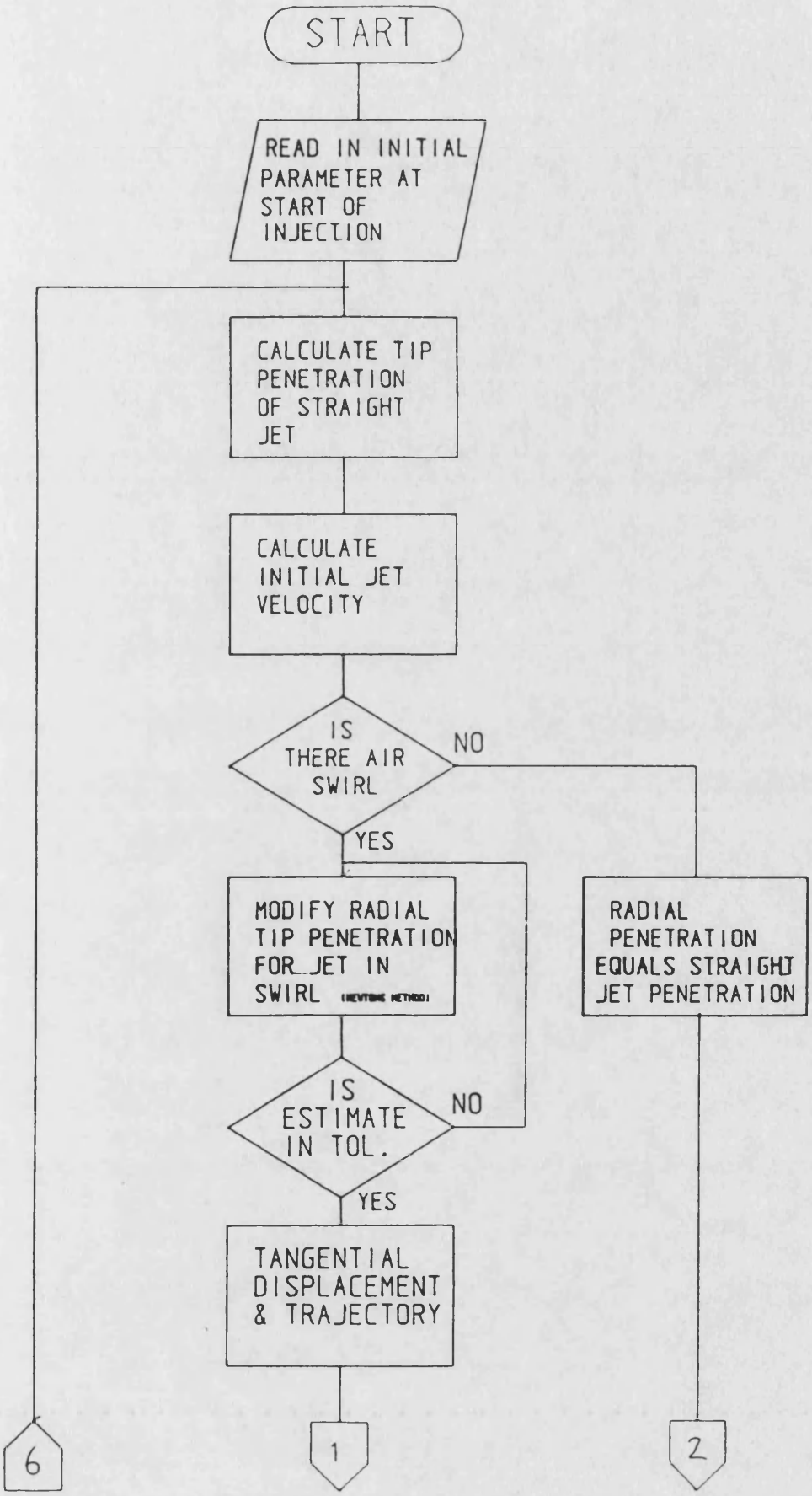

Figure 6.17 Flow diagram for main Jet program.

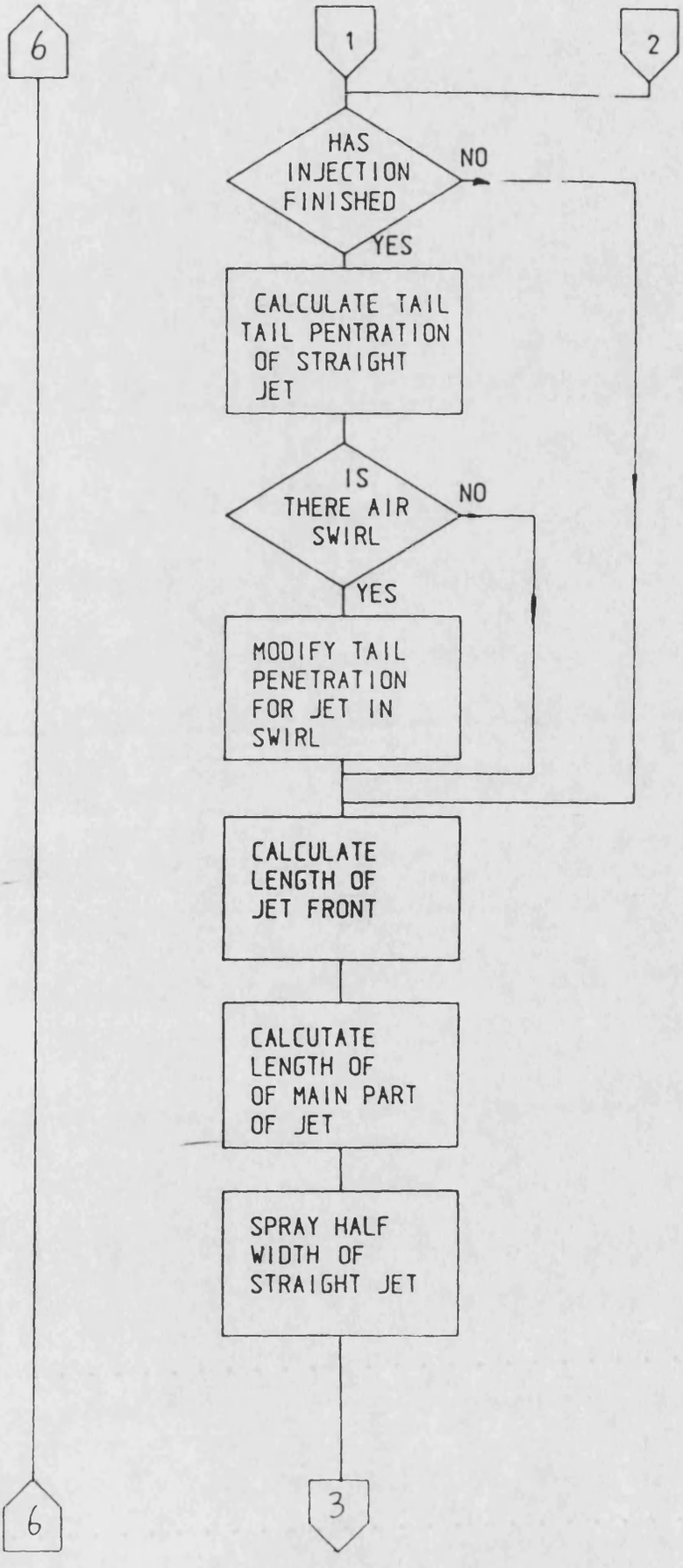

Figure 6.17 Flow diagram for main Jet program. (cont.)

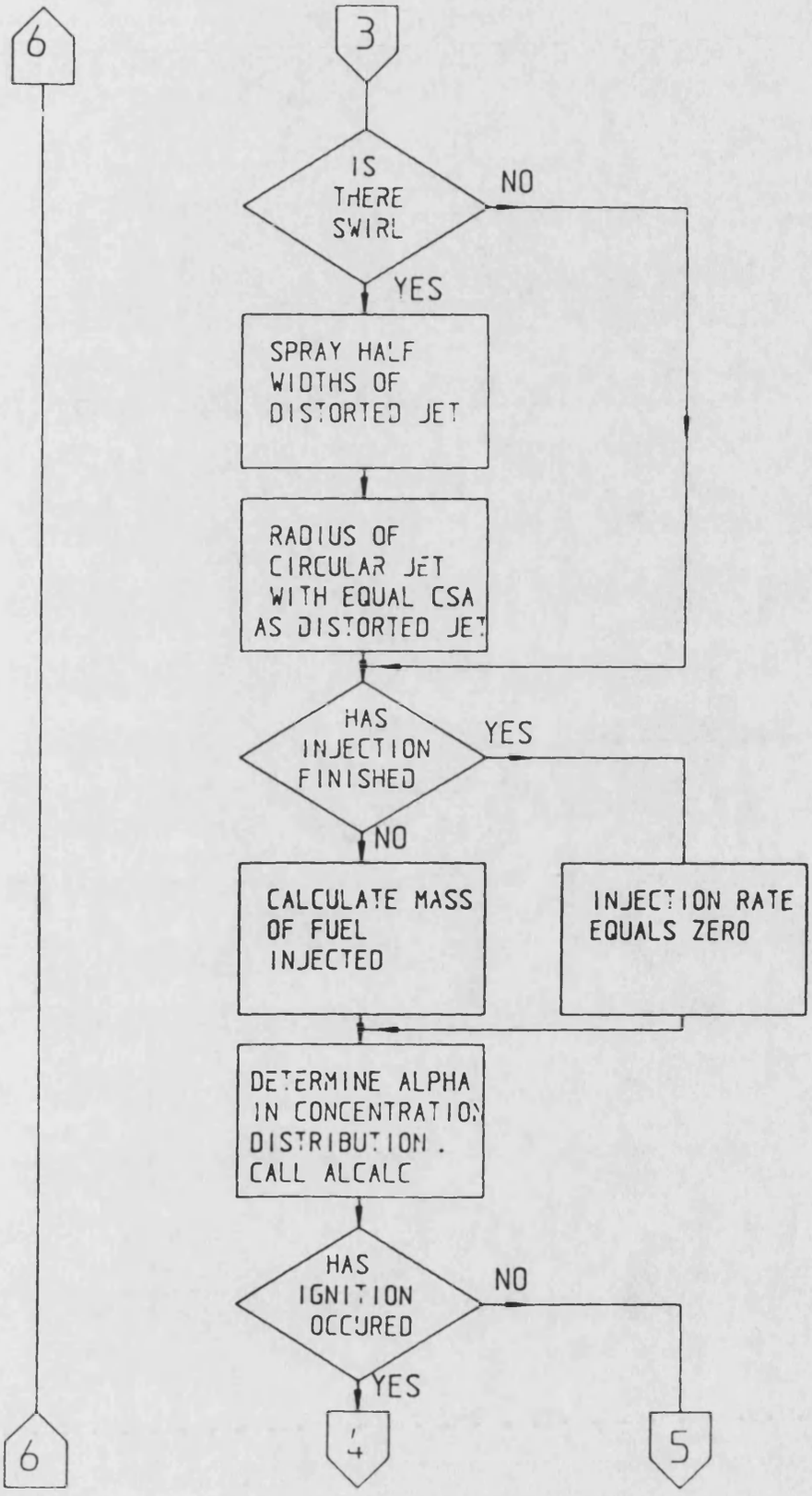

Figure 6.17 Flow diagram for main Jet program. (cont.)

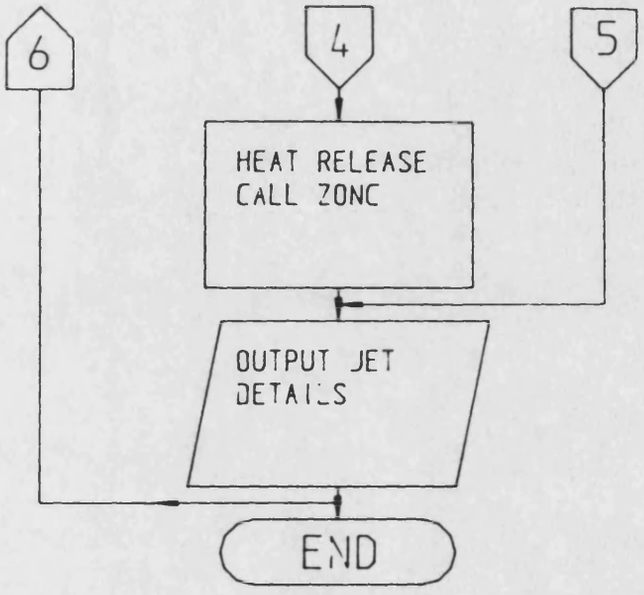

Figure 6.17 Flow diagram for main Jet program. (cont.)

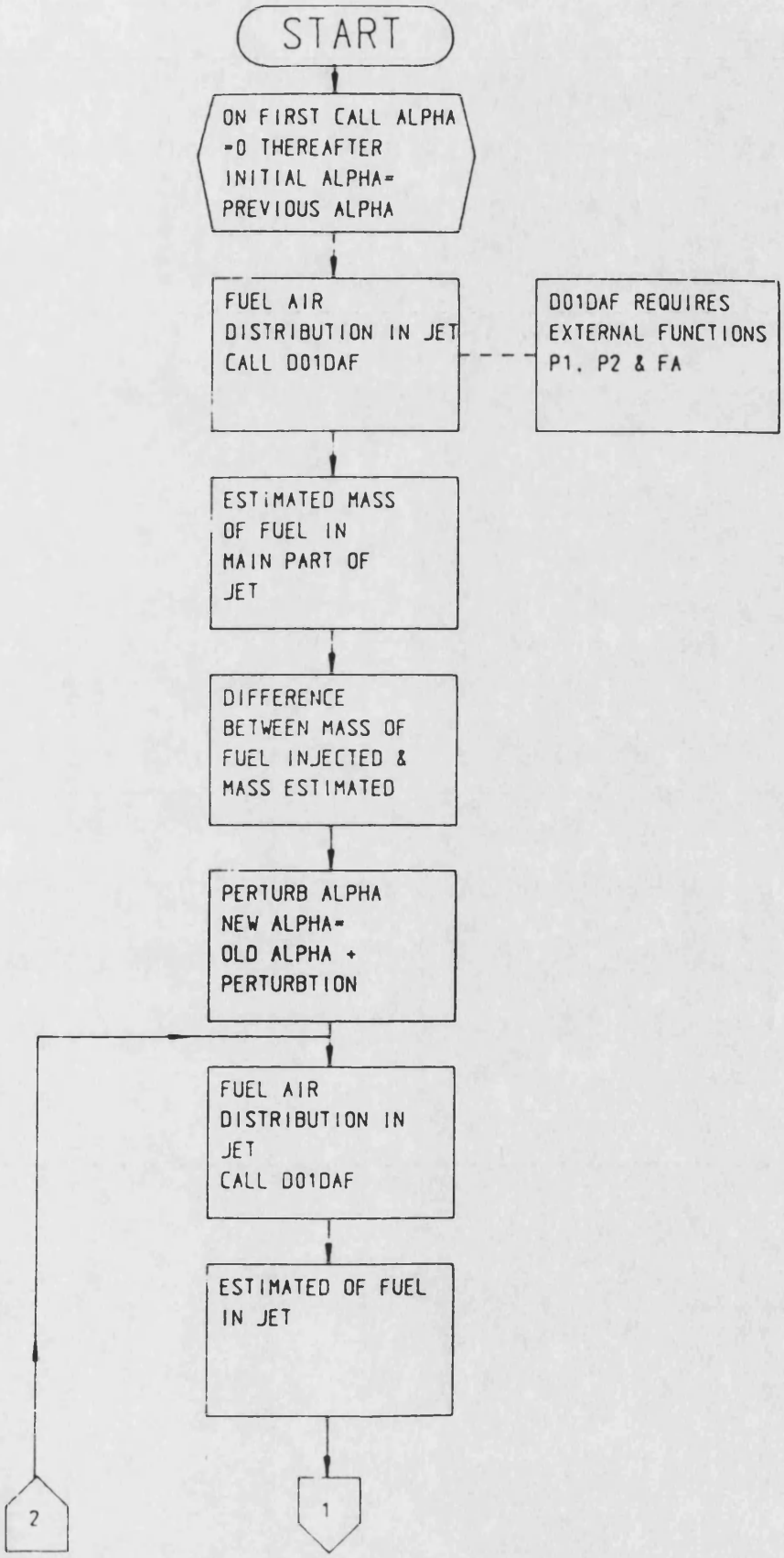

Figure 6.18 Flow diagram for subroutine Alcalc.

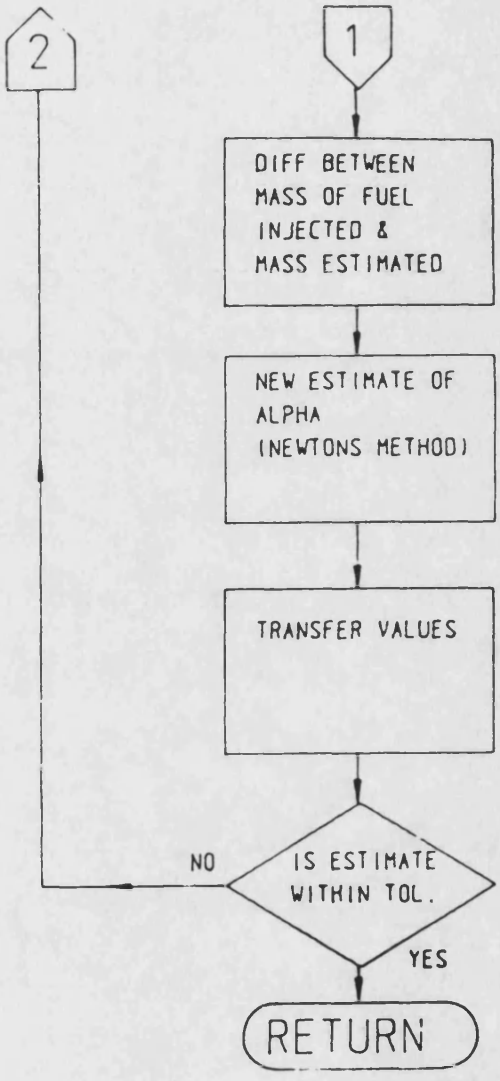

Figure 6.18 Flow diagram for subroutine Alcalc. (cont.)

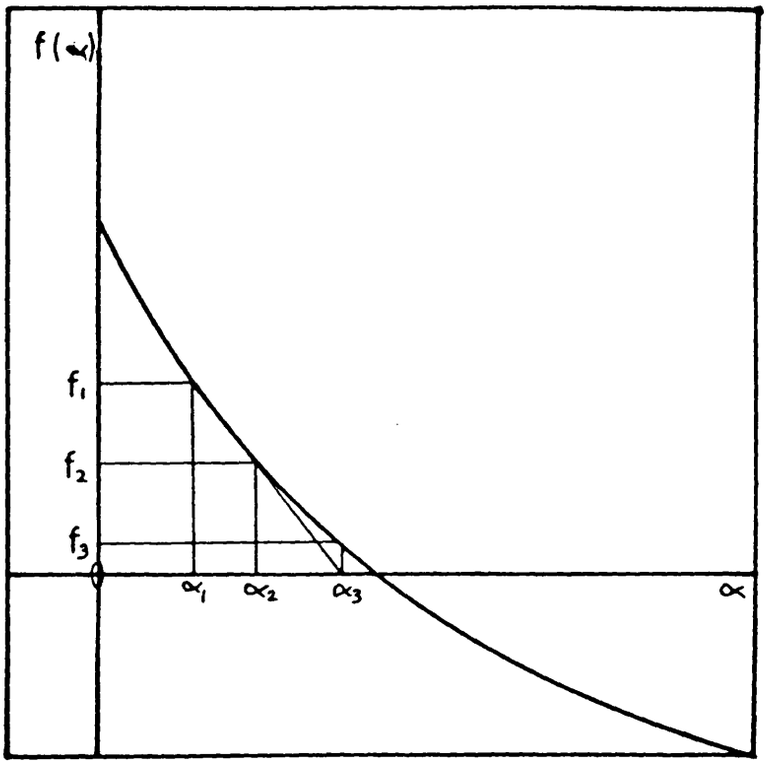

Figure 6.19 Iteration mthod (Newton) used to determine $\alpha(t)$.

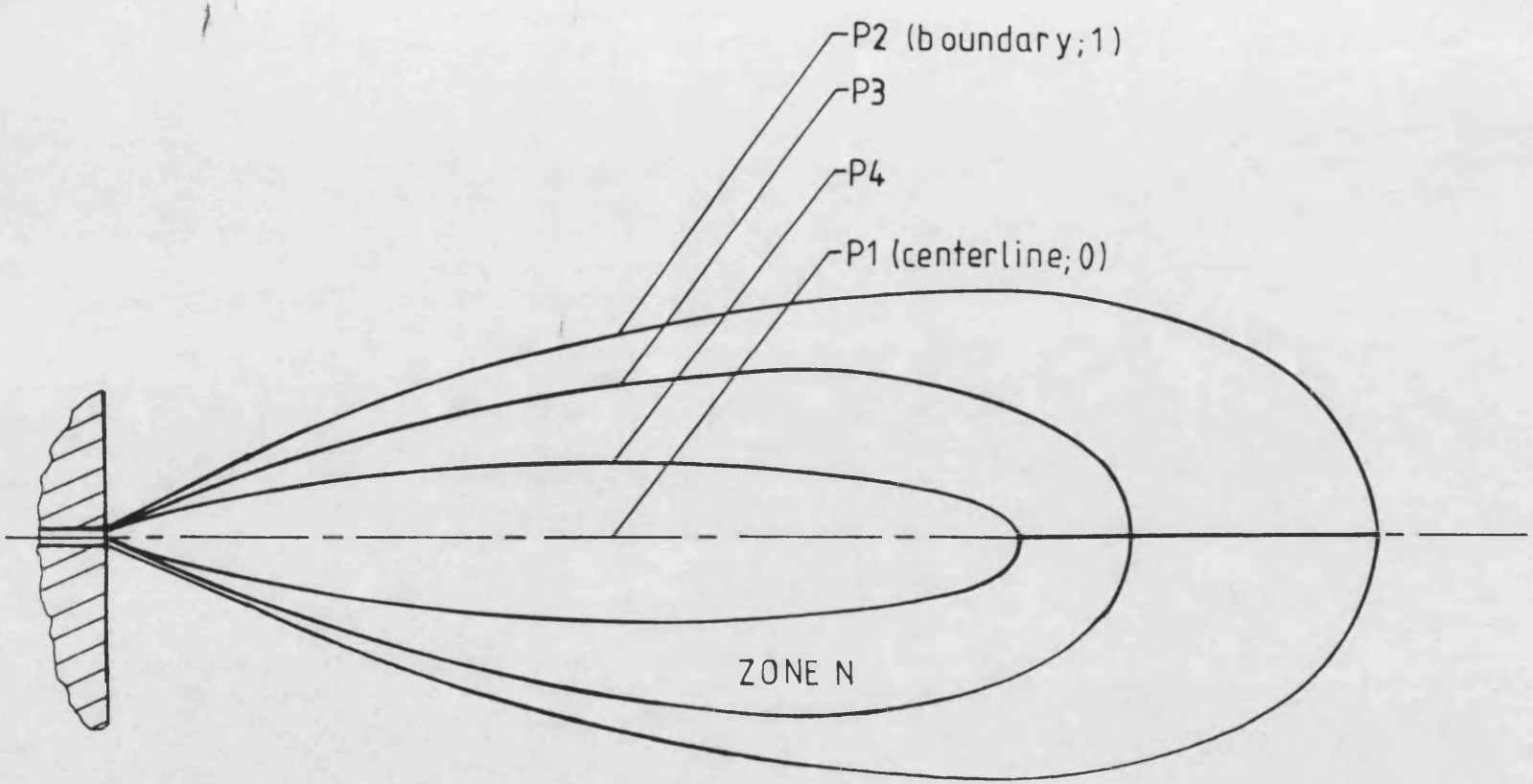

Figure 6.20 Boundary functions P1, P2, P3 & P4 used for zone & jet boundaries.

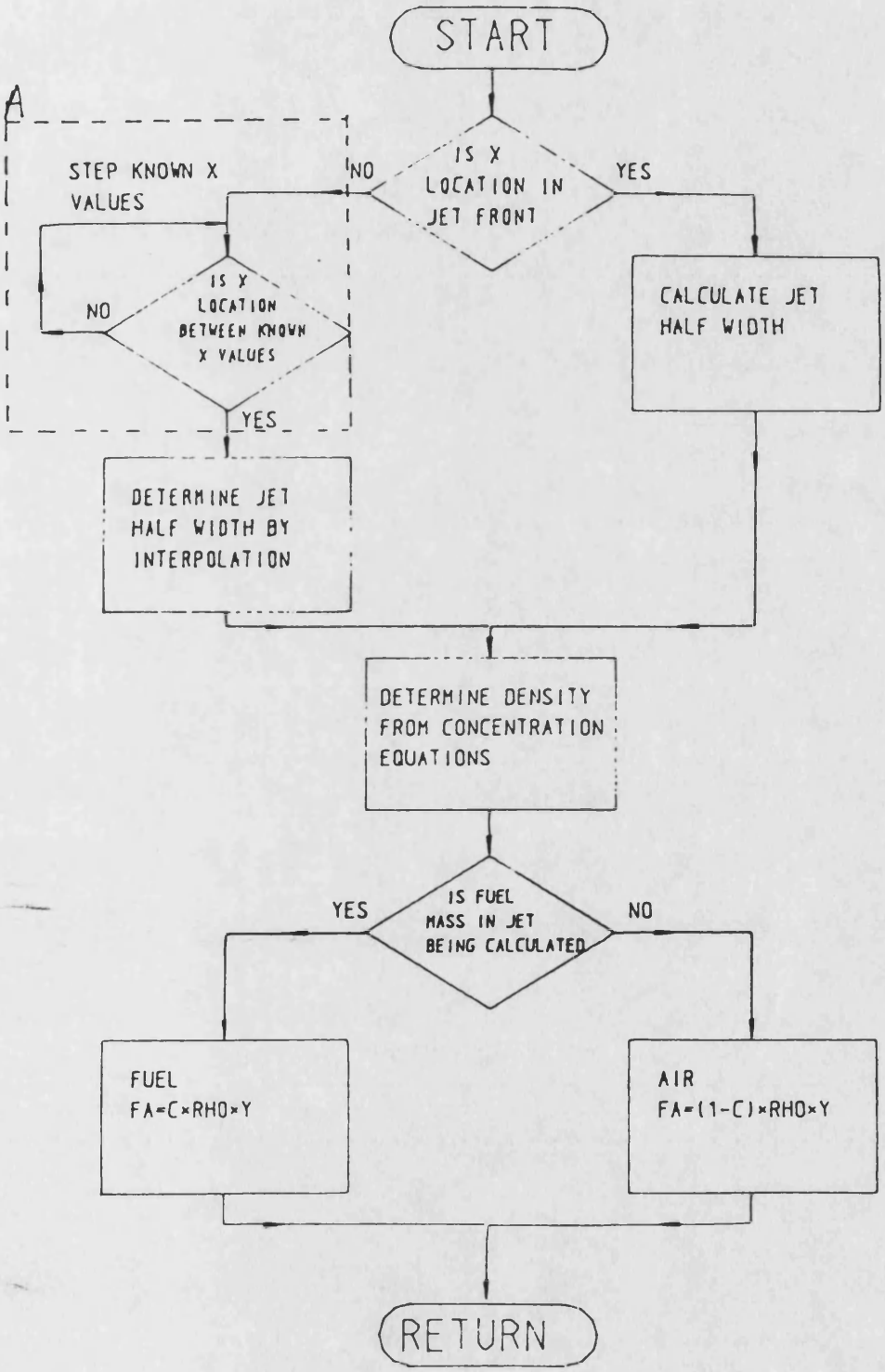

Figure 6.21 Flow diagram for function fa.

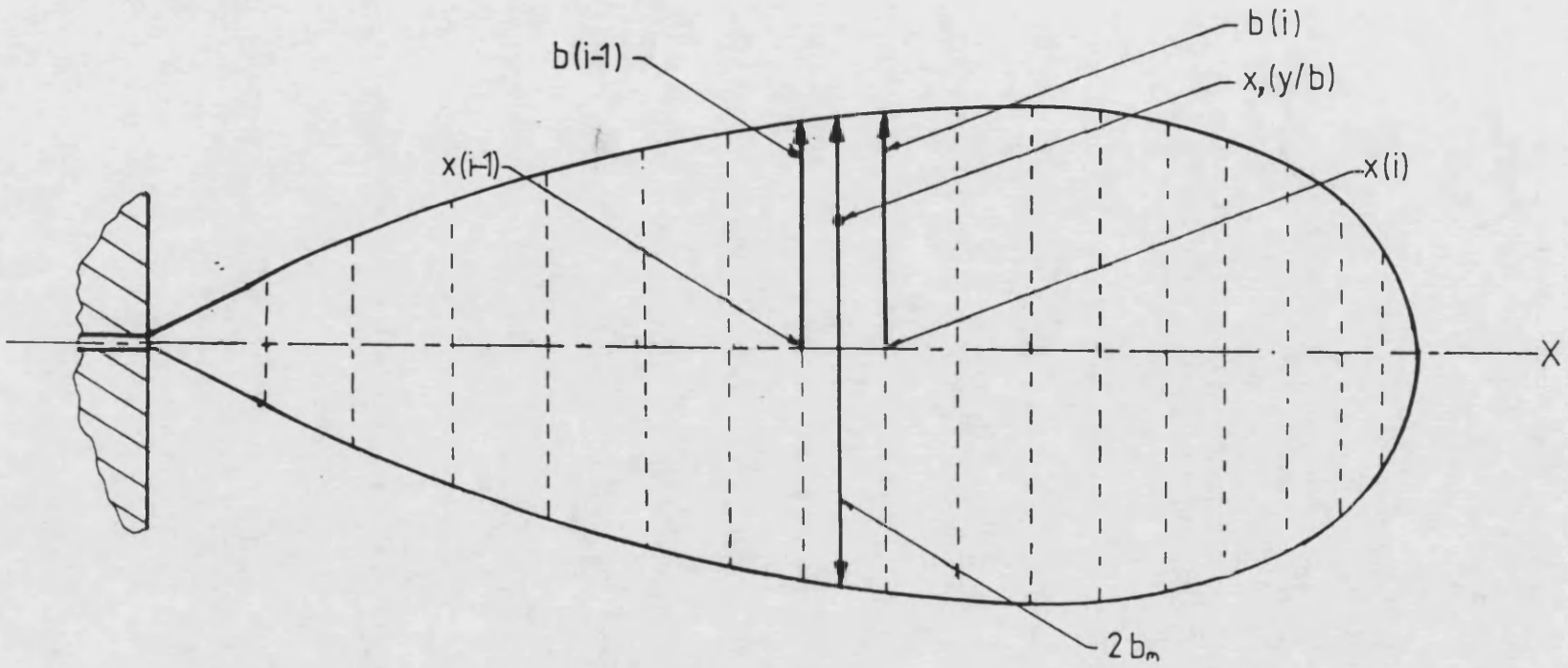

Figure 6.22 Interpolation method for jet width b_m at point (x,(y/b)).

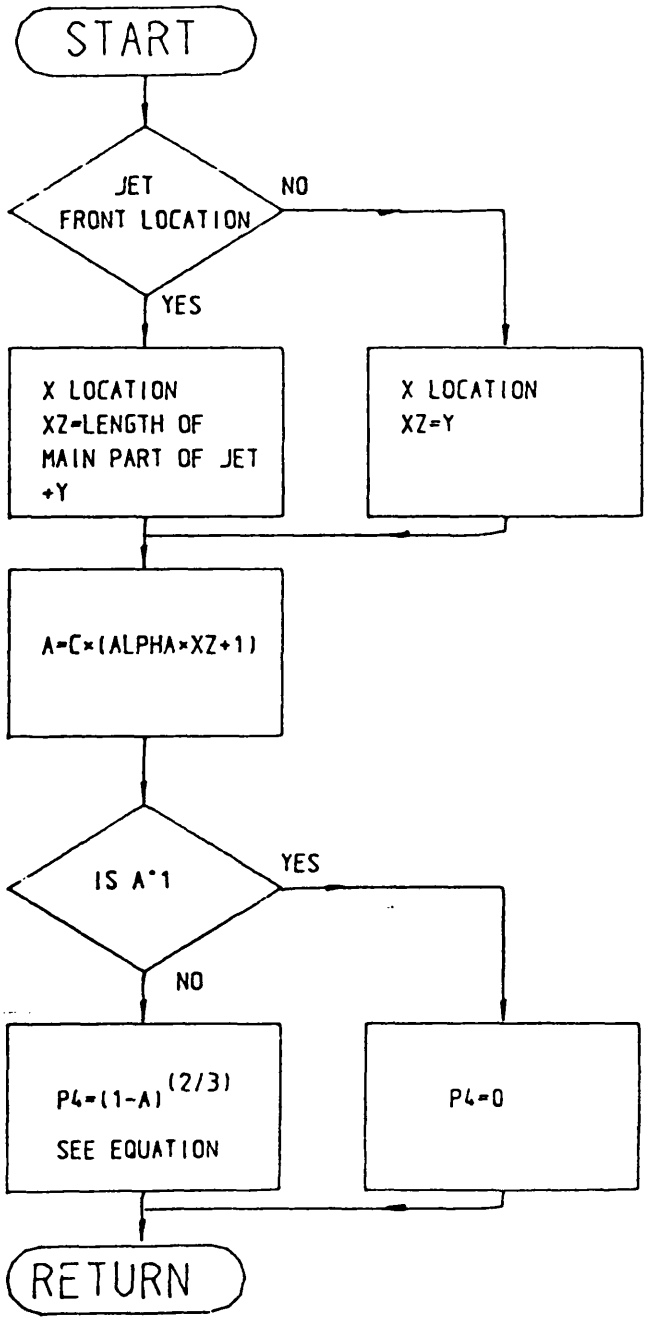

Figure 6.23 Flow diagram for function P4

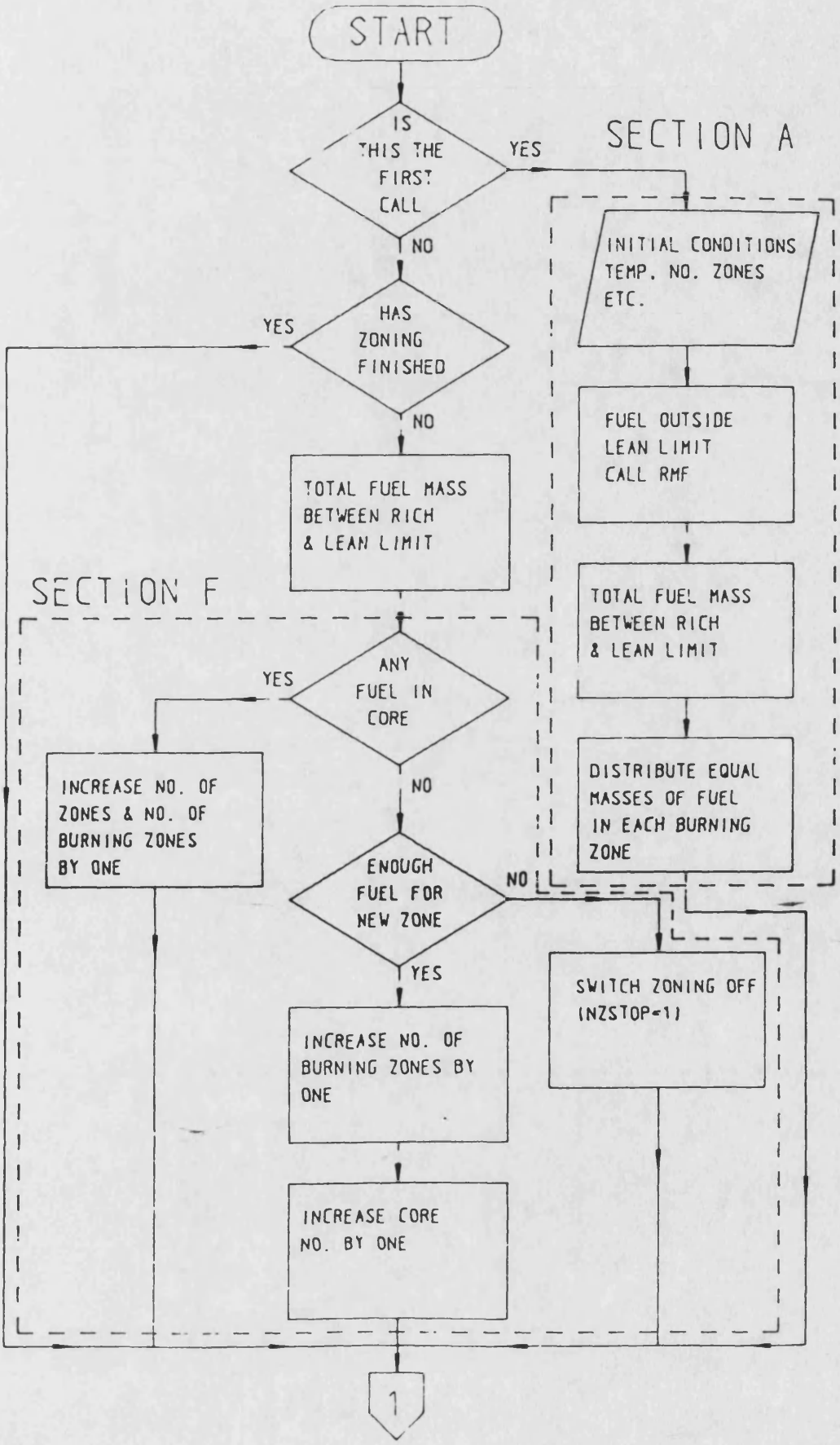

Figure 5.24 Flow diagram for subroutine zone

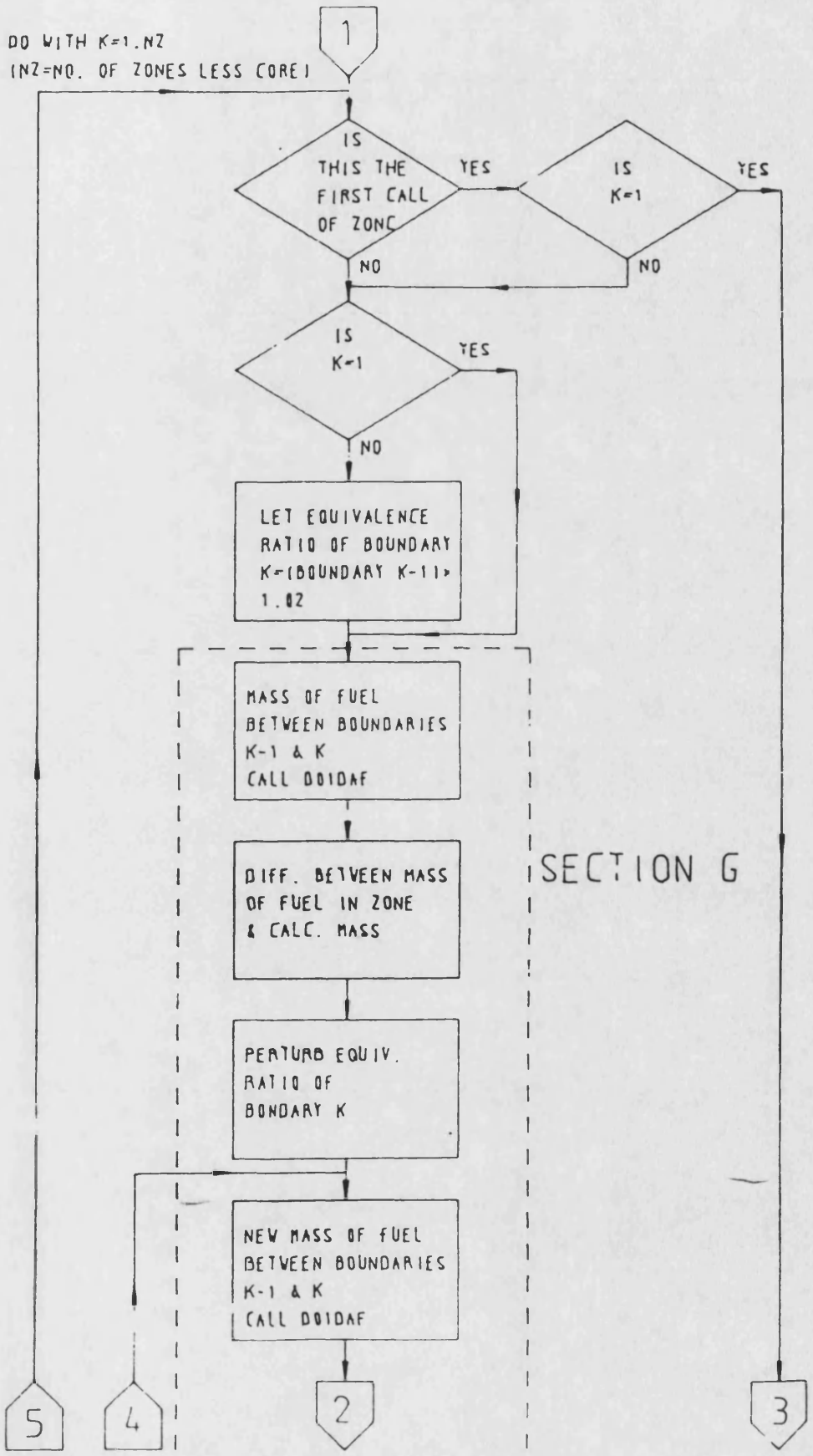

Figure 5.21 Flow diagram for subroutine ZONE (part)

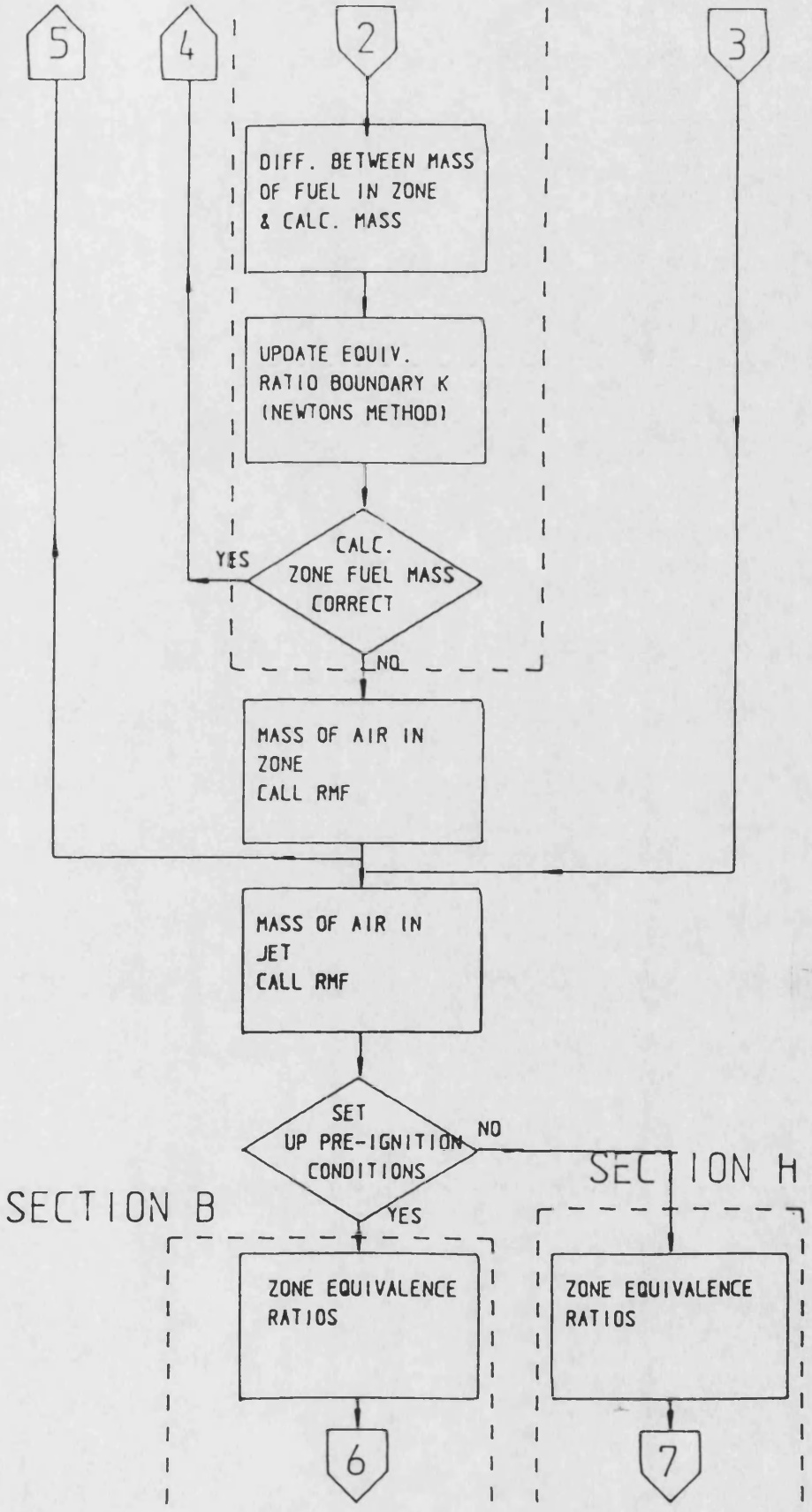

Figure 6.24 Flow diagram for subroutine zone. (cont.)

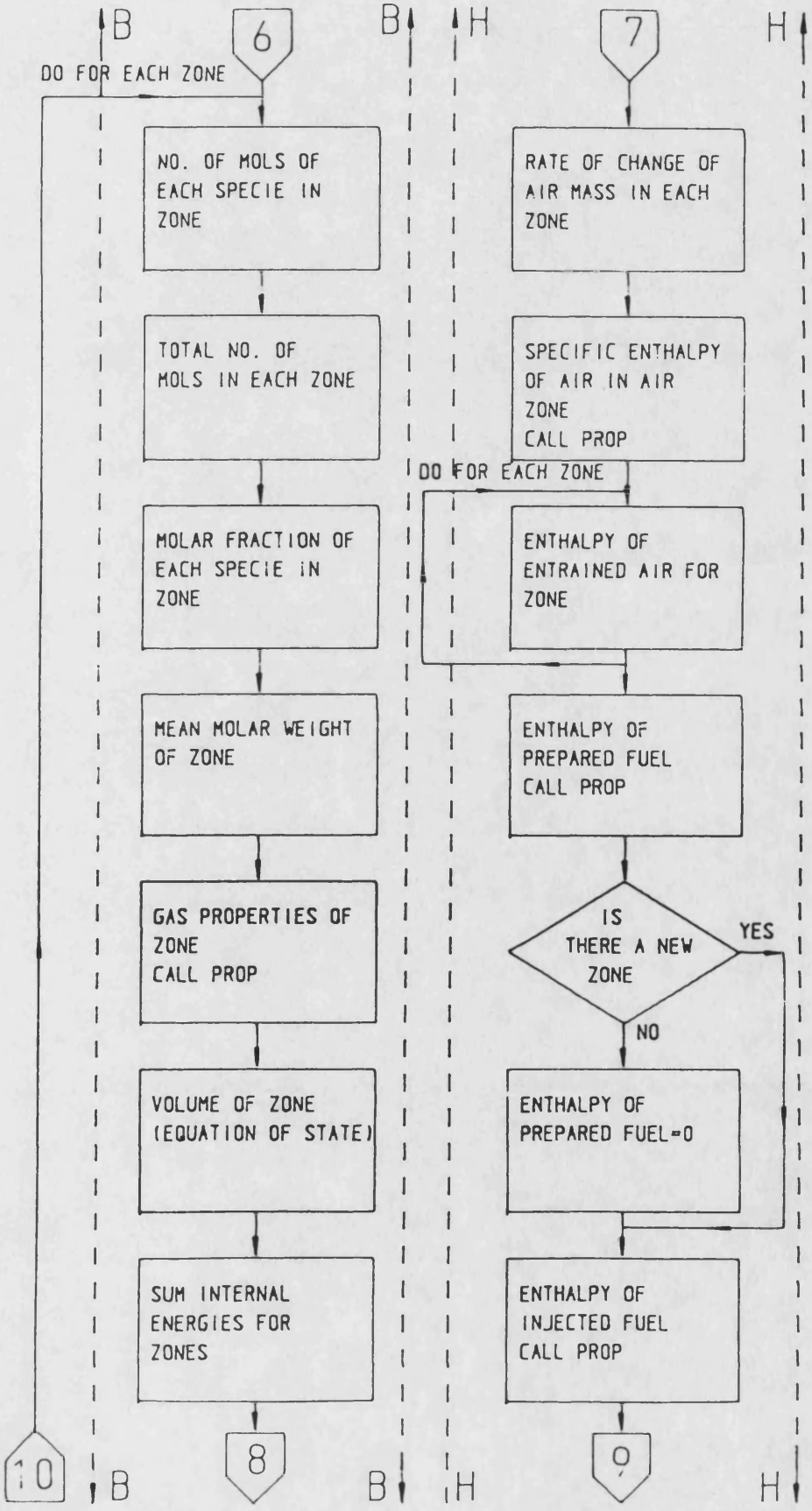

Figure 6.24 Flow diagram for subroutine zonc. (cont.)

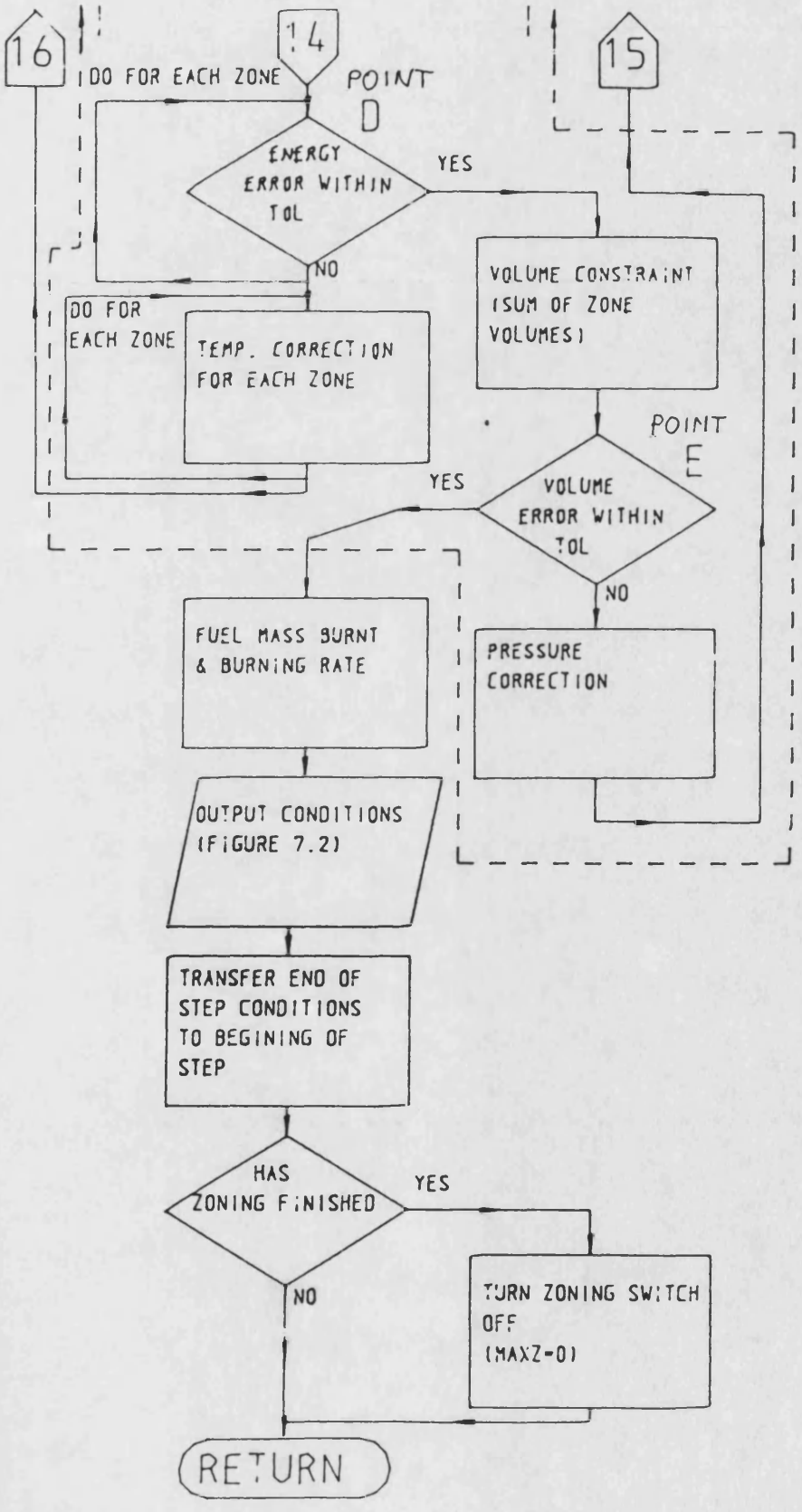

Figure 6.24 Flow diagram for subroutine zonc. (cont.

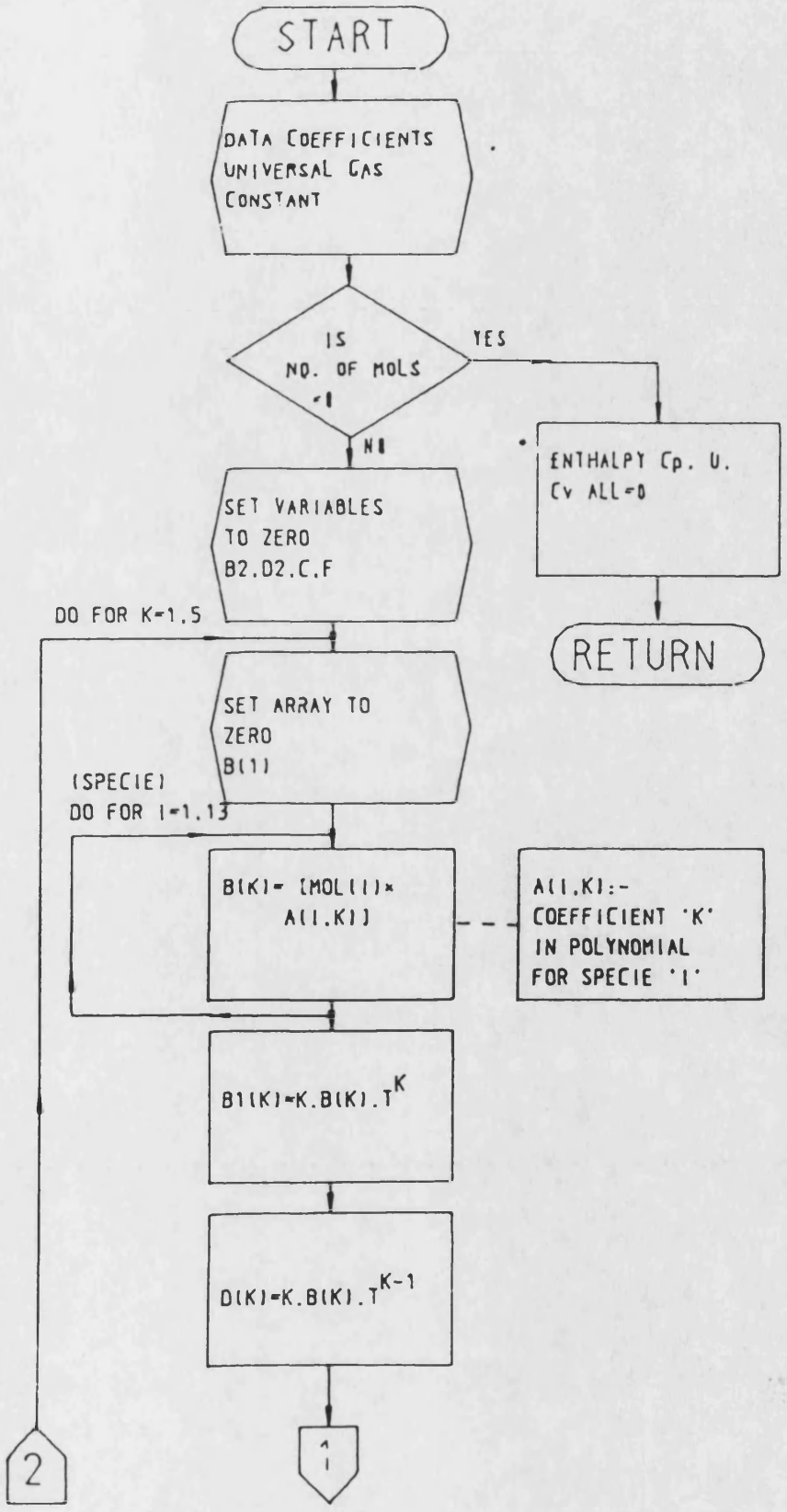

Figure 6.25 Flow diagram for subroutine prop.

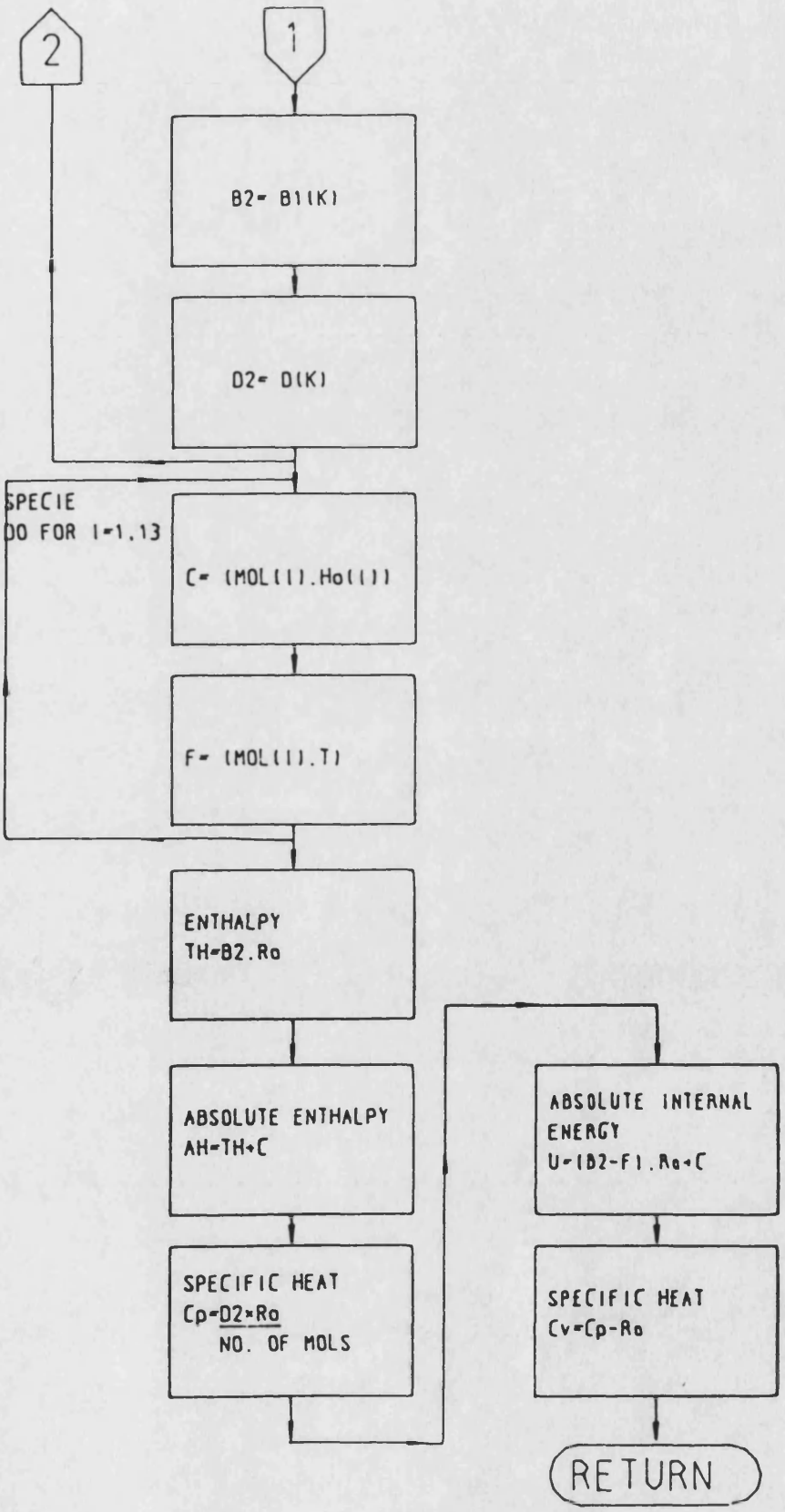

Figure 6.25 Flow diagram for subroutine prop. (cont.)

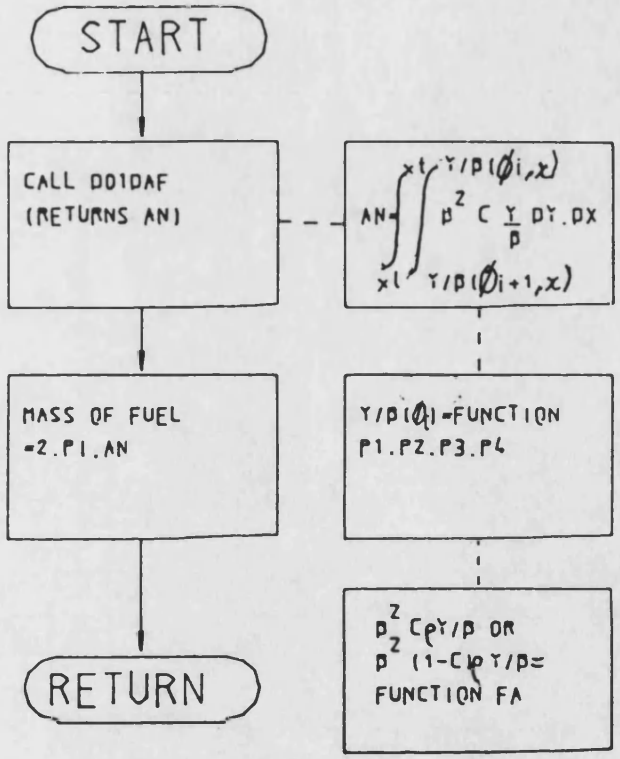

Figure 6.26 Flow diagram for function rmf.

CHAPTER 7

Theoretical Results.

Chapter 7: Theoretical Results

7.1 Introduction

The experimental combustion chamber contains a number of cavities, as shown in figure 7.1. in which a large proportion of the combustion chamber air may reside. However, during the initial stages of combustion. very little fuel will mix with the air hidden in these cavites. Therfore, to simulate this in the computer model, the fuel air mixing before ignition was restricted to the air within the combustion bowl. In addition, after igniton. the fuel/air mixing was restricted to the original air mass within the combustion bowl; ie mixing of the fuel with the air in the cavities was prevented. However there was no volume constraint, so the combustion gases within the bowl were allowed to expand into these cavities & compress the cooler trapped gas without mixing.

This restriction on mixing improved the model predictions for the experimental combustion tests. However, these tests were all done at lean overall air/fuel ratios of between 80:1 & 40:1 (between 50:1 & 25:1 based only on the mass in the combustion bowl). With richer mixtures, mixing of the fuel with the cavity air would play a more important part. During the later stages of combustion. combustion products & a little fuel would diffuse into the cavity air even at lean fuel/air mixtures. although this should not significantly affect the results.

7.2 Heat Release Predictions

Eleven experimental conditions, which covered a wide range of conditions, were simulated by the computer model. The first set of computer runs used the same injection parameters, pressures & temperatures that were measured or set in the experimental tests. The simulation of test 140, which was a typical low swirl & temperature test, will be considered first. The initial conditions used by the program for this test were as follows:-

chamber temperature	-	773 K
hot wall temperature	-	867 K
head temperature	-	606 K
chamber pressure	-	35 bar
fuel injection pressure	-	200 bar
ignition delay	-	3.00 ms
pre-mixed burning duration	-	1.15 ms
air swirl	-	157 rad/s

Table 7.1 shows the program's numerical output for this test, which tabulates the spray trajectory, width, mass injected & concentration prarameter at each step. The tip trajectory, which is a function of the tip radial penetration (xtw) & the spray's angular deflection have been plotted in figure 7.2. Superimposed on this figure is the combustion bomb chamber wall. Also included in the figure for comparison is the trajectory from the simulation of test 273 (873 K, 55 bar, 786 rad/s).

This diagram demonstrates the crudeness of the jet mixing model, which does not consider the constraints

imposed by the chamber walls. In the low swirled case, the spray is deflected by an insignificant amount before it reaches the chamber wall at step 6. Even at the high swirl level of test 273 the spray boundary almost reaches the wall by step 6. This problem is further higlighted by the findings made from the combustion & spray films shown in chapter 4. which showed that the spray in this type of bomb is deflected less in swirl than would be predicted by the model.

Thus to be of practical use, a combustion model needs to take into account the effects of wall mixing. as combustion in nearly all DI diesel engines involve a certain amount of wall mixing

This figure also illustrates how the mixing rate is greater for the high swirled case with quicker growth of the spray boundaries.

Table 7.2a shows the initial conditions output by the combustion subprogram at the point of ignition. The zones have been approximated to the mean chamber temperature of 773 K. Also the fuel core is effectively non-existent & most of the fuel is within the burning zones (2,3 & 4) except for a sizeable portion (17.6%) below the lean limit. in the air zone (1). The equivalence ratios for the zones. have been reproduced schematically in figure 7.3. The lean & rich limits for the equivalence ratios were 0.5 & 2.5 respectively. Table 7.2b shows the resulting temperatures & pressures etc. following the pre-mixed combustion, which lasted for 1.2 ms. All the burning zones show a marked temperature increase. apart from

the insignificant central zone (no. 5). The low temperature in this zone is due to its small size, which reduces the accuracy to which its properties are calculated. The highest zone temperature is achieved by zone 4, which is closest to the stoichiometric ratio.

The air zone temperature has increased from 773 K to 839 K, due to the compression caused by the burning zones (heat transfer between zones is not modelled). Nearly all the chemical energy within the main burning zones has been released, ie there is 89.96 mg of fuel within the burning zones (2,3 & 4) & of this 86.49 mg has been burnt. (Note: The model is based on four sprays, so the fuel mass within each zone should be multiplied by 4 to get the total fuel mass.)

At the next step shown in table 7.2c, further air has been entrained into the zones & the fuel mass burnt has increased to 87.066 mg. Although there has been further heat release between this & the last step, energy lost through heat transfer has kept the pressure & mean temperature effectively constant.

After this step there is a gentle drop off in pressure & temperature. The fuel mass in the air zone, which constitutes 17.6% of the mass injected, is not entrained into the burning zones.

The overall results for pressure, temperature, burning rate & mass fraction burnt for this condition have been plotted & are shown in figures 7.4 to 7.7. Also plotted on these graphs are the experimental results of test 140. Figure 7.7 shows that although

17.6% of the fuel in the theoretical prediction is unused, approximately 22.5% more fuel is consumed than in the experimental test. There are several possible reasons for this large discrepancy: The energy lost through heat transfer could have been underestimated in the heat release calculation for the experimental condition; gas could have leaked passed the shafts carbon sealing rings during the combustion & thus reduced the pressures reached; the mass of fuel injected could have been overestimated by the theoretical model.

In this case, the experimental injected mass, according to the capillary equipment, was 79.6 mg. where as the figure obtained from the heat release analysis was 72.16 mg. The mass injected according to the combustion model was 112.85 mg. In addition, the model uses a simple equation (6.20) to predict the fuel mass injected, which is based on a pressure drop accross an orifice. However, in the experimental tests, the fuel injection pressure is measured in the fuel line just before the injection nozzle. Before the fuel reaches the nozzle orifice, it has to lift and pass the needle valve within the nozzle. Clearly, this will produce a pressure drop, so that the effective pressure across the nozzle orifice will be less than the pressure measured in the fuel line. The difference between the two masses may then be attributed to this, as the injection pressure used by the model is based on the experimental values. Therfore it appears that the discrepancy between the two is primarily due an overprediction of the fuel mass injected by the combustion model. A contribution to this error by the other two possible explanations

should not be discounted though. In particular, the heat transfer correlation used in the experimental analysis was derived from the Annand correlation (79), which was developed for use with an engine, not a combustion bomb.

At high temperature & high swirl conditions, the differences between the theoretical & experimental results were more pronounced. This may be illustrated by comparing the theoretical analysis of test 260 with the corresponding experimental result. The initial conditions for this test & the analysis were as follows:-

chamber temperature	-	873	K
hot wall temperature	-	934	K
head temperature	-	797	K
chamber pressure	-	45	bar
fuel injection pressure	-	220	bar
injection duration	-	2.34	ms
ignition delay	-	1.46	ms
pre-mixed burning duration	-	0.70	ms
air swirl rate	-	786	rad/s

The first six steps are shown in tables 7.3a to 7.3f The mass fraction of fuel injected in the non-burning air zone (no. 1) has been reduced to just 2.4 %, because of the shorter ignition delay. There is also a substantial amount of fuel in the rich core at the start of ignition, 30% of the mass injected at that time. In addition, the ignition delay plus the pre-mixed phase is slightly shorter than the injection duration.

By the end of the 6th step the three initial burning zones have increased to seven & the fuel rich core has been consumed. The peak zone temperature reached was 2875 K (step 2, zone 5),which had an equivalence ratio just below stoichiometric.

The temperature of the air zone, decreased to below the coldest wall temperature, which is physically impossible in a constant volume bomb. This impossible condition results from the way the heat transfer loss is distributed between zones, ie as a function of zone temperature & mass. This was an improvement over the Shahed et al model (6,31), which distributed the heat loss as a function of zone mass only. The model may be qualitatively improved if the heat loss were divided between zones as a function of zone mass & temperature differences, ie:-

$$q_i = \frac{\left(\text{zone mass}_i \times \left(T_z - T_w\right)\right)}{\sum_{z=1}^{n} \left(\text{zone mass}_i \times \left(T_z - T_w\right)\right)} \times \text{TOTAL H.T.} \quad - 7.1$$

where i stands for zone no.

Figures 7.87 to 7.11 compare the overall results for the program with the experimental results. The differences between the two are quite pronounced. The peak burning rate for the model, along with the pressures and temperatures are significantly higher & the combustion is much shorter. Also, as before, the mass of fuel burnt by the model is much larger, although this discrepancy may again be attributed to the reasons given in the previous example.

A probable reason for the shorter combustion & higher peak burning rate, is oversensitivity by the jet mixing model to the effects of swirl. Possibly, the effects of swirl were more pronounced in the experimental tests used to develop the jet mixing model, than they were in these experimental tests.

As the two previous examples indicated that too much fuel was being injected by the model, further computer runs were done with reduced injection pressure. In particular, the two previous simulations of tests 140 & 260 were repeated.

The overall results for the new simulation of test 140 are shown in figures 7.12 to 7.15. These all show a slight improvement over the previous predictions. A reduction in the peak values for pressure, temperature, burning rate & mass fraction burnt are the primary differences, although they are still slightly high.

In the simulation of test 260, the reduced injection pressure has improved the overall results as shown in figures 7.16 to 7.19. The predictions are still poor though, because of the sensitivity of the model to swirl; the mixing rates are still too high.

As the jet mixing model has been proven to be over sensitive to swirl, further computer runs were undertaken with the swirl level set to the minimum experimental value. ie 73.5 rad/s. In addition, the fuel injection pressure was reduced so as to produce the same mass injected as was achieved experimentally.

Figures 7.20 to 7.23 show the results of this from the new simulation of test 260. The pressure curve is now much closer to the experimentally obtained result, although now the mixing rate, during the initial stages, is too low. This has reduced the pre-mixed spike to 2/3rds of the experimental value. where as in the previous example it was 4 times this value.

Peak diffusion burning is now greater than the predicted pre-mixed spike as well as the experimental diffusion burning rate. So although the initial mixing rate in the model is slow during the initial stage, it quickly accelerates so that the pressure & mass burnt exceeds the experimental values. Thus. the combustion duration is still shorter than the experimental time although it is now three times longer than the previous prediction. This type of result was repeated when the computer input swirl level was reduced on other high swirl tests. A further example is shown in figure 7.24 to 7.27 for the simulation of test 273.

There is a large amount of air in cavities outside the combustion bowl as explained earlier, (1/3rd total) & this may well have inhibited the later combustion stages by the means described previously. Therefore it may partly ba a fault of the combustion bomb that the later stages of combustion are extended, compared to the predicted results.

On the other hand, the combustion model does not include wall effects, which will reduce the later

mixing rates by comparison with a spray, which is allowed to penetrate indefinitely into higher air velocities (see figure 7.2). The model does however include the effects of fresh air depletion, which to a certain extent, reduces the mixing rates. At present, the fresh air depletion submodel does not inhibit the mixing rate until the spray volume reaches the chamber volume. Clearly, as this situation is approached, the shortage of fresh air available for burning must start to inhibit the mixing rates. Therefore the mixing rates could be inhibited in the model as this situation is approached. Also the fresh air depletion submodel could be improved, so as to inhibit further the later stages of mixing. These adjustments would really be a simplification & substitute for a wall mixing submodel.

7-3 Zonal Specie Concentration

It should be borne in mind that the purpose of the chemical equilibrium program was to provide data for the determination of gas properties & the rate of heat release. It was not designed to provide detailed information on pollutant formation (NOx) or the more unusual species that are formed during the combustion of normal diesel fuel. However, an example of the theoretical results will be presented, although they have not been compared with or verified by experimental tests.

Figure 7.28 shows the hydrogen specie histories for a typical combustion zone as it moves from a rich to lean equivalence ratio. Also included on the graph are the zone temperature & equivalence ratio histories. The curves start at 0.9 ms after ignition. because this particular zone was not formed until then.

At a high equivalence ratio & low temperature, there is a large amount, in molar terms, of the specie H_2. As the equivalence ratio decreases, this specie reduces, as it is converted to H_2O. At the high temperatures around stoichiometric, there is a small temporary increase in the species of atomic H and hydroxyl OH. Although the specie atomic H appears to be a flat line on the bottom of the graph, in molar terms it reached about 2%.

Figure 7.29 shows the carbon & NO spe cies. The behavior of the carbon species CO & CO_2 are similar to that for the hydrogen species of H_2 & H_2O. At

a rich equivalence ratio, where there is a shortage of oxygen, there is an excess of CO. As the equivalence ratio reduces, the CO specie decreases & CO_2 increases.

The nitrogen monoxide specie history in not really representative of what might be found in an engine, because the formation & in particular the decomposition rate, are slow enough to make the assumption of chemical equilibrium invalid considering the combustion time. However the figure does show that the maximum concentration of NO occurs when there is an excess of oxygen & the combustion temperature is high. Furthermore, the program does include an option to freeze out the NO level (stop the decomposition) at its high temperature value, although the assumption of chemical equilibrium does make the initial NO formation rate too high.

7.4 Model Computation Time & Numerical Stability

In terms of actual central processor unit time (CPU secs), the program takes approximately 60 CPU minutes of Honeywell Multics time to do between 30 & 60 steps of 0.2 ms each. The run time for any individual test is primarily a function of the number of final zones: eg test 260, with fuelling equal to the experimental condition & low swirl, did 32 steps in 60 CPU minutes with a final zone number of 17. On the other hand the simulation of test 181 had a final zone number of 9 & took 36 CPU minutes to do 39 steps (65 steps/CPU hour).

Most of the computation time is taken up in determining the value of the zone equivalence ratio boundaries & by the subroutine 'confin'. The subroutine confin determines the new concentration profiles & equivalence ratio of the jet boundary after fresh air depletion.

The zone equivalence ratio boundaries are determined by an iterative technique as described in the previous chapter, with numerous calls to the subroutine d01daf. D01daf is used to solve the double integral equations of 6.33, 6.38 & 6.39 for the fuel & air masses within the zones and the whole jet.

This area of computation may possibly be speeded up by increasing the iterative convergence rate or writing a purpose built subroutine to replace the general NAG routine d01daf.

The computation time cannot be reduced by decreasing

the accuracy of the convergence criteria, as the program either fails to converge in its iterative procedures or fails completly.

In its present form, it still occassionally fails & the source of these failures can invariably be traced back to the NAG routine d01daf. This is another reason for writing a purpose built subroutine to replace the NAG routine d01daf.

The other parts of the program contribute little to the overall computation time, eg the jet mixing part of the main program contributes just under 30 CPU seconds of computation time for fifty steps.

7-5 Model Restrictions & Limits

The results presented here have highlighted some of the restrictions & limits of the model. In its present form it is only really applicable to low swirl, high temperature conditions with a short ignition delay.

With ignition delays over 0.5 ms, the lack of a pre-mixed burning submodel, makes realistic predictions impossible, as the duration of the pre-mixed phase is unknown. For ignition delays below 0.5 ms & with low swirl levels, very little fuel is available for pre-mixed burning, which makes this phase of combustion relatively unimportant in heat release terms. Under these conditions the pre-mixed burning duration is short and a constant value could be used.

If a pre-mixed model were introduced, there would have to be some transition from the pre-mixed phase to the mixing or diffusion controlled stage. One possible method would be to control the initial pre-mixed or diffusion phase by rate controlled reactions. These rate controlled reactions could then be used in the mixing phase, when the rate of reaction would then be dependent on the rate at which fuel is prepared. However, it would be desirable to introduce the assumption of chemical equilibrium in the later stages of combustion, as this would be computationally quicker although more complex.

An ignition delay model was not included in the model, because it would have made comparison of the

combustion model with the experimental results more difficult. However, if it were so desired, a simple empirical model could be easily introduced.

The model also ignores impingement of the spray on the chamber wall & its effect on the mixing & combustion rates. In most small DI diesel engines, wall impingement plays an important part in the combustion. At present their is little detailed information on wall mixing under quiescent conditions & even less under swirled conditions. The extension of this model to include wall mixing would be difficult, although not impossible. The main problem would be trying to split the spray up into zones when there is a much more complex distribution of fuel & air then the present distribution.

Mixing after fresh air depletion was not done on a strict theoretical basis. The inclusion of a wall mixing model would not necessarily include this either. Further work needs to be done in this area as this part of the combustion phase plays an important part in the final levels of pollutants produced.

Time	Penetration of Jet							Shape of Cross Section				Inj.Fuel	Conc.Fac.
	Tip				Tail								
t ms	xt cm	xtw cm	xxx cm	ang. deg	xl cm	xlw cm	ang. deg	b1 cm	b2 cm	b3 cm	b cm	Mfl mg	Alpha
0.20	1.87	1.87	1.10	0.07	0.00	0.00	0.00	0.11	0.13	0.11	0.12	10.26	1.00000E+00
0.40	2.81	2.81	0.55	0.24	0.00	0.00	0.00	0.32	0.44	0.36	0.37	20.51	0.00000E+00
0.60	3.55	3.55	0.44	0.52	0.00	0.00	0.00	0.45	0.65	0.53	0.54	30.77	4.03463E+00
0.80	4.19	4.19	0.38	0.89	0.00	0.00	0.00	0.57	0.88	0.78	0.75	41.02	1.75171E+01
1.00	4.76	4.76	0.33	1.34	0.00	0.00	0.00	0.69	1.10	1.00	0.94	51.28	2.93856E+01
1.20	5.28	5.28	0.30	1.86	0.00	0.00	0.00	0.81	1.31	1.20	1.13	61.54	3.99958E+01
1.40	5.76	5.75	0.28	2.46	0.00	0.00	0.00	0.91	1.52	1.38	1.30	71.79	5.01363E+01
1.60	6.21	6.19	0.26	3.12	0.00	0.00	0.00	1.01	1.73	1.55	1.46	82.05	5.89530E+01
1.80	6.63	6.61	0.25	3.85	0.00	0.00	0.00	1.11	1.93	1.70	1.61	92.30	6.70921E+01
2.00	7.03	7.00	0.24	4.63	0.00	0.00	0.00	1.20	2.13	1.85	1.76	102.56	7.45610E+01
2.20	7.42	7.37	0.23	5.47	0.00	0.00	0.00	1.29	2.33	1.99	1.90	112.81	8.16307E+01
2.40	7.79	7.73	0.22	6.36	1.59	0.79	0.00	1.38	2.52	2.12	2.03	112.81	8.81460E+01
2.60	8.16	8.07	0.21	7.30	1.84	1.31	0.02	1.46	2.71	2.25	2.17	112.81	1.01762E+02
2.80	8.51	8.39	0.21	8.29	2.14	1.72	0.05	1.55	2.90	2.38	2.30	112.81	1.17532E+02
3.00	8.86	8.71	0.20	9.33	2.44	2.06	0.09	1.63	3.09	2.51	2.43	112.81	1.33532E+02
3.20	9.20	9.01	0.20	10.40	2.72	2.37	0.14	1.71	3.28	2.63	2.56	112.81	1.50094E+02
3.40	9.54	9.30	0.20	11.52	2.98	2.65	0.20	1.79	3.47	2.75	2.69	112.81	1.67595E+02
3.60	9.88	9.58	0.20	12.68	3.23	2.91	0.27	1.87	3.67	2.86	2.82	112.81	1.85659E+02
3.80	10.22	9.85	0.20	13.87	3.48	3.15	0.36	1.95	3.86	2.98	2.94	112.81	2.04711E+02
4.00	10.56	10.11	0.20	15.10	3.71	3.38	0.45	2.03	4.05	3.09	3.07	112.81	2.24602E+02
4.20	10.90	10.37	0.20	16.36	3.93	3.60	0.54	2.11	4.25	3.20	3.19	112.81	2.45302E+02
4.40	11.25	10.62	0.20	17.65	4.14	3.81	0.65	2.19	4.45	3.31	3.32	112.81	2.66996E+02
4.60	11.59	10.86	0.20	18.98	4.35	4.01	0.77	2.27	4.65	3.42	3.44	112.81	2.89690E+02
4.80	11.94	11.09	0.21	20.33	4.55	4.20	0.89	2.36	4.85	3.54	3.57	112.81	3.13640E+02
5.00	12.30	11.32	0.21	21.71	4.74	4.39	1.03	2.44	5.06	3.65	3.70	112.81	3.38874E+02
5.20	12.65	11.54	0.21	23.12	4.93	4.56	1.17	2.52	5.27	3.76	3.83	112.81	3.65368E+02
5.40	13.02	11.76	0.21	24.56	5.12	4.74	1.32	2.61	5.49	3.87	3.96	112.81	3.93274E+02
5.60	13.39	11.97	0.22	26.01	5.30	4.91	1.47	2.70	5.71	3.98	4.09	112.81	4.22649E+02
5.80	13.76	12.18	0.22	27.50	5.48	5.07	1.64	2.79	5.93	4.10	4.23	112.81	4.53608E+02
6.00	14.14	12.39	0.22	29.00	5.65	5.23	1.81	2.88	6.16	4.21	4.36	112.81	4.86325E+02
6.20	14.53	12.58	0.23	30.52	5.82	5.38	1.99	2.97	6.40	4.32	4.50	112.81	5.21020E+02
6.40	14.93	12.78	0.23	32.07	5.99	5.53	2.17	3.06	6.63	4.44	4.64	112.81	5.57317E+02
6.60	15.33	12.97	0.24	33.64	6.15	5.68	2.36	3.16	6.88	4.56	4.78	112.81	5.95570E+02
6.80	15.73	13.16	0.24	35.22	6.31	5.83	2.56	3.25	7.12	4.67	4.92	112.81	6.35817E+02
7.00	16.15	13.34	0.24	36.82	6.47	5.97	2.77	3.35	7.37	4.79	5.07	112.81	6.78182E+02
7.20	16.57	13.52	0.25	38.44	6.63	6.11	2.98	3.45	7.63	4.91	5.22	112.81	7.22721E+02
7.40	16.99	13.70	0.25	40.08	6.78	6.24	3.20	3.55	7.89	5.04	5.37	112.81	7.69669E+02
7.60	17.43	13.87	0.25	41.73	6.93	6.37	3.42	3.65	8.16	5.16	5.52	112.81	8.19009E+02
7.80	17.87	14.04	0.26	43.40	7.08	6.50	3.65	3.76	8.43	5.28	5.67	112.81	8.70810E+02
8.00	18.31	14.21	0.26	45.08	7.23	6.63	3.89	3.86	8.71	5.41	5.83	112.81	9.25131E+02
8.20	18.77	14.37	0.27	46.78	7.37	6.76	4.13	3.97	8.99	5.53	5.99	112.81	9.82050E+02
8.40	19.23	14.53	0.27	48.49	7.52	6.88	4.38	4.08	9.27	5.66	6.15	112.81	1.04165E+03
8.60	19.69	14.69	0.27	50.21	7.66	7.00	4.63	4.19	9.56	5.79	6.31	112.81	1.10401E+03
8.80	20.17	14.85	0.28	51.95	7.80	7.12	4.89	4.30	9.86	5.92	6.48	112.81	1.16921E+03
9.00	20.65	15.00	0.28	53.69	7.94	7.24	5.15	4.42	10.16	6.05	6.64	112.81	1.23731E+03
9.20	21.13	15.15	0.29	55.45	8.07	7.35	5.42	4.53	10.47	6.19	6.81	112.81	1.30840E+03
9.40	21.63	15.30	0.29	57.22	8.21	7.47	5.70	4.65	10.78	6.32	6.98	112.81	1.38256E+03
9.60	22.13	15.45	0.29	59.00	8.34	7.58	5.98	4.77	11.09	6.45	7.15	112.81	1.45987E+03
9.80	22.63	15.59	0.30	60.79	8.47	7.69	6.26	4.89	11.41	6.59	7.33	112.81	1.54038E+03
10.00	23.14	15.73	0.30	62.59	8.60	7.80	6.55	5.01	11.74	6.73	7.51	112.81	1.62418E+03

Table 7.1 Details for spray trajectory, etc. output by jet program for the simulation of test 140.

TIME 0.0 ms

	TEMPERATURE DEGREES K	EQUIVALENCE RATIO	LOWER BOUNDARY RATIO	ZONE VOLUME (m**3)	FUEL MASS (kg)
ZONE 1	773.0	0.031	0.000	0.5698E-04	0.4873E-05
ZONE 2	773.0	0.667	0.500	0.1075E-04	0.7927E-05
ZONE 3	773.0	0.992	0.847	0.7256E-05	0.7497E-05
ZONE 4	773.0	1.449	1.157	0.4994E-05	0.7927E-05
ZONE 5	773.0	2.092	2.500	0.1700E-06	0.3661E-06

PRESSURE BAR	TEMPERATURE MEAN (K)	FUEL MASS INJECTED (milligrams)	FUEL MASS BURNT (milligrams)	BURNING RATE (kg/sec)	ENTRAINMENT RATE (1 JET) (kg/sec)
35.000	773.0	112.815	0.000	0.0000E+00	0.0000E+00

****

Table 7.2a Predicted zone & mean conditions at ignition for the simulation test 140.

TIME 1.2 ms

	TEMPERATURE DEGREES K	EQUIVALENCE RATIO	LOWER BOUNDARY RATIO	ZONE VOLUME (m**3)	FUEL MASS (kg)
ZONE 1	839.2	0.108	0.284	0.2350E-04	0.4873E-05
ZONE 2	2026.8	0.463	0.395	0.2104E-04	0.7497E-05
ZONE 3	2291.3	0.601	0.536	0.1853E-04	0.7497E-05
ZONE 4	2589.7	0.786	0.673	0.1627E-04	0.7497E-05
ZONE 5	913.4	1.128	1.066	0.4542E-06	0.8502E-06

PRESSURE BAR	TEMPERATURE MEAN (K)	FUEL MASS INJECTED (milligrams)	FUEL MASS BURNT (milligrams)	BURNING RATE (kg/sec)	ENTRAINMENT RATE (1 JET) (kg/sec)
69.316	1494.6	112.815	86.490	0.1504E+00	0.2220E-03

****

Table 7.2b Predicted zone & mean conditions after first step for the simulation of test 140.

TIME 1.9 ms

	TEMPERATURE DEGREES K	EQUIVALENCE RATIO	LOWER BOUNDARY RATIO	ZONE VOLUME (m**3)	FUEL MASS (kg)
ZONE 1	832.0	0.110	0.312	0.2291E-04	0.4873E-05
ZONE 2	2022.4	0.465	0.405	0.2025E-04	0.7497E-05
ZONE 3	2259.3	0.586	0.528	0.1873E-04	0.7497E-05
ZONE 4	2535.6	0.752	0.650	0.1660E-04	0.7497E-05
ZONE 5	1182.0	1.096	0.993	0.6324E-06	0.8678E-06

PRESSURE BAR	TEMPERATURE MEAN (K)	FUEL MASS INJECTED (milligrams)	FUEL MASS BURNT (milligrams)	BURNING RATE (kg/sec)	ENTRAINMENT RATE (1 JET) (kg/sec)
69.310	1494.6	112.815	87.066	0.2881E-02	0.1162E-04

****

Table 7.2c Next step (table 7.2b).

IIIC 9.0 us

	TEMPERATURE DEGREES	EQUIVALENCE RATIO	LOWER BOUNDARY RATIO	ZONE VOLUME (m**3)	FUEL MASS (Kg)
ZONE 1	873.0	0.808	0.000	0.7200E-04	0.7169E-06
ZONE 2	873.0	0.829	0.500	0.3392E-05	0.3617E-05
ZONE 3	873.0	1.618	1.334	0.1898E-05	0.3617E-05
ZONE 4	873.0	2.197	1.925	0.1406E-05	0.3617E-05
ZONE 5	873.0	3.370	2.500	0.1282E-05	0.4929E-05

PRESSURE BAR	TEMPERATURE MEAN (K)	FUEL MASS INJECTED (milligrams)	FUEL MASS BURNT (milligrams)	BURNING RATE (kg/sec)	ENTRAINMENT RATE (1 JET) (kg/sec)
45.000	873.0	69.824	0.000	0.0000E+00	0.0000E+00

****

Table 7.3a Predicted zone & mean condition at igntion
for the simulation of test 260.

TIME 0.7 ms

	TEMPERATURE DEGREES K	EQUIVALENCE RATIO	LOWER BOUNDARY RATIO	ZONE VOLUME (m**3)	FUEL MASS (kg)
ZONE 1	853.2	0.013	0.000	0.2710E-04	0.7169E-06
ZONE 2	1767.2	0.275	0.156	0.1330E-04	0.3617E-05
ZONE 3	2168.7	0.479	0.400	0.9510E-05	0.3617E-05
ZONE 4	2428.0	0.628	0.561	0.8206E-05	0.3617E-05
ZONE 5	2875.8	0.966	0.700	0.2162E-04	0.1192E-04
ZONE 6	928.2	5.164	2.500	0.4827E-07	0.4547E-06

PRESSURE BAR	TEMPERATURE MEAN (K)	FUEL MASS INJECTED (milligrams)	FUEL MASS BURNT (milligrams)	BURNING RATE (kg/sec)	ENTRAINMENT RATE (1 JET) (kg/sec)
76.722	1455.4	99.749	84.944	0.2427E+00	0.4430E-03

****

Table 7.3b Conditions after pre-mixed combustion: test 260.

TIME 2.2 ms

	TEMPERATURE DEGREES K	EQUIVALENCE RATIO	LOWER BOUNDARY RATIO	ZONE VOLUME (m**3)	FUEL MASS (kg)
ZONE 1	775.2	0.018	0.023	0.1653E-04	0.7169E-06
ZONE 2	1666.7	0.227	0.148	0.1409E-04	0.3617E-05
ZONE 3	1942.0	0.363	0.308	0.1040E-04	0.3617E-05
ZONE 4	2138.3	0.467	0.420	0.8902E-05	0.3617E-05
ZONE 5	2518.5	0.662	0.515	0.2403E-04	0.1192E-04
ZONE 6	2851.7	1.178	0.918	0.4962E-05	0.3482E-05
ZONE 7	883.0	2.761	2.500	0.9746E-07	0.2767E-06

PRESSURE BAR	TEMPERATURE MEAN (K)	FUEL MASS INJECTED (milligrams)	FUEL MASS BURNT (milligrams)	BURNING RATE (kg/sec)	ENTRAINMENT RATE (1 JET) (kg/sec)
32.565	1563.2	109.723	100.459	0.7758E-01	0.2365E-03

****

Table 7.3c Step 3, test 260.

TIME 1.1 ms

	TEMPERATURE DEGREES K	EQUIVALENCE RATIO	LOWER BOUNDARY RATIO	ZONE VOLUME (m**3)	FUEL MASS (kg)
ZONE 1	759.3	0.019	0.238	0.1433E-04	0.7169E-06
ZONE 2	1858.2	0.227	0.257	0.1153E-04	0.3617E-05
ZONE 3	1973.6	0.373	0.338	0.2806E-05	0.3617E-05
ZONE 4	2093.7	0.440	0.408	0.8856E-05	0.3617E-05
ZONE 5	2353.5	0.572	0.473	0.2551E-04	0.1192E-04
ZONE 6	2615.1	0.781	0.707	0.6164E-05	0.3482E-05
ZONE 7	2822.9	1.144	0.899	0.3664E-05	0.2660E-05
ZONE 8	878.1	4.069	2.500	0.1452E-07	0.1295E-06

PRESSURE BAR	TEMPERATURE MEAN (K)	FUEL MASS INJECTED (milligrams)	FUEL MASS BURNT (milligrams)	BURNING RATE (kg/sec)	ENTRAINMENT RATE (1 JET) (kg/sec)
36.379	1634.3	119.698	112.613	0.6077E-01	0.4588E-04

****

Table 7.3d Step 4, test 260.

IIMC_1.3_ps

	TEMPERATURE DEGREES K	EQUIVALENCE RATIO	LOWER BOUNDARY RATIO	ZONE VOLUME (m**3)	FUEL MASS (Kg)
ZONE 1	748.2	0.012	0.314	0.1382E-04	0.7169E-06
ZONE 2	1976.5	0.348	0.324	0.1046E-04	0.3617E-05
ZONE 3	2009.4	0.325	0.373	0.2329E-05	0.3617E-05
ZONE 4	2076.7	0.440	0.418	0.8754E-05	0.3617E-05
ZONE 5	2261.1	0.533	0.462	0.2608E-04	0.1192E-04
ZONE 6	2437.4	0.679	0.628	0.6522E-05	0.3482E-05
ZONE 7	2707.1	0.822	0.757	0.4227E-05	0.2660E-05
ZONE 8	2824.9	1.027	1.277	0.5063E-06	0.3389E-06

PRESSURE BAR	TEMPERATURE MEAN (K)	FUEL MASS INJECTED (milligrams)	FUEL MASS BURNT (milligrams)	BURNING RATE (kg/sec)	ENTRAINMENT RATE (1 JET) (kg/sec)
36.679	1639.6	119.698	115.905	0.1686E-01	0.9744E-05

****

Table 7.3e Step 5, test 260.

TIME 1.5 ms

	TEMPERATURE DEGREES K	EQUIVALENCE RATIO	LOWER BOUNDARY RATIO	ZONE VOLUME (m**3)	FUEL MASS (kg)
ZONE 1	736.5	0.019	0.359	0.1364E-04	0.7169E-06
ZONE 2	2040.3	0.382	0.366	0.2967E-05	0.3617E-05
ZONE 3	2030.9	0.414	0.398	0.2170E-05	0.3617E-05
ZONE 4	2067.1	0.446	0.430	0.8691E-05	0.3617E-05
ZONE 5	2200.8	0.515	0.462	0.2652E-04	0.1192E-04
ZONE 6	2320.2	0.625	0.585	0.6786E-05	0.3482E-05
ZONE 7	2537.8	0.780	0.681	0.4602E-05	0.2660E-05
ZONE 8	2757.8	1.223	1.037	0.4838E-06	0.3754E-06

PRESSURE BAR	TEMPERATURE MEAN (K)	FUEL MASS INJECTED (milligrams)	FUEL MASS BURNT (milligrams)	BURNING RATE (kg/sec)	ENTRAINMENT RATE (1 JET) (kg/sec)
25.848	1625.0	119.698	116.320	0.1673E-02	0.4044E-05

****

Table 7.3f Step 6, test 260.

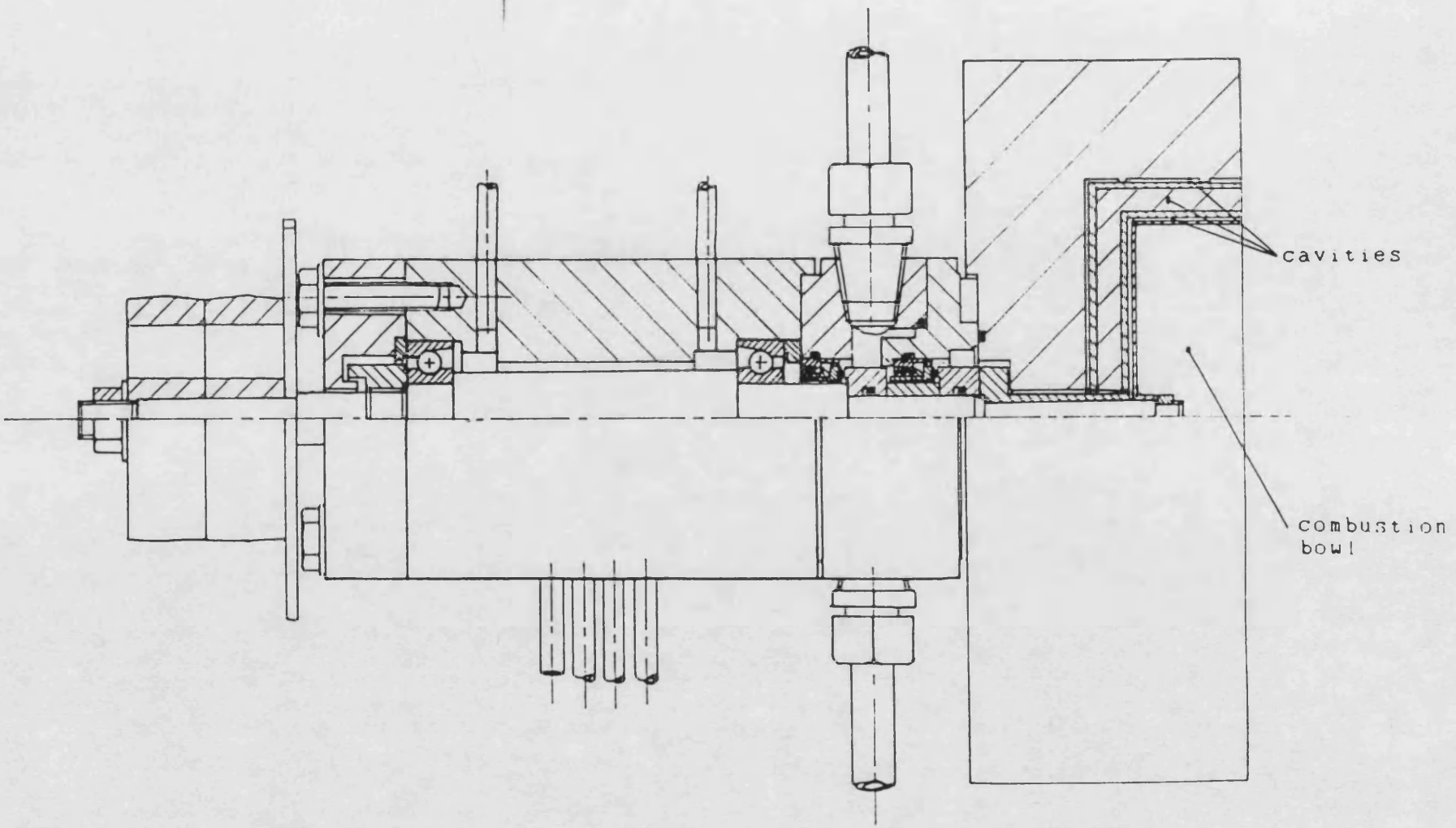

Figure 7.1 Cavities in which air may reside outside combustion bowl.

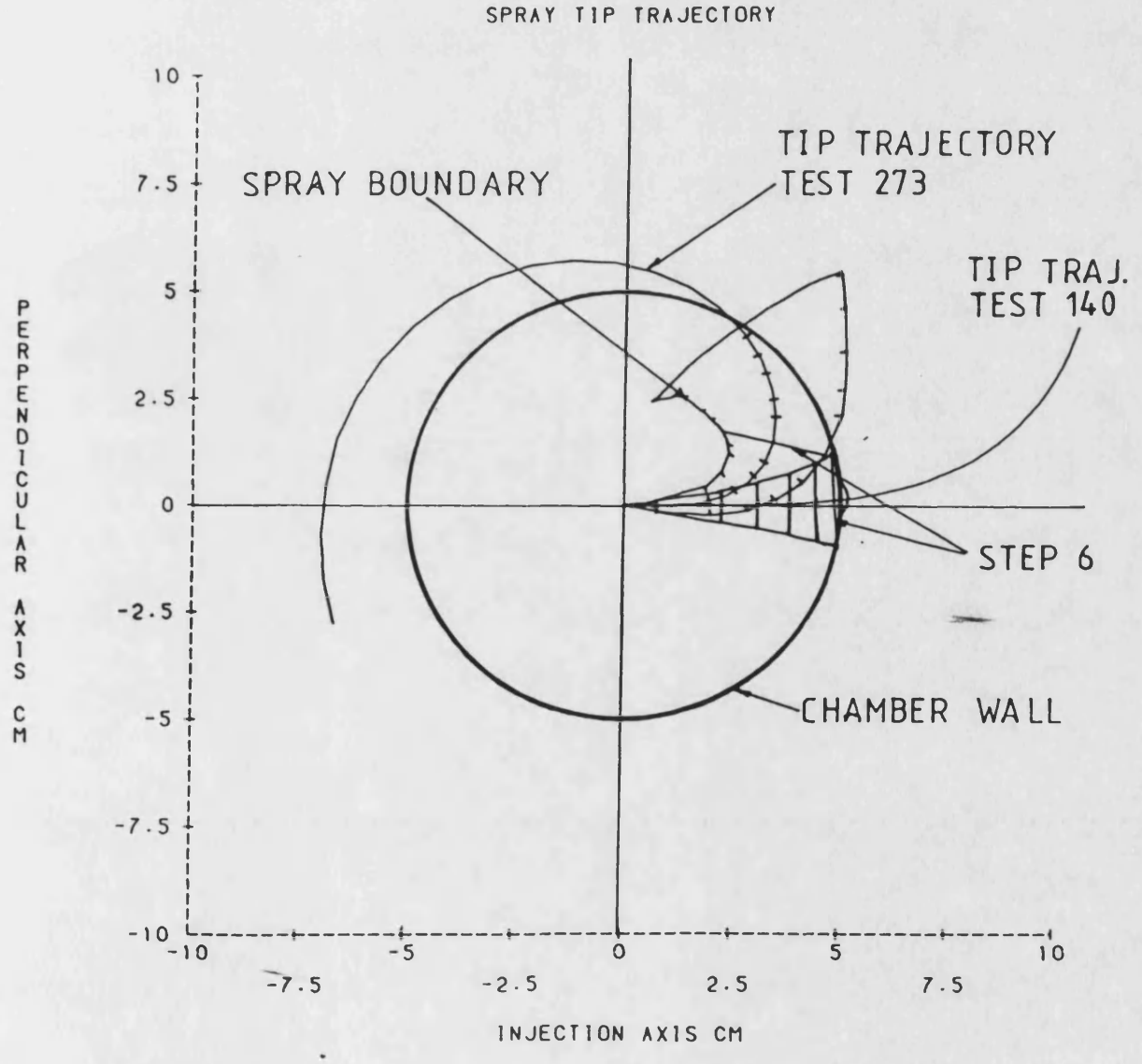

Figure 7.2 Predicted spray trajectory for tests 140 & 273 superimposedonto combustion bowl.

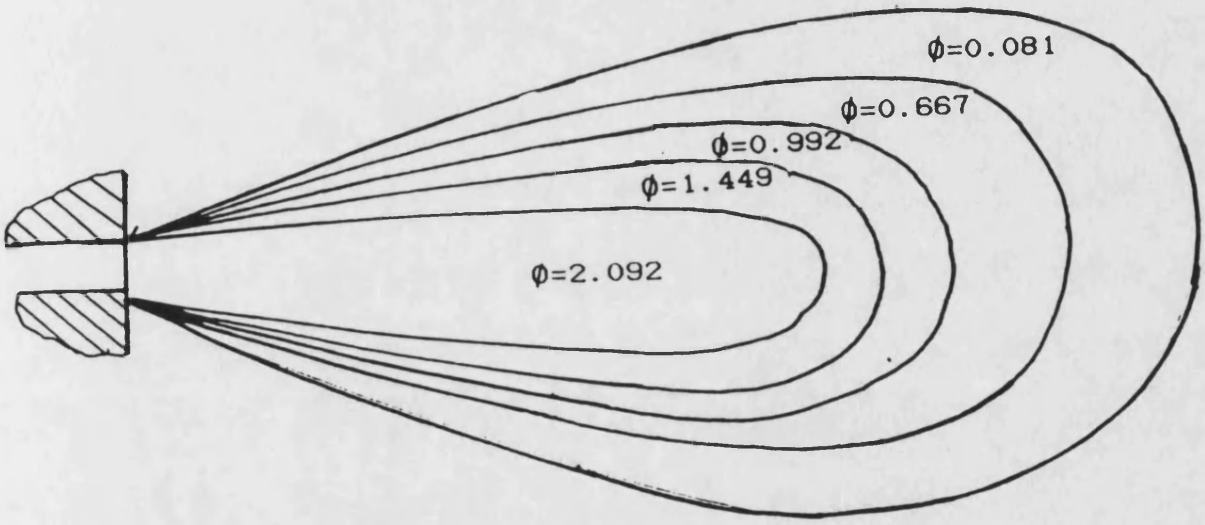

Figure 7.3 Schematic representation of equivalence ratios, taken from table 7.2a for the simulation of test 140.

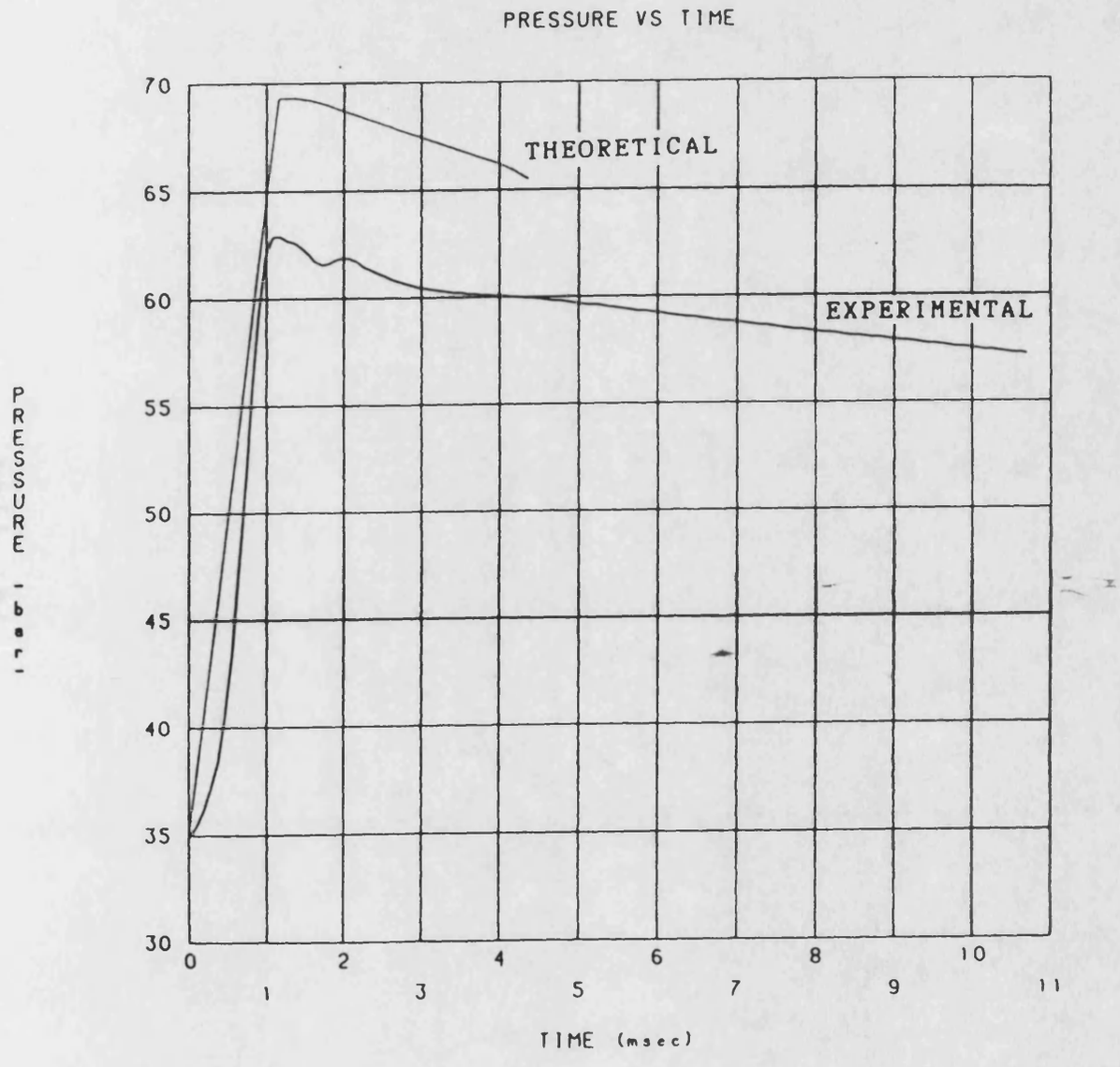

Figure 7.4 Theoretical & experimental pressure curves for test 140.

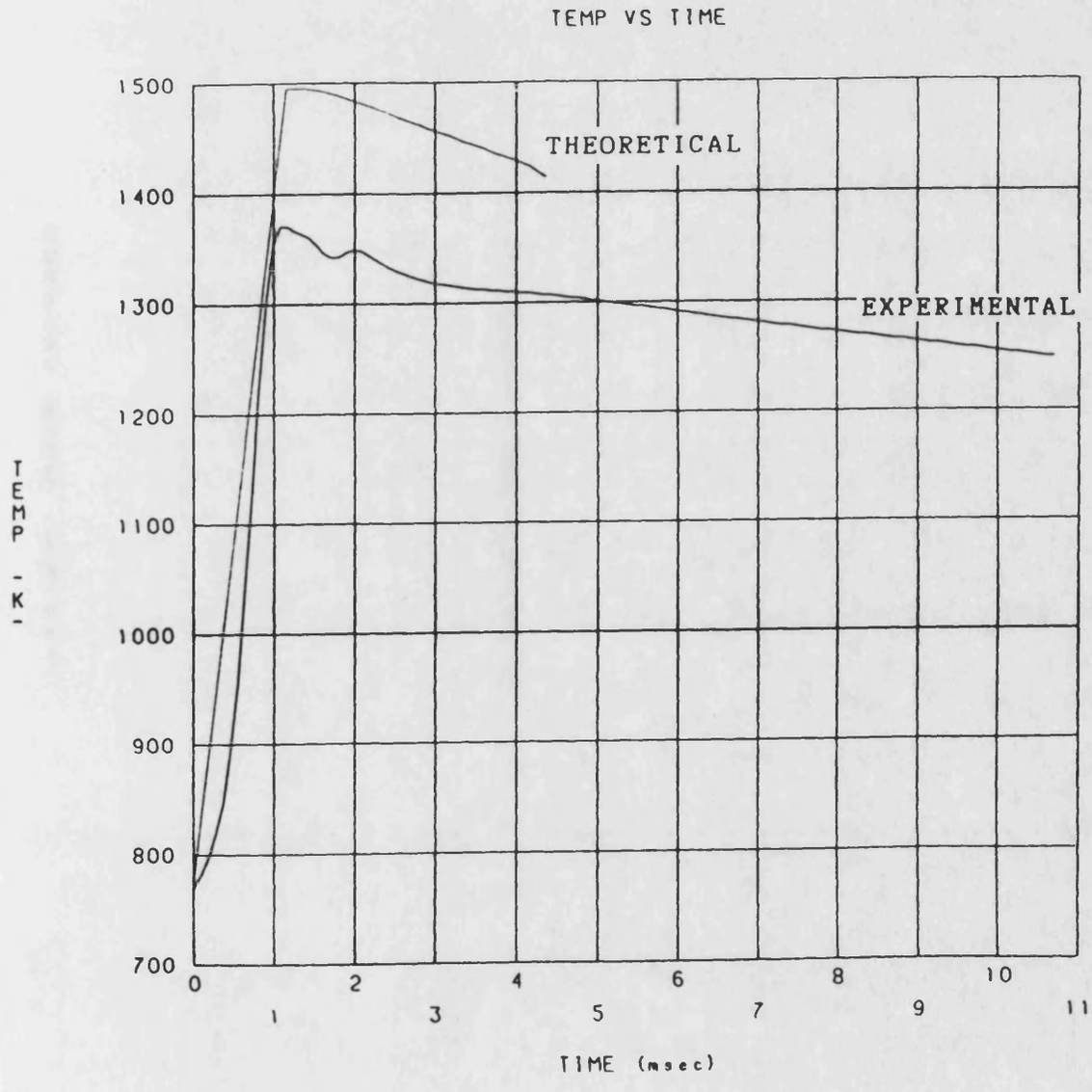

Figure 7.5 Theoretical & experimental temperature curves for test 140

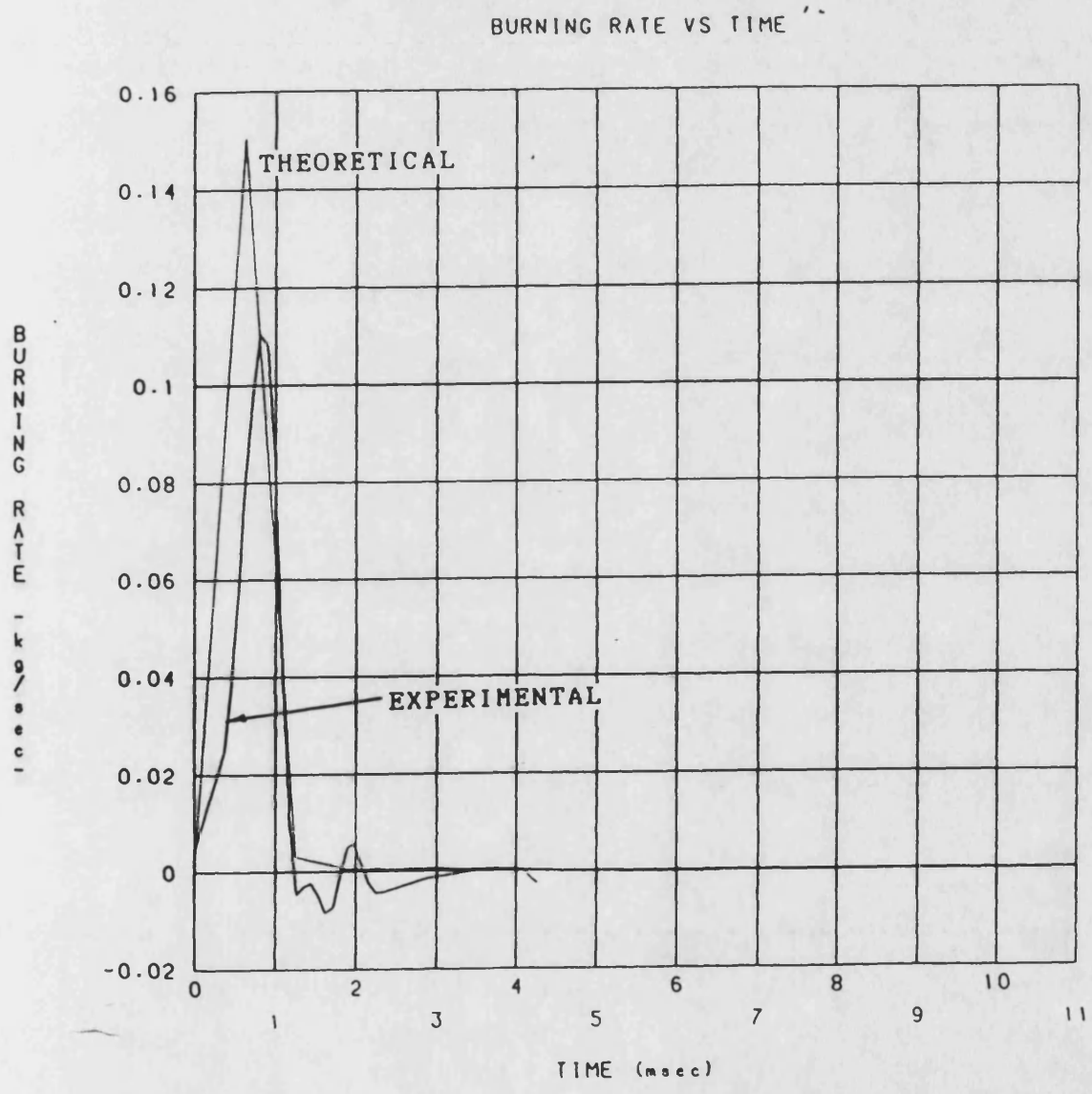

Figure 7.6 Theoretical & experimental burning rate curves for test 140.

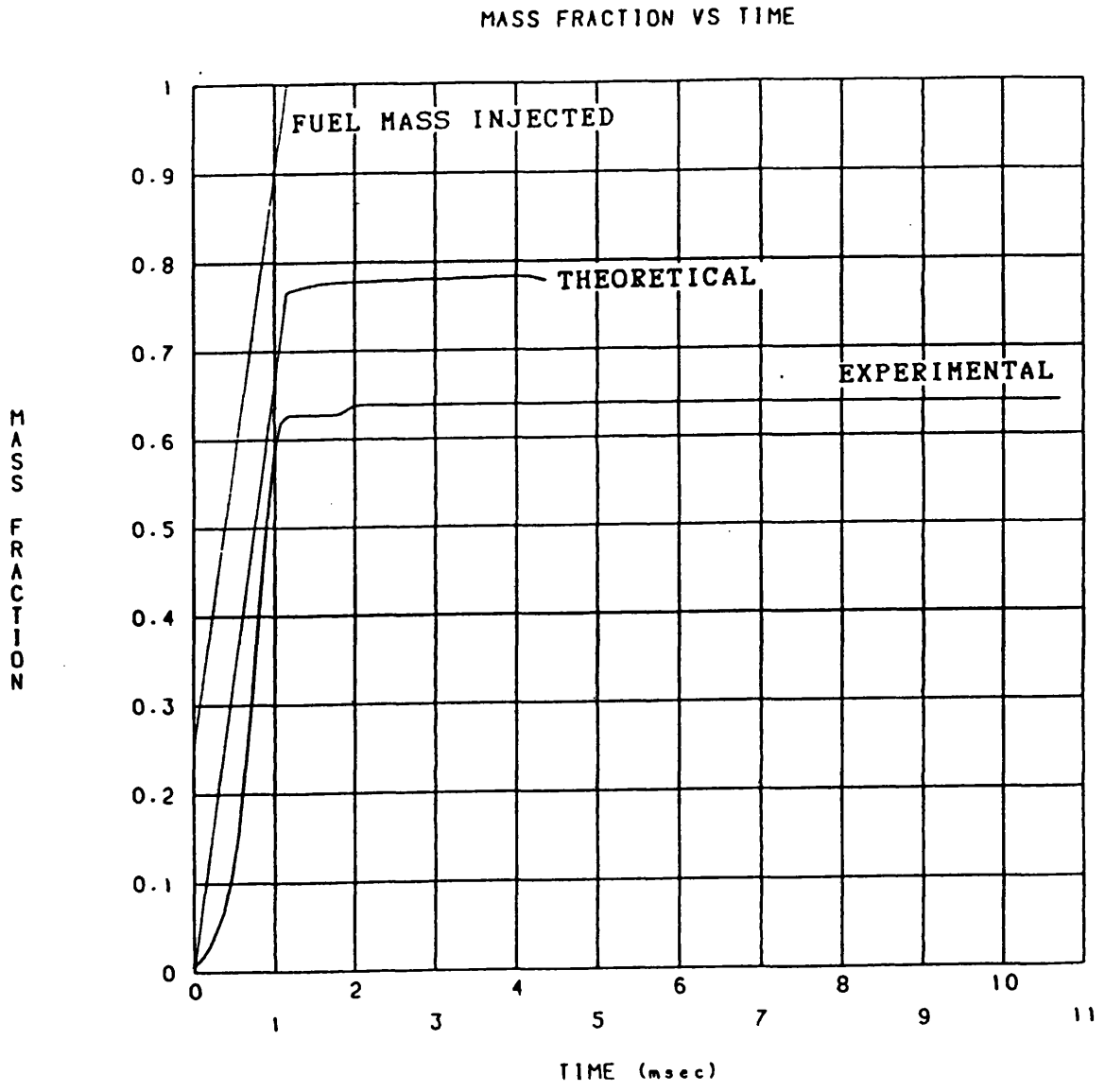

Figure 7.7 Theoretical & experimental mass fraction curves for test 140.

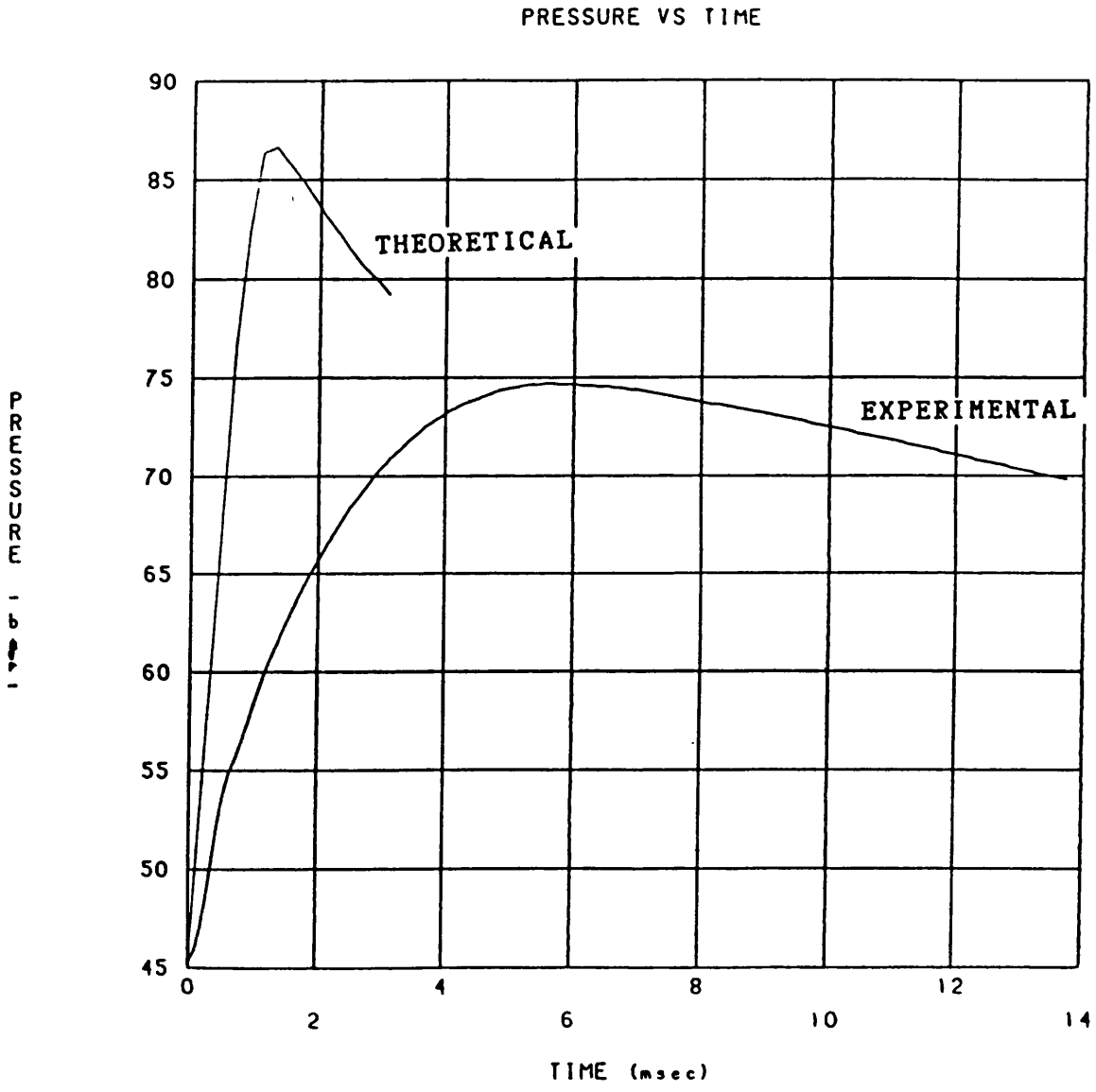

Figure 7.8 Theoretical & experimental pressure curves for test 260.

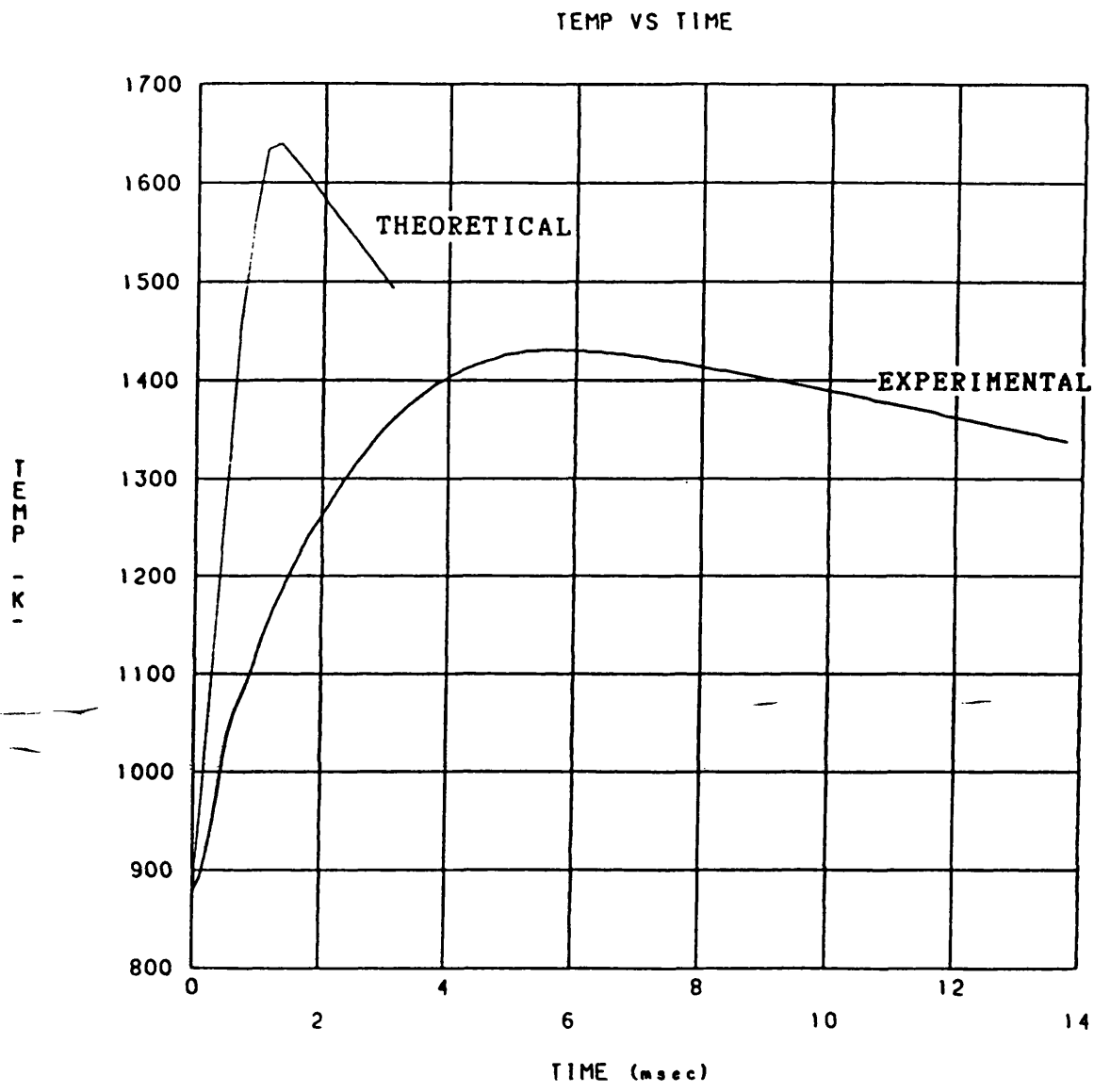

Figure 7.9 Theoretical & experimental temperature curves for test 260

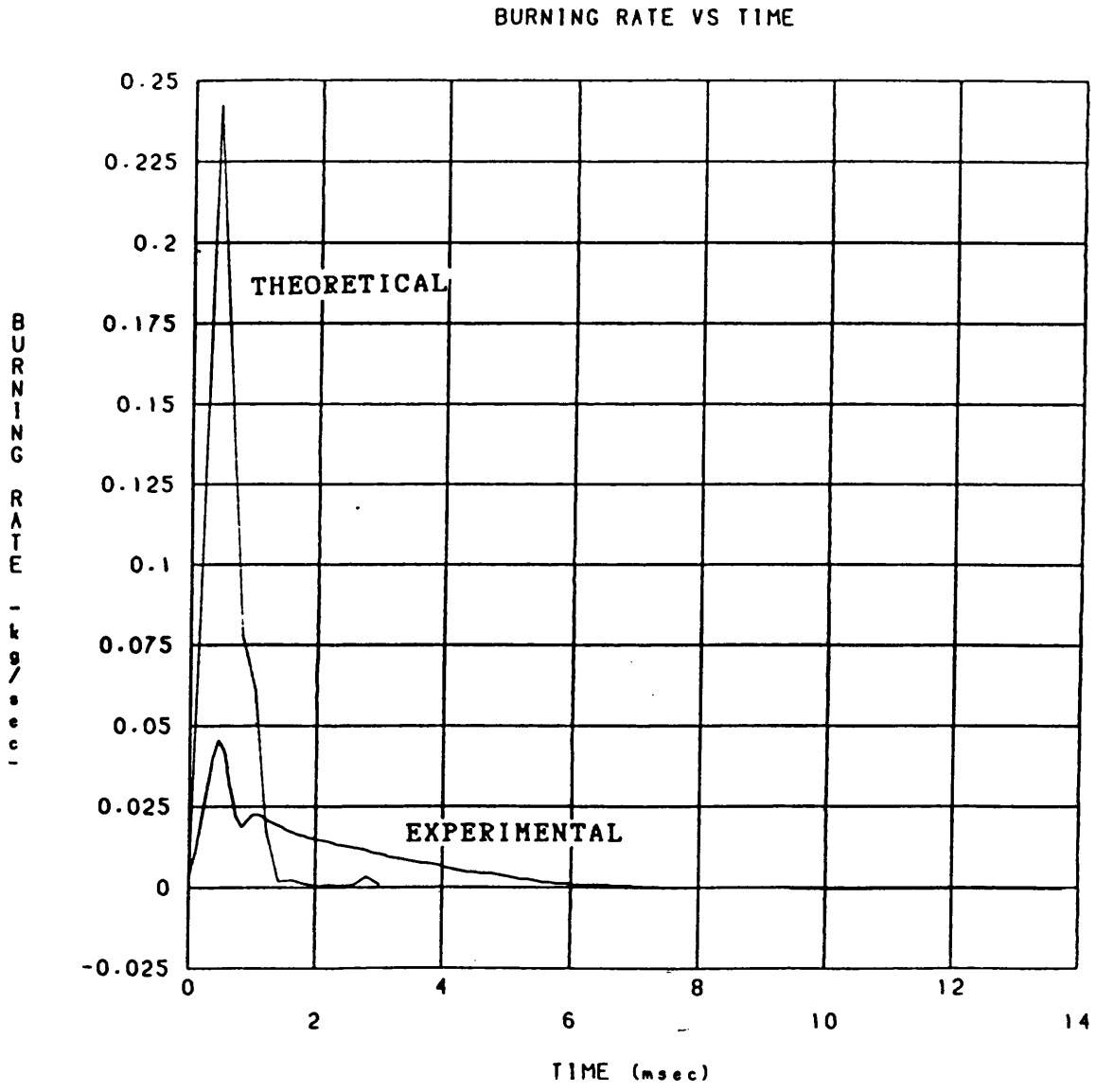

Figure 7.10 Theoretical & experimental burning rate curves for test 260.

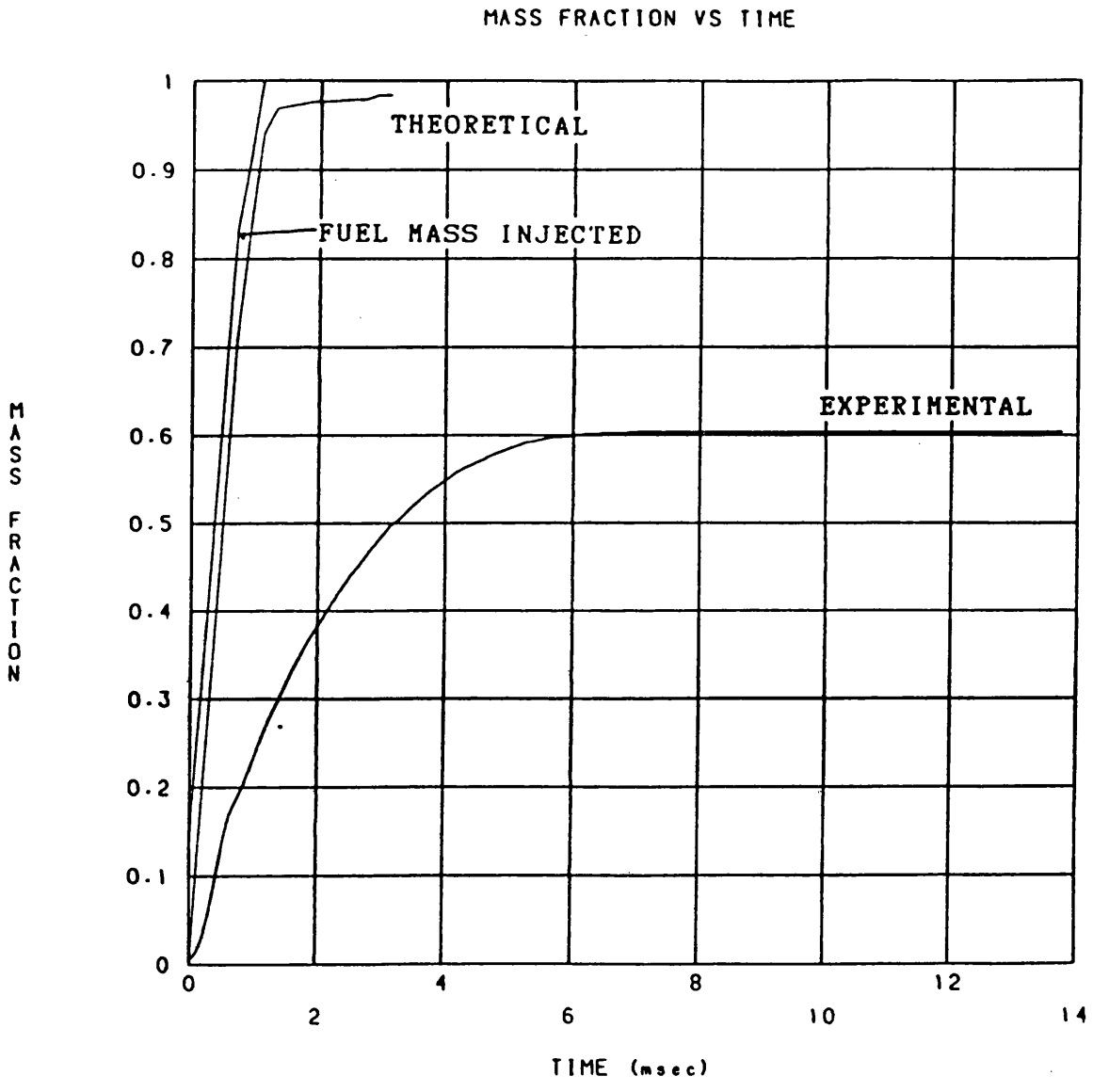

Figure 7.11 Theoretical & experimental mass fraction curves for test 260.

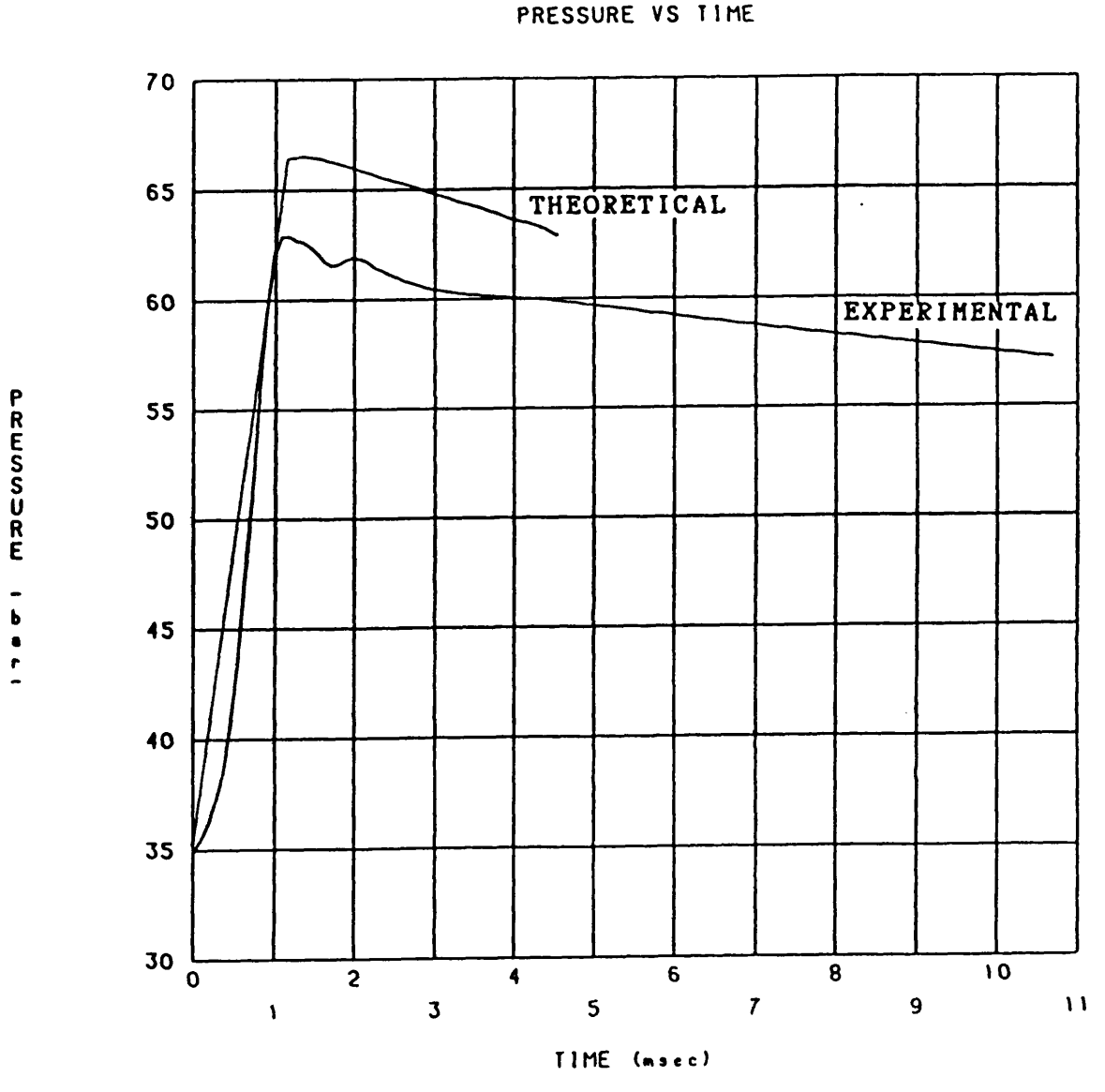

Figure 7.12 Theoretical & experimental pressure curves for test 140 (reduced injection pressure).

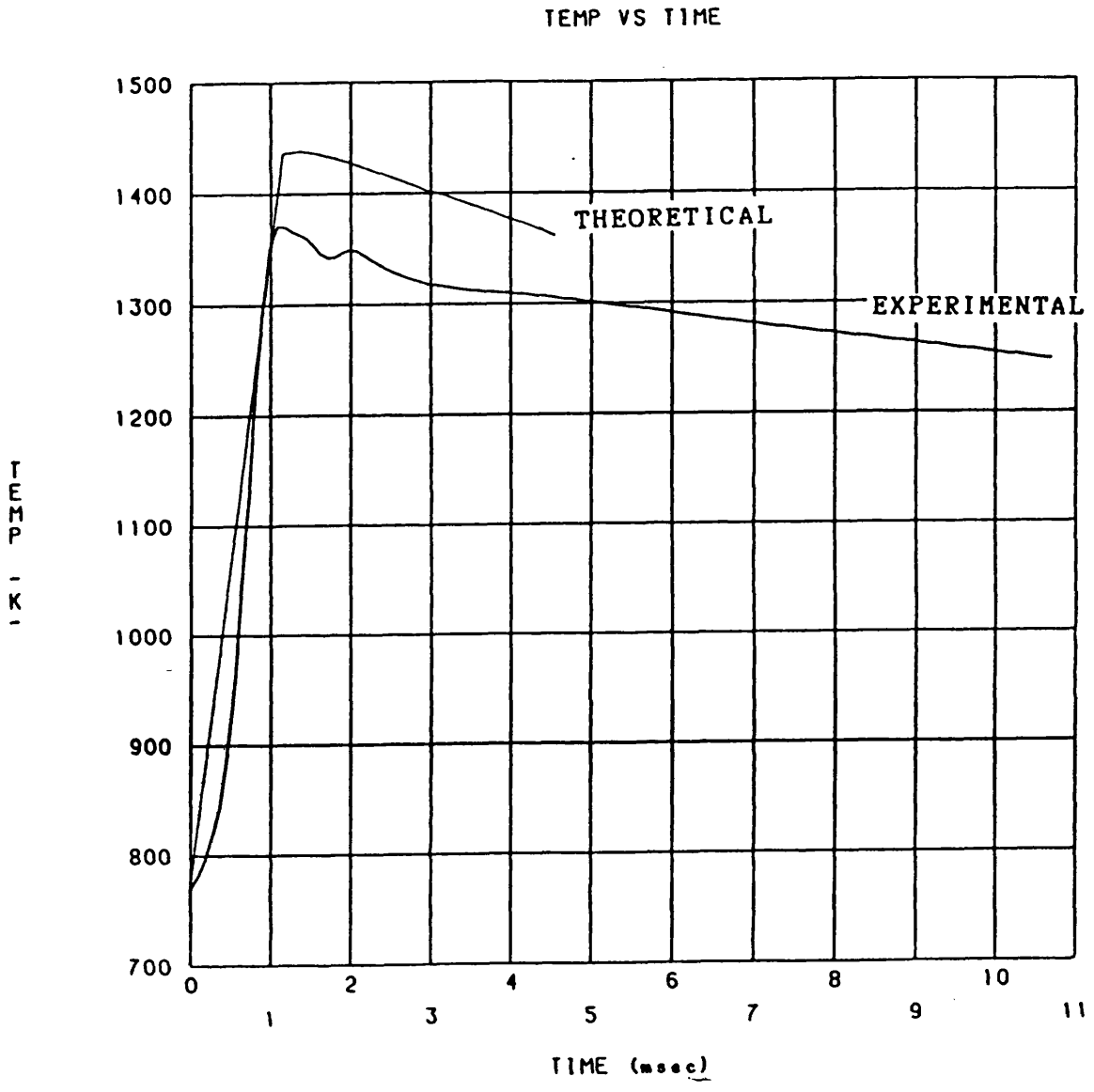

Figure 7.13 Theoretical & experimental temperature curves for test 140 (reduced injection pressure).

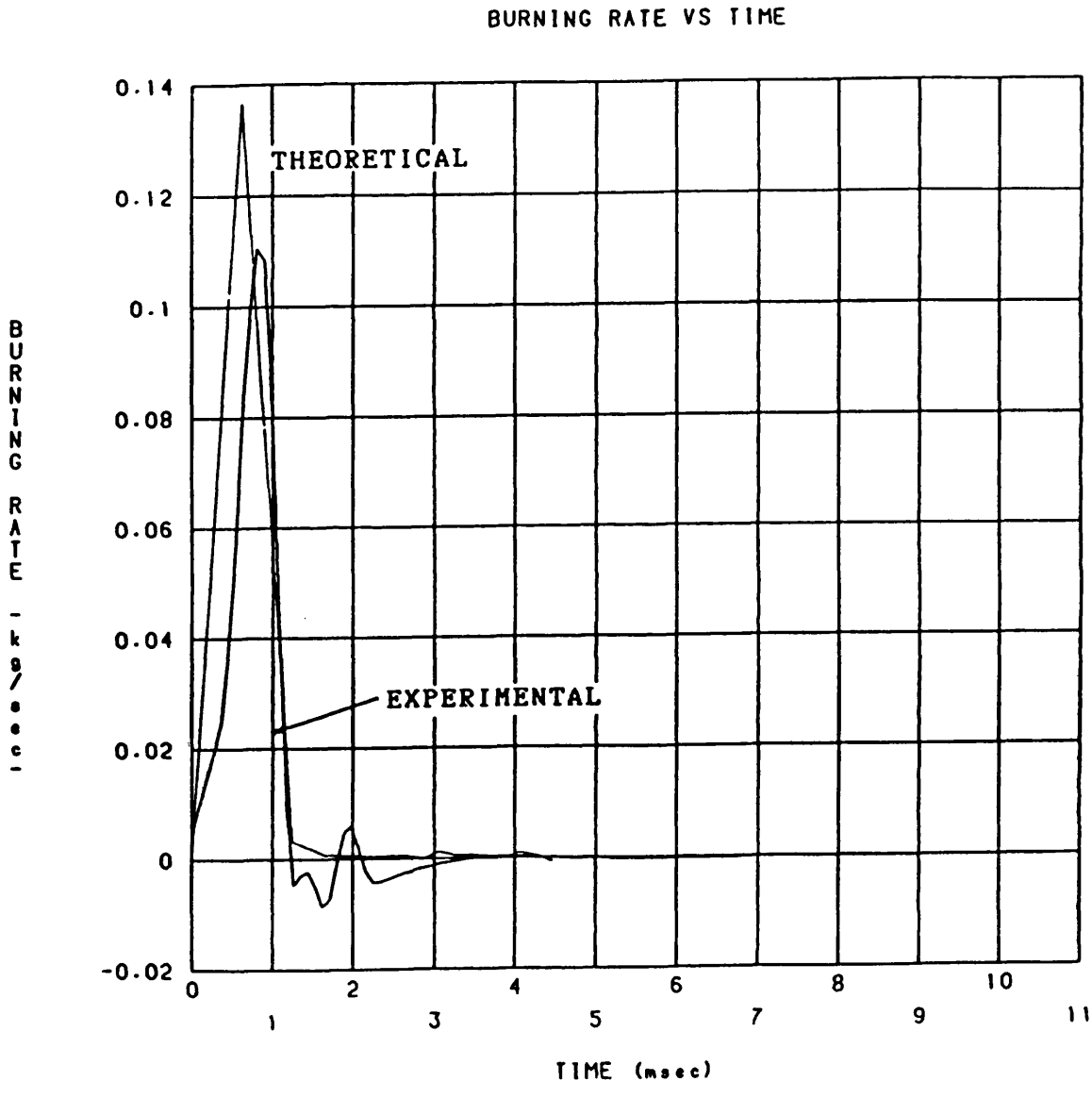

Figure 7.14 Theoretical & experimental burning rate curves for test 140 (reduced injection pressure).

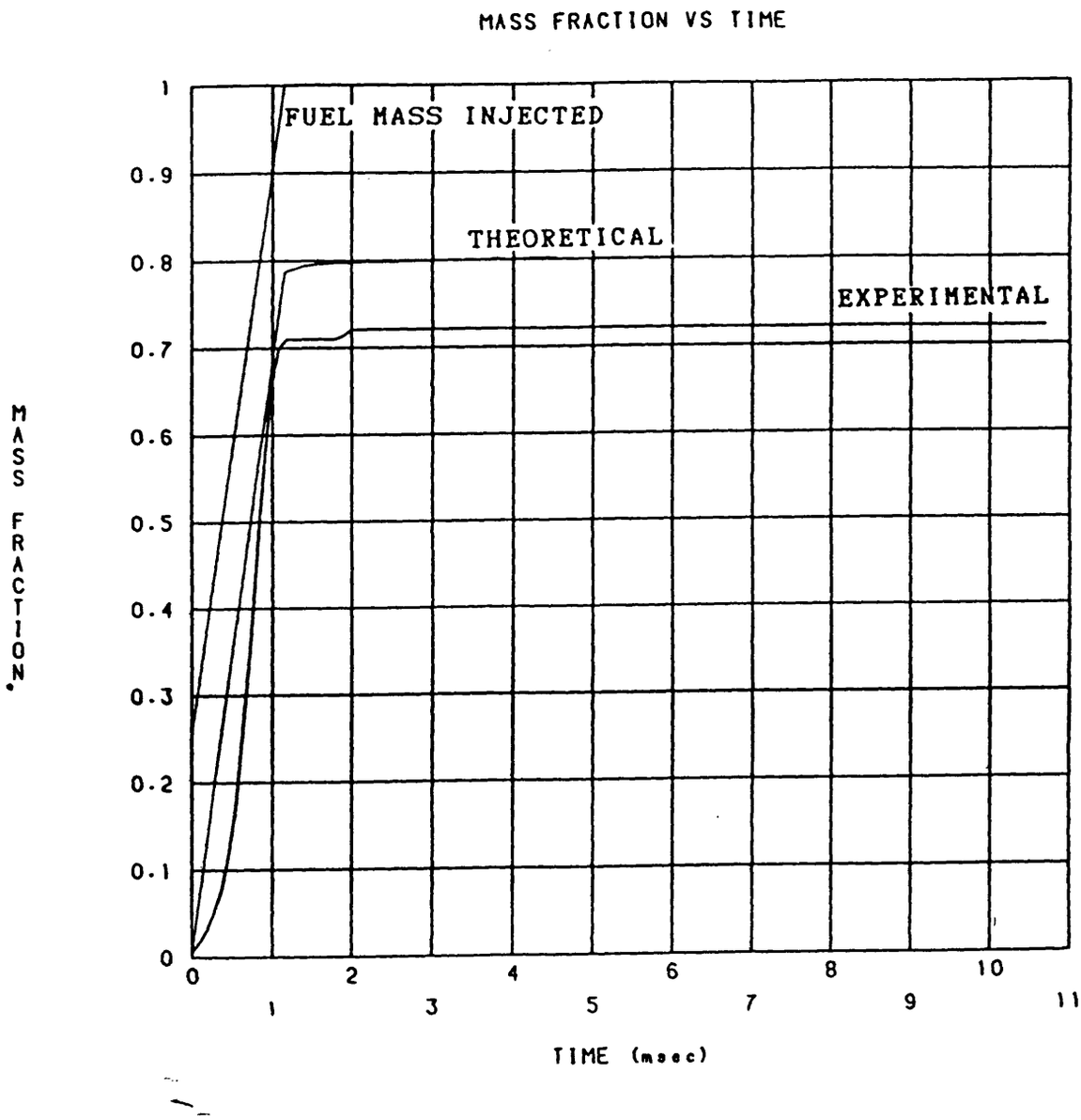

Figure 7.15 Theoretical & experimental mass fraction curves for test 140 (reduced injection pressure).

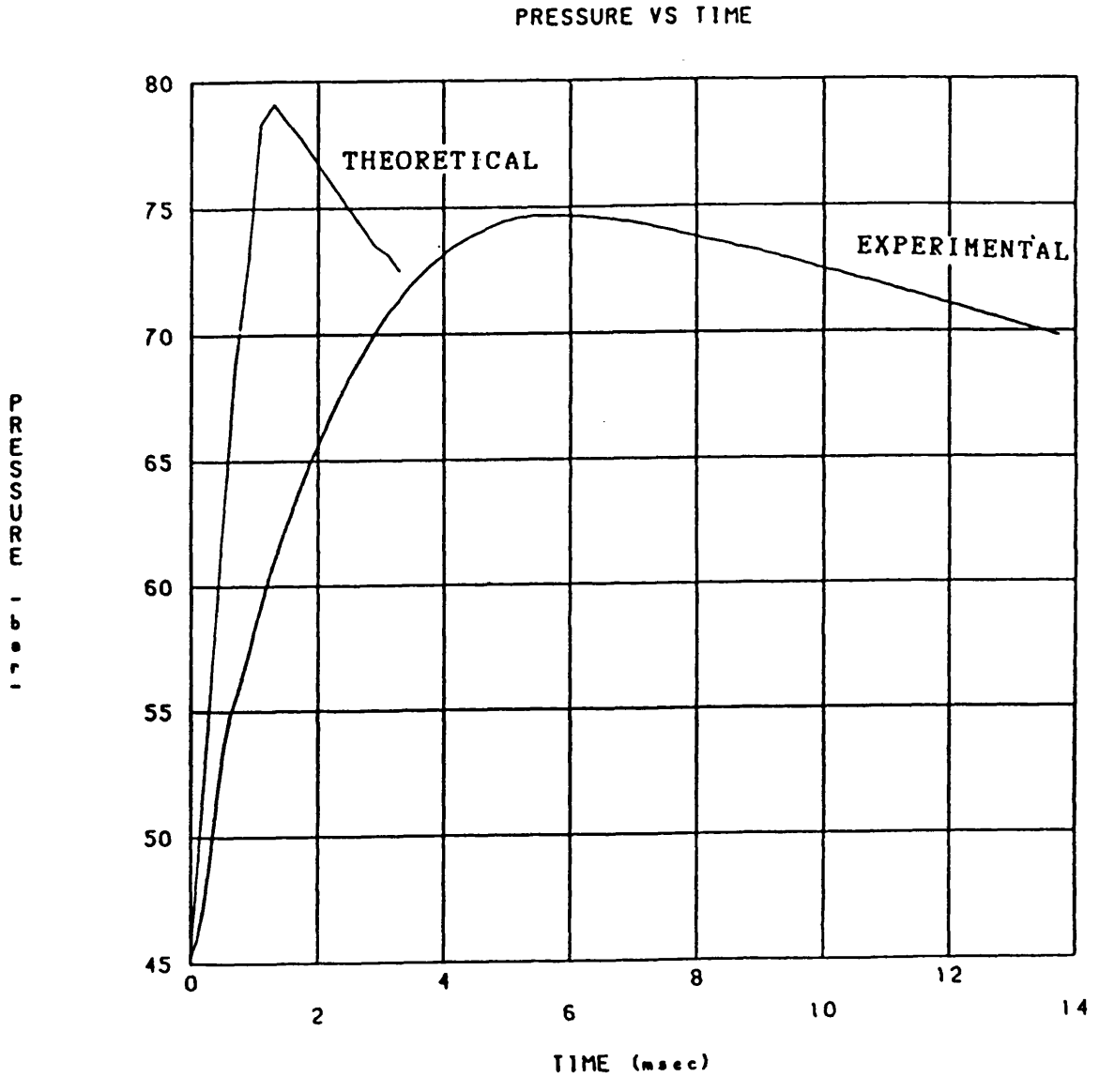

Figure 7.16 Theoretical & experimental pressure curves for test 260 (reduced injection pressure).

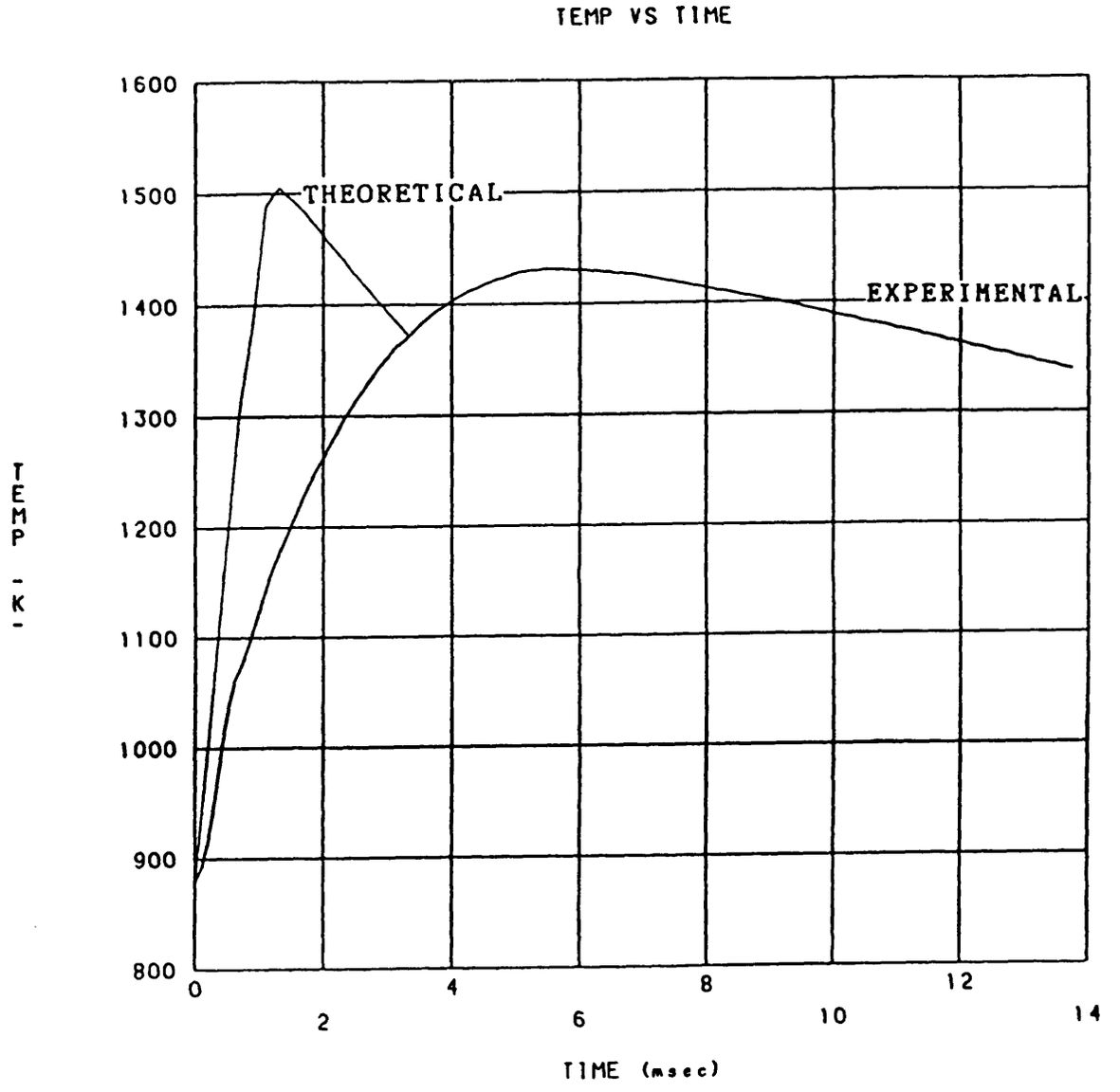

Figure 7.17 Theoretical & experimental temperature curves for test 260 (reduced injection pressure).

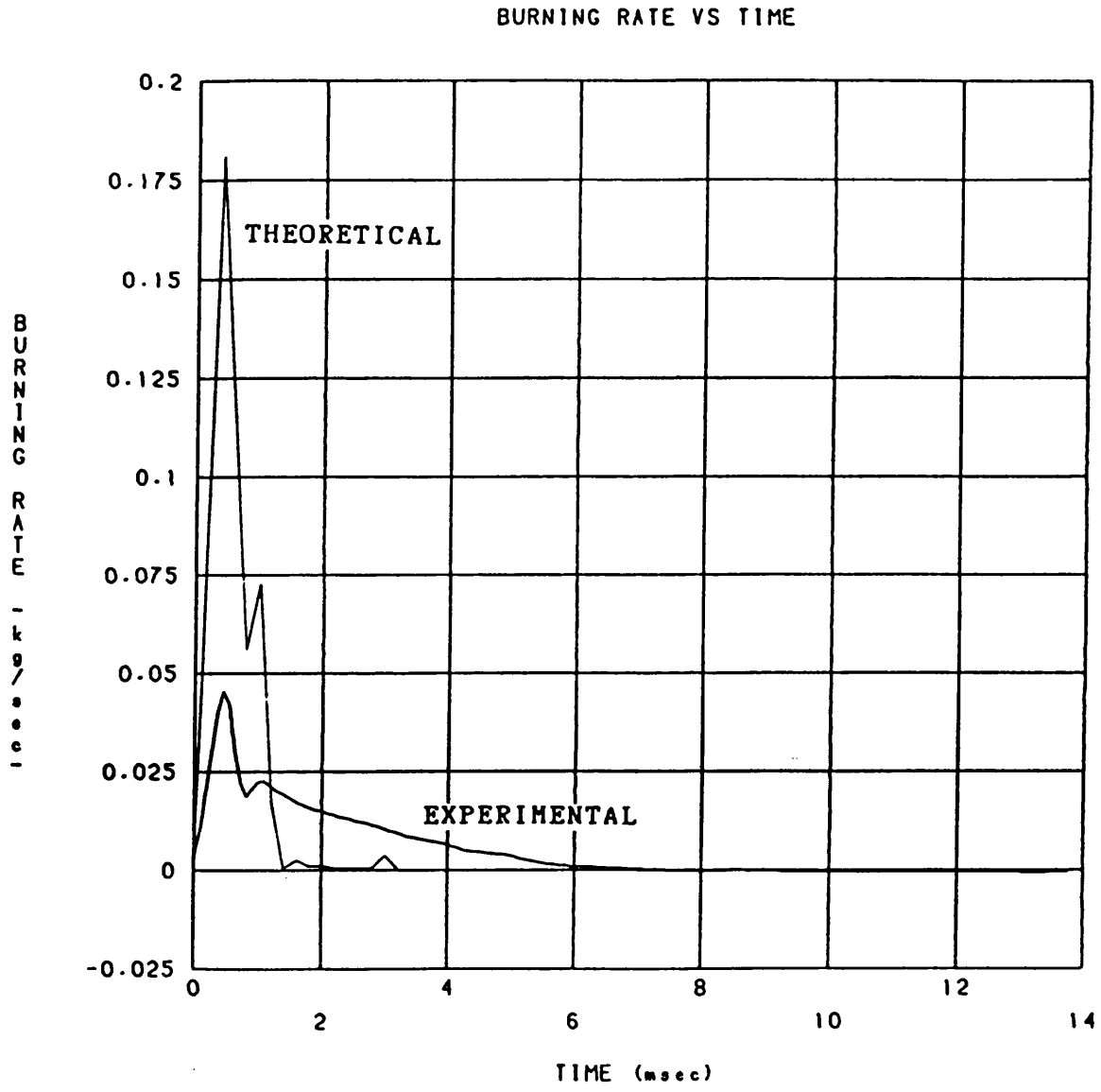

Figure 7.18 Theoretical & experimental burning rate curves for test 260 (reduced injection pressure).

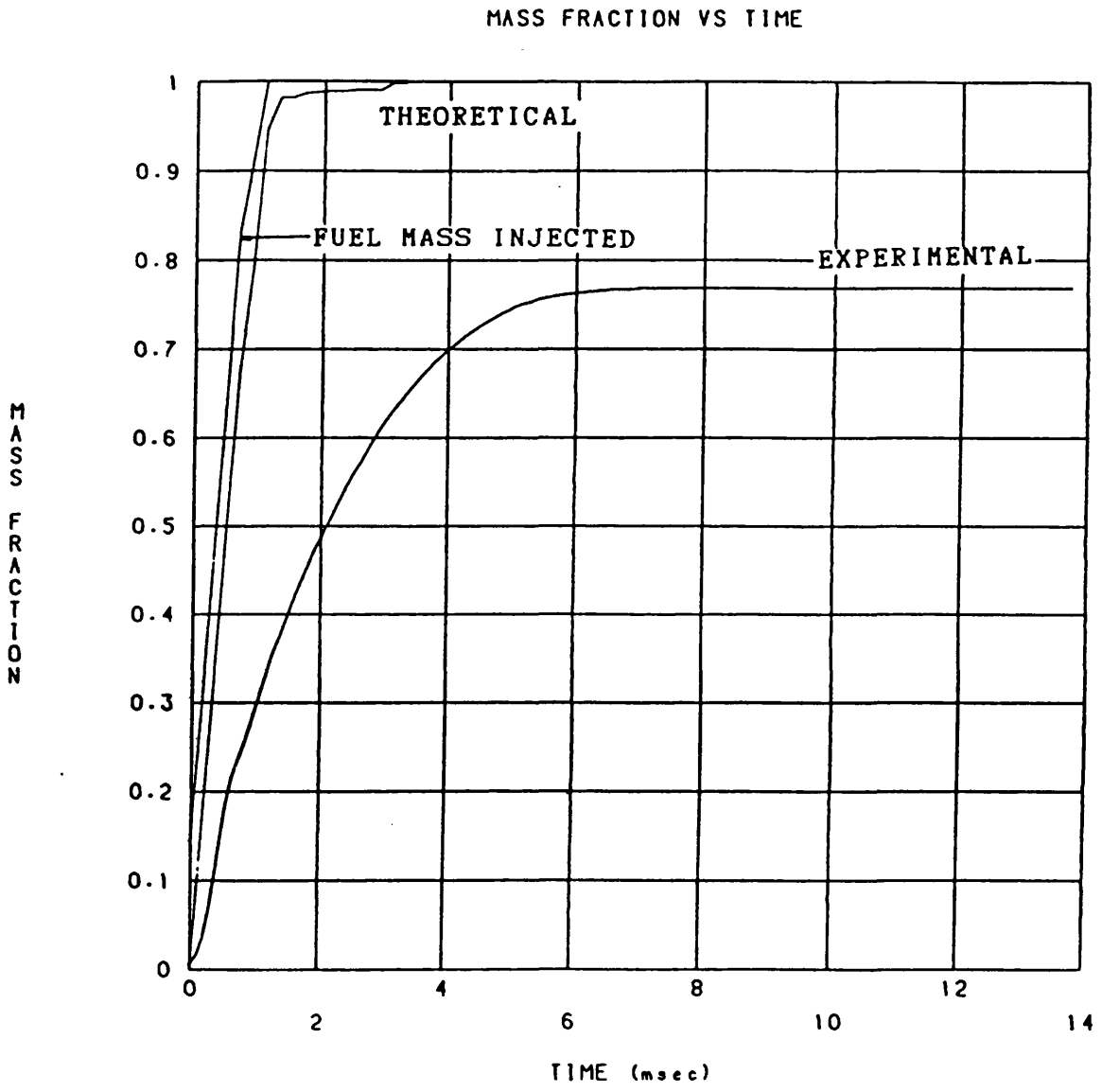

Figure 7.19 Theoretical & experimental mass fraction curves for test 260 (reduced injection pressure).

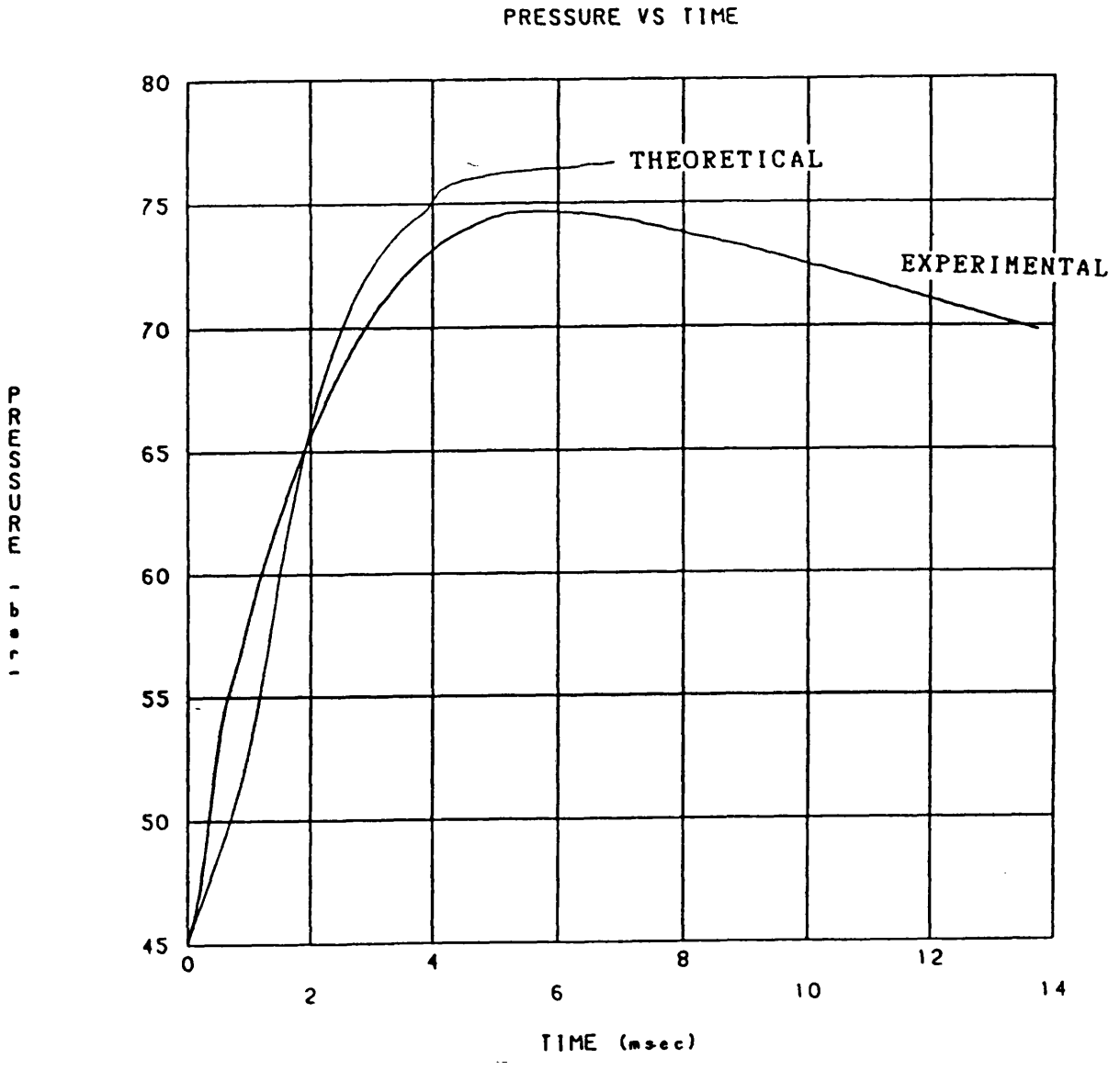

Figure 7.20 Theoretical & experimental pressure curves for test 260 (equal fuelling & reduced swirl).

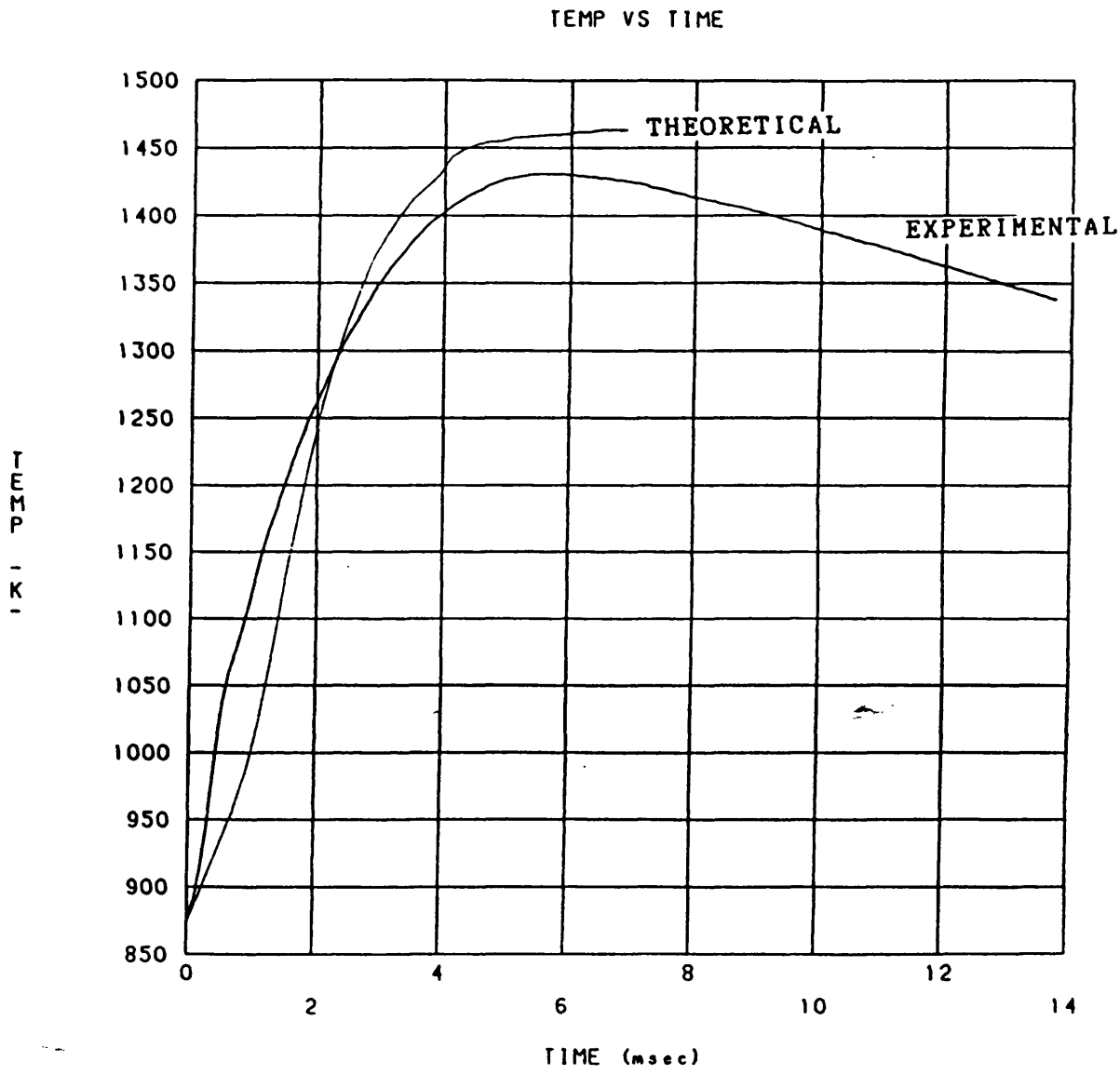

Figure 7.21 Theoretical & experimental temperature curves for test 260 (equal fuelling & reduced swirl).

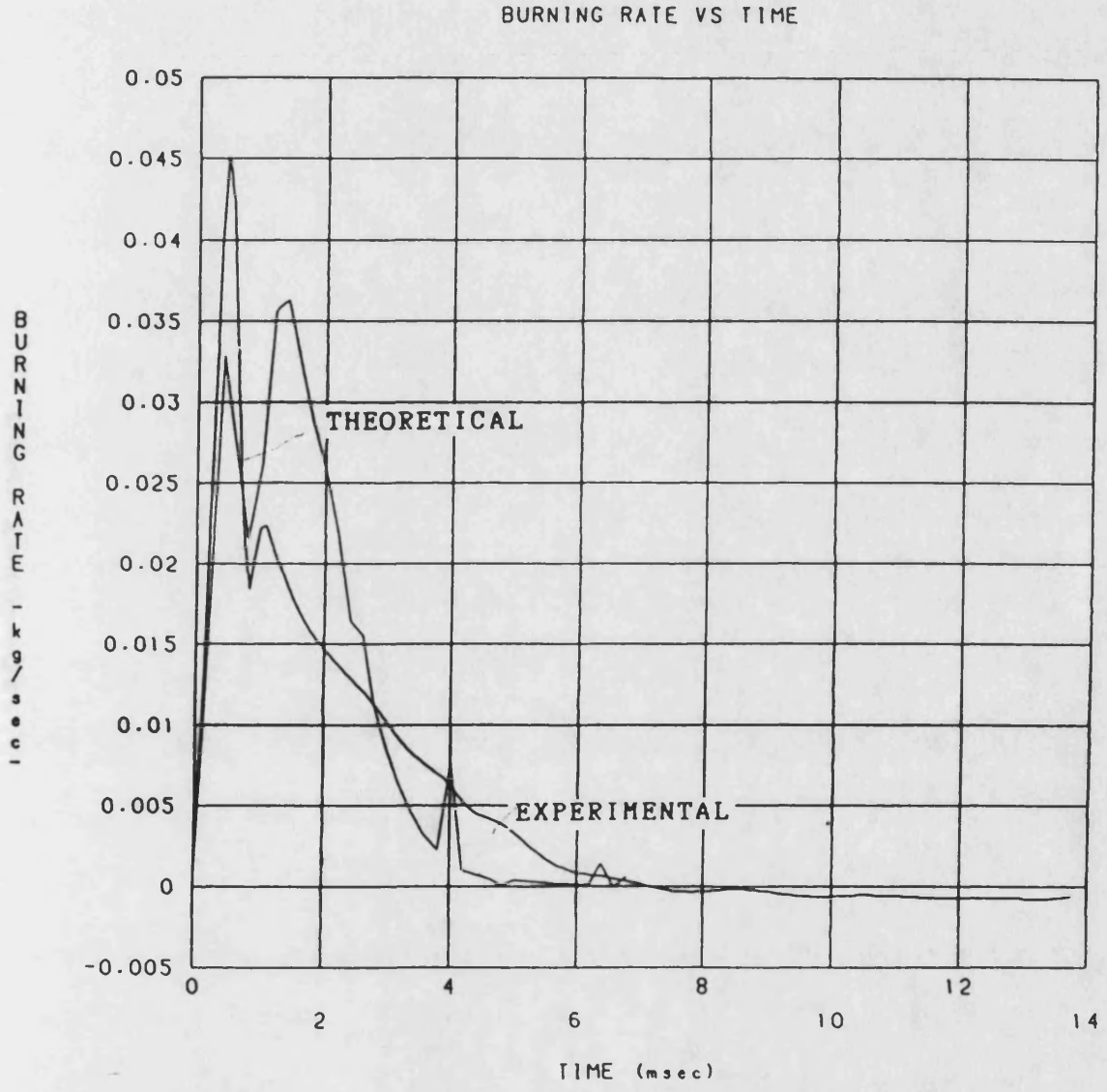

Figure 7.22 Theoretical & experimental burning rate curves for test 260 (equal fuelling & reduced swirl).

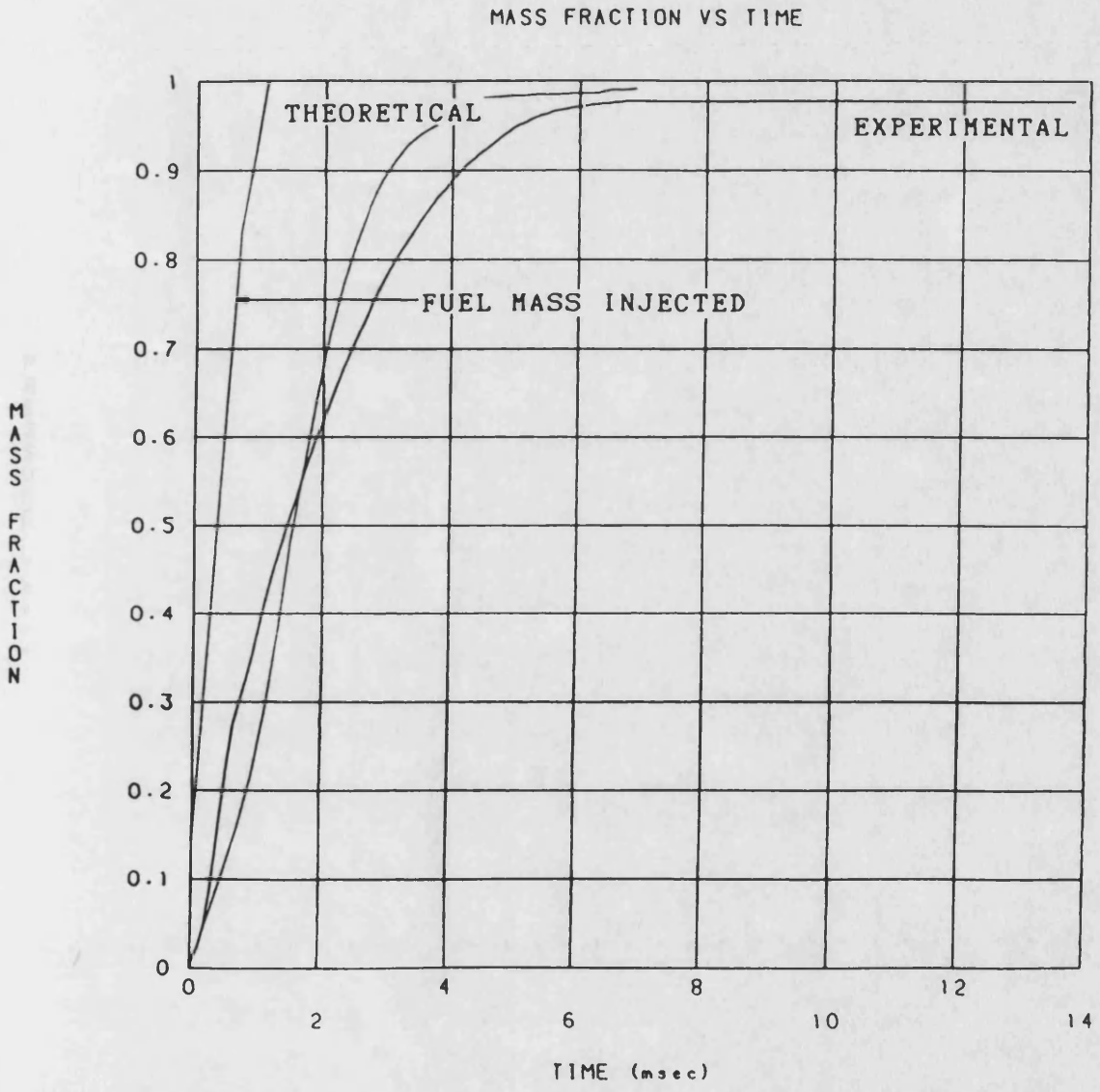

Figure 7.23 Theoretical & experimental mass fraction curves for test 260 (equal fuelling & reduced swirl).

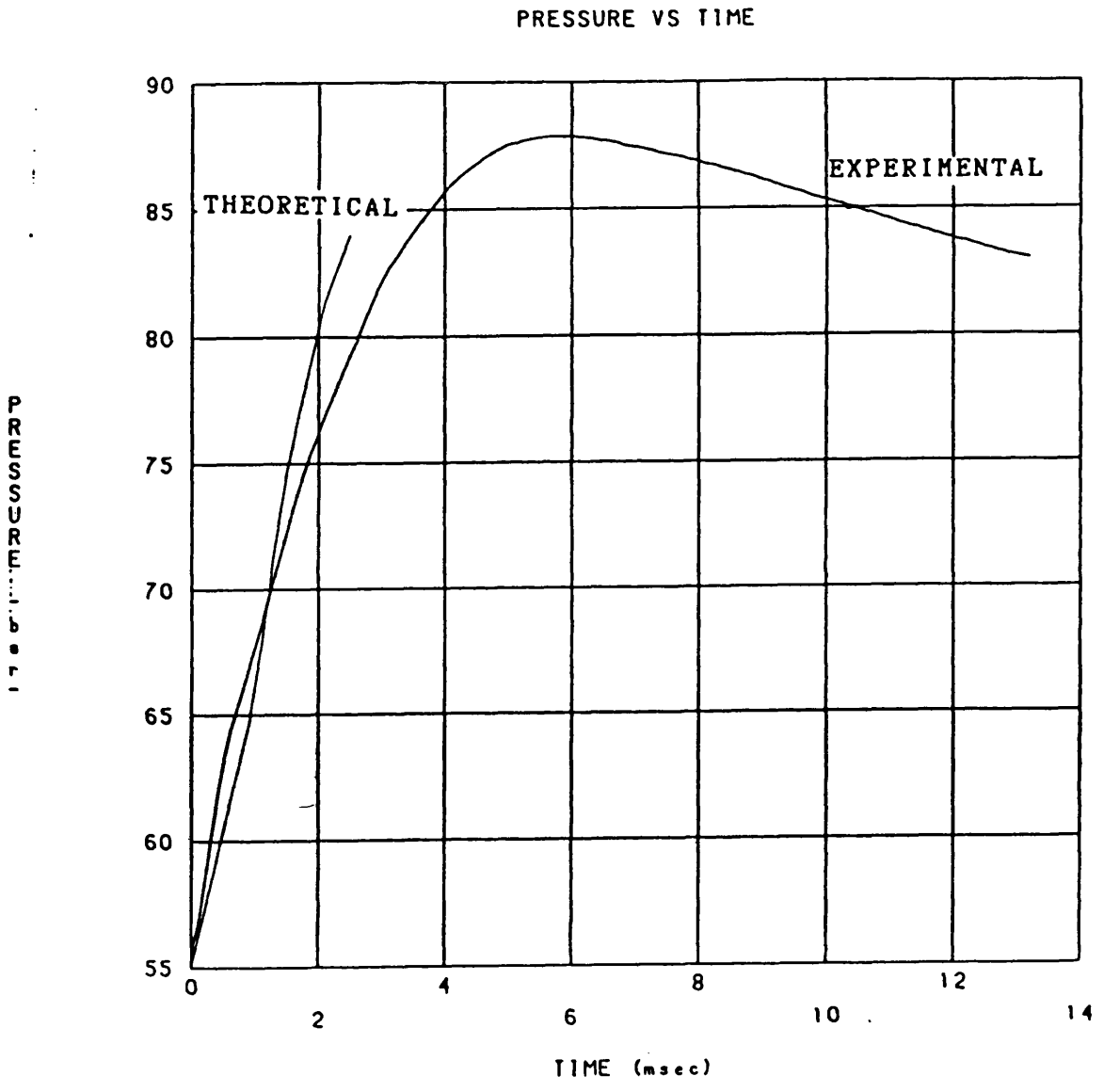

Figure 7.24 Theoretical & experimental pressure curves for test 273 (equal fuelling & reduced swirl).

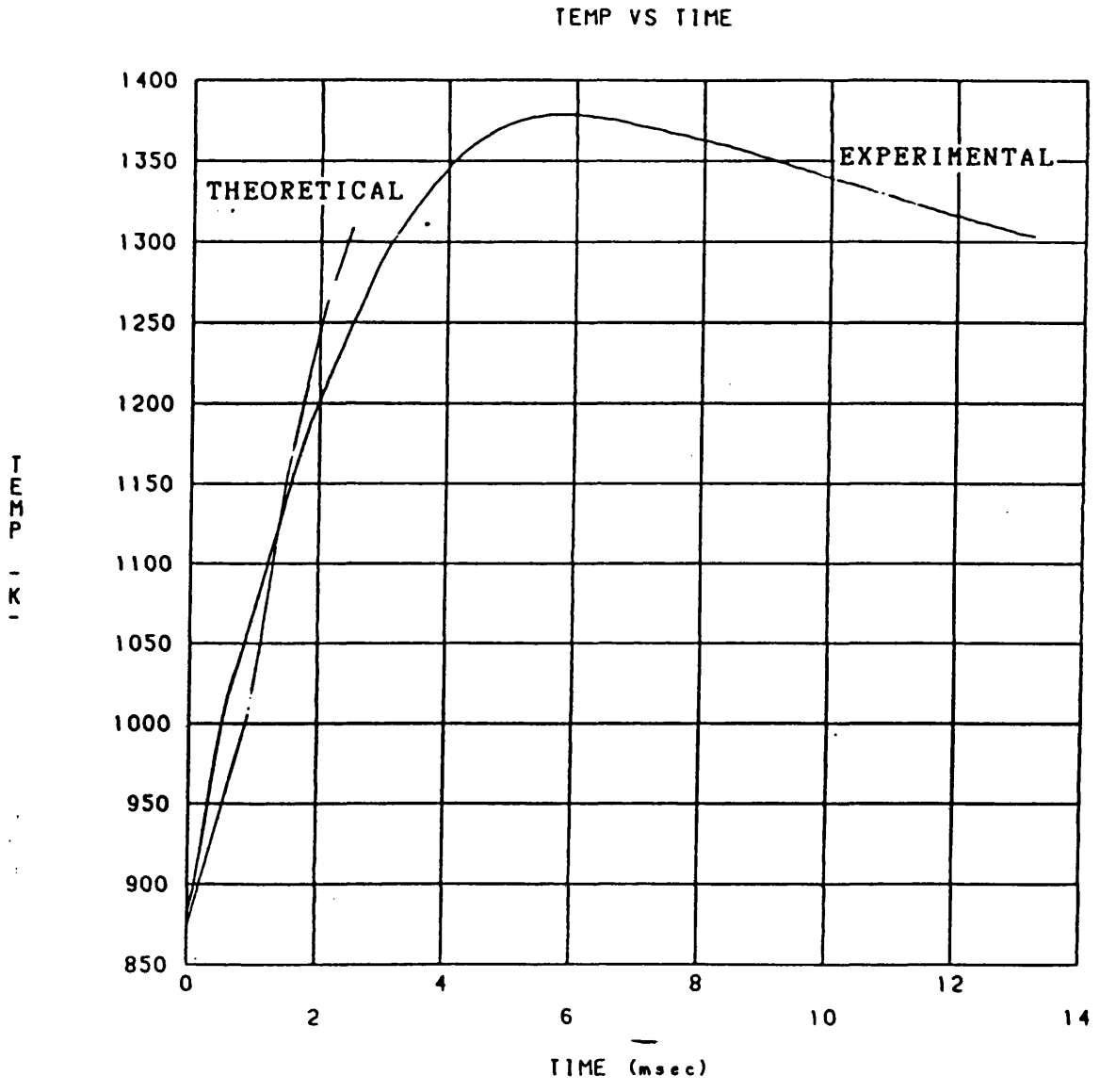

Figure 7.25 Theoretical & experimental temperature curves for test 273 (equal fuelling & reduced swirl).

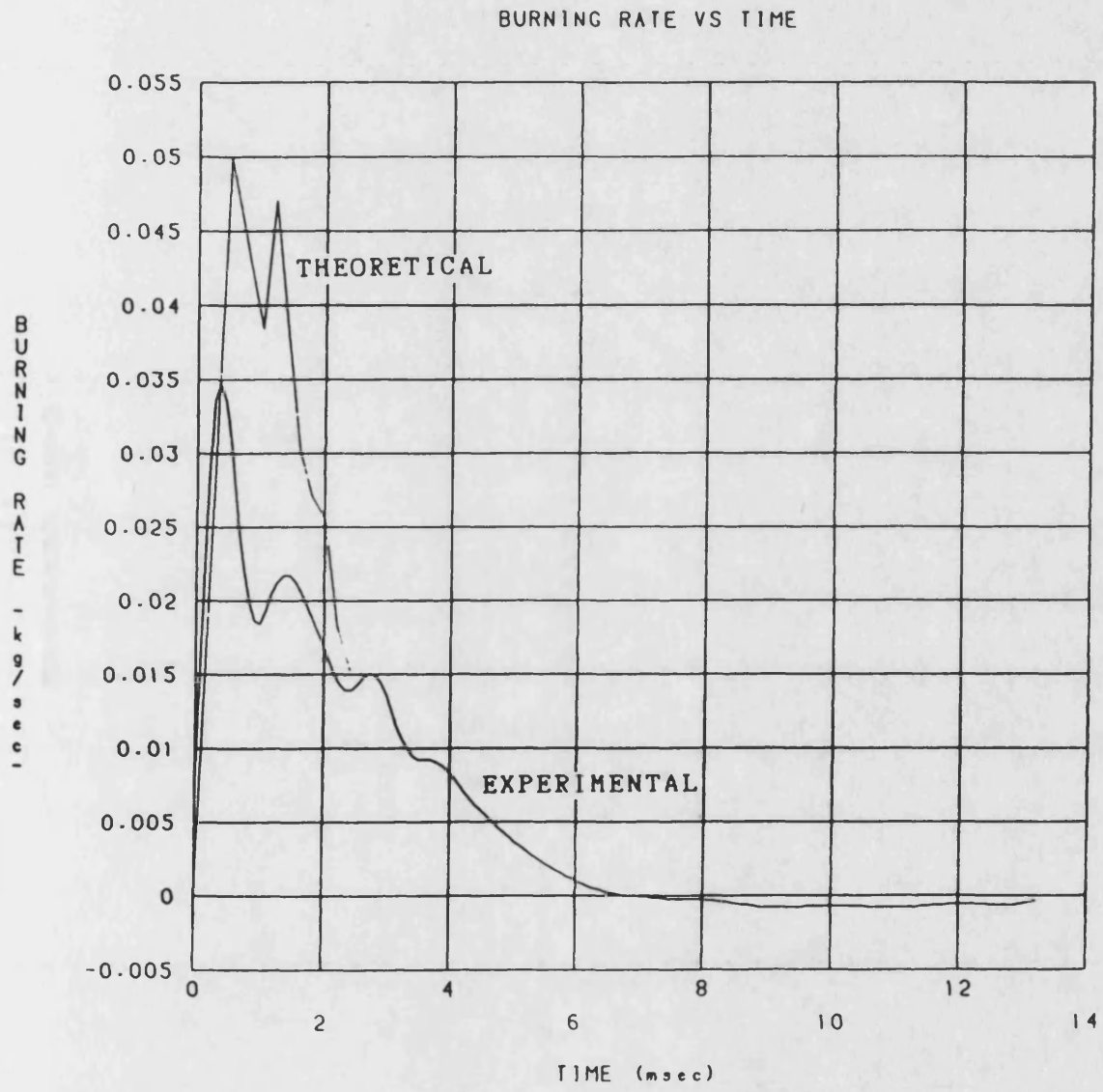

Figure 7.26 Theoretical & experimental burning rate curves for test 273 (equal fuelling & reduced swirl).

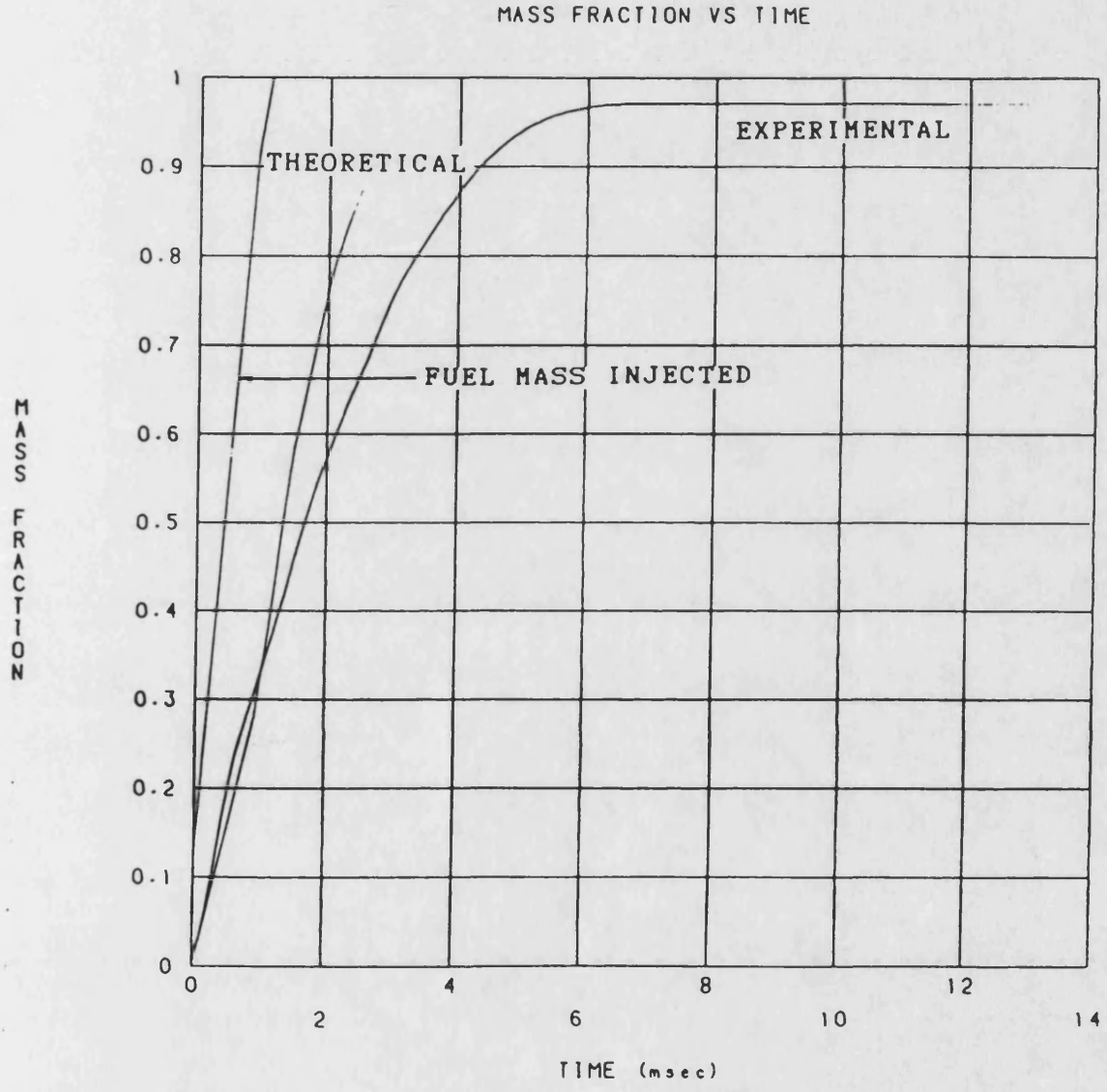

Figure 7.27 Theoretical & experimental mass fraction curves for test 273 (equal fuelling & reduced swirl).

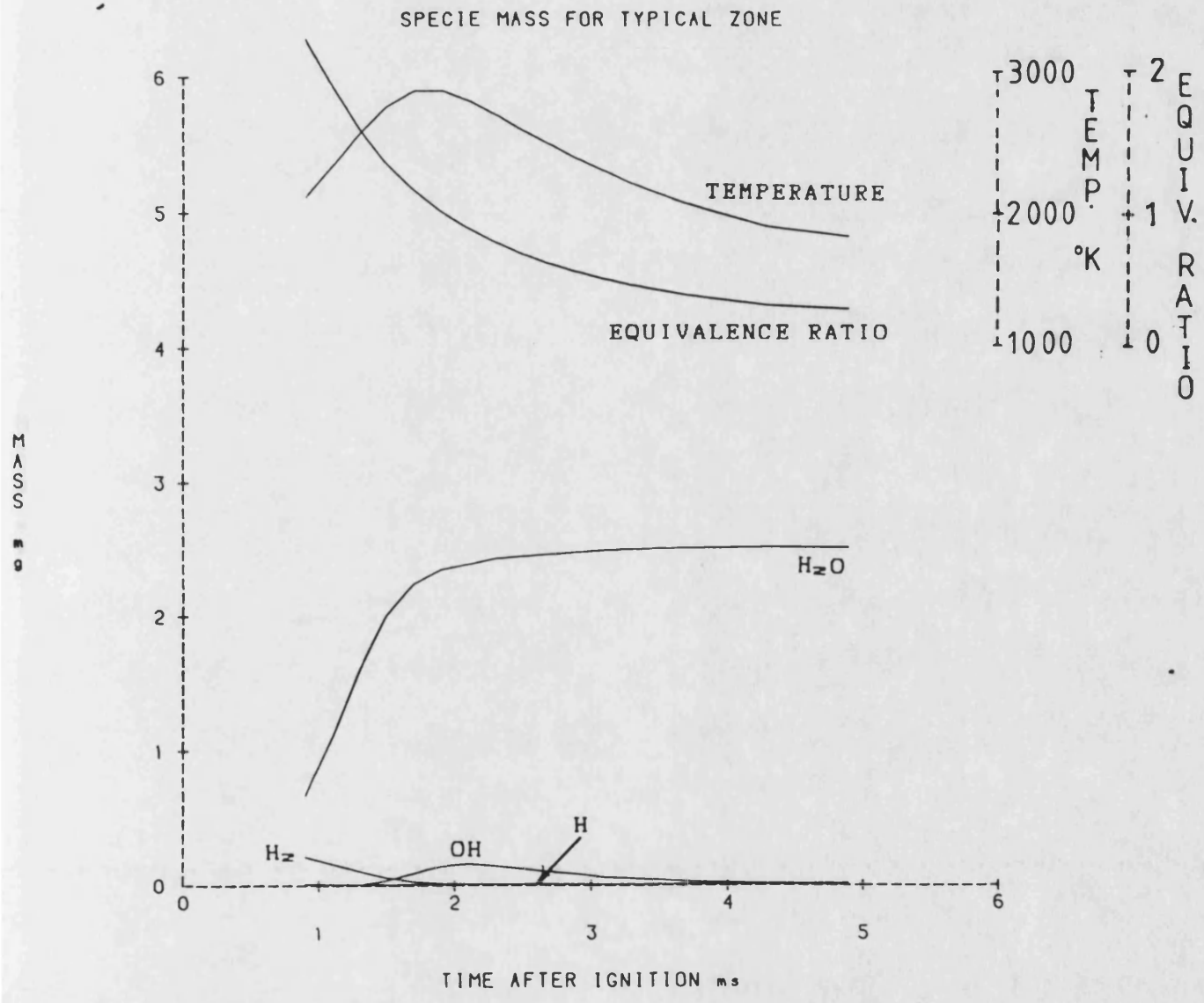

Figure 7.28 Hydrogen Specie Histories for a typical zone.

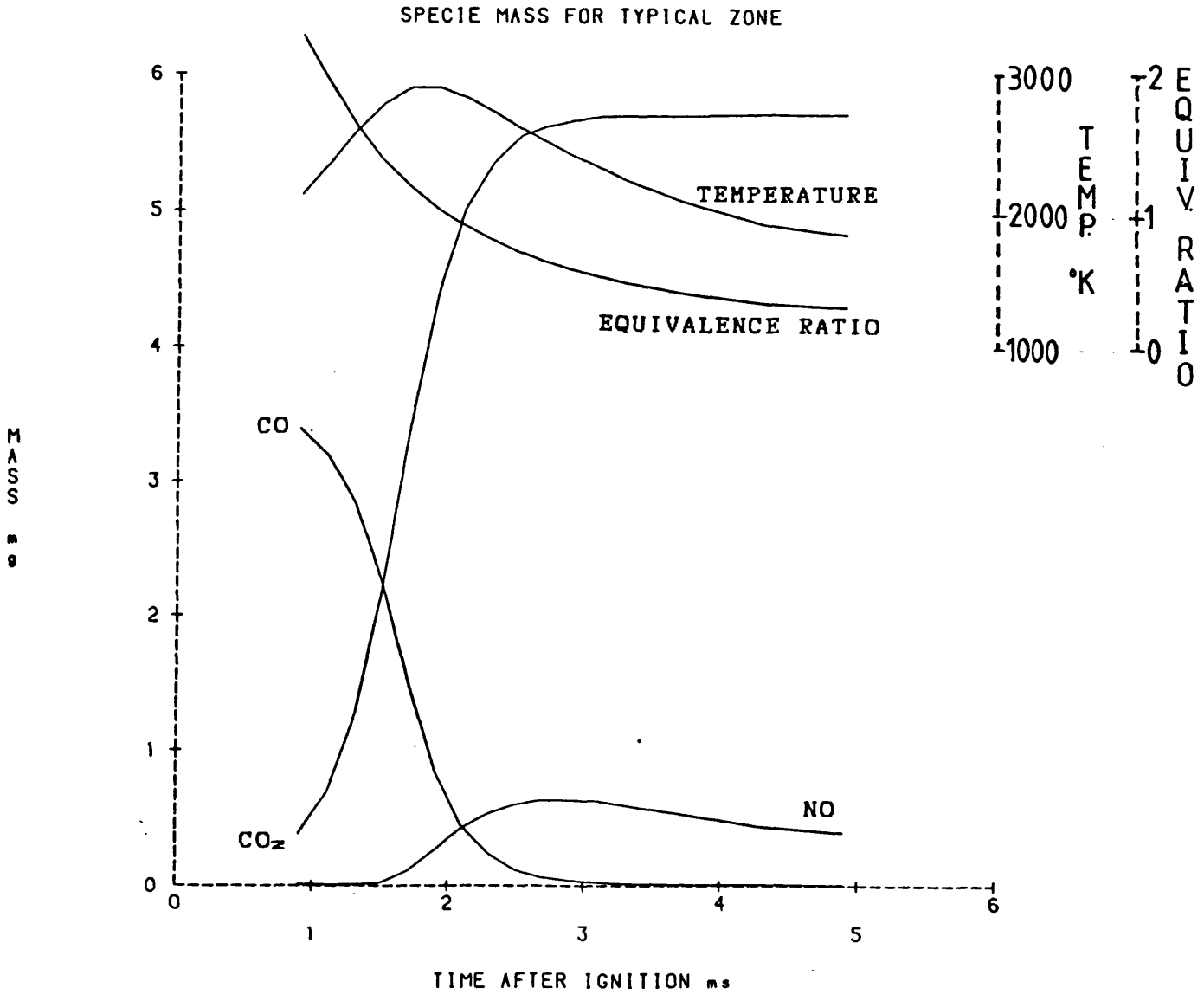

Figure 7.29 Carbon & Nitrogen Monoxide Specie Histories for a typical zone.

CHAPTER 8

Conclusions.

Chapter 8: Conclusions

Cold Injections into Nitrogen

A short film series of injections into room temperature nitrogen were succesfully completed. Drum swirl rates upto 17,500 rpm, which generated gas swirl rates upto 8000 rpm, with chamber pressures upto 55 bar, were achieved. However, the method of illumination only allowed information about spray trajectories to be obtained.

At the highest swirl rates and pressures, the spray, although deflected, still reached the chamber wall (fig. 4.11). No upwind wall jet was produced at this condition with the fuel being swept away by the swirl generating drum.

The spray penetrations were compared with experimental correlations and the closest agreement was achieved with an equation by Chiu, Shahed and Lyn (31) at low swirl levels. At high swirl levels, their correlation overestimated the effects of swirl, but this was partly due to the type of swirl generated in the combustion bomb. However, the closeness of this correlation was probably due to similarities between these experimental tests and those from which the correlation were derived. In addition their correlation was not comprehensive in the fact that it ignored the effects of certain experimental parameters (eg nozzle hole diameter/ length ratio).

Combustion films

A further short series of good combustion films in terms of image quality, were produced. In these tests, slightly higher levels of swirl were achieved, with drum swirl rates upto 20,000 rpm (approx 9000 rpm gas swirl rate). The effect of swirl on the spray trajectories was less pronounced, than in the cold tests, due to the lower air densities caused by the high gas temperatures.

Conditions within the combustion chamber approached those that may be found in a diesel engine. The most severe conditions achieved were an initial air temperature of 513 C and pressrue of 55 bar, which produced an ignition delay of 2.19 ms). All the films showed that ignition occured in the downwind side of the spray close to the wall (ie 3/4 of the distance from the nozzle to the wall). However, all the films were shot at conditions where ignition was longer or as long as the injection duration.

Heat Release Results

A reasonable number (79 total) of heat release results were produced which simulated the conditions that may be found in a diesel engine. These results demonstrated that this unique combustion could simulate diesel type combustion, with pre-injection chamber pressure of 55 bar, nominal air temperatures upto 600 C (with one at 655 C) and drum swirl rates upto 20,000 rpm (approx. 9,000 rpm gas swirl rate). The shortest ignition delay achieved was almost exactly 1 ms, which was much shorter than the

injection duration of 2.5 ms. The heat release diagrams produced would have been fairly typical for a normally aspirated diesel engine, although possibly rather noisy (eg fig. 5.13), with a relatively large pre-mixed spike. However heat release results were produced which consisted of 75% of diffusion type combustion.

The effects of pressure, temperature and swirl on the combustion process were examined and the most interesting of these was the effect of swirl on ignition delay. Generally, the results demonstrated that the ignition delay decreased with increasing swirl, although this was not conclusive. The uncertainty of this conclusion was due to the effect of swirl on the experimental apparatus and the mean gas temperature.

It was not possible to maintain the same wall temperatures at different swirl levels but at the same nominal gas temperature. In addition, the gas temperature was only measured at three locations, so it was not possible to determine the mean gas temperature very accurately or the exact temperature distribution within the combustion chamber. However, the effect of swirl on the ignition delay at the nominal gas temperature of 600 C was quite pronounced (see figs. 5.23 to 5.25).

A further interesting effect of swirl was its influence on the peak burning rate at different initial conditions. The effect appeared to be related to the severity of the initial conditions; ie as the temperature and pressure increased there was a

transition from the peak burning rate increasing with swirl to the peak burning rate either being unaffected by the level of swirl or decreasing with swirl (see figure 5.48). This behavior may be attributed to the combined effects of swirl on the ignition delay and the fuel/air mixing rate. Increasing the swirl increases the mixing rates, but also (apparently) decrease the ignition delay. A shorter ignition delay decreases the time available for pre-mixed fuel to be prepared, but higher swirl levels will increase the mixing rates. At severe conditions (high pressure and temperature) the effect of swirl on ignition delay becomes more dominant.

Combustion Model

With a few modifications, the multizone combustion model developed from the work of Shahed, Chiu and Lyn (31,46) was able to reproduce the heat release results obtained from the combustion bomb. However, the model was only really applicable to low swirl, high temperature (short ignition delay) conditions. With longer ignition delays the lack of a pre-mixed burning submodel became important.

The restriction to low swirl levels was mainly due to the simplicty of the jet model, which overestimated the effects of swirl on the mixing rates. The jet mixing model did not include the effect of wall mixing either. However, the combustion submodel, which is superimposed onto the jet mixing model, could be adapted to a more sophisticated jet mixing model. With the addition of an ignition delay and a pre-mixed combustion model, a much more useful and

universal model might be obtained. The model could be further improved, if the potential to model emissions was also developed.

CHAPTER 9

Suggestions for Further Work.

Chapter 9: Suggestions for further work

Combustion bomb design

This work has highlighted certain areas of design, which, in hindsight, could be improved.

This combustion work, theoretical and practical, has shown that too much air exists in cavities (between the heating coils) outside the combustion bowl. This large proportion of air increases the effective heat transfer and reduces the mixing rate in the later stages of combustion. A new design would need to reduce the proportion of air in these cavities.

The effect of swirl on the ignition delay was not conclusive, partly because the swirl level could not be altered independently of the head temperature. If the head temperature could be controlled independently (with heating coils?), then this would reduce its influence on the results as well as possibly producing a more uniform temperature distribution within the combustion chamber.

A further modification, which would help produce a uniform temperature distribution, would be to improve the thermal isolation of the swirl generating drum from the shaft. This would have the additional benefit of protecting the seals from the high chamber temperatures.

The rotary mechanical seals between the shaft and combustion chamber were not always reliable, partly

because their design was constrained by the earlier design of the combustion chamber. The sealing could be improved if three seals were used in series with the two closest to the combustion chamber configured so that the buffer oil between them was at a higher pressure than the chamber pressure. In this way, the buffer oil would properly lubricate the seals and assist with the sealing. The pressure between these two seals would need to be much higher than the combustion chamber pressure (the reverse of the present situation) so that the combustion pressures could be contained. However with this design, there would be a risk of oil seepage into the chamber.

A much stiffer shaft with less overhang of the drum would also be obtained if the ball bearings were replaced with journal bearings. The best location for these would be between the seals and as close to the drum as possible. A stiffer shaft would also allow higher operating speeds as well as more effective sealing.

Finally, the optical head could be improved so as to provide better visual access under high swirl conditions. In addition, the window sealing could be changed so that cooling would be unnecessary, thus allowing higher chamber temperatures. They could also be flush mounted internally, so as to reduce turbulence generation around the window edges.

Experimental Work

The exact level of swirl and the mean velocity distribution within the bomb was not examined fully. Some work was done with hot wire anemometry equipment under cold conditions, as well as the swirl level being estimated from velocity measurements within an equivalent water rig (see chapter 1). However, better measurements could be obtained with laser anemometry equipment used in conjunction with the optical head. Results obtained in this way would also be more useful when used with information obtained from films.

It has never been possible to accurately predict the heat transfer rates during the combustion phase, as a suitable correlation for these circumstances does not appear to be available. However, if surface mounted heat transfer probes were mounted in the head, the relative levels of heat transfer during the combustion phase could be measured.

All of the films produced, even at the highest swirl levels, showed that little spray deflection was achieved. If it was desired to produce an overswirled (highly deflected spray), then this could be achieved by reducing the nozzle hole size, without sacrificing the quality of the injection.

Combustion Model

The combustion model has a lot of potential, although to be of any real use, further work needs to done in the following areas:-

1. Jet mixing model: This is the most important & weakest part of the model. It would not be difficult to improve it, without any need to alter the combustion submodel.

2. Wall mixing model: At present this is not included, although wall affects are particularly important in small DI diesel engines.

3. Fresh air depletion: A qualitative model was included, but this could be improved so that it had a better theoretical and experimental basis.

4. Ignition delay: No ignition delay model was included although it would be fairly simple to include a simple empirical model.

5. Pre-mixed burning: If this were included the model could be extended to cover a much wider range of realistic conditions.

6. Emissions: The model already includes the ability to predict NO_x pollution and it would be fairly easy to develop this. Other emission models could also be included.

References

1. LILLY L.R.C.
"Diesel Engine Reference Book",Butterworths (publishers) Ltd., 1984.

2. MONAGHAN M.L. & PETTIFER H.F.
"Air Motion & its Effect on Diesel Performance & Emissions", SAE 810255, 1978.

3. CHIGIER N.
"Energy, Combustion & Environment", McGraw-Hill book Company, 1981

4. PACKER J.P. & WALLACE F.J.
"Jet Mixing Studies for Swirled DI Diesel Combustion Chambers. UMIST Presentation, 1981.

5. LYN W.T & VALDMANIS E.
"The Effects of Physical Factors on Ignition Delay", Proc. Instn. Mech. Engrs. 1966-67, Vol. 181 Pt. 2A No. 1

6. EL WAKIL M.M., MYERS P.S. & UYEHARA O.A.
"Fuel Vaporisation & Ignition Lag in Diesel Combustion", SAE Transactions, Vol. 64, 1956, pp 712-729

7. JONG-YUL HA et al.
"Investigation on the Initial Part and the Spray Formation Delay of Diesel Spray", SAE 830451, 1983.

8. HENEIN N.A.
"Combustion & Emissions Formation in Fuel Sprays Injected in Swirling Air" SSAE 710220, 1971

9. HENEIN N.A.
"Analysis of Pollutant Formation and Control & Fuel Economy In Diesel Engines", Energy & Combustion Science, Student Ed. 1, Univ. of Sheffield, 1975

10. PEREZ J.M. & LANDEN E.W.
"Exhaust Emission Charteristics of Pre-combustion Chamber Engines", SAE 680421, 1968

11. KHAN I.M. and GRIGG H.C.
"Progree of Diesel Combustion Research",CIMAC, 9th International Congress on Combustion Engines, Stockholm ,Sweden, paper A-18, May 1971

12. SMITH GEORGE W.
"Kinetic Aspects of Diesel Soot Coagulation" SAE 820466, 1982

13. MATSUI Y., KAMIMOTO J. and MATSUOKA S.
"Formation and Oxidation Processs of Soot Particulates in a DI Diesel Engines - An Experimental Study via the Two-Color Method", SAE 820464, 1982

14. KHAN I.M.
"Formation and Combustion of Carbon in a Diesel Engine", Proc. Instn. Mech. Engrs. 1969-70, Vol. 184 Pt. 3J

15. LAVOIE G.A., HEYWOOD J.B. & KECK J.C.
"Experimental & Theoretical Study of Nitric Oxide Formation in Internal Combustion Engines", Combustion, Science & Technology, 1970, Vol. 1, pp 313-326

16. WHITEHOUSE N.D. & BALUSWAMY N.
"Calculations of Gaseous Products During Combustion in a Diesel Engine Using a Four Zone Model", SAE 770410, 1977

17. KHAN I.M., GREEVES. G. & WNG C.H.T.
"Factors Affecting Smoke & Gaseous Emissions from Direct Injection Injection Engines and a Method of Calculation", SAE 730169, 1973

18. LEE D.W.
"The Effect of Nozzle Design & Operating Conditions on the Atomization & Distribustion of Fuel Sprays", NACA Report 425, 1932

19. LEVY J.M.
"Higher Hydrocarbon Combustion 1. Proimary Process in Fuel-Rich Acetylene Combustion", Combustion & Flame 46, 7-16 (1982)

20. WIEDEMANN B. & HOFBAUER P.
"Data Base for Light-Weight Automotive Diesel Power Plants", SAE 780634, 1978

21. MONAGHAN M.L.
"The High Speed Direct Injection Diesel for Passenger Cars", sAE 810477, 1981

22. LYN W.T.
"The Spectrum of Diesel Combustion Research", Proc. Instn. Mech. Engrs. 1969-70, Vol. 184 Pt. 3J

23 EISELE E. & BINDER K.
"Improvements with the High-Speed DI Diesel", Engineering by Adaption, D22-1, 1979

24. MELTON R.B. & ROGORSKI A.R.
"The Interaction of Air Motion, Fuel Spray & Combustion Process", ASME Journal of Engineering for Power, 1972

25. SASS R.
"Compressorless Diesel Engines", Springer, Berlin 1929

26. MEHLIG H.
Auto-Tech Z. 37 (1934)

27. BORMAN G.L. & JOHNSON J.H.
"unsteady Vaporization Histories & Trajectories of Fuel Drops Injected into Swirling Air" SAE 598B, 1962

28. NEWMAN J.A. & BRZUSTOWSKI T.A.
"Behavior of a Liquid Jet near the Thermodynamic Critical Region", AIAA Jounrnal, Vol 9, No. 8, pp 1595-1602, 1971

29. SAVERY C.W. & BORMAN G.L.
"Experiments on Droplet Vaporization at Supercritical Pressures", Proc. AIAA 8th Aerospace SIC meeting, 1970

30. WALLACE F.J. & PACKER J.P.
"Jet Mixing Studies for HIgh Swirl DI Diesel Combustion Chambers", Combustion Presentation, UMIST, 1981

31. CHIU W.S., SHAHED S.M. & LYN W.T.
"A Transient Spray Mixing Model for Diesel Combustion", SAE 760128, 1976

32. RIFE J. & HEYWOOD J.B.
"Photographic and Performance Studies of Diesel Combustion with a Rapid Compression Machine", SAE Trans. Vol. 83, No. 4, paper 740948, 1974

33. VARA PRASAD C.M. & KAR SUBIR
"An Investigation on the Diffusion of Momentum & Mass of Fuel in a Diesel Spray" ASME Journal of Engineering for Power, 1977

34. VARA PRASAD C.M. & KAR SUBIR
"An Investigation of the Influence of Back Pressure on the Diffusion of Mass & Momentum of Fuel in Diesel Sprays", ASME Journal of Engineering for Power, 1978

35. MELTON Jr R.B.
"Diesel Fuel Injection Viewed as a Jet Phenomenon", SAE 710132, 1971

36. ABRAMOVICH G.N.
"The Theory of Turbulent Jets", MIT Press, 1963

37. KEFFER J.F. & BAINES W.D.
"The Round Turbulent Jet in a Cross-Wind", Journal of Fluid Mechanics, Vol. 15. Pt. 4, 1963

38. ADLER D. & LYN W.T.
"The Evaporation & mixing of a Liquid Fuel Spray in a Diesel Air Swirl", Symposium on Diesel Engine Combustion, Inst. Mech. Engrs., 1970

39. WAY R.J.B.
"Investigation of Interaction between Swirl & Jets in Direct Injection Diesel Engines Using a Water Model", SAE 770442, 1977

40. PACKER J.P.
"Diesel Type Combustion Studies in High Swirl Chambers", Ph.D Thesis, Univ. of Bath, 1983

41. KOBAYASHI H., KAMIMOTO T. & MATSUOKA S.
"A Photographics & Thermodynamic Study of Diesel Combustion in a Rapid Compression Machine", SAE 810259, 1981

42. IKEGAMI M., MIWA K. & INADA M.
"A study on Ignition & Combustion of a Diesel Spray by Means of a Rapid Compression Machine", Bull. of the JSME, Vol. 24, No. 195-13, Sept. 1979

43. FUJIMOTO H., SHIMADO T. & SATO G.T.
"Investigations on Combustion in Diesel Engines using a Constant Volume Combustion Chamber", Bull of the JSME, Vol 22, No. 174-15, Dec 1979

44. LAKSHMINARAYAN P.A. & DENT J.C.
"Interferometric Studies of Vapourizing & Combusting Sprays", SAE 830244, 1983

45. WILSON M.
"Integral Modelling of Jets of Variable Composition in Generalised Crossflows" Ph.D Thesis, Univ. of Bath, 1986

46. SHAHED S.M., CHIU W.S. & LYN W.T.
"A Mathematical Model of Diesel Combustion", Diesel Engine Combustion", Instn. Mech. Eng. 1975, C94/75

47. DENT J.C. & DERHAM
"Air Motion in a Four-Stroke Direct Injection Diesel Engine", Proc. Instm. Mech. Engrs. 1974, Vol 188, 21/74

48. RHP. Standard Bearings Handbook, Rhp General Bearings Division, 1981

49. HARRIS C.M. & CREDE C.E.
"Shock & Vibration Handbook", McGraw-Hill Book Co. Inc., 1961

50. GREEN W.G.
"Theory of Machines", Blackies & Son Ltd, 1962, pp 977

51. BALCI M
"Heat Release Studies in a Constant Volume Combustion Bomb", MSc Thesis, University of Bath, 1984

52. TAYLOR D.H. & WALSHAM B.E.
"Combustion Process in a Medium Speed Dieesl Engine", Diesel Engine Combustion, Proc. Instn. Mech. Engrs., Vol 184. Pt. 3J (1970) pp 67-76

53. DENT J.C.
"A Basis for the Comparison of Various Experimental Methods for Studying Spray Penetration",

54. FUJIMOTO H., TANEBE H., KUNIYOSHI H. SATO G.T.
"Investigations on the Characteristics of Diesel Spray", Bull of the JSME, Vol 25. No. 200, Feb 1982

55. HAY N. & JONES P.L.
"Comparison of Various Correlations for Spray Penetration", SAE 720776, 1972

56. HENEIN N.A. & BOLT J.
"Ignition Dealy in Diesel Engines" SAE 670007, 1967

57. WHITE C.L.
"Combustion Rig Program Documentation", Sch of Engineering, Univ. of Bath, 1985

58. STRINGER F.W., CLARKE A.E. & CLARKE J.S.
Lucas Engng Rev. 5, 2, 30-41 (1971)

59. WOLFER, H.H
"Ignition Lag in Diesel Engines",
VDI-Furshung-Sheft 392 (1938)

60. LYN W.T.
"Combustion in Compression Ignition Engines"
London Univ Ph.D Thesis, 1953

61. ADLER D. & BARON A.
"Prediction of a Three-Dimensional Circular Turbulent Jet In Crossflow", AIAA Journal, Vol 17, No. 2, (1978)

62. SHIRAKASHI M. & TOMITA Y.
"The Diffusion of Jets in Crossflows", Bull of the JSME, Vol. 21, No. 157-15, July 1978

63. SCOTT W.M. & WATTS R.
"Air Motion & Fuel Distribution Requirements in J High-Speed Direct Injection Diesel Engines", Proc. Instn. Mech. Engrs., 1969-70, paper 17, Vol 184, Pt. 3J

64. SPALDING D.B.
"Combustion & Mass Transfer", Pergamon Press, Oxford, 1979

65. VARA PRASAD G.M & SUBIR KAR
"An Investigation of the Influence of Back Pressure in the Diffusion of Mass & Momentum of Fuel in Diesel Sprays", ASME J. Eng. for Power, Vol 100, pp241, 1978

66. WHITEHOUSE N.D. & WAY R.
"Rate of Heat Release in Diesel Engines & its Correlation with Fuel Injection Data", Proc. Instn. Mech. Engrs. 1969-70, Vol 184, Pt. 3J

67. SHIPINSKI J., MYERS P.S. & UYEHARA O.A.
"A Spray-Droplet Model fro Diesel Combustion", Proc. Instn. Mech. Engrs. 1969-70, Vol 184, Pt 3J

68. IKEGAMI M. & NAGAO F.
"An Analysis of Combustion Knock in Diesel Engines", Proc. Instn. Mech. Engrs., 1969

69. AUSTEN A.E.W & LYN W.T.
"Relation between Fuel Injection & Heat Release in a Direct-Injection Engine & the Nature of the Combustion Processes", Pro. Instn. Mech. Engrs. No. 1, 1960-61 pp 47-62

70. BASTRESS E.K., CHNG K.M. & DIX D.M.
"Model of Combustion & Nitrogen Oxide Formation in Direct Injection Compression-Ignition Engines", SAE 719053, 1971

71. GRIGG H.C. & SYED M.H.
"The Problem of Predicting Rate of Heat Release in Diesel Engines", Proc. Instn. Mech. Engrs. 1969-70, Vol 184, Pt 3J

72. WHITEHOUSE N.D. & SAREEN B.K.
"Prediction of Heat Release in a Quiescent Chamber Diesel Engine Allowing for Fuel/Air Mixing", SAE 740084, 1974

73. BALUSWAMY N.
"Spatial & Temporal Distribution of Gaseous Pollutants in a Diesel Engine Combustion Chamber", Ph.D Thesis, Univ. of Manchester, 1976

74. HODGETTS D. & SHROFF H.D.
"More on the Formation of Nitric Oxide in a Diesel Engine", Instn. of Mech. Engrs, C95/75, 1975

75. MEGUERDICHIAN M.
"Mixture Formation and Heat Release in Diesel Engines", Ph.D Thesis, Univ. of London, 1978

76. HIROYASA H., TOSHIKAZO K. & MASATAKA A.
"Development & Use of a Spray Combustion Modeling to Predict Diesel Engine Thermal Efficiency & Pollutant Emissions", Bull of the JSME, Vol 26, No. 214-12 to 14, April 1983, pp 569-591

77. ADLER D. & LYN W.T.
"The Evaporation & mixing of a Liquid Fuel Spray in a Diesel Air Swirl", Symposium on Diesel Engine Combustion, Instn. of Mech. Engrs., 1970

78. COX M.G. & HAYES J.G.
"Curve Fitting: A Guide & Suite of Algorithms for the Non-Specialist User",National Physical Laboratory Report NAC 26, Dec 1973

79. ANNAND W.J.D.
"Heat Transfer in the Cylinders of Reciprocating Internal CombustionEngines", Proc. Instn Mech. Engrs., Vol. 177, No. 36, 1963, pp 973-990

80. BENSON R.S.
"Advanced Engineering Thermodynamics", Pergamon Press, 2nd Ed., 1977

81. THERMODYNAMICS RESEARCH CENTRE HYDROCARBON PROJECT. "Selected Values of Properties of Hydrocarbons & Related Compounds", Texas A & M University, 1979

82. NUMERICAL ALGORITHMS GROUP
"Fortran library Manual Mark 2", 1984

83. WHITE C.L.
"Multi-Zone Combustion Model Documentation",Sch of Engineering, Univ. of Bath, 1986